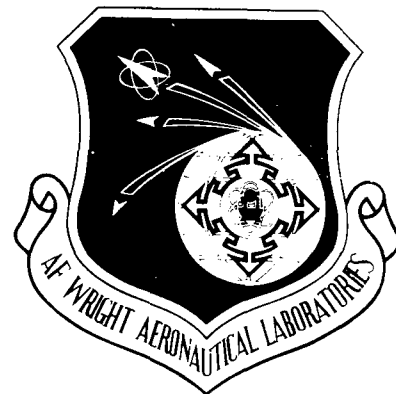AFWAL-TR-85-4009
ADA165214

HIGH STRAIN RATE MATERIAL BEHAVIOR

A. M. RAJENDRAN
S. J. BLESS

University of Dayton
300 College Park Avenue
Dayton, Ohio 45469

December 1985

20040218344

This technical report has been reviewed and is approved for publication.

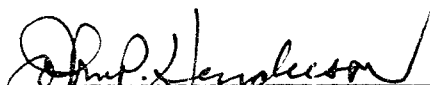
THEODORE NICHOLAS, Matl's Rsch Engr
Metals Behavior Branch
Metals and Ceramics Division
Materials Laboratory

ALLAN W. GUNDERSON, Tech Area Mgr
Metals Behavior Branch
Metals and Ceramics Division
Materials Laboratory

FOR THE COMMANDER

JOHN P. HENDERSON, Chief
Metals Behavior Branch
Metals and Ceramics Division
Materials Laboratory

REPORT DOCUMENTATION PAGE

1a. REPORT SECURITY CLASSIFICATION	1b. RESTRICTIVE MARKINGS
Unclassified	

2a. SECURITY CLASSIFICATION AUTHORITY	3. DISTRIBUTION/AVAILABILITY OF REPORT
2b. DECLASSIFICATION/DOWNGRADING SCHEDULE	Approved for public release; distribution unlimited.

4. PERFORMING ORGANIZATION REPORT NUMBER(S)	5. MONITORING ORGANIZATION REPORT NUMBER(S)
UDR-TR-84-138	AFWAL-TR-85-4009

6a. NAME OF PERFORMING ORGANIZATION	6b. OFFICE SYMBOL (If applicable)	7a. NAME OF MONITORING ORGANIZATION
University of Dayton Research Institute		Air Force Wright Aeronautical Lab. Materials Lab (AFWAL/MLLN)

6c. ADDRESS (City, State and ZIP Code)	7b. ADDRESS (City, State and ZIP Code)
300 College Park Avenue Dayton, Ohio 45469	Wright-Patterson Air Force Base Ohio 45433

8a. NAME OF FUNDING/SPONSORING ORGANIZATION AFWAL/ML Materials Laboratory	8b. OFFICE SYMBOL (If applicable) AFWAL/ML	9. PROCUREMENT INSTRUMENT IDENTIFICATION NUMBER F33615-82-C-5126

8c. ADDRESS (City, State and ZIP Code) AF Wright Aeronautical Laboratories Materials Laboratory (AFWAL/ML) Wright-Patterson AFB, Ohio 45433	10. SOURCE OF FUNDING NOS.			
	PROGRAM ELEMENT NO.	PROJECT NO.	TASK NO.	WORK UNIT NO.
11. TITLE (Include Security Classification) High Strain Rate Material Behavior	62102F	2422	05	03

12. PERSONAL AUTHOR(S)
A. M. Rajendran, S. J. Bless

13a. TYPE OF REPORT	13b. TIME COVERED	14. DATE OF REPORT (Yr., Mo., Day)	15. PAGE COUNT
Final	FROM Aug. 82 TO Sept. 85	1985 December	218

16. SUPPLEMENTARY NOTATION

17.	COSATI CODES		18. SUBJECT TERMS (Continue on reverse if necessary and identify by block number)
FIELD	GROUP	SUB. GR.	strain rate, spall, Hopkinson bar, impact response, shock waves, Bodner-Partom model

19. ABSTRACT (Continue on reverse if necessary and identify by block number)

High strain rate material behavior of 1020, C1008, HY100 steels, OFHC copper, 7039-T64 aluminum, and BeO was characterized. Data were obtained from split Hopkinson bar (SHB) and plate impact test configurations. A high speed photographic system was used to obtain dynamic stress-strain data from necking Hopkinson bar specimens. The state variable based viscoplastic constitutive model of Bodner and Partom was considered for the material modeling. Computer programs and special purpose subroutines were developed to use the Bodner-Partom model in the STEALTH finite difference code. A unique iterative algorithm was developed to evaluate the model constants from both tensile SHB and plate impact test data. The model constants were determined for the five metals. Both tension and compression SHB and plate impact tests were successfully simulated using the Bodner-Partom model constants.

20. DISTRIBUTION/AVAILABILITY OF ABSTRACT	21. ABSTRACT SECURITY CLASSIFICATION
UNCLASSIFIED/UNLIMITED ☒ SAME AS RPT. ☐ DTIC USERS ☐	Unclassified

22a. NAME OF RESPONSIBLE INDIVIDUAL	22b. TELEPHONE NUMBER (Include Area Code)	22c. OFFICE SYMBOL
Theodore Nicholas	(513) 255-2689	AFWAL/MLLN

DD FORM 1473, 83 APR   EDITION OF 1 JAN 73 IS OBSOLETE.

(Block 19 Continued).

Spall data were obtained from plate impact tests. Spall was modeled through critical spall stress and Tuler-Butcher models. The spall model constants were determined for the selected materials through extensive simulations of plate impact tests with STEALTH and SWAP, a method of characteristics code.

New experimental techniques for high strain rate characterization were developed and reported. These techniques include a double flyer plate experiment to study recompaction of voids and a Cranz-Schardin camera to resolve intermediate contours in Taylor impact tests.

PREFACE

TABLE OF CONTENTS

LIST OF ILLUSTRATIONS

LIST OF ILLUSTRATIONS (Continued)

LIST OF ILLUSTRATIONS (Continued)

LIST OF TABLES

SECTION 1

INTRODUCTION

It is well known that the mechanical properties of materials may be influenced by strain rate. Many materials do not exhibit strain-rate dependency at quasi-static strain-rate levels. However, most structural materials show rate sensitivity above a particular strain-rate level, typically 100/s. The magnitude of strain-rate effects, especially in metals, has been a topic of numerous investigations.

Several applications of structural materials involve impulsive loading. Resulting deformations are often very complicated. The material behavior may involve a high rate of strain, large deformation, high pressure and high temperature due to adiabatic heating. Dynamic materials characterization is especially important in the analysis of weapons effects; problems include structural response to explosive loading as well as local failure from impact of gun-launched and explosively-launched projectiles.

Within the last decade, the development of finite element/difference codes has provided additional analytical capability in understanding these problems. It is now well established that the material descriptions can affect the computational results very significantly (see, for example Reference 1). In most computations, the material behavior parameters have been indirectly determined by adjusting input parameters in order to obtain agreement with experimental observations (a process known as "post shot prediction"). This indirect method of obtaining material properties such as dynamic yield strength can often be misleading since error in the physical model can be masked by unrealistic material descriptions. Since dynamic material property data are not readily available, and there are no simple tests from which to obtain these data, code users have often been unable to apply sophisticated constitutive relations for describing materials.

1

For example, most computer codes still do not account for the strain-rate and pressure dependence of yield and flow stresses.

Nicholas (Reference 2) describes in detail the various experimental techniques that are being currently used by several investigators to characterize materials under dynamic loading conditions. The present report describes the combined experimental and theoretical efforts undertaken to model the high strain-rate material response of 1020, HY100, C1008 steels, OFHC copper, 7039-T64 aluminum, and BeO ceramic. This work is an extension of the results presented by Rajendran et al., (Reference 3). The report also describes the development of new techniques for high strain characterization: a double flyer plate experiment to study spall and recompaction, and a Cranz-Schardin camera to observe transient profiles in Taylor impact specimens.

Dynamic tensile and compressive loading under a one-dimensional stress state was achieved with a split Hopkinson bar (SHB). SHB data were extended to higher strains, strain-rates, and mean stresses by high speed photography of necking specimens. The plate-impact test provided spall threshold data and yield strength at very high strain-rate levels.

The state variable based visco-plastic constitutive theory of Bodner and Partom (Reference 4) was used to characterize the metals investigated in this program. A series of automated computer programs were developed to evaluate the model parameters from SHB (Tension) and plate impact test results. The SHB tension and compression tests were simulated with the developed model parameters and compared with the actual test results. The plate impact tests were numerically simulated through a state-of-the-art general purpose finite difference code, called 'STEALTH', using the Bodner-Partom (BP) model parameters for each material. For this purpose, special purpose subroutines describing the BP-model were developed for STEALTH.

Two failure criteria were considered. The first criterion was time independent and based on a critical spall stress. The

2

second was based on a critical value for a time dependent integral as proposed by Tuler and Butcher. A zone model for spall in ceramics was also developed and verified. Failure model parameters were obtained from the numerical simulations of the plate impact tests.

SECTION 2
EXPERIMENTAL PROGRAM

The experimental techniques considered for investigating high strain rate material response were the split Hopkinson bar and the one-dimensional plate impact test configurations. These two tests encompass extremes of stress and strain states. The conventional SHB test exerts a uniaxial stress state in which all three strain components are non-zero. On the other hand, plate impact leads to a uniaxial strain state in which all three stress components are non-zero. The experimental program also included an unconventional SHB test which employed high speed photography of necking instabilities. This 'necking SHB test' provides an effective method to extend the SHB data to higher strains, strain-rates, and mean stress. In this section, the experimental techniques are described and the principal results are summarized.

A parallel activity on this contract has been development of new experimental techniques for high strain rate characterization. Two approaches have been pursued. The first is a double flyer plate technique to study recompaction of voids. The second is use of a Cranz-Schardin camera to resolve intermediate contours in Taylor impact tests. Results of these development efforts are reported in Section 2.4.

2.1   SPLIT HOPKINSON BAR

The split Hopkinson bar provides one of the few research tools for investigating the behavior of materials under uniaxial stress loading at strain rates above 300 s^{-1}. The University's Hopkinson bar has been designed to measure tensile, as well as compressive, stress-strain relationships.

2.1.1   Technique

A split Hopkinson bar consists of three in-line bars, a striker bar, a pressure bar, and a transmission bar, as shown in Figure 1. The University's bars are 12.7mm in diameter. The striker bar is launched by a torsional spring. Its speed is

4
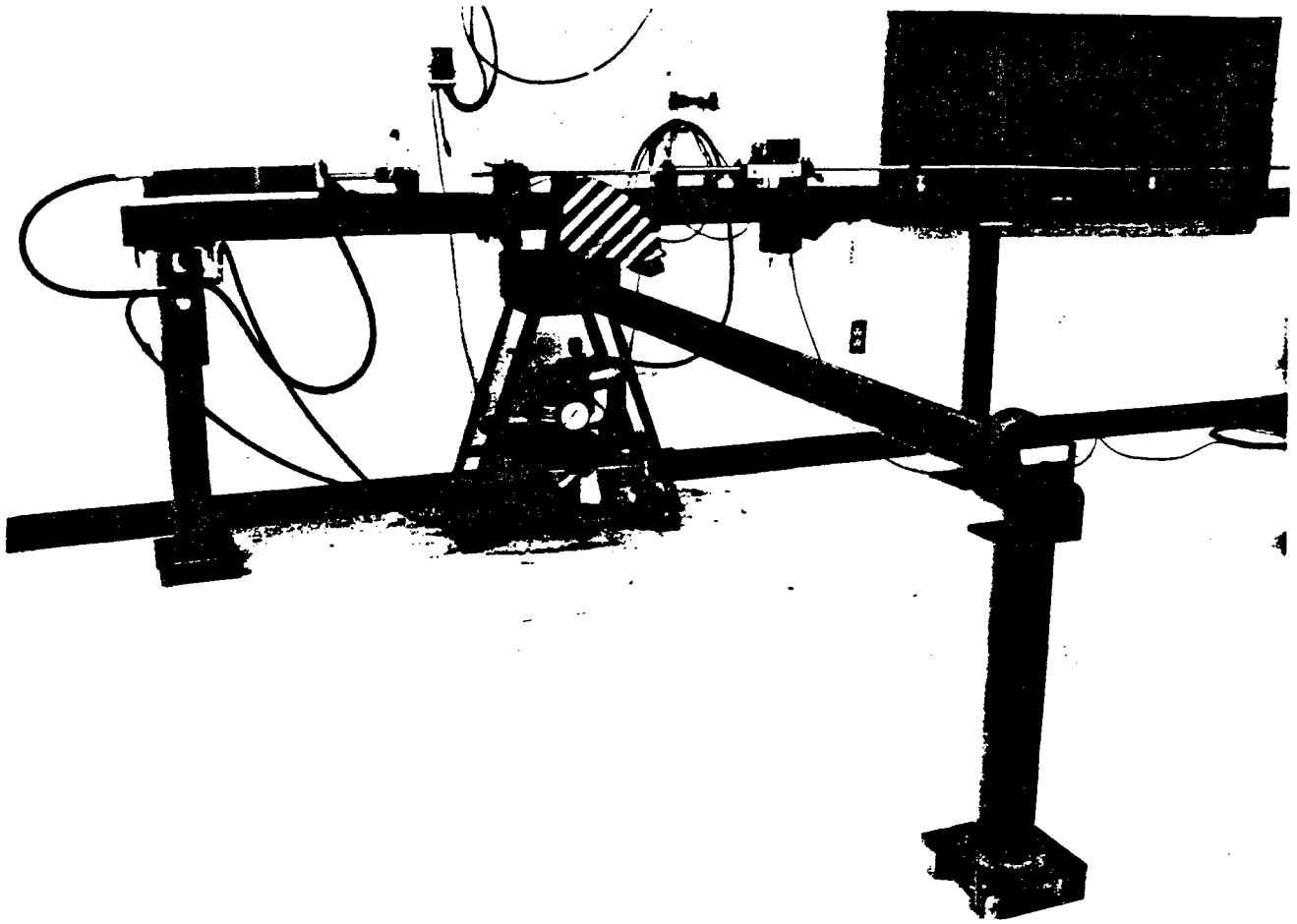
Figure 1. Hopkinson Bar Apparatus.

measured as it crosses two lamp/photodetector stations. The
striker bar strikes the pressure bar, producing an elastic com-
pressive stress wave traveling at $c_E = \sqrt{E/\rho}$, where E is Young's
modulus and ρ the mass density of the bar. The duration of the
stress wave is twice the transit time through the striker bar,
300 μs. For compressive tests, a button sample is placed between
the pressure and transmission bars. For tensile tests, a collar is
placed around the specimen to transmit the compressive pulse from
the pressure bar to the transmission bar. The pressure wave
reflects at the free end of the transmission bar and returns as a
tensile wave. The specimen, shown in Figure 2, is screwed into
both the transmission bar and the pressure bar. The specimen is
loaded in tension by the tensile pulse arriving in the transmission
bar. Analyses of the stress waves reflected and transmitted by the
sample can be used to deduce the stress-strain history of the
specimen. The Hopkinson bar apparatus used in this program is
essentially identical to that described by Nicholas (Reference 5)
and Bless et al., (Reference 6). The essential equations used to
calculate specimen stress and strain have been described by these
and other authors. A brief account is given here for completeness.

Strain gauges are placed equi-distant from the
sample. When the bar apparatus is used as a compression test, the
initial compressive pulse is transmitted to the sample. The
incoming pulse is partially transmitted through the sample, and
partially reflected. Since the bars are of much larger cross
section than the specimen, the boundary condition imposed is nearly
one of constant velocity, or, equivalently, strain rate.

The specimen stress is given by:

$$\sigma_{sp} = E \frac{A_b}{A_s} \varepsilon_t \tag{1}$$

where E and ε_t are the Young's modulus of the bar and the trans-
mitted strain, respectively, and A_b/A_s is the ratio of bar cross
sectional area to sample cross sectional area. The specimen strain
rate is given by:
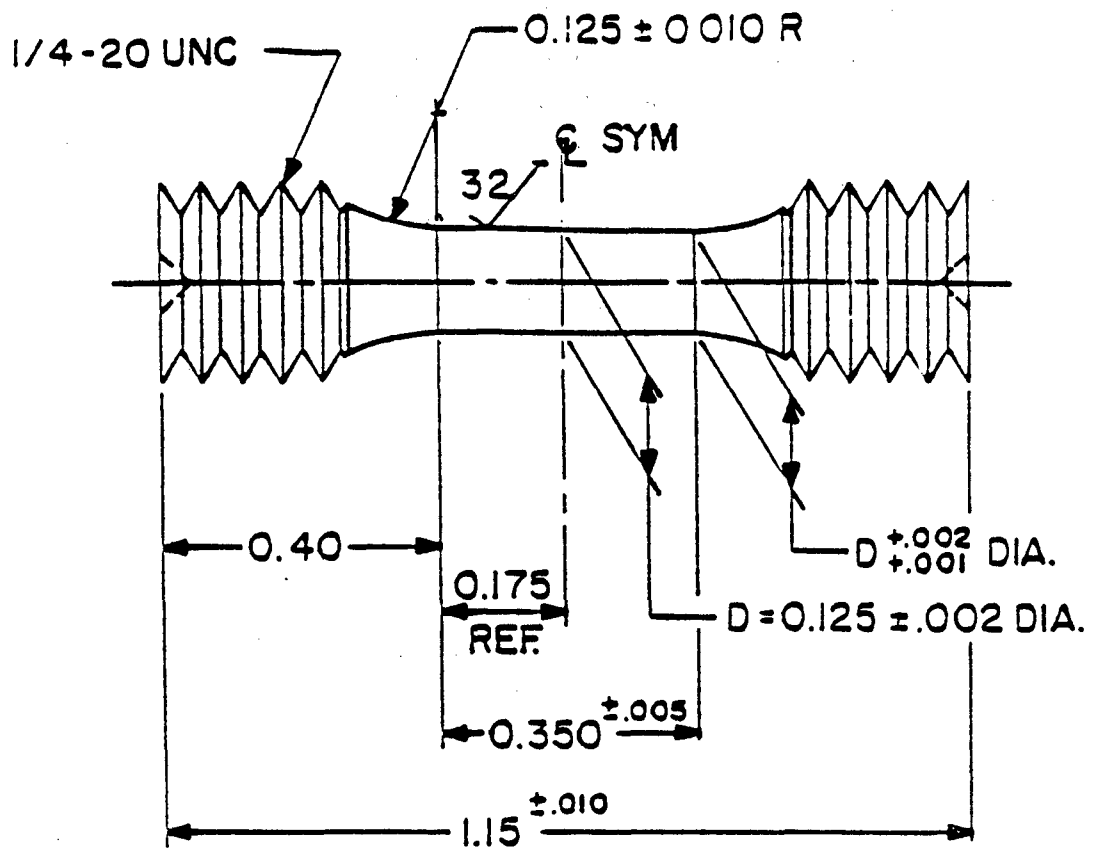
Figure 2.   Hopkinson Bar Specimen Design
             (Dimensions in Inches).

7

$$\dot{\varepsilon}_{sp} = - \frac{2c}{\ell} \varepsilon_r \qquad (2)$$

where ℓ is the sample length, and ε_r is the reflected strain.

These equations show that the specimen strain is obtained by integrating the strain pulse reflected from the specimen, the specimen stress is proportional to the transmitted strain pulse, and the strain rate is proportional to the reflected strain pulse. The equations show that high strain rates are obtained by high striker velocities or short sample lengths. The equations are not valid for elastic response because equilibrium is not achieved during the time needed for the sample to "ring up" to the bar boundary conditions, as discussed above.

The above equations give average, or engineering, stress and strain. True stress and strain can be computed from:

$$\sigma_T = \sigma_{sp}(1+\varepsilon_{sp}) \qquad (3)$$

and

$$\varepsilon_T = \ell n(1+\varepsilon_{sp}) \qquad (4)$$

(Stress and strain are negative in compression.) These equations are valid only when the stress and strain are uniform along the length of the specimen.

2.1.2   Test Results

Dynamic stress-strain material characterization tests were performed on five materials; 1020 steel, C1008 steel, HY100 steel, OFHC copper, and 7039-T64 aluminum. The strain rate range for the tension tests was from 150 to 1800 s^{-1}. The maximum strain rate range for the compression tests was from 160 to 4000 s^{-1}. The results from these tests are summarized in Tables 1 and 2. Each entry in Table 1 is the average of at least two separate tests. The tables list the maximum observed stresses. In cases when tensile failure occurred on the first pulse, these correspond to conventional ultimate stresses.

The dynamic stress-strain results, from the Hopkinson bar apparatus, were extremely consistent from test to test. Figure

TABLE 1

SUMMARY OF TENSILE TESTS

a. 1020 Steel

max eng stress (Kbar)*	max eng strain	strain rate s^{-1}
5.8	0.28	1000
5.9		1100
5.4		400
4.4	0.25	static

b. OFHC Copper

2.6	0.25	875
2.8	0.30	1100
2.9	0.30	1100
2.8	0.30	1100
2.5	0.20	725
3.5	0.60	1800
1.5	0.58	static

c. C1008 Steel

6.30	0.30	1000
6.60	0.48	1750
4.56	0.09	290
5.00	0.18	550
5.32	0.33	1050
4.52	0.09	300
5.00	0.18	600
5.05	0.25	800
5.27	0.35	1100
3.20	0.23	static
3.17	0.23	static

TABLE 1

SUMMARY OF TENSILE TESTS (continued)

d. HY100 Steel

max eng stress (Kbar)*	max eng strain	strain rate s^{-1}
8.7	0.05	150
9.9	0.11	350
11.3	0.17	640
11.5	0.31	960
12.0	0.30	1100
8.8	0.06	180
10.3	0.13	450
11.4	0.23	650
11.7	0.31	930
12.0	0.30	1200
8.8	0.23	static
8.8	0.23	static

e. 7039-T64 Aluminum

4.7	0.12	750
4.6	0.06	300
4.6	0.13	500
4.6	0.16	800
4.8	0.14	800
4.7	0.13	550
4.6	0.07	350
4.3	0.20	static
4.3	0.22	static

* 1 Kbar = 14,504 psi

   = 100 MPA

   = 10^9 dynes/cm^2

10

TABLE 2

SUMMARY OF COMPRESSION TESTS

max eng stress (Kbar)	max eng strain	strain rate range s^{-1}
a. 1020 Steel		
10.0	0.32	2500 – 800
9.8	0.30	2000 – 500
8.2	0.23	1200 – 300
8.5	0.25	1300 – 500
b. OFHC Copper		
9.0	0.6	3500 – 500
9.5	0.6	4000 – 500
7.0	0.5	3000 – 500
7.5	0.5	3100 – 500
c. C1008 Steel		
11.0	0.5	1700 – 3200
10.0	0.4	800 – 2400
8.0	0.25	400 – 2000
d. HY100 Steel		
7.5	0.08	100 – 160
9.0	0.13	200 – 800
11.0	0.14	200 – 1000
4.8	0.08	100 – 500
3.2	0.006	10 – 50
10.5	0.16	500 – 1200
12.0	0.18	600 – 1500
e. 7039-T64 Aluminum		
8.5	0.45	1200 – 3300
7.5	0.35	1500 – 2400
6.9	0.30	600 – 2000

3 shows the results from two tests, conducted at roughly the same strain rate, for each of the five materials. It can be seen from the figure that the results are essentially identical and this is typical of most of the tests conducted under this study.

Quasi-static tensile tests were also conducted to compare the stress-strain data with the dynamic test data. Table 1 summarizes the quasi-static and tensile SHB data. The compression SHB data are summarized in Table 2.

a.   1020 steel

Previous SHB data on 1020 steel have been reported by Nicholas (Reference 5) and Bless et al., (Reference 6). These data contain an unusual amount of scatter, and they cannot be used to evaluate strain rate sensitivity. Additional tests were conducted in order to clarify the behavior of this material. The same stock was used as Bless et al., (Reference 6). Tests were repeated at each strain-rate level, spanning 400 to 1200 s^{-1}. The new data were obtained based on the repeatability of tests at each level. The data for the dynamic tensile tests are presented in terms of an eyeball curve fit of the SHB results. A typical curve fit and the actual data are shown in Figure 4. The results from all tensile tests conducted on the 1020 steel, are shown in Figure 5. The flow stress for a strain rate of 1200 s^{-1} was approximately 15% higher than the quasi-static flow stress, and less than 5% higher than the flow stress for a strain rate of 400 s^{-1}. Hence, there was no significant change in yield stress in the dynamic regime. However, the dynamic yield stress is a few percent higher than the static yield stress.

Compression tests on 1020 steel were conducted for strain rates ranging from 300 - 2500 s^{-1}. The strain rate in compression tests decreased linearly as a function of time, as shown in Figure 6. The results of the compression tests, for three levels of strain rate, are presented in Figures 7 to 9. These figures include the engineering and true stress - strain curves, along with the strain rate - time behavior. They also indicate a slight rate dependence.
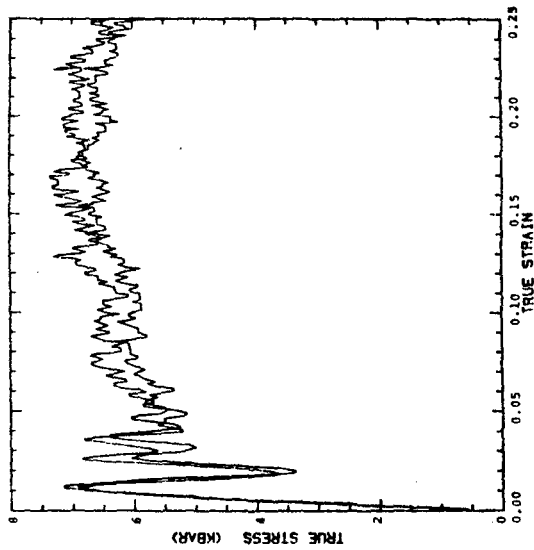
a. 1020 Steel
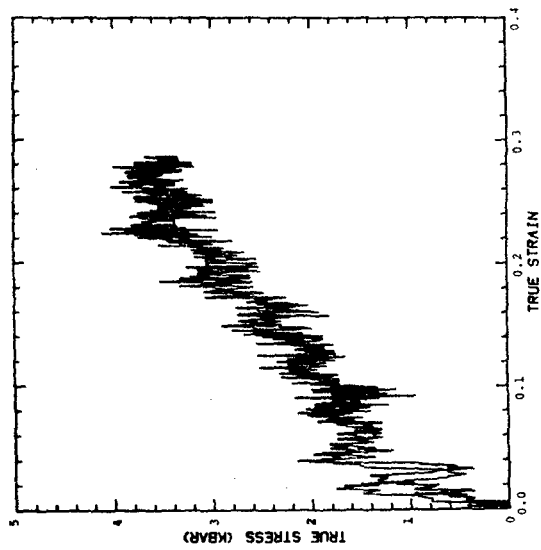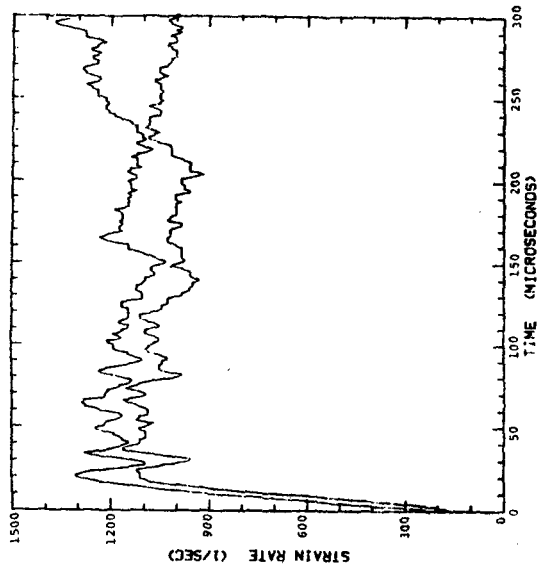
b. OFHC Copper
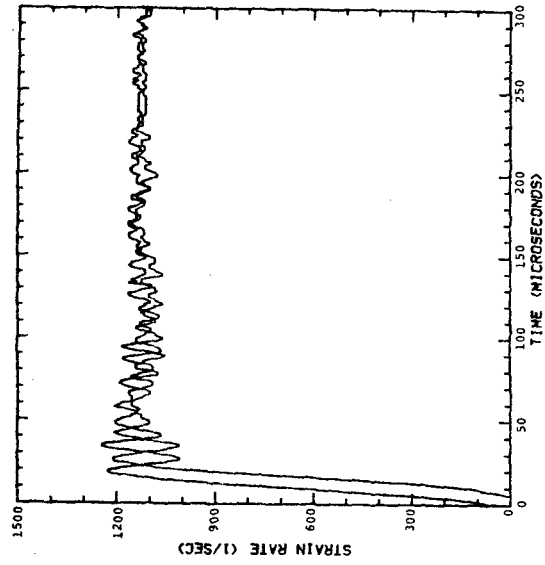
Figure 3. Results of the Dynamic Tensile SHB Tests Illustrating
the Repeatability of the Tests.
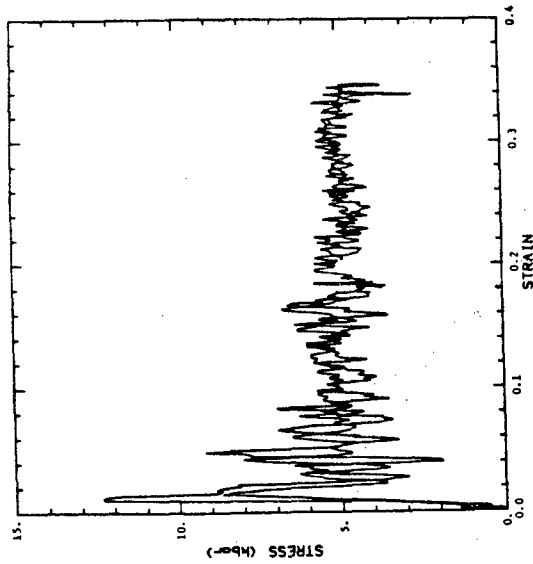
c. C1008 Steel
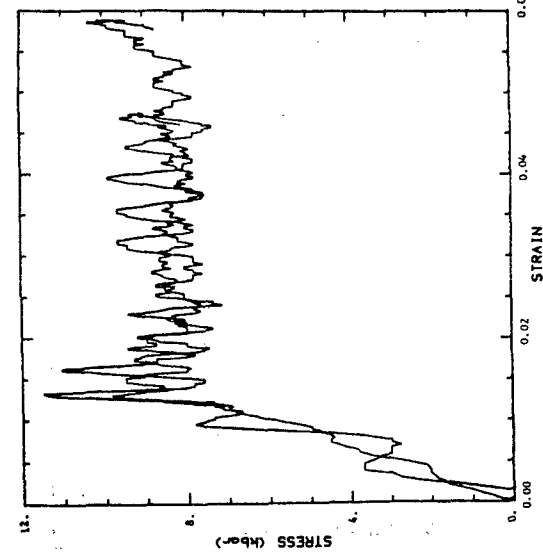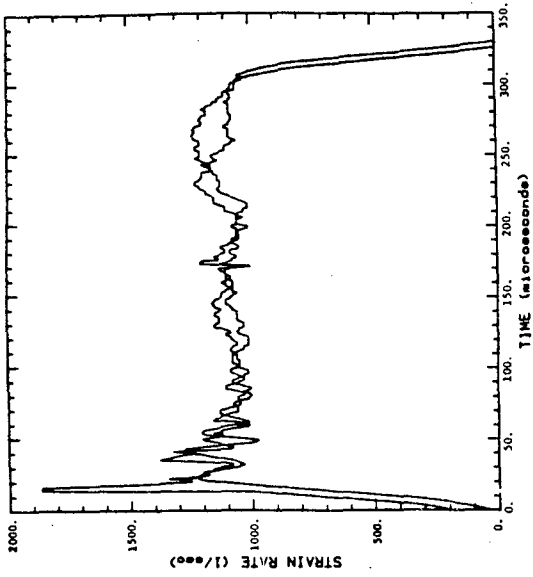
d. HY100 Steel
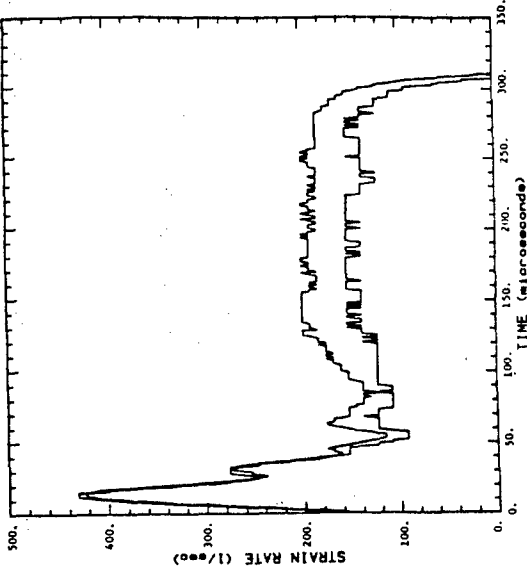
Figure 3 (cont'd). Results of the Dynamic Tensile SHB Tests Illustrating the Repeatability of the Tests.

14
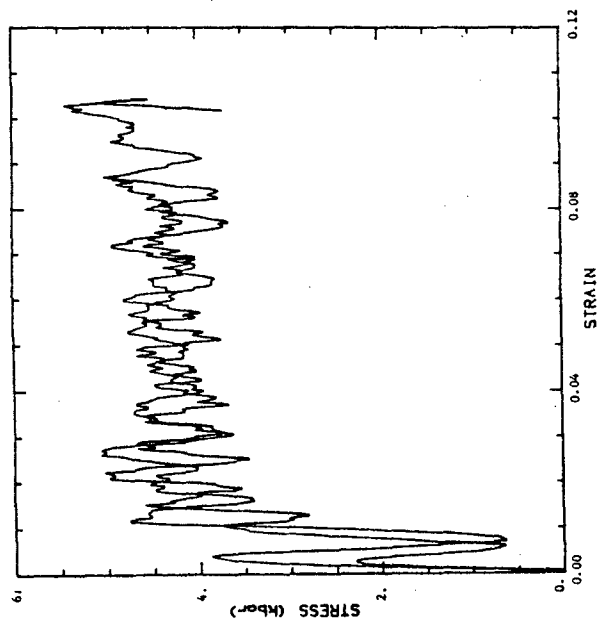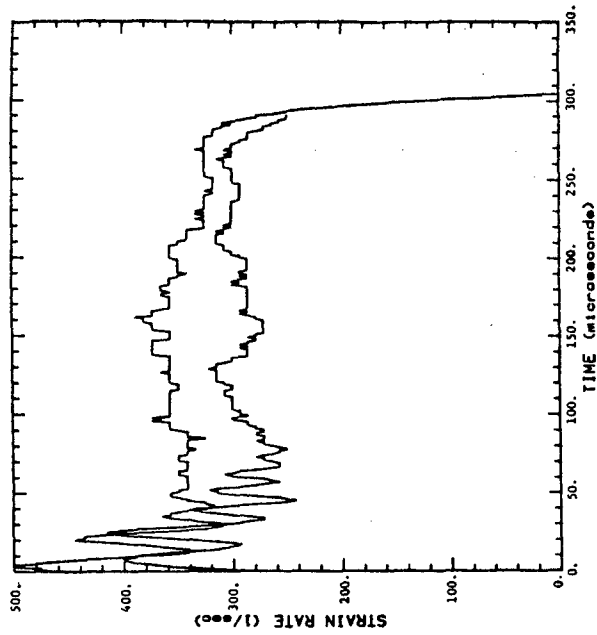
e. 7039-T64

Figure 3 (cont'd). Results of the Dynamic Tensile SHB Tests
Illustrating the Repeatability of the Tests.

15
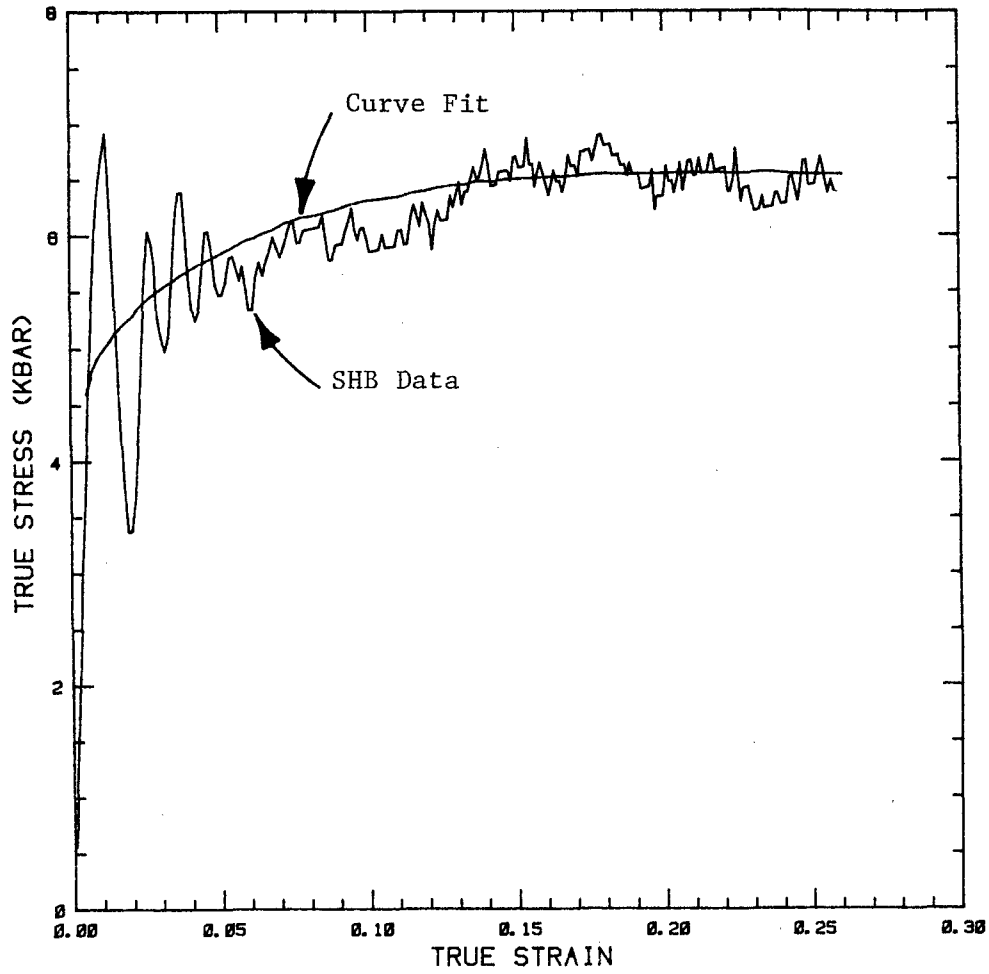
Figure 4.   Curve Fit and Original Data for a
             Dynamic Tensile SHB Test on 1020 Steel.
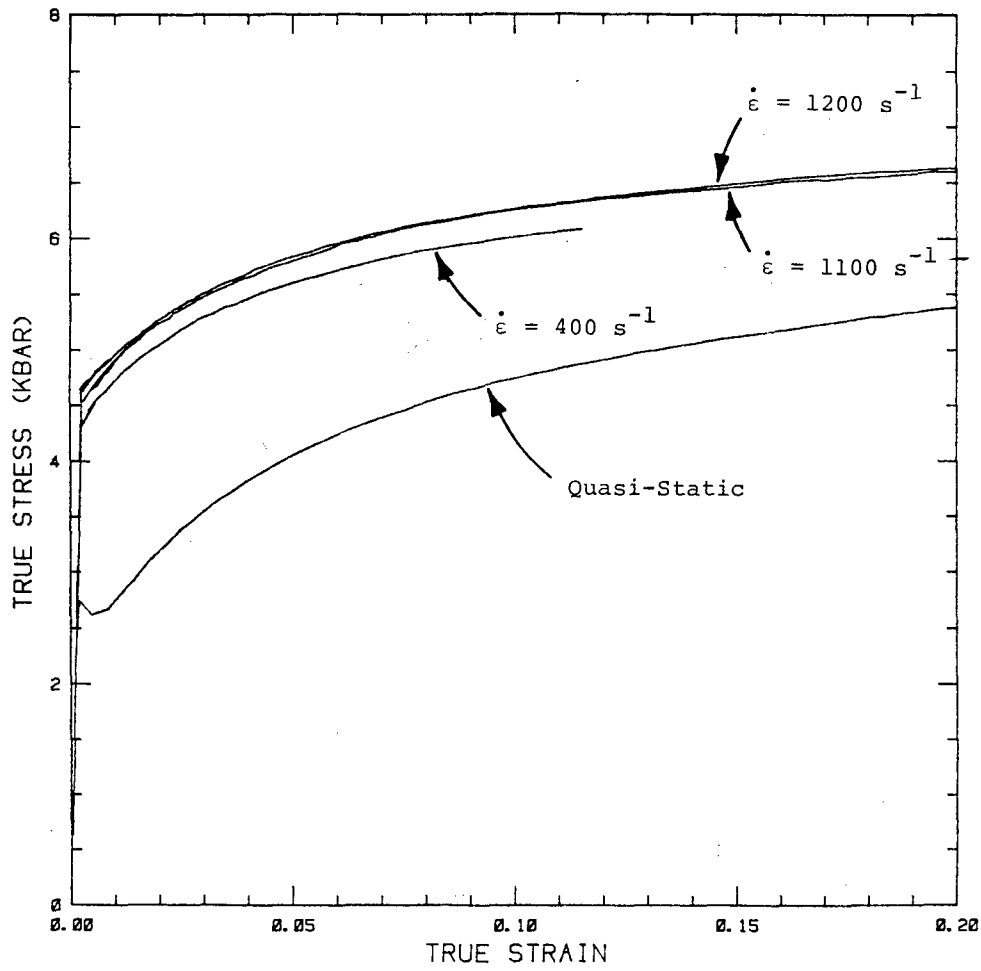
Figure 5.   Results of the Dynamic and Static Tensile
            Tests on 1020 Steel.
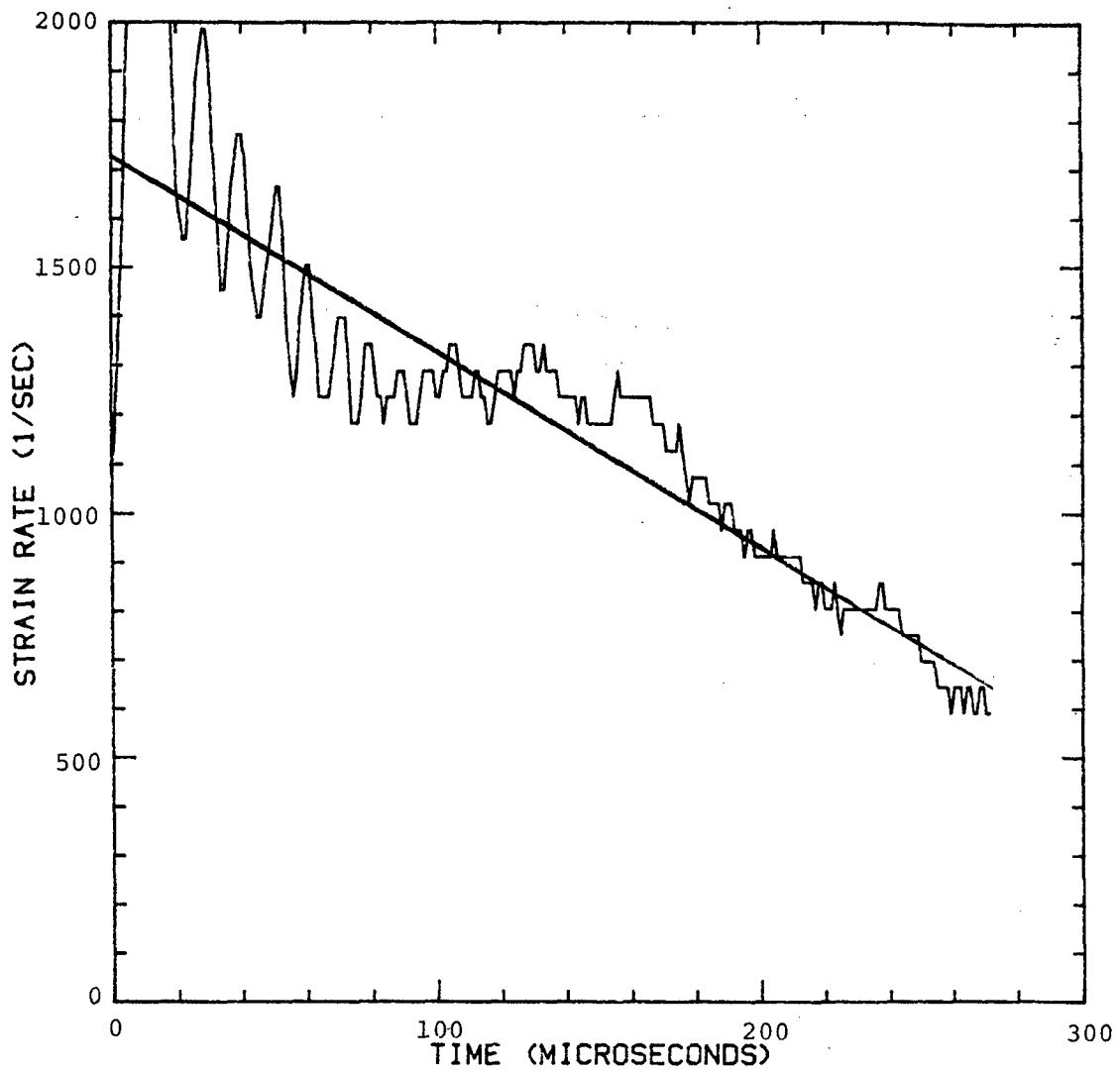
Figure 6.   Strain Rate vs. Time for a Compression
Test on 1020 Steel.
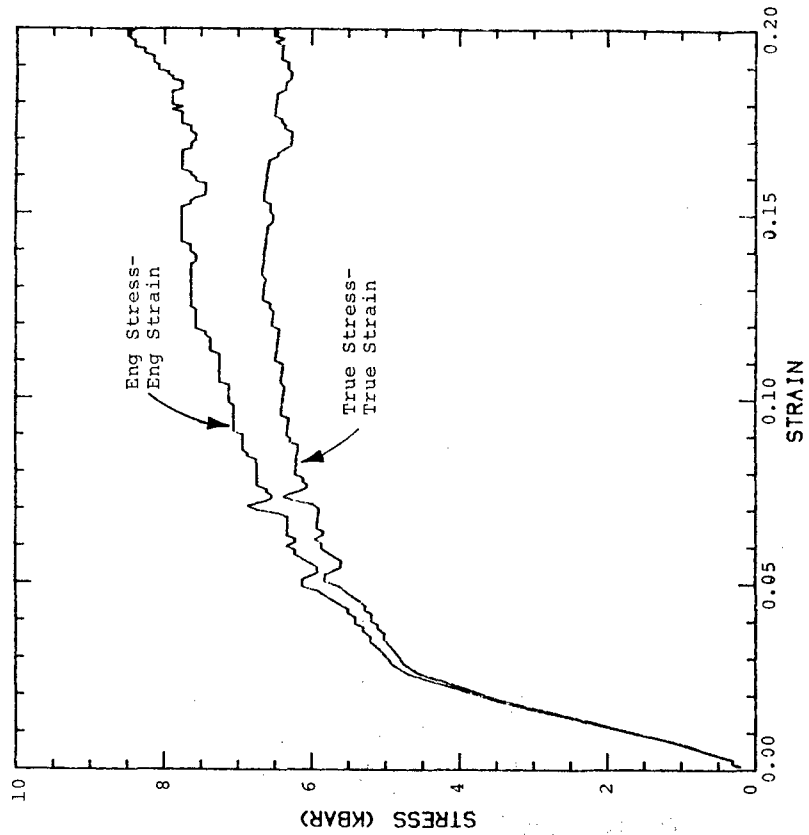
a. Stress–Strain
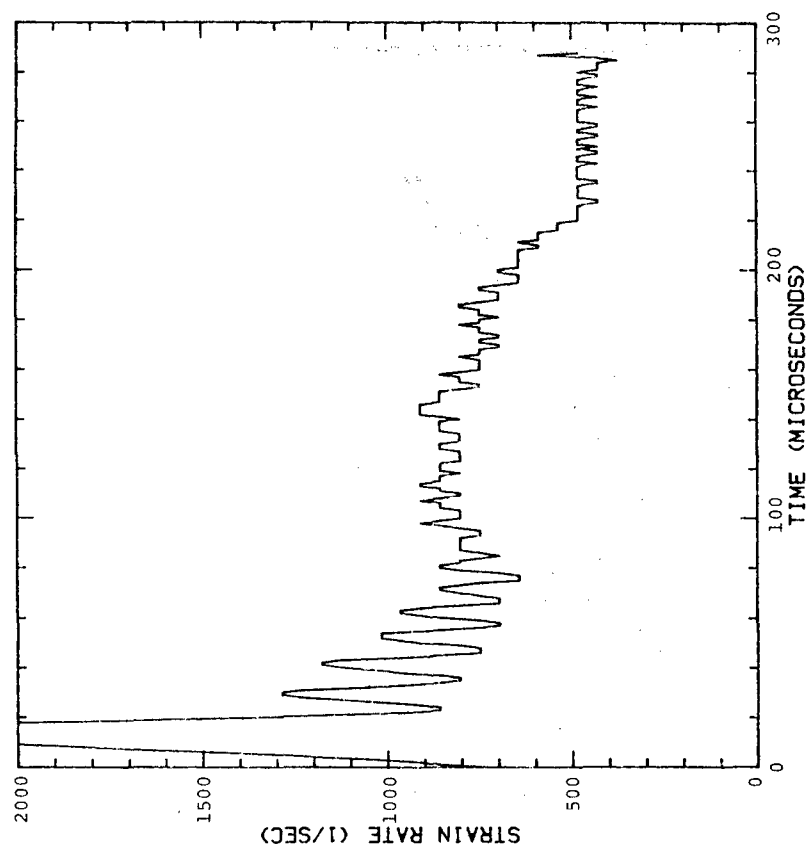
b. Strain Rate–Time

Figure 7.   Results From the Lowest Strain Rate Level
             Compressive SHB Test of 1020 Steel.

19
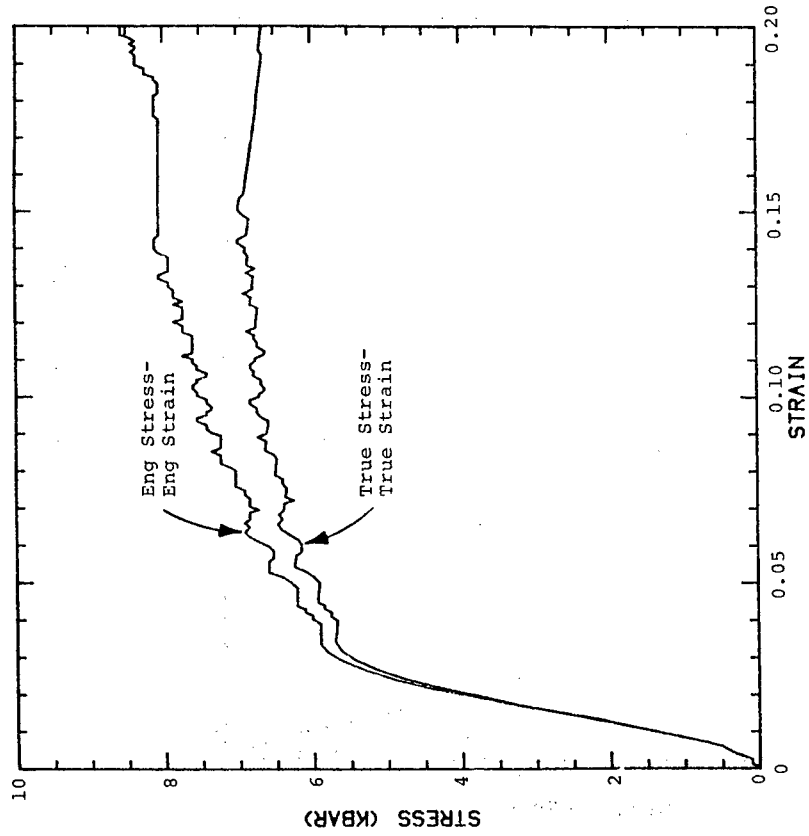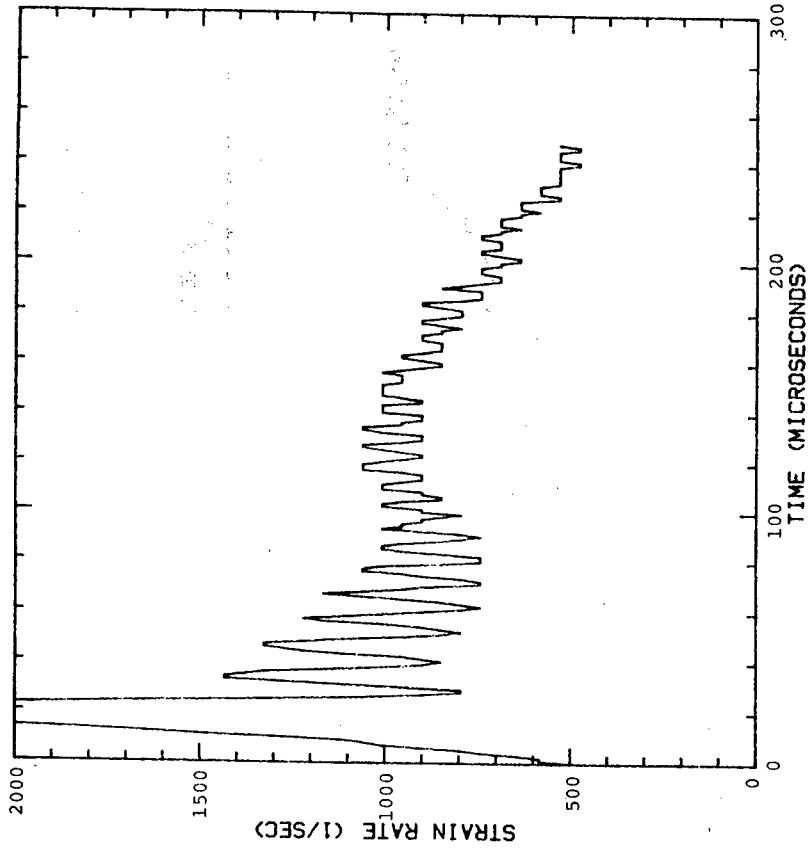
a.   Stress—Strain

b.   Strain Rate—Time

Figure 8.   Results From the Middle Strain Rate Level
Compressive SHB Test of 1020 Steel.

20
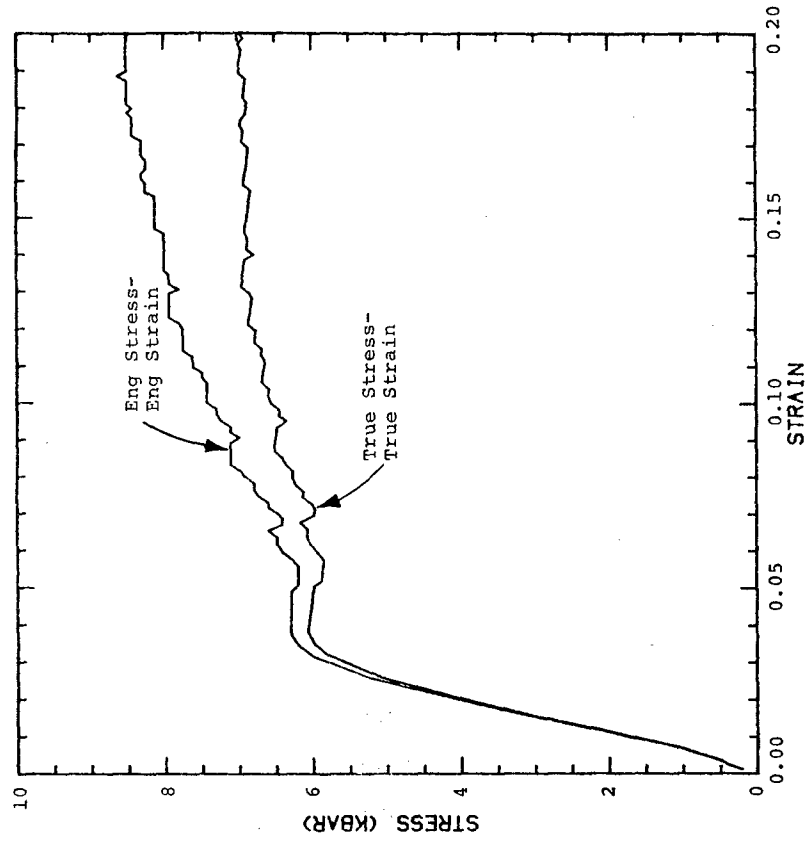
a. Stress-Strain
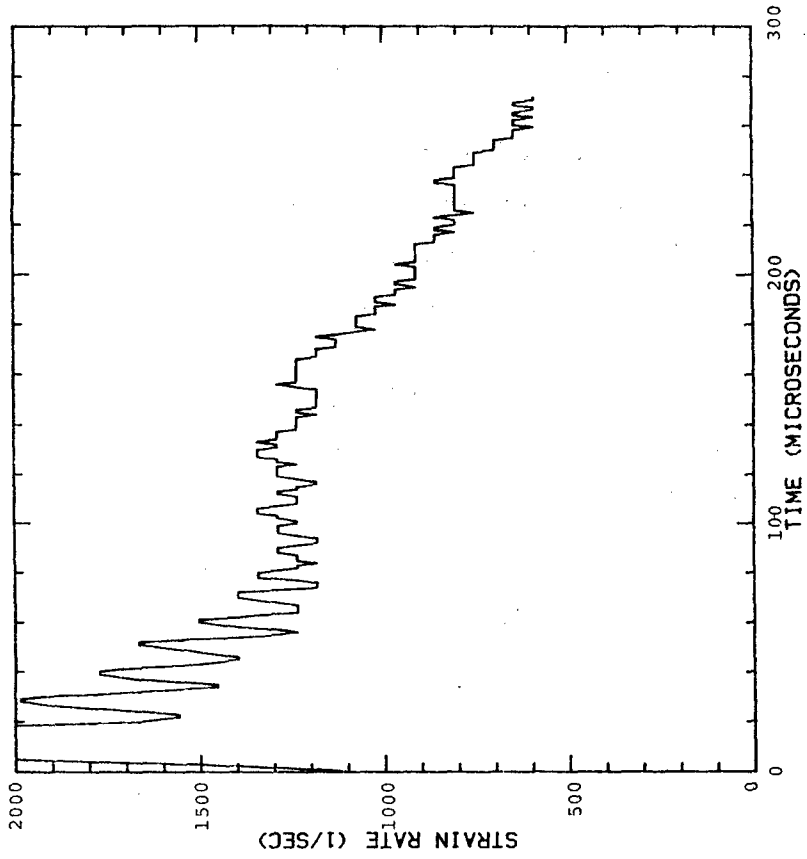
b. Strain Rate-Time

Figure 9.   Results From the Highest Strain Rate Level
Compressive SHB Test of 1020 Steel.

21

b.   OFHC copper

        Dynamic tensile tests on the OFHC copper were
conducted at strain rates ranging from 700 to 1800 s^{-1}. The OFHC
copper was annealed, after machining, at 1000°F for 2 hours and
oven cooled. Figure 10 shows an example of the rough data and
smoothed fit. The results from all tensile tests on OFHC copper
are shown in Figure 11. The dynamic SHB and static tensile
results indicate that the OFHC copper is extremely rate sensitive
and strain hardening.

        Compression tests on OFHC copper were con-
ducted for strain rates ranging from 500 to 4000 s^{-1}. Stress-
strain and strain rate-time data for three levels of strain rate
are presented in Figures 12 to 14. The observed "overshoot" is
believe to be an artifact caused by friction between the specimen
and the bars.

c.   C1008 steel

        C1008 material was supplied by the David
Taylor Naval Ship R&D Center (DTNSRDC). Data for C1008 steel were
obtained for strain rates ranging from 290 to 1750 s^{-1}. Static
tensile tests were also conducted. The data are shown graphically
in Figure 15.

        The flow stress for a strain-rate of 1750 s^{-1}
was approximately three times the static flow stress. From the
SHB tensile test data, it is clear that C1008 is an extremely rate
dependent material even at low strain-rate levels.

        Compression tests on C1008, conducted for
strain rates ranging from 800 to 2500 s^{-1}, are presented in
Figures 16 to 18. Rate dependence again is evident.

d.   HY100 steel

        HY100 steel alloy was supplied by the David
Taylor Naval Ship R&D Center. Ten dynamic tensile SHB tests and
one static test were conducted. The results from different strain
rate level tensile tests conducted on the HY100 steel, are shown
in Figure 19. The HY100 steel showed moderate rate dependent
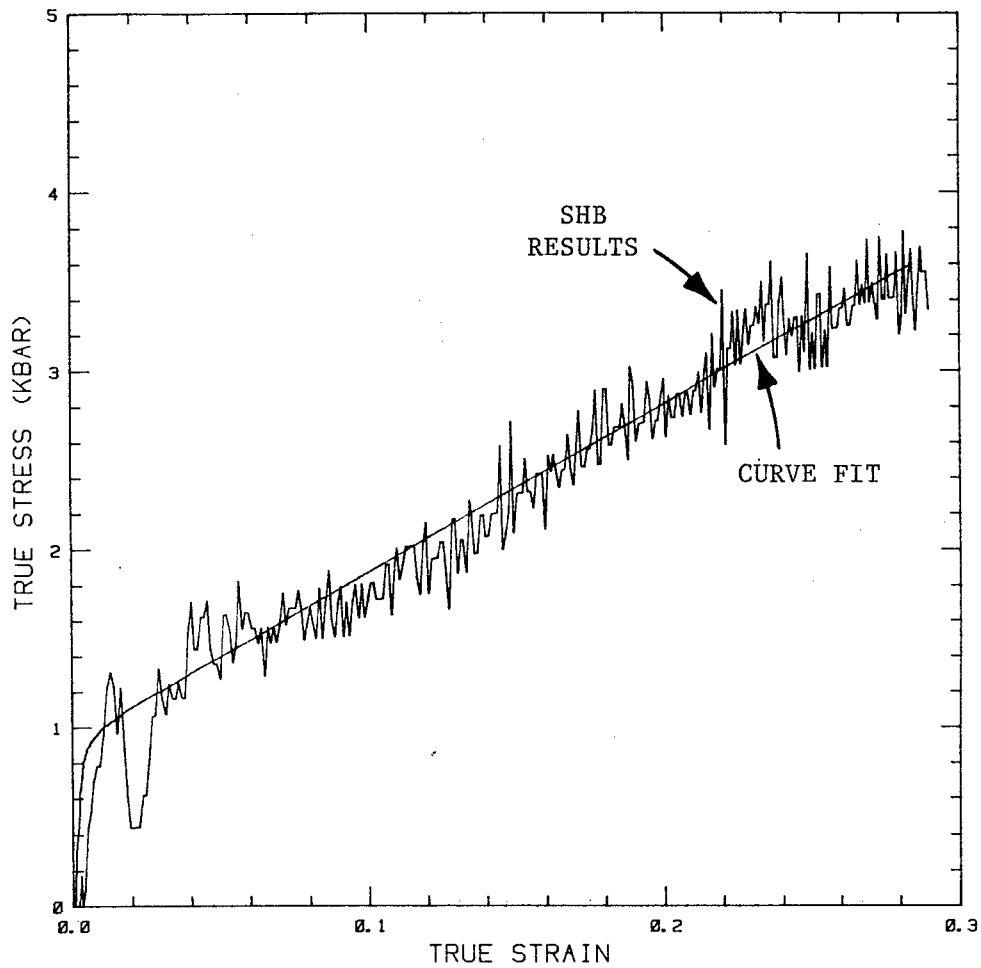
Figure 10.   Curve Fit and Original Data for a
             Dynamic Tensile Test on OFHC Copper.
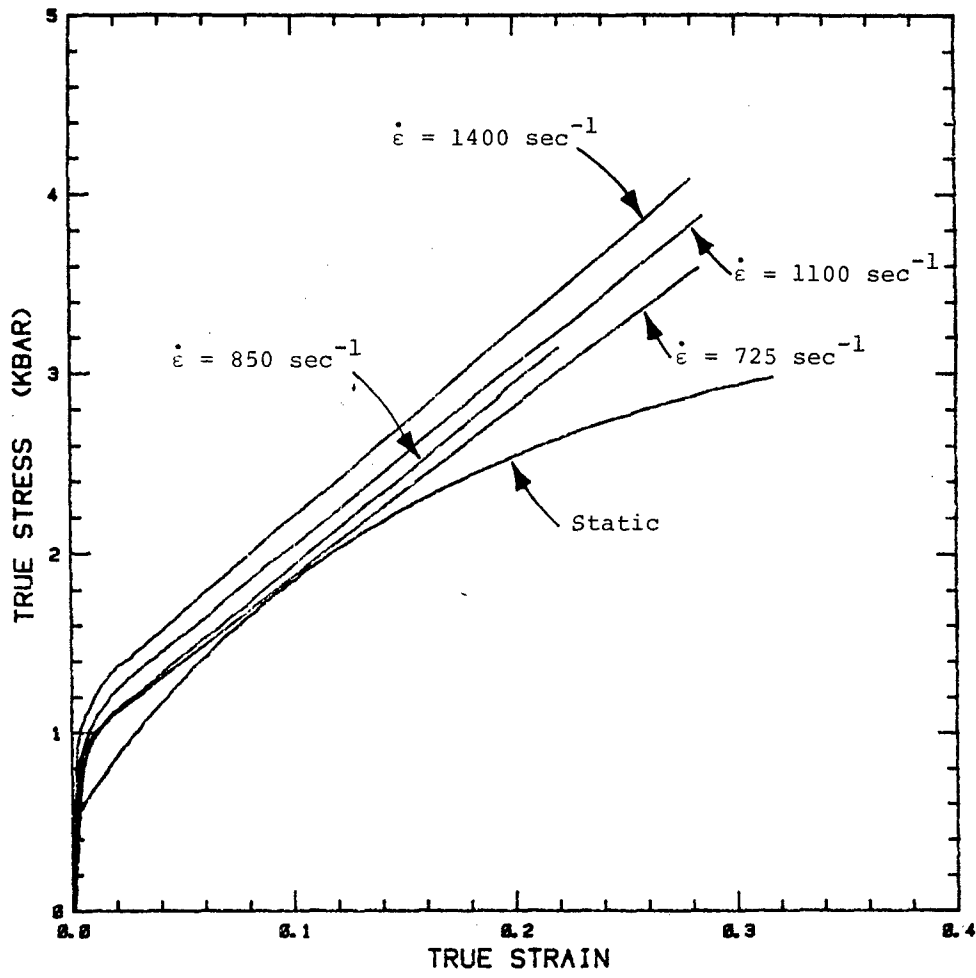
Figure 11.   Results of the Dynamic and Static Tensile
             Tests on OFHC Copper.

24
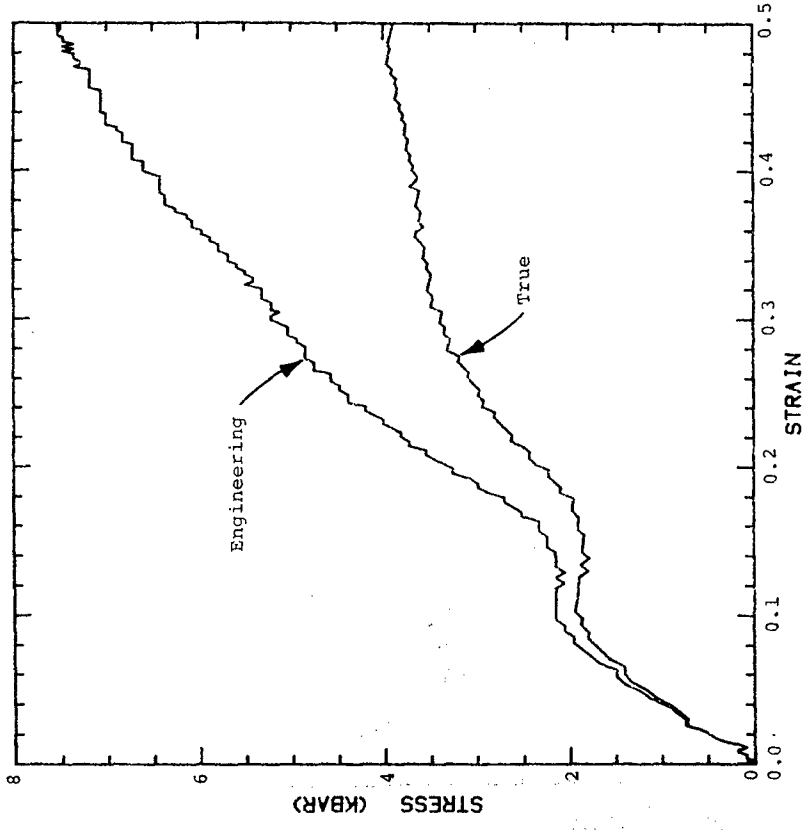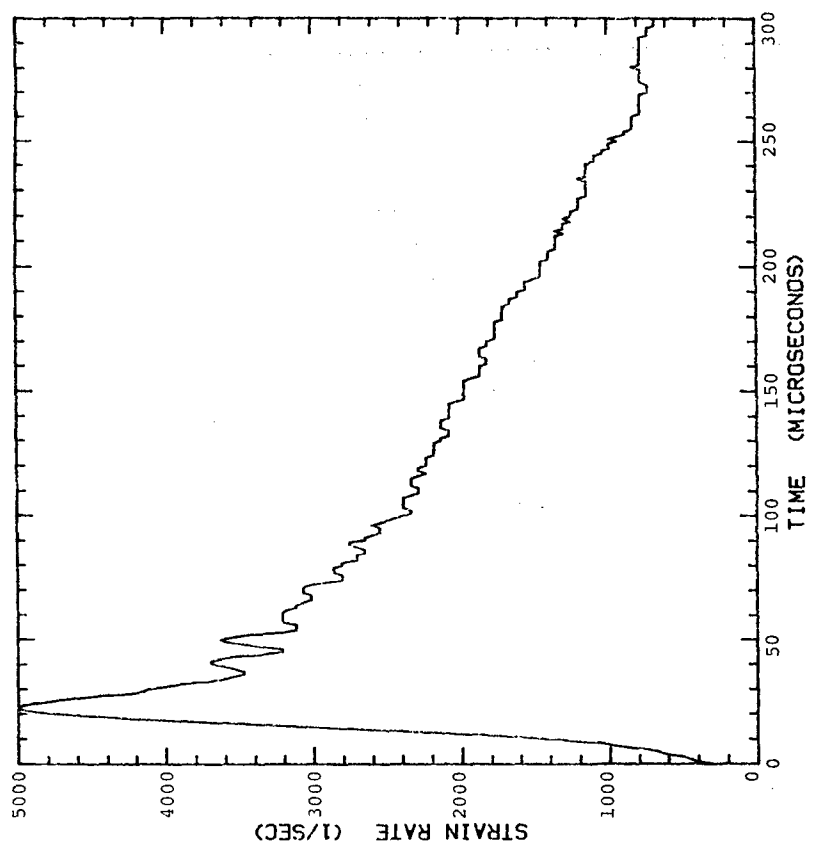
a. Stress-Strain

b. Strain Rate-Time

Figure 12. Results From the Highest Strain Rate Level
Compressive SHB Test on OFHC Copper.

25

b.   Strain Rate-Time

a.   Stress-Strain

Figure 13.   Results From the Middle Strain Rate Level
Compressive SHB Test on OFHC Copper.
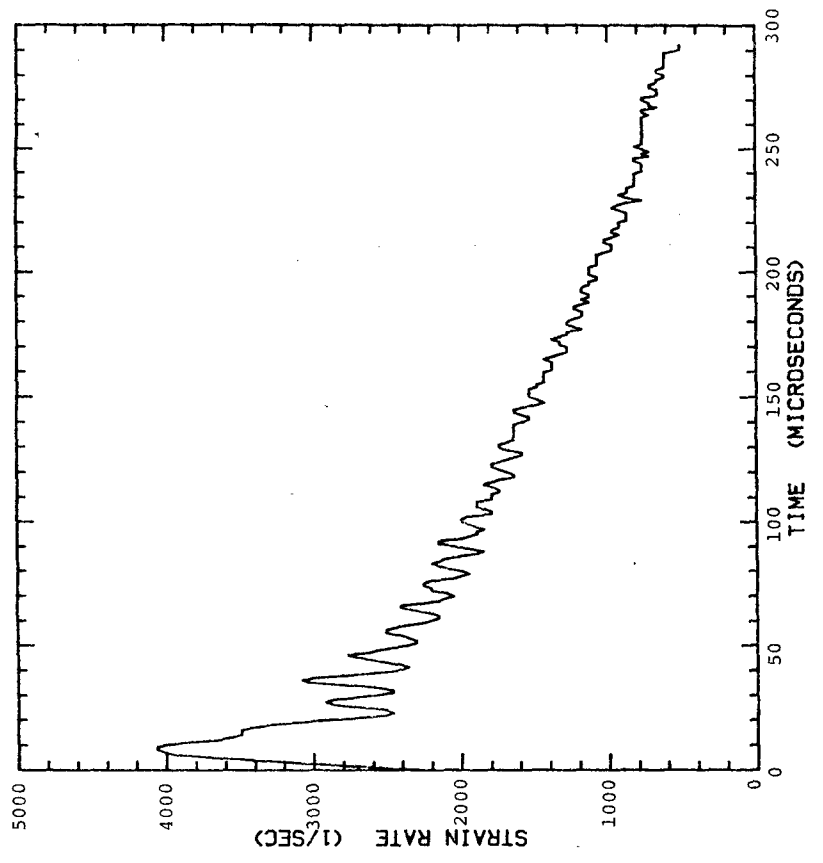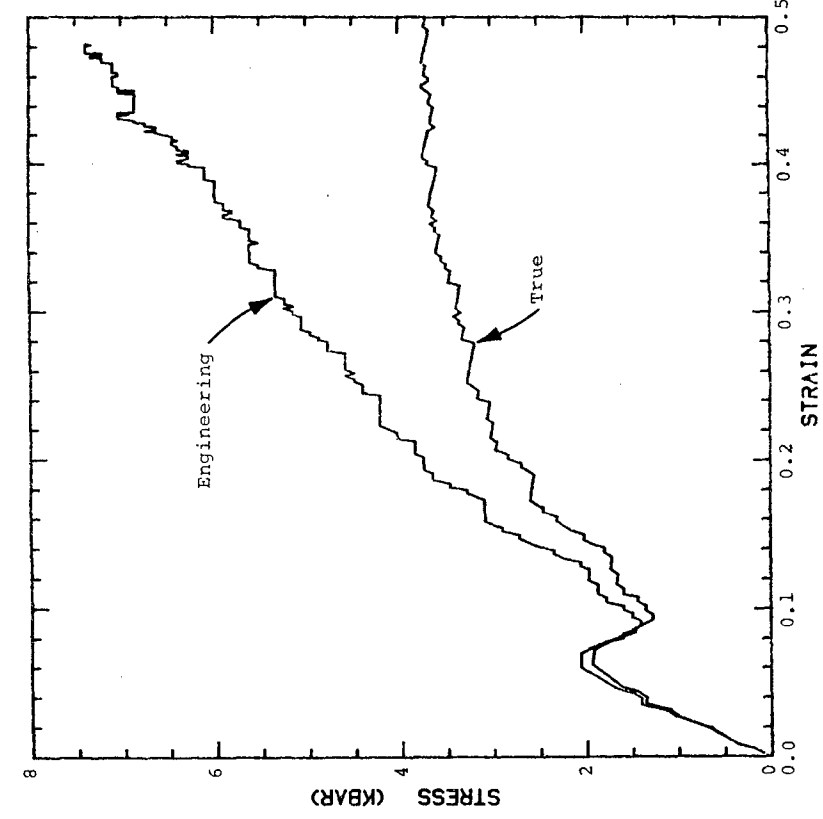
h.   Strain Rate-Time

a.   Stress-Strain

Figure 14.   Results From the Lowest Strain Rate Level
Compressive SHB Test on OFHC Copper.

27
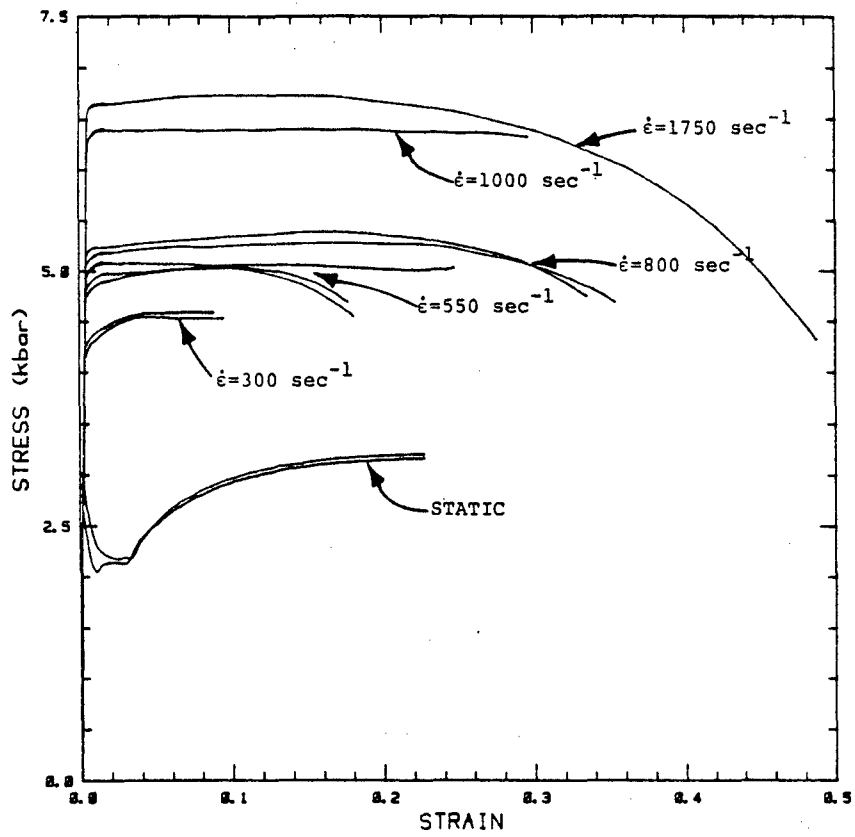
Figure 15.   Results of the Dynamic SHB and Static
              Tensile Tests on C1008 Steel.

28
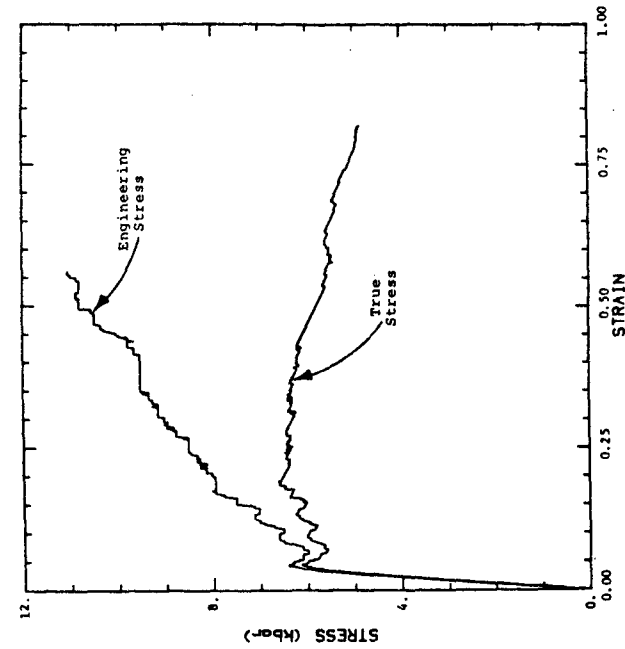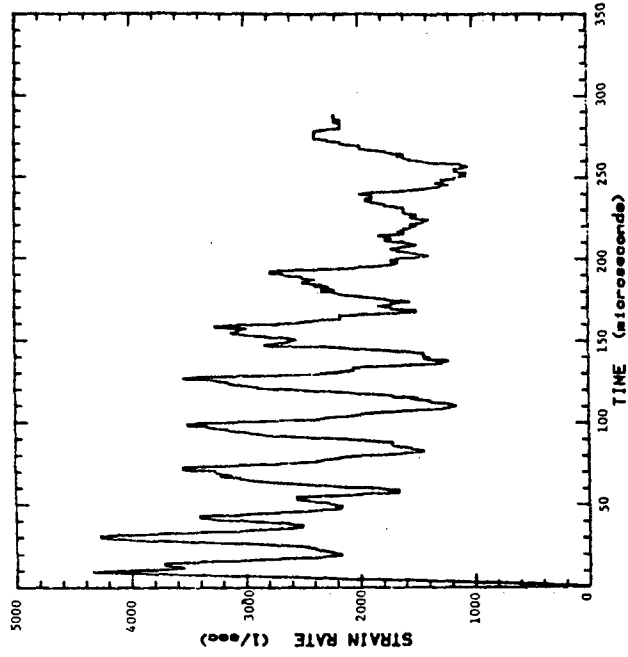
b. Strain Rate vs. Time

a. Stress-Strain

Figure 16. Results from the Highest Strain Rate Level Compressive SHB Test of C1008 Steel.
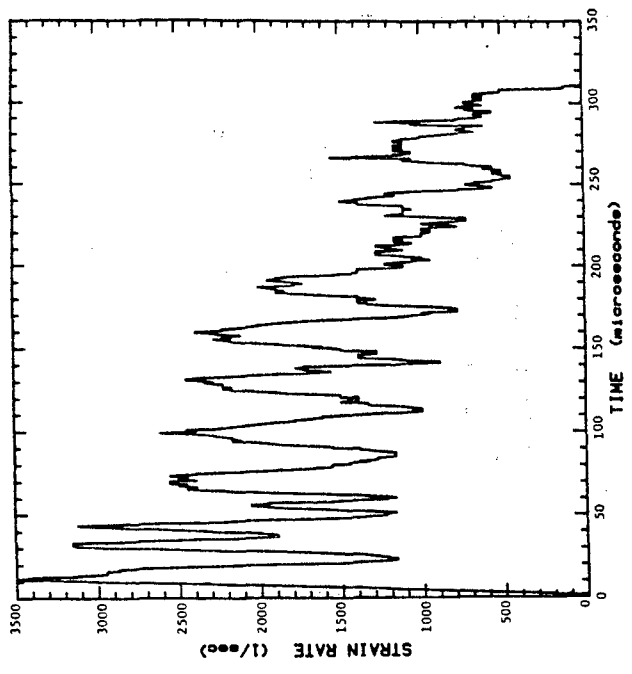
b. Strain Rate vs. Time.
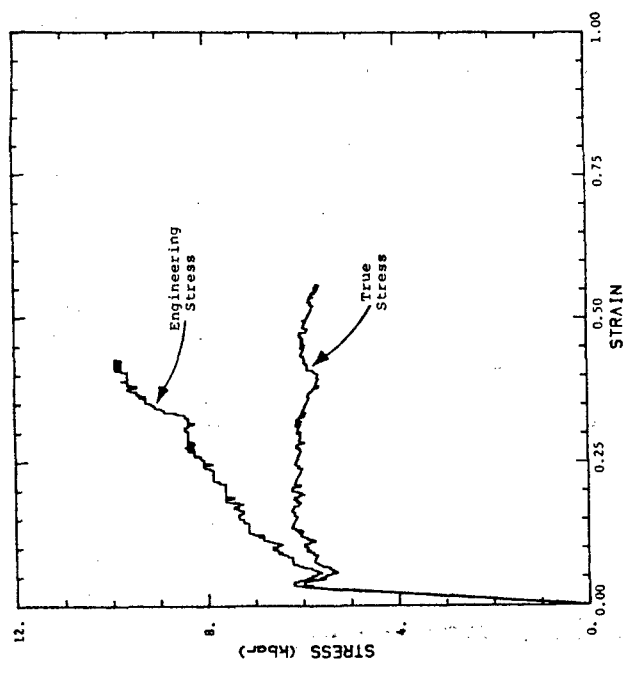
a. Stress-Strain

Figure 17.   Results from the Mid-Strain Rate Level Compressive SHB
Test of C1008 Steel.

30
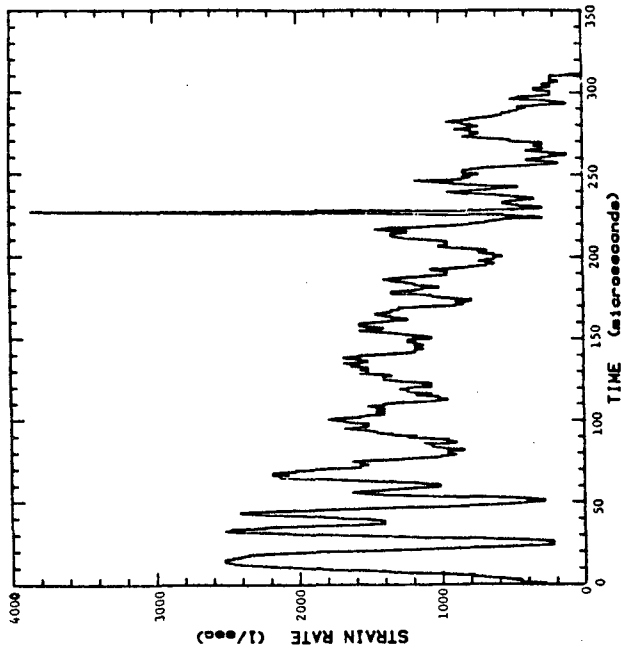
b. Strain Rate vs. Time
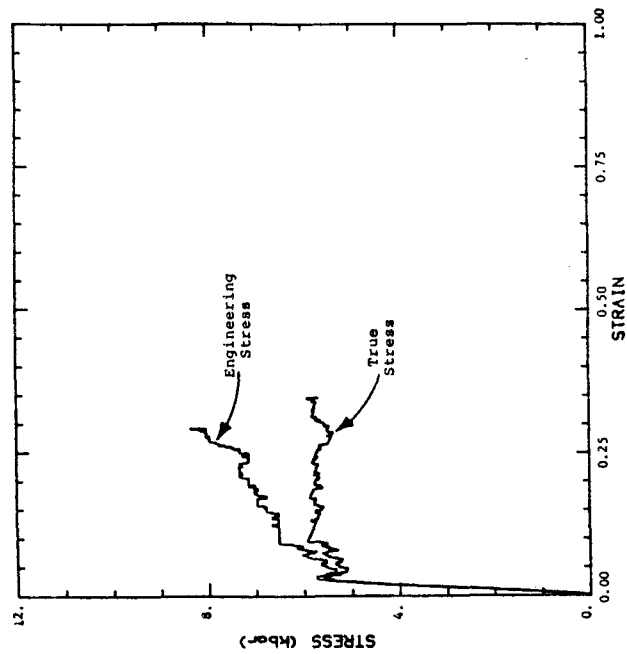
a. Stress-Strain

Figure 18.   Results from the Lowest Strain Rate Level Compressive
             SHB Test of C1008 Steel.
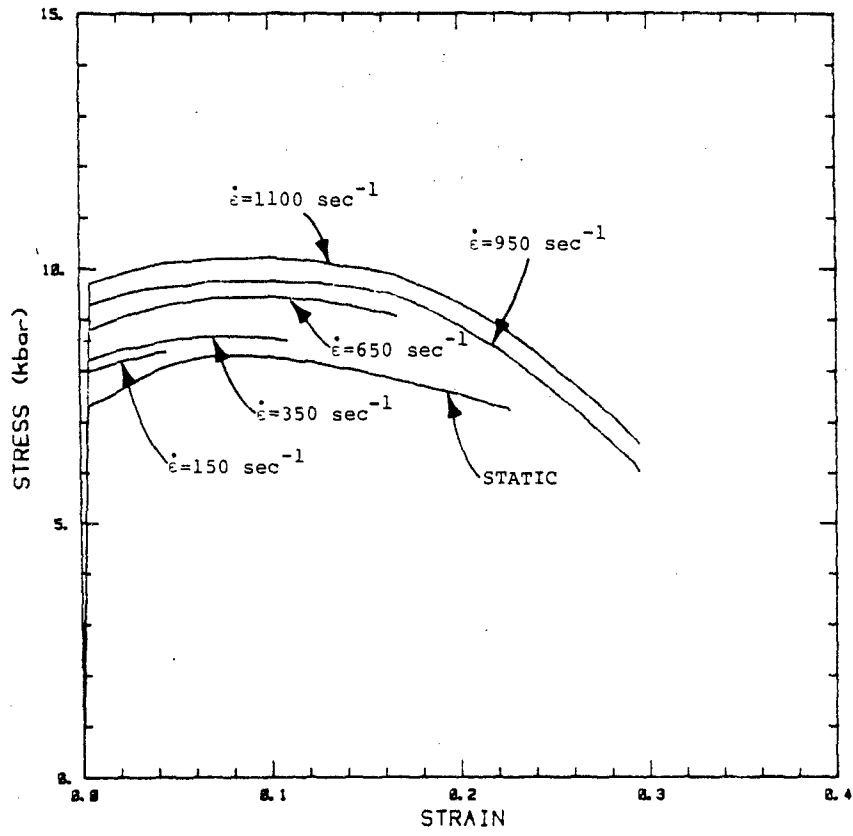
Figure 19.   Results of the Dynamic SHB and Static Tensile
             Tests on HY100 Steel.

behavior. However, the dynamic flow stress levels were not substantially different than the quasi static flow stress. This material also exhibited moderate rate dependency at low strain rate levels.

Compression tests were conducted for strain rates ranging from 500 to 1500 s^{-1}. It was difficult to obtain good data from the compression test on the HY100 steel because the high yield strength of the material required high striker bar launch velocities. High striker bar velocity resulted in noise in the bar, which, coupled with the low ε_r signal (equation 2), made the strain rate difficult to interpret. Useful data were only obtained in two of the eight tests, which are summarized in Table 2. The corresponding stress-strain curves and the strain rate vs. time for two compressive SHB tests are shown in Figures 20 and 21.

e.   7039-T64 aluminum

DTNSRDC also supplied 7039-T64 aluminum alloy for testing. The SHB samples were machined from supplied plate stock. Table 1 lists the tensile data available, which span the strain rates 300 to 800 s^{-1}. The results are summarized in Figure 22. It can be clearly seen from the dynamic and static tensile tests that the 7039-T64 aluminum is a strain rate independent material for strain rates up to 800 s^{-1}. This result was also born out by the compression data.

Compression tests were conducted for strain rates ranging from 600 to 2000 s^{-1}. Table 2 provides a summary of the compression tests. The results are presented in Figures 23 to 25. These figures include the true stress-strain curves along with the strain rate vs. time behavior. Figure 26 presents a summary. Note that there is a tendency for the true stress to decrease slightly for larger strain. This is believed to be a consequence of "barreling" of the specimen. The data beyond the stress maximum are probably not reliable.

The results from the compression tests agreed with the results from the dynamic and static tensile tests, as

33
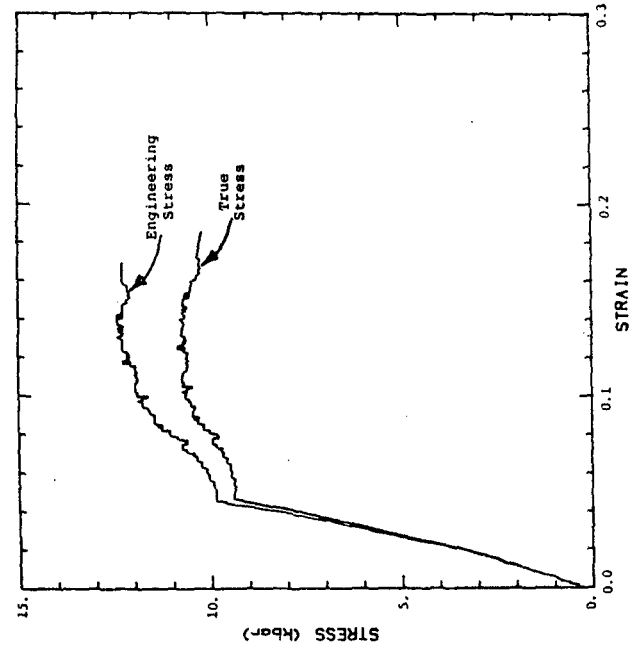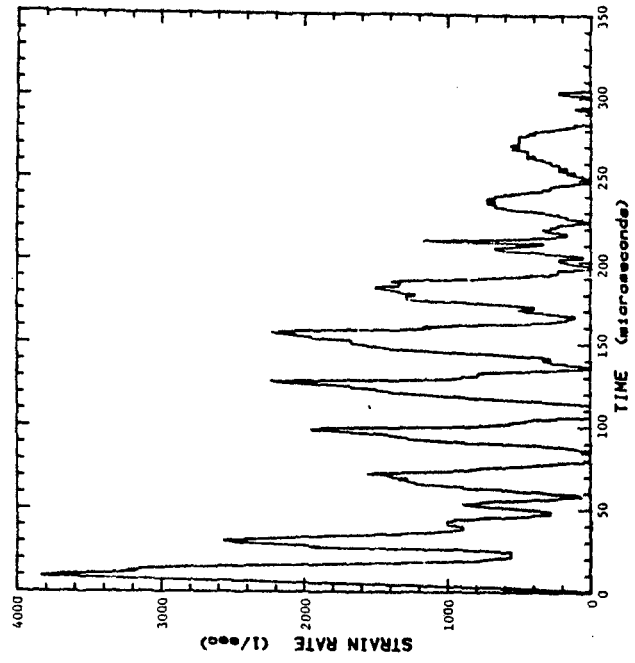
b. Strain Rate vs. Time

a. Stress-Strain

Figure 20.   Results from a Compressive SHB Test on HY100 Steel.

34
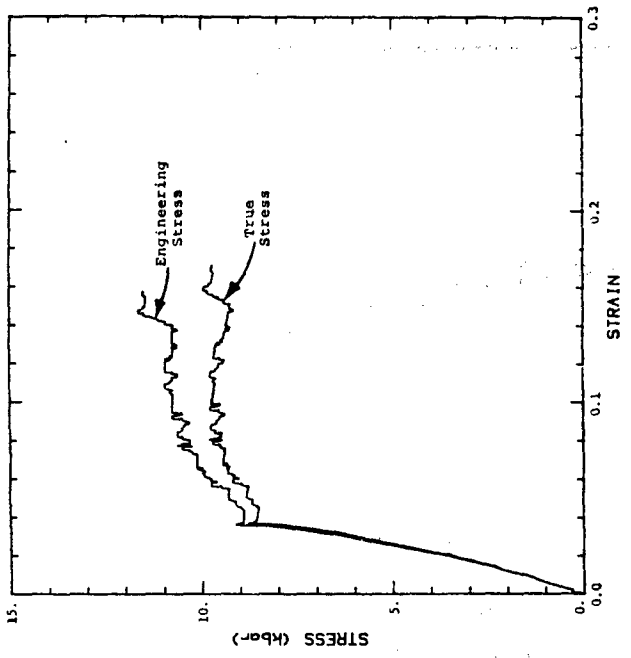
b. Strain Rate vs. Time
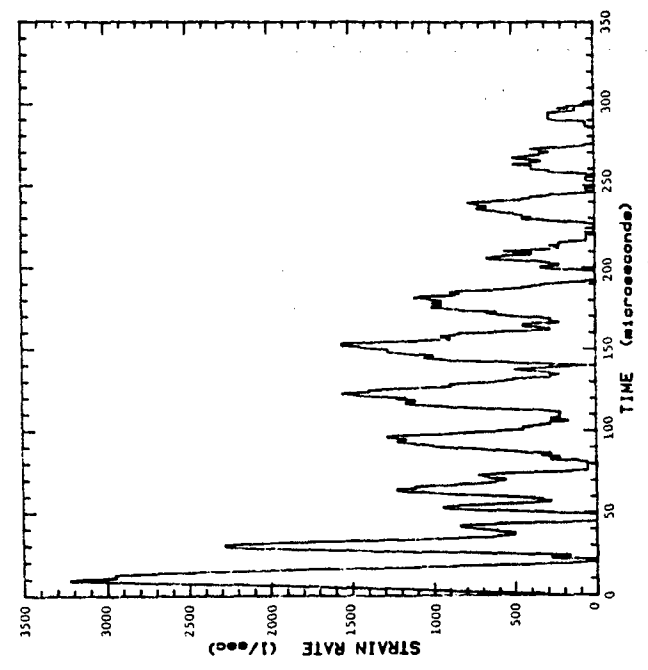
a. Stress-Strain

Figure 21.   Results from a Compressive SHB Test on HY100 Steel.

35
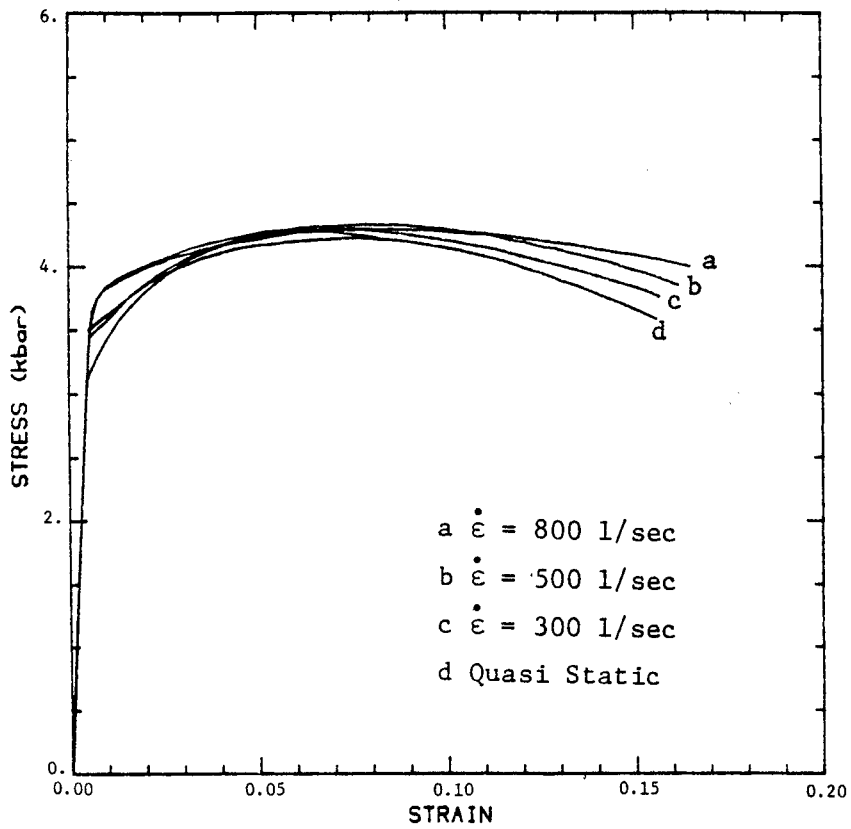
Figure 22. Results of the Dynamic SHB and Static
Tensile Tests on 7039-T64 Aluminum.
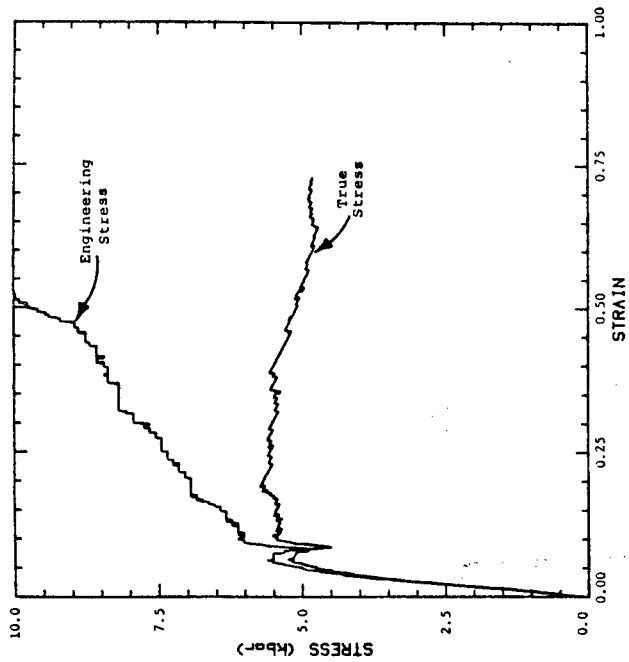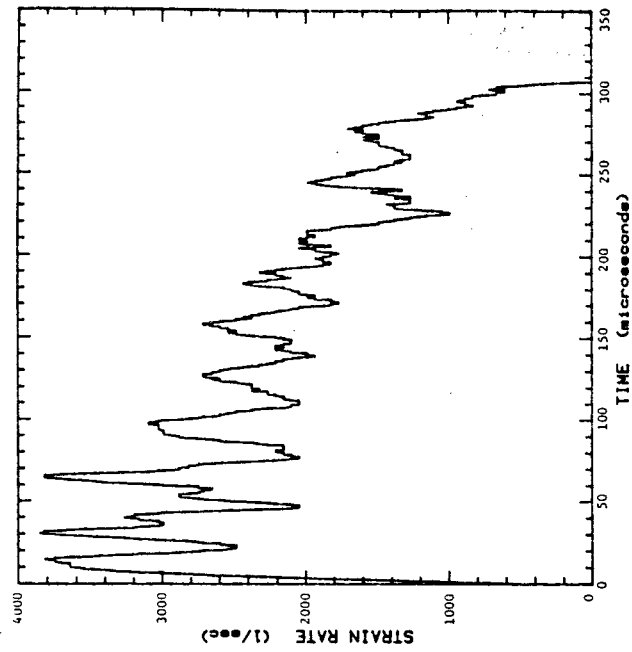
b. Strain Rate vs. Time

a. Stress-Strain

Figure 23. Results from the Highest Strain Rate Level Compressive SHB Test of 7039-T64 Aluminum.

37
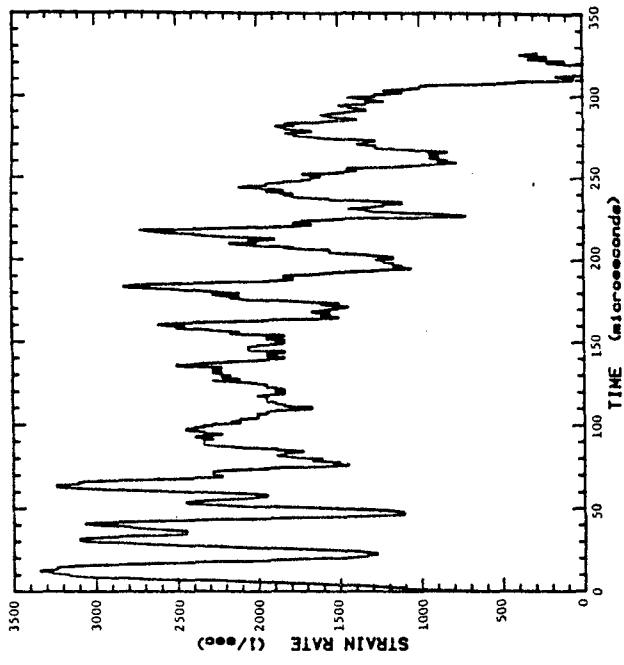
b. Strain Rate vs. Time
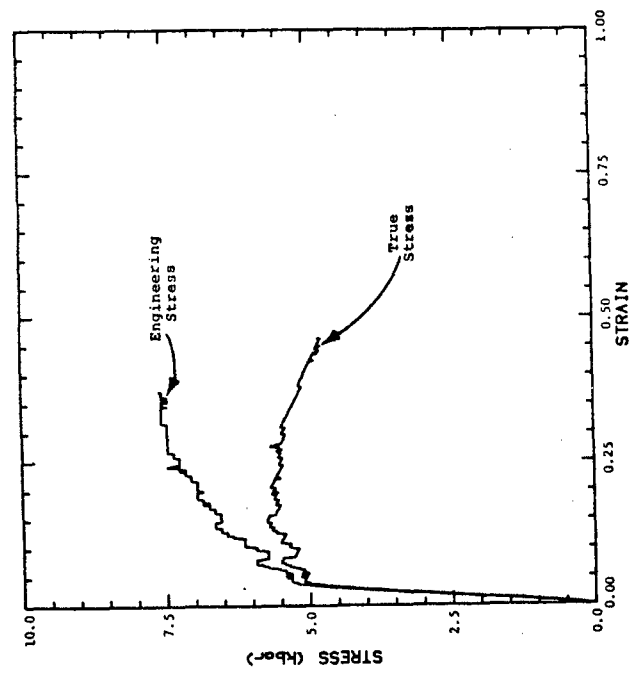
a. Stress-Strain

Figure 24.   Results of the Mid-Range Strain Rate Level Compressive
SHB Test of 7039-T64 Aluminum.
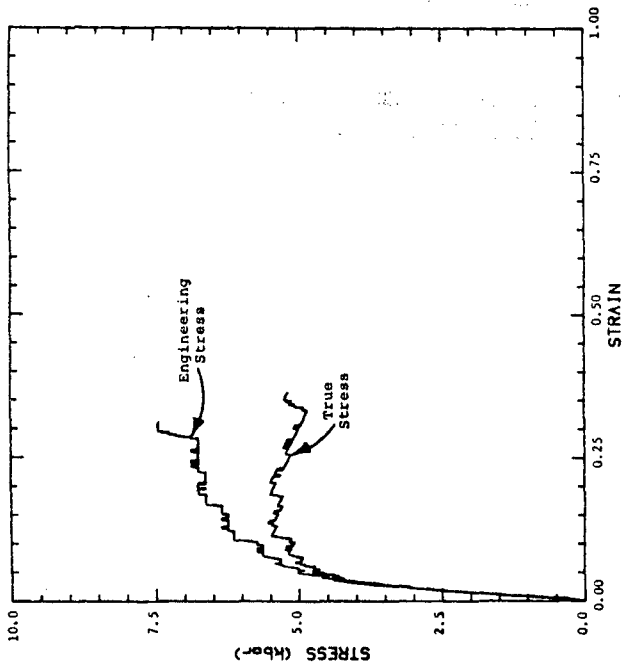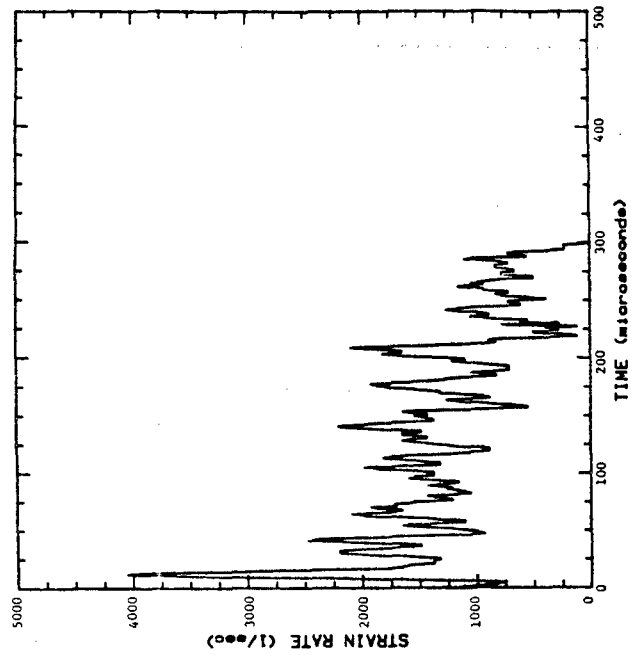
b. Strain Rate vs. Time.

a. Stress-Strain

Figure 25. Results from the Lowest Strain Rate Level Compressive SHB Test of 7039-T64 Aluminum.
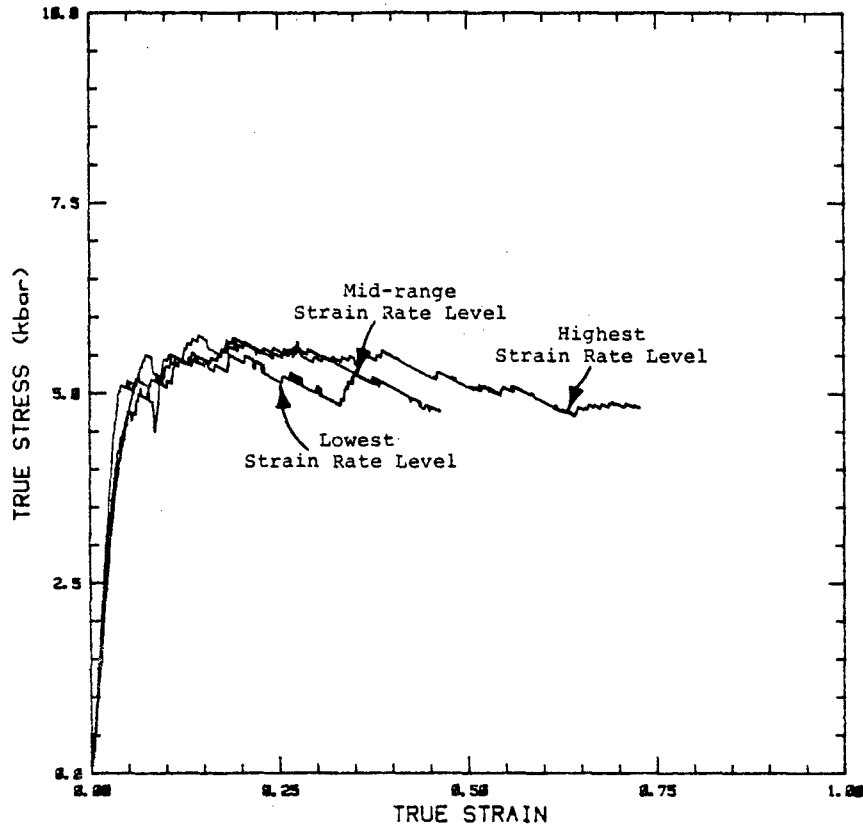
Figure 26.   The Compressive Stress-Strain Behavior of
7039-T64   for Three Different Strain Rate
Levels.

40

shown in Figure 27. This is consistent with lack of rate dependence. This also confirms the material isotropy; tests under tension and compression showed the same behavior. Since the strain rate history was different for the tensile and compression tests, isotropy could not be directly evaluated for the visco-plastic materials such as HY100 and C1008 steel.

2.2   NECKING HOPKINSON BAR TEST

The results reported in the preceeding sections were for one-dimensional stress state conditions. The ratio of mean stress (σ_m) to effective stress (σ_{eff}), was equal to 1/3. This stress trajectory limits the ability to use Hopkinson bar experiments to interpret impact-induced tensile fracture in flat plate impact tests where the mean stress to effective stress ratio is high ($\gg 1$). Because of this, available data generally show that the value of plastic strain associated with fracture is often several times greater in a SHB test than in a plate impact test. Hence, there is a critical need to develop experimental techniques to obtain dynamic stress-strain data at intermediate values of σ_m / σ_{eff}.

2.2.1   Analysis

Conventional tensile tests, in which load and displacement are measured, cannot be used to determine constitutive parameters beyond the point of maximum load. As Considere (Reference 7) first observed, an instability occurs at maximum load. Beyond this point, the increase in strength due to strain hardening cannot compensate for the increase in stress due to area reduction and necking occurs. The additional sample elongation (post elongation) is greater if the material flow stress increases with increasing strain rate.

As the neck develops, the material away from the neck begins to unload, and most of the plastic deformation takes place in a localized region. To evaluate the stress state at ductile failure, it is necessary to describe the deformation in the neck region.

41
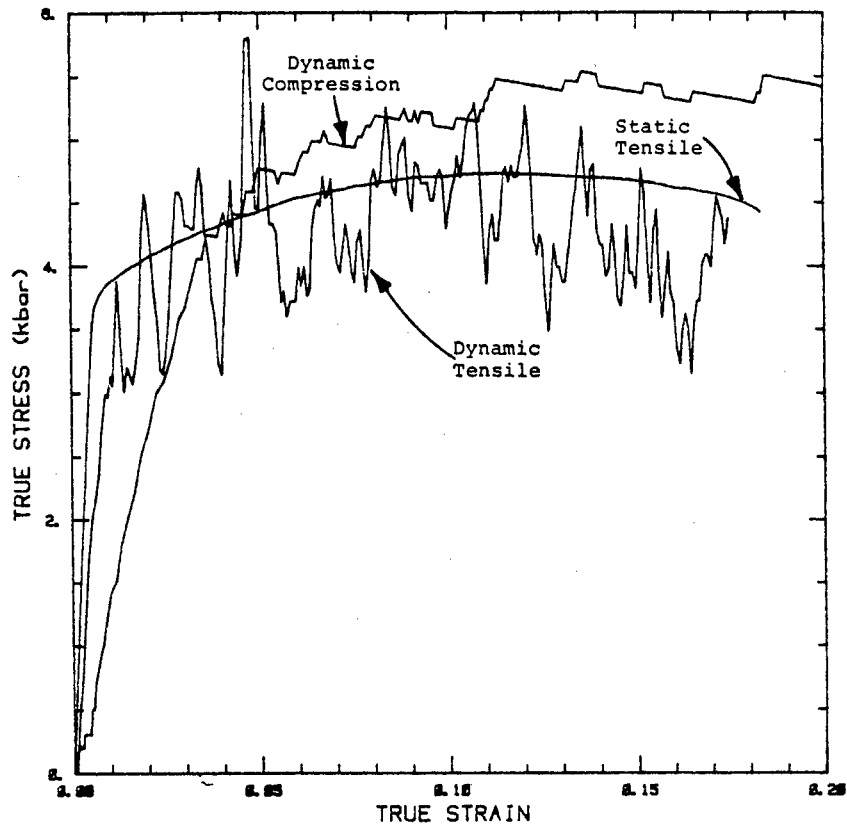
Figure 27. Results for Static Tensile, Dynamic Tensile SHB, and Dynamic Compressive SHB Tests for 7039-T64 Aluminum.

The classical work of Bridgman (Reference 8) provides an approximate method to obtain the effective stress and the strain at the neck from the measurement of the minimum radius of the neck (a) and the radius of curvature (R) of the neck profile. The axial strain, ε_z, across the neck is assumed uniform and equal to:

$$\varepsilon_z^p = 2 \ln(d/d_o) \tag{5}$$

where d is the current neck diameter and d_o is the original diameter. The effective plastic strain, ε_{eff}^p, can be expressed by the following relationship:

$$\varepsilon_{eff}^p = \sqrt{\frac{2}{9}\left\{(\varepsilon_z^p - \varepsilon_\theta^p)^2 + (\varepsilon_\theta^p - \varepsilon_r^p)^2 + (\varepsilon_r^p - \varepsilon_z^p)^2\right\}} \tag{6}$$

The plastic incompressibility condition ($\varepsilon_r^p + \varepsilon_z^p + \varepsilon_\theta^p = 0$) leads to:

$$\varepsilon_r^p = \varepsilon_\theta^p = -\frac{\varepsilon_z^p}{2} \tag{7}$$

Combining equations (6) and (7), the effective plastic strain becomes,

$$\varepsilon_{eff}^p = \varepsilon_z^p \tag{8}$$

The effective stress, σ_{eff}, is related to the true stress, σ_T, which is equal to the load (as determined from the SHB strain gage data) divided by the area of the minimum cross section.

$$\sigma_{eff} = B \; \sigma_T \tag{9}$$

where the correction factor B is given by

$$B = \frac{1}{(1+2R/a) \; \ln(1+a/2R)} \tag{10}$$

Here a is half the diameter and R is the radius of curvature of a circle that osculates the specimen at the necked silhouette. Since

43

B and σ_T are known, σ_{eff} can be calculated from equation 9. The effective stress vs. effective strain curve can be constructed from Bridgman's equations.

Hancock and Mackenzie (Reference 9) conducted tests on notched tensile specimens under quasi-static loading conditions and used Bridgman's analysis to calculate the stress states at ductile failure. The validity of the Bridgman approximation was independently checked by Norris et al., (Reference 10). It was found that at 100 percent strain, the error in flow stress computed by the Bridgman analysis was only 10 percent.

It is important to validate the extension of Bridgman's solution for high rate deformation. For this purpose, a finite element analysis (FEA) simulation of a dynamic tensile test was performed with the MAGNA (Reference 11) program. Attempts were also made to use a finite difference program, called STEALTH (Reference 12) for further validation of Bridgman analysis.

a.   MAGNA

The first objective of the FEA computation was to validate the Bridgman analysis for dynamic deformation. The evaluation of the neck was numerically simulated. The computed contours were then treated as input data for a Bridgman analysis. The effective stress that was inferred from the Bridgman analysis was compared with the actual value used in the code. If the Bridgman analysis is accurate, the stress values will compare well.

To aid the calculation, a shallow-notched tensile specimen geometry as shown in Figure 28 was considered. The corresponding finite element mesh for one quarter of the specimen is shown in Figure 29. The number of 4-node isoparametric elements was 440. The total number of nodes were 441. Finer elements were used around the minimum cross section area. Transient dynamic analysis was carried out with the MAGNA-code. Using the 'RESTART' facility provided by MAGNA, the solutions were carried out for a duration of 250 microseconds through several computer runs. The full Newton-Raphson method

44
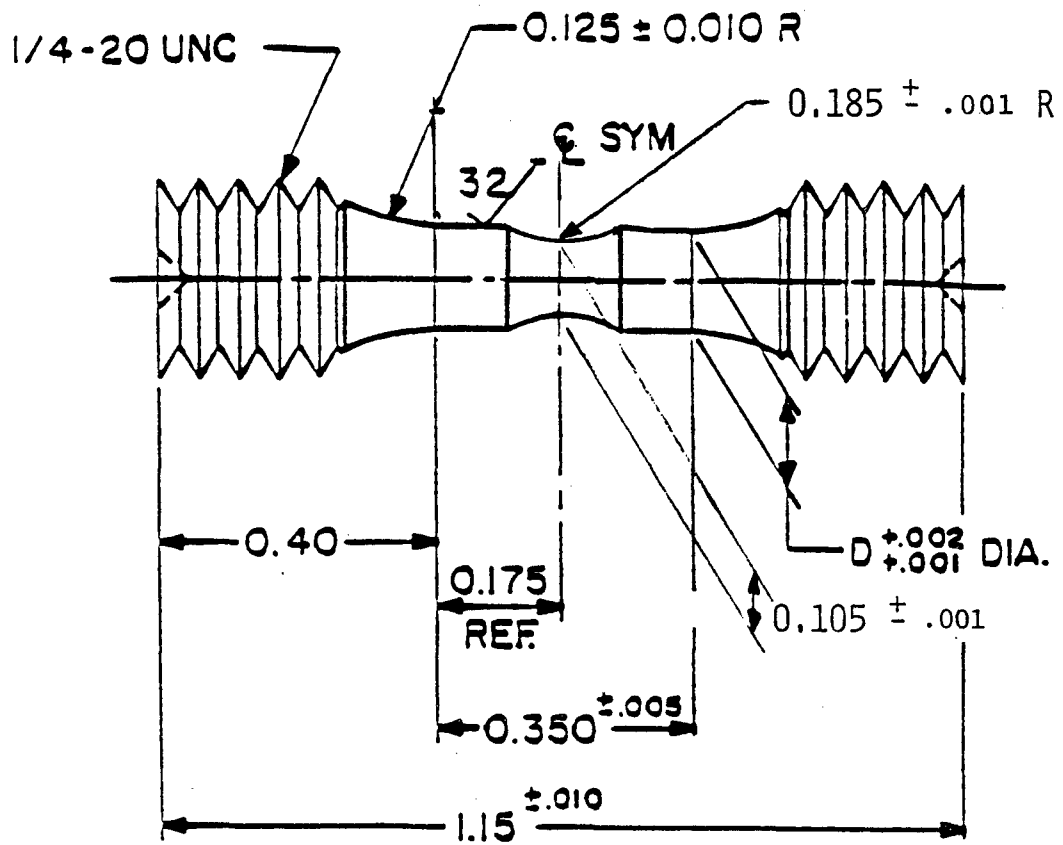
Figure 28.   Shallow-Notched Tensile Specimen Geometry.
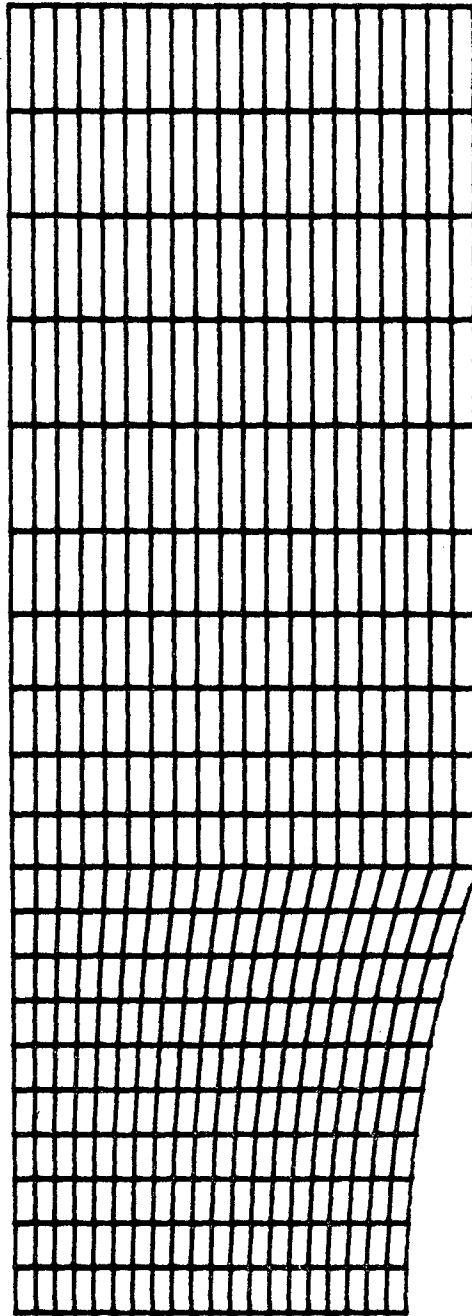
Figure 29. Finite Element Mesh for Shallow-
            Notched Specimen Geometry.

was used to calculate the stiffness matrix. This means that the global stiffness matrix was updated at each equilibrium iteration. The solution was stable and convergence was achieved with a maximum of 5-7 iterations. The convergence tolerances were through displacements and nodal forces. Stringent tolerance limits were specified for each run to obtain a stable solution with the increasing applied displacement. The full displacement history of the specimen that was used in these simulations is given in Figure 30.

For Bridgman's analysis, contours of the notch at time intervals 50, 100, 150, 200, and 250 microseconds were plotted from the MAGNA post-processor files. A polynomial curve was fit to the profiles of the notch at the five time intervals. Values of a and R were estimated from these profiles. The effective strain and effective stresses were calculated using equations 8 and 9. The σ_T in equation 9 is readily available from the FEA results. The stress-strain curve obtained through the Bridgman equations and the corresponding stress-strain data used in the FEA compared extremely well as can be seen from Figure 31.

The FEA was carried out for a maximum strain of 50 percent. Beyond this strain value, the time step for a stable solution had to be very much smaller and the time steps for stable solution became unreasonably small. The cost to extend this solution was unacceptable and the FEA was terminated. However, the validity of the extension of the Bridgman solution to high rate deformation was reasonably justified by these limited results.

b.   STEALTH

Since the simulation of a notched tensile specimen, through the finite element code MAGNA turned out to be time consuming and very expensive, the general purpose, state-of-the-art finite difference code, "STEALTH' was considered as an alternative. The first objective was to investigate the ability of STEALTH to simulate the notch tensile test.

47
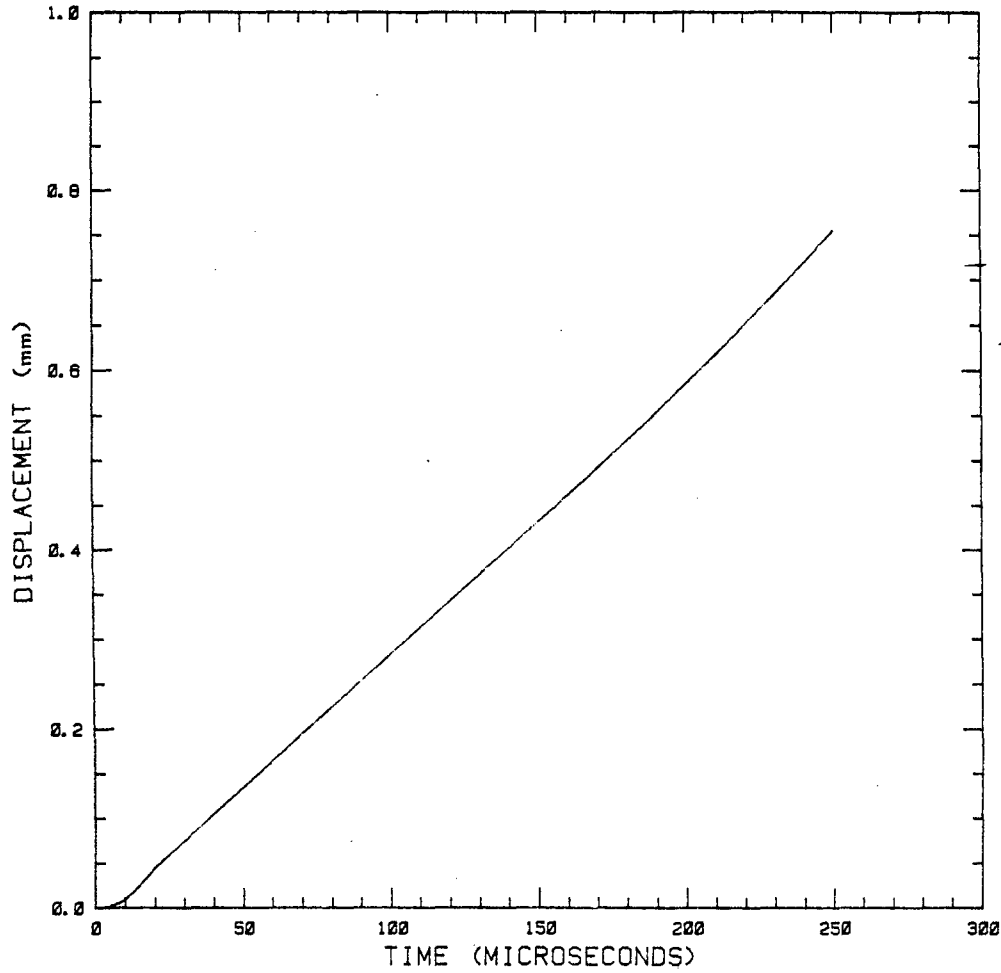
Figure 30.   Displacement Used in the Finite Element
             Analysis of the Shallow-Notched Hopkinson
             Bar Specimen.
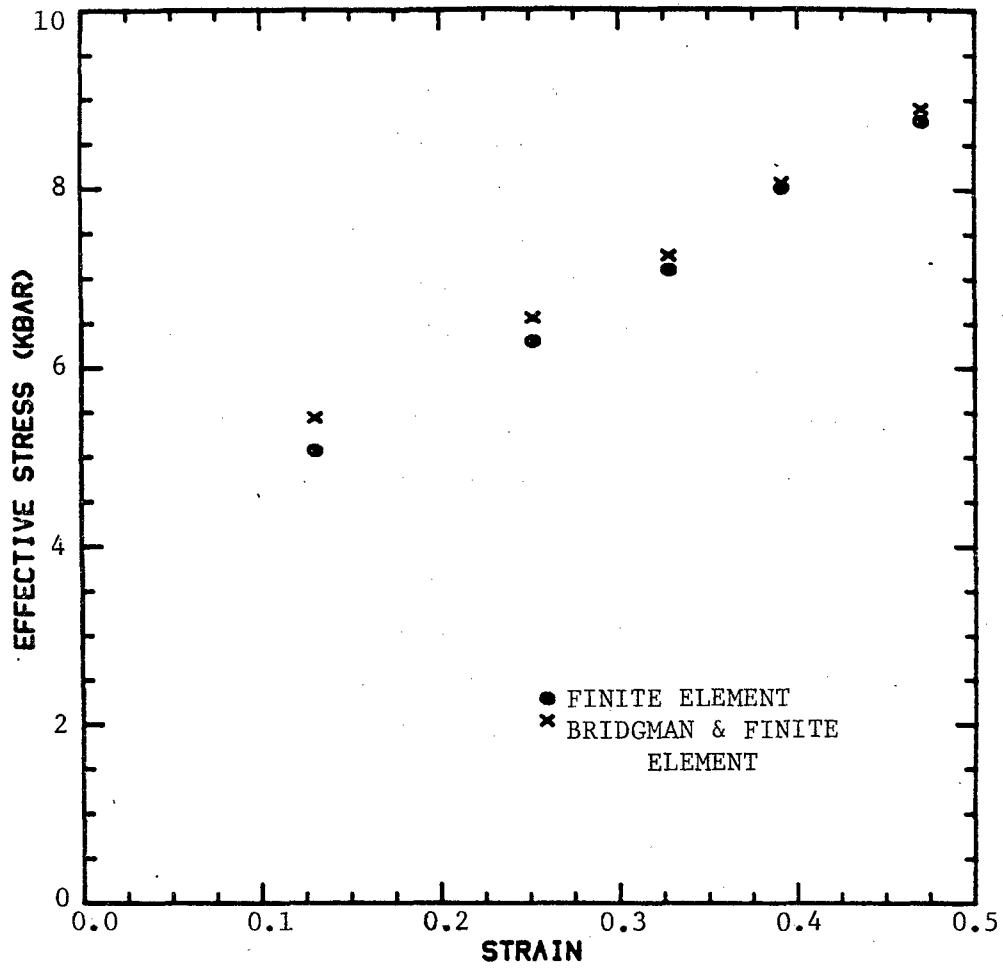
Figure 31. Comparison of the Experimental Stress Calculated Using Bridgman's Analysis and the Finite Element Analysis Results.

The finite element mesh that was used in MAGNA was selected as a finite difference grid for STEALTH. A typical plot of this grid from STEALTH is shown in Figure 32. The solutions were carried out for 15 microseconds. The material was idealized as elastic-perfectly plastic. The pressure (mean stress) and the axial stress distributions along the radial distance from the axis at time 5, 10, and 15 microseconds of the deforming specimen are shown in Figures 33 and 34. It can be seen from the figures that the distributions which were smooth initially become unsmooth. This could have been caused by the spurious wave reflections from the free boundaries. The numerical noise associated with the finite difference scheme could be another reason. The pressure and stress vs. time at the axis is plotted in Figures 35 and 36. These plots show clearly the spurious numerical noise due to continuous wave reflections from the boundaries.

The undeformed (t=0) and deformed specimen configurations at t=5, 10, and 15 are shown in Figure 37. As the specimen was stretched axially, the ratio of the radius of a minimum cross section to the radius of curvature of the notch profile increased.

The solutions were stopped at 15 microseconds due to the numerical oscillations of the pressure and stresses. Efforts have been undertaken to minimize the effects of numerical noise on the results.

The FEA results substantiated the extension of Bridgman analysis to dynamic loading regimes. The next step was to develop techniques for obtaining the parameters a and R from necking SHB tests. As mentioned earlier, for this purpose, a novel high speed photographic system was developed and the details are discussed in the following section.

2.2.2   Technique

Until now, the experimental complexities involved in dynamic tensile tests have precluded the extension of the Bridgman analysis to high strain rate deformation. To overcome

50
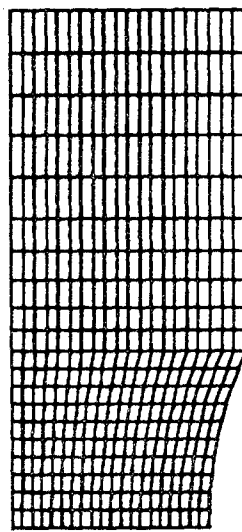
Figure 32.   Grid Used By the Finite Differance Code 'STEALTH'
              To Simulate the Shallow-Notched SHB Specimen.
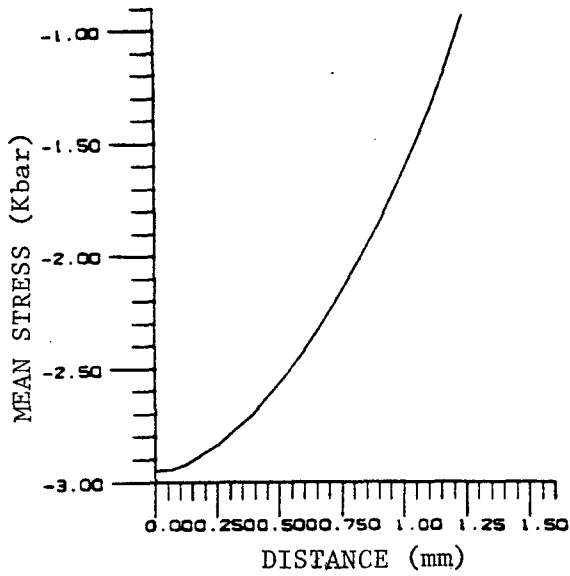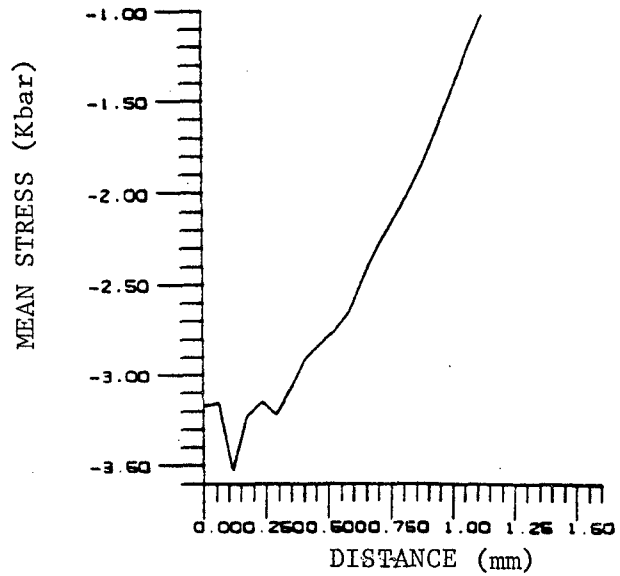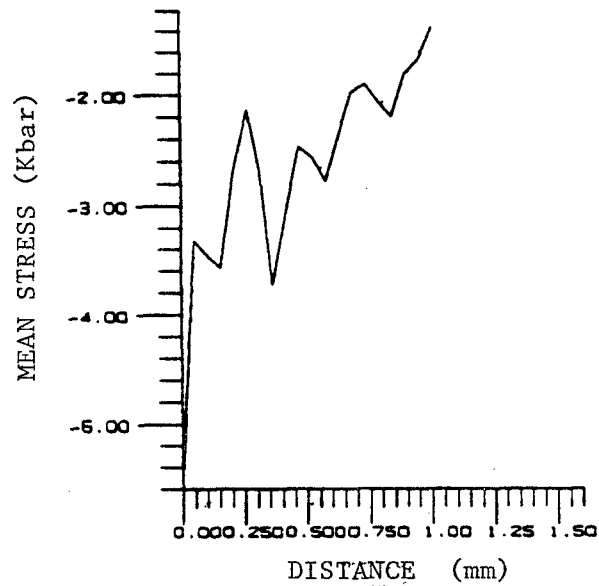
Figure 33.   Mean Stress Distribution Along the Radius
of the Minimum Cross Section from STEALTH.

52

a. t = 5 μs

b. t = 10 μs
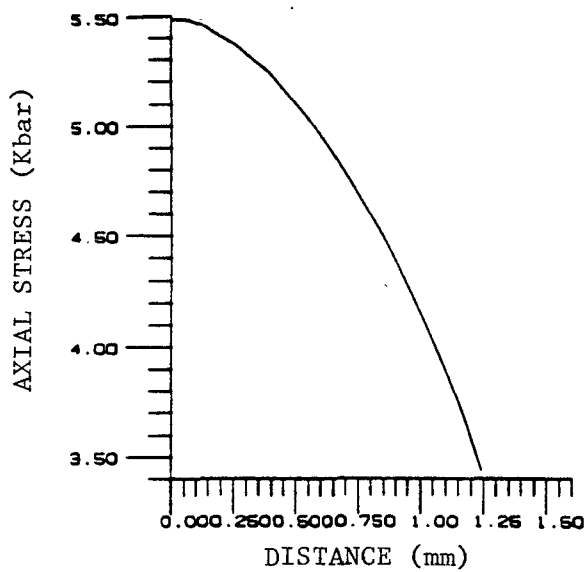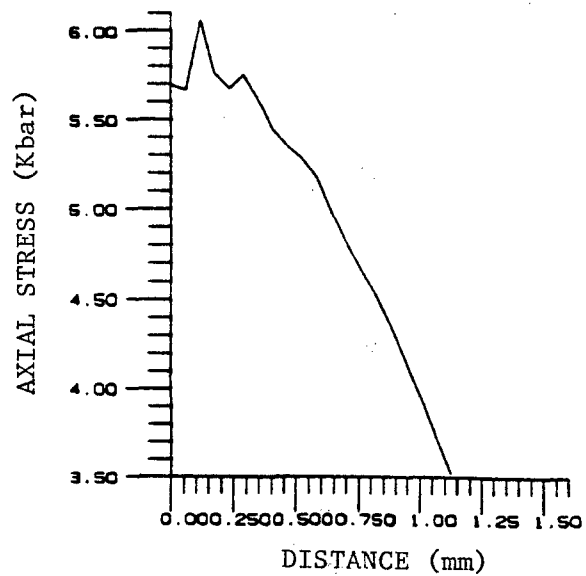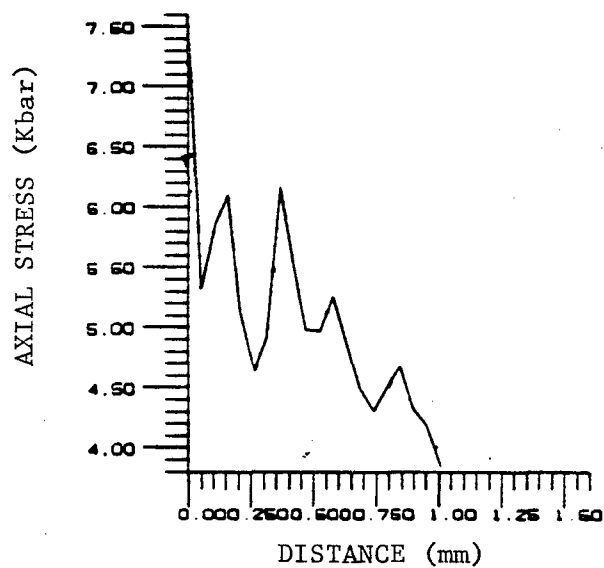
c. t = 15 μs

Figure 34. Axial Stress Distribution Along the Radius
of the Minimum Cross Section from STEALTH.

53
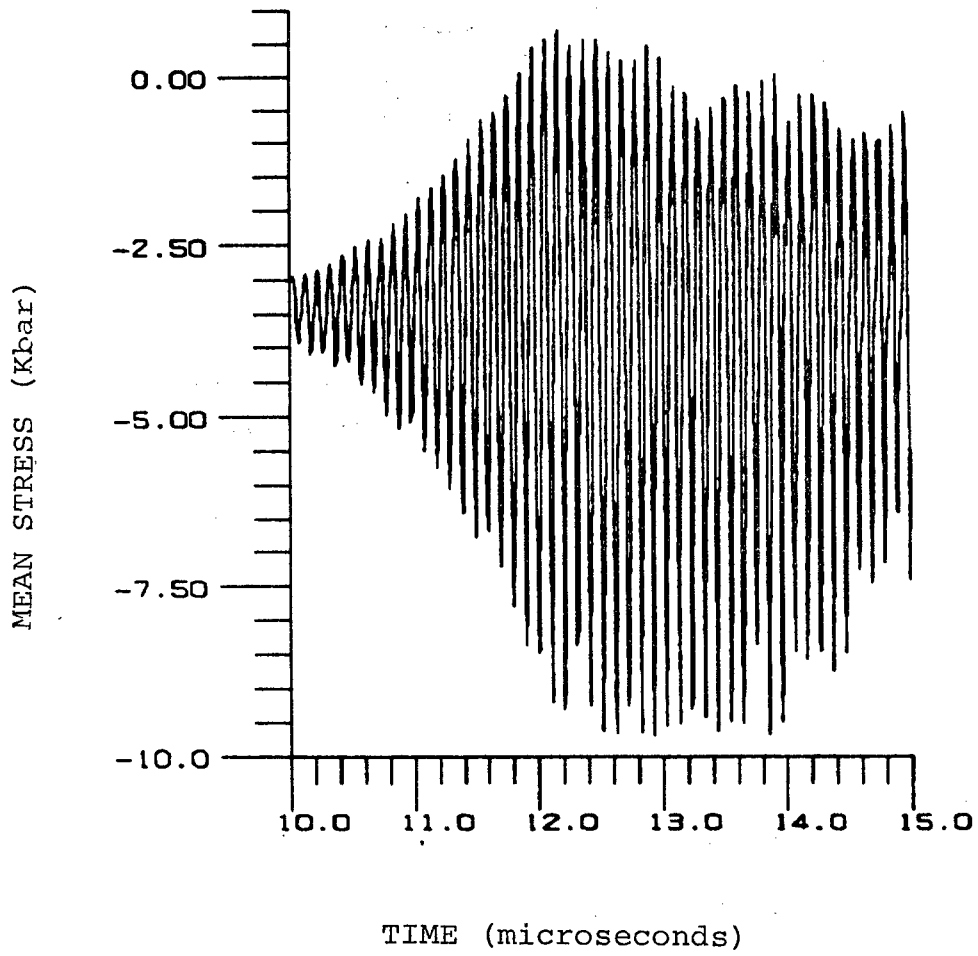
Figure 35.   Mean Stress History at the Axis of
The Minimum Cross Section from STEALTH.
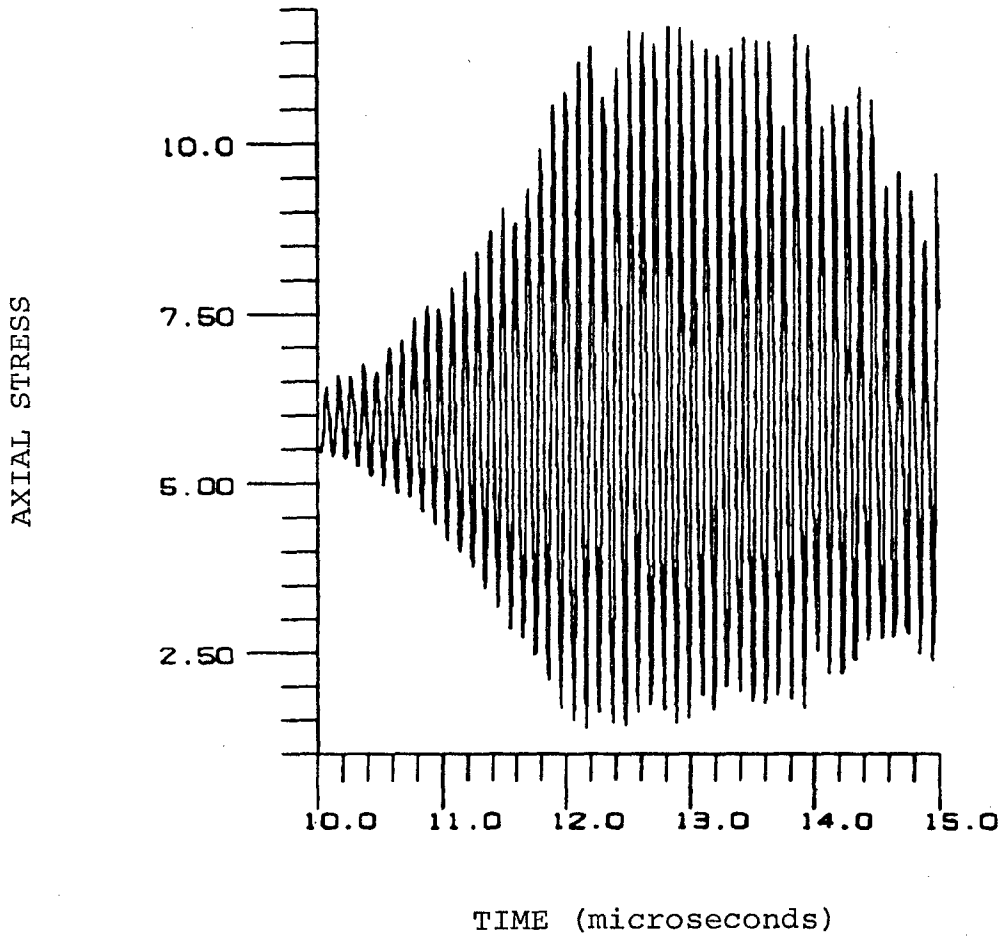
Figure 36.   Axial Stress History at the Axis of
The Minimum Cross Section from STEALTH.

a. t = 0.   b. t = 5 μs

c. t = 10 μs
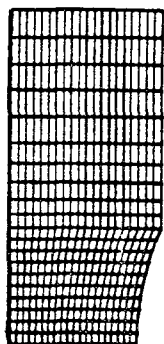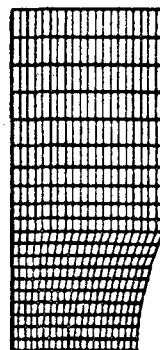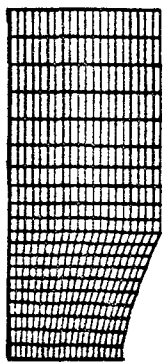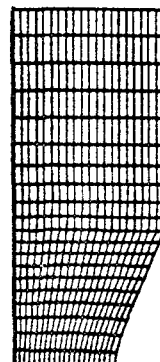
d. t = 15 μs

Figure 37.   Notched Specimen Configuration at Different
              Time Intervals from STEALTH.

this hurdle, a photographic system using an LED (light-emitting diode) illuminator and a 35mm rotating drum camera has been developed by Cross et al., (Reference 13).

The deformation of SHB specimens is cylindrically symmetric, so back lit silhouette photography is adequate. Since back lit photography is very efficient, use of relatively weak sources is feasible. It was found that a Fairchild FLV104 LED (light-emitting diode) cooled with liquid nitrogen was sufficient. The LED was driven with pulse currents up to 6amp with durations of up to 100ns at repetition rates of 5kHz. The peak emmision wavelength of the LED is 670nm which requires a film with an extended red sensitivity. Kodak 2479 was selected.

The back-lit photographs were obtained with a 35mm rotating drum camera. The camera is continuous access; framing was accomplished by pulsing the illuminator. The drum speed was 300 m/s. The magnification was about 1.2. The resolution in the object plane was 40 lp/mm. The SHB specimens themselves were about 3.2mm in diameter so that the specimen diameter could be determined to about one part in 128. Figure 38 illustrates a sample photograph of a necking specimen.

Synchronization is critical for successful correlation of neck profile measurements with load-displacement records. Signals from the two strain gauges and synch pulses indicating each LED flash were recorded on digital oscilloscopes. In this way, precise registration of the two strain gauge signals and the various photographic images was possible.

The strain gauge signals are synchronous with each other; however, unlike the photographs, they are not "real time" devices because of the finite time required for a sound wave to propagate from the sample to the gauge locations. The offset time could be read directly from the strain gauge records, for it is one-half the time between an arrival of a wave traveling to the sample and the arrival of the corresponding reflection.

Prints of the photographic images for data analysis were conveniently prepared with a commercial microfilm printer.
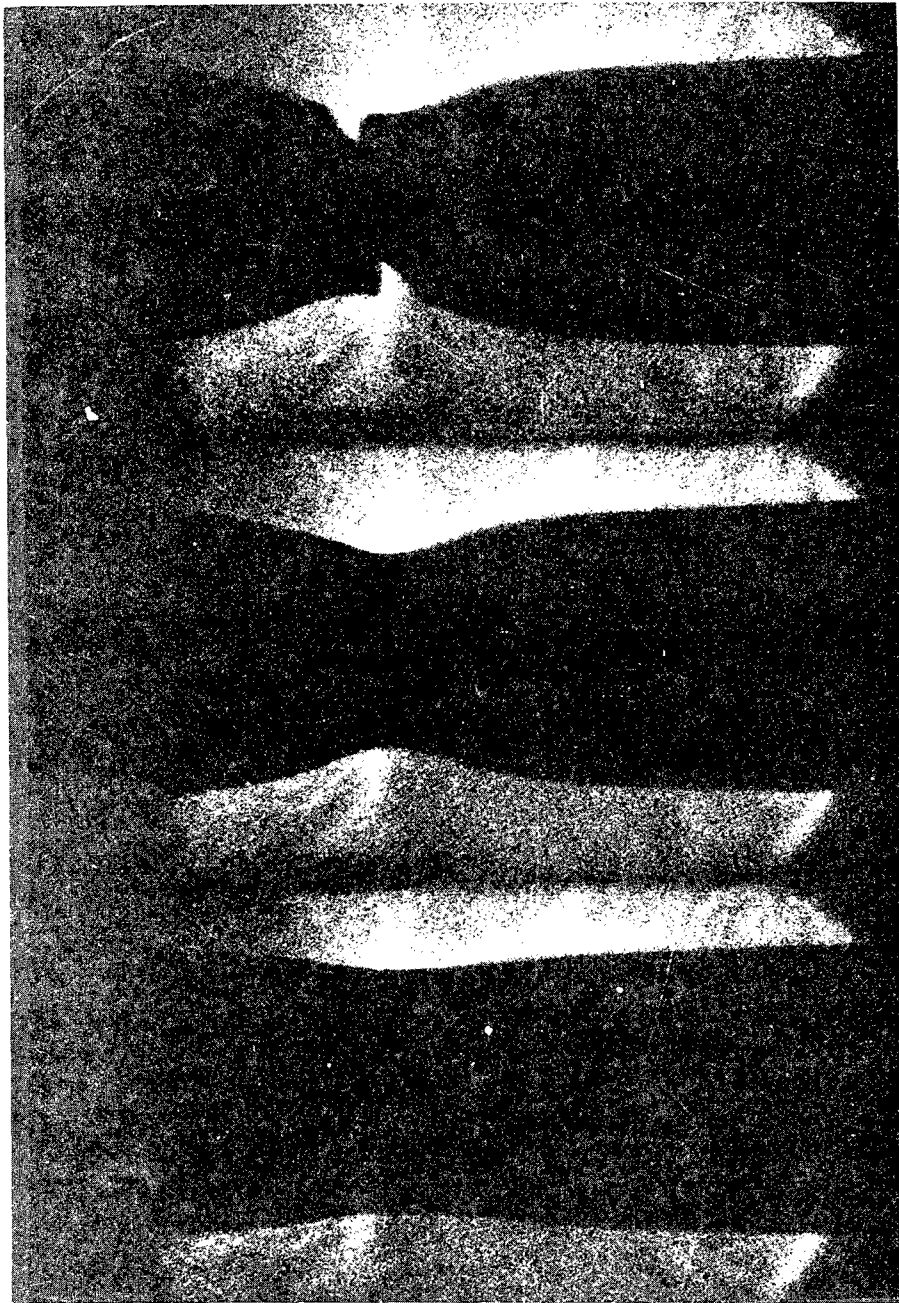
Figure 38.   Sample Photograph of a Necking SHB Specimen.
             (Sequential Photograph, Time Increases Upward.)

In order to calculate R, cross sections were digitized and fit with a second order curve. The sample radius, a, was determined from measurements taken from the photographic prints.

It was observed that the uncertainty in the measurement of 'a' was about one percent. The resulting error in the strain due to this uncertainty was sensitive to the strain level. For a strain of 0.01, the relative error could be 100 percent; whereas, for a strain of 0.5, the relative error was about 4 percent. Thus, the uncertainty in the large strain measurements is reasonably small. An uncertainty in stress of 2 percent results from an uncertainty in 'a' of 1 percent; thus, errors in 'a' do not cause appreciable errors in stress. Stress is also little affected by errors in R. Even for large defor-mations, a 10 percent uncertainty in R causes an uncertainty in stress of only 2 percent. Thus, significant errors do not arise from uncertainties in the measurements.

2.2.3   Test Results

High speed photographs of necking specimens were obtained for each of the five metals included in this study. Maximum striker bar velocities were used in order to obtain the highest possible uniform strain rates before necking, 1000 to 1500 s^{-1}. Three tests were performed for each material. The results are summarized in Table 3. In Table 3, "uniform" refers to strains measured away from the necking zone. The term 'local' is used to indicate that the measurements were from the necking area. In some of these tests, the onset of necking was observed during the first tensile pulse. In other materials, significant growth of local necking was not observed during the first pulse. In Table 3, the strain at the onset of necking was based on discernable deviations in the photographs. The actual onset could have occurred slightly before this time as can be seen from the strain vs. time plots reported in the following sections. For C1008 steel, OFHC copper, and the 7039-T64 aluminum the onset of necking occurred during the second tensile pulse. In these

TABLE 3

SUMMARY OF NECKING HOPKINSON BAR RESULTS

Material	Test #	Uniform Strain at Onset of Necking (%)	Local Strain at Failure (%)	Local Strain at End of 1st Pulse (%)	Effective Stress at End of 1st Pulse (Kbar)
1020	HB-185	21.	80	80.	8.3
1020	HB-186	24.	96	96.	8.6
1020	HB-187	24.	85	85.	8.1
OFHC	HB-173	60.	210	33.	3.8
OFHC	HB-180	59.	200	32.	3.7
OFHC	HB-181	54.	210	53.	4.2
HY100	HB-241	28.	105	62.	11.7
HY100	HB-242	36.	104	56.	10.9
HY100	HB-249	23.	124	66.	12.0
C1008	HB-243	52.	134	38.	5.8
C1008	HB-244	52.	138	43.	6.0
C1008	HB-248*	--	---	--	---
7039-T64	HB-245*	--	---	--	---
7039-T64	HB-246	25.	54	18.	5.3
7039-T64	HB-247	25.	52	18.	5.4

*Poor Photographs made 'a' and 'R' calculations impossible.

cases, the local and the uniform strains are the same since necking has not been initiated.

a.   1020 steel

Three necking SHB experiments were conducted on 1020 steel; the results are summarized in Table 3. Local strain at the minimum cross section of the specimen was determined from the photographs. It was compared with the average strain calculated from the Hopkinson bar data, as shown in Figure 39. The local strain agrees with the average strain until the onset of necking at about 70 μs. After the onset of necking, the local strain increases rapidly. The maximum value of local strain is almost 70 percent. At this point, the specimens failed. As the specimen necks, the strain rate accelerates. For strain above 30 percent, the average strain rate is approximately 5000 s^{-1}.

Bridgman observed that, for a number of materials, a relationship exists between the effective strain and the ratio of specimen diameter to the radius of curvature of the neck. Figure 40 contains a plot of Bridgman's results and the results for the experiments on 1020 steel. The dynamic data falls below the trend observed by Bridgman in static tests. This is apparently due to the material behavior, rather than inertial effects, because similar data for 6061-T6 aluminum were found to lie above the Bridgman data (Bless et al., Reference 6).

The effective stress was calculated as described by equations 9 and 10. The effective stress vs. localized strain and true stress vs. localized strain plots, for each experiment, are shown in Figure 41. There is little change in flow stress at the large strain and high strain rates associated with the neck instability. The specimens failed at an effective stress of 8.3 Kbar and a localized strain of 85%, as summarized in Table 3.

61
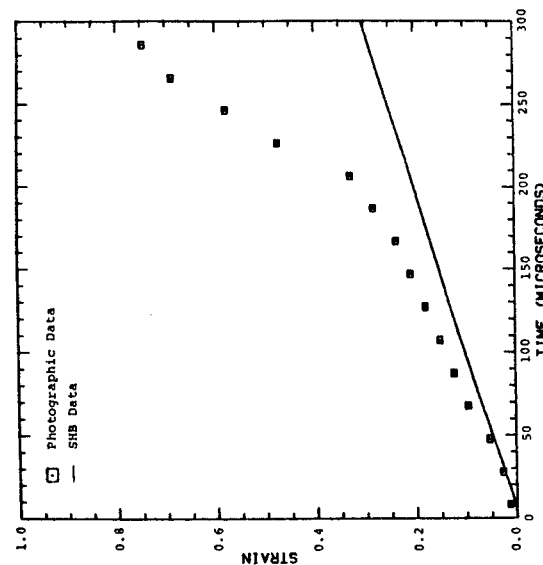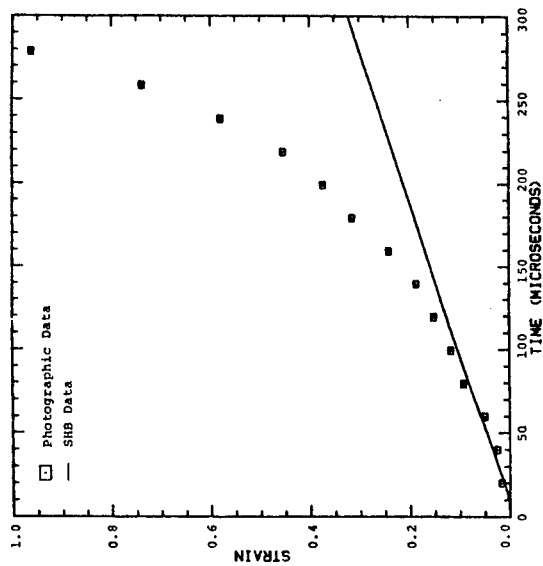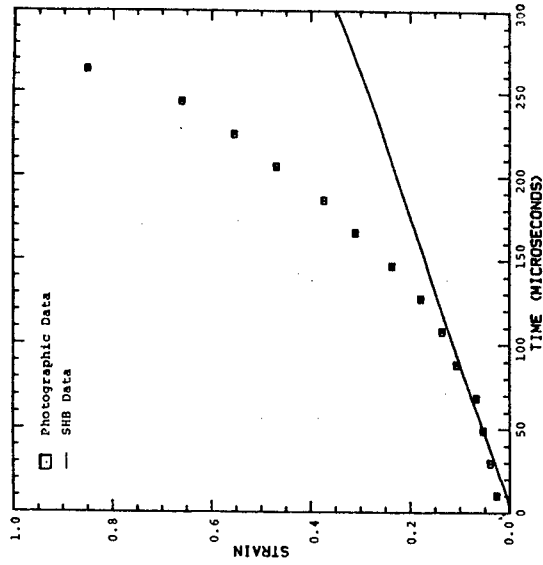
Figure 39. Comparison of the Strain Calculated from the
Photographs with the Strain Calculated from the
Hopkinson Bar for 1020 Steel.
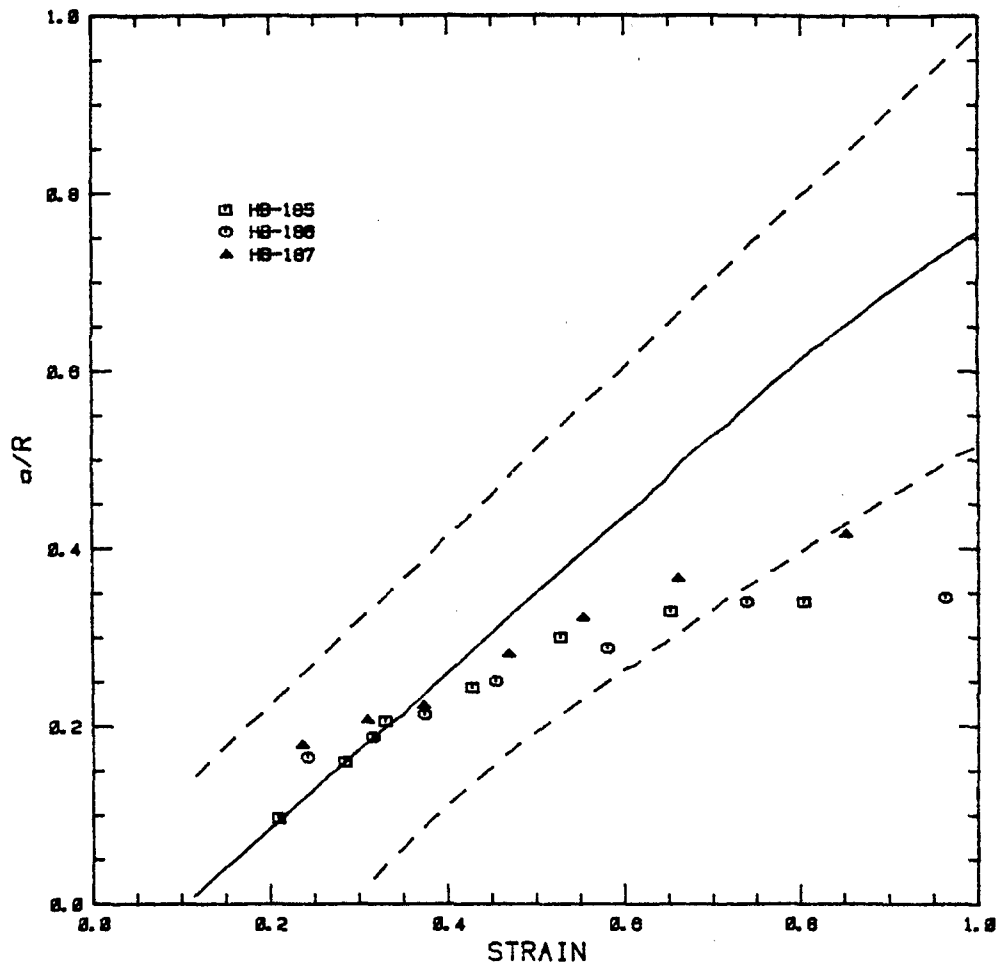
Figure 40.   Comparison of Bridgman's Observed Necking
             Behavior and the Necking Behavior of 1020 Steel.
             (Solid line is mean, dotted lines are extremes.)
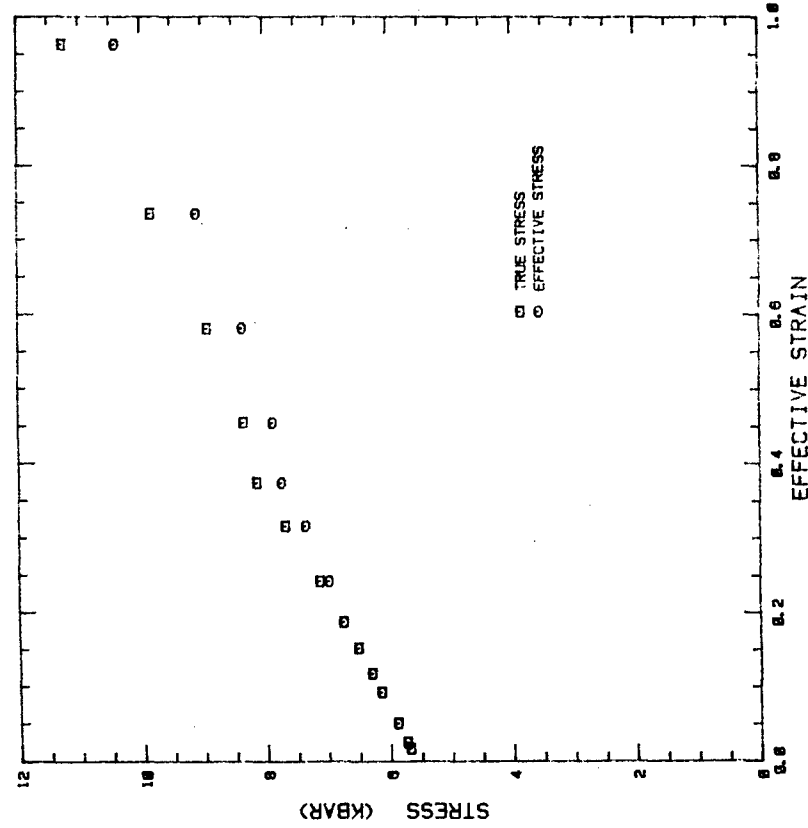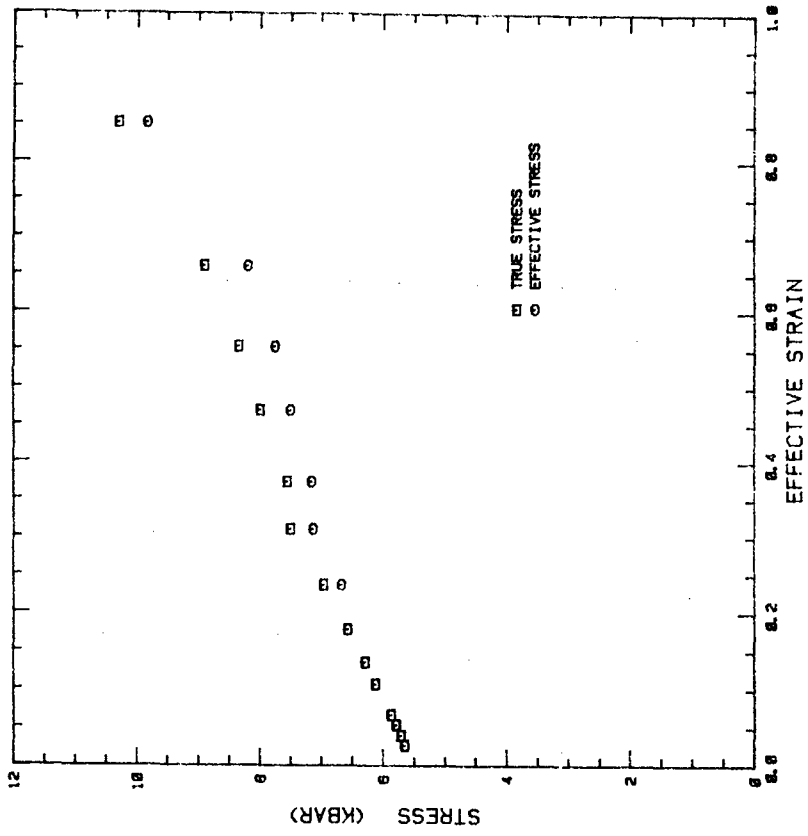
Figure 41. The Effective Stress Calculated from the Necking 1020 Experiments.
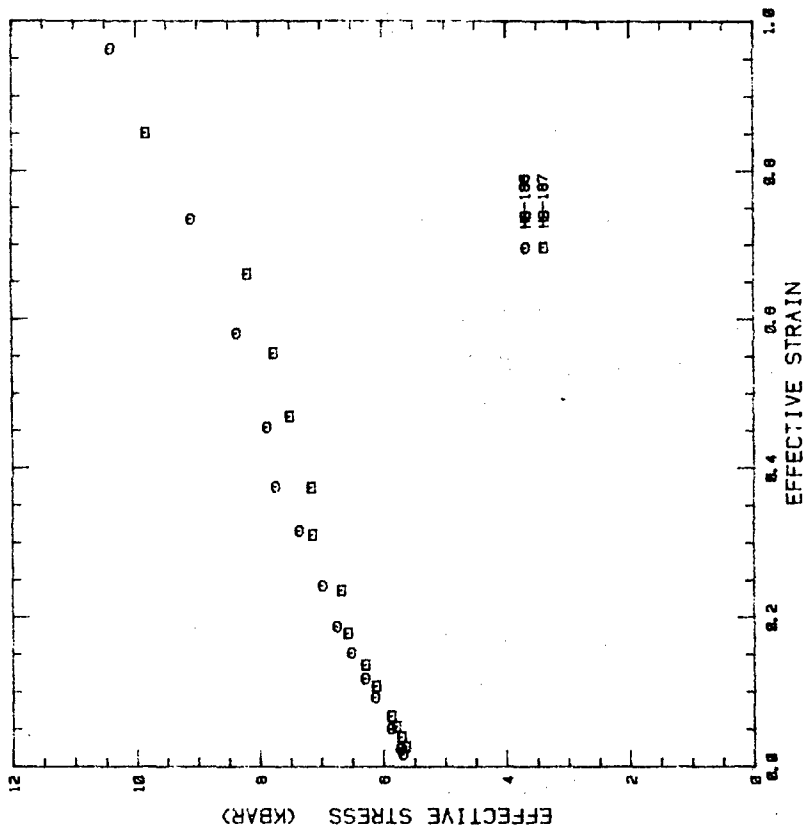
c.   Combined Plot

Figure 41 (cont'd).   The Effective Stress Calculated from the Necking 1020 Experiments.

b.   OFHC copper

Three necking experiments were conducted on the OFHC copper, and the results are summarized in Table 3. These experiments were conducted at a high striker bar velocity, yet necking did not occur during the first pulse. The local strain in the neck is compared to the average strain in Figure 42. The strains from the two independent techniques compared very well for each test.

At the end of the first pulse, the tensile specimens had reached a strain of 30% to 50% with no observable necking. The difference between the results for tests HB-173 and HB-180 and test HB-181 is due to the higher strain rate of test HB-181 ($1400 \ s^{-1}$ as opposed to $800 \ s^{-1}$). During the second pulse, necking began at strains near 60% and proceeded rapidly to a localized failure strain of 200%. This result agrees with those of Bauer and Bless (Reference 14) and Fyfe and Rajendran (Reference 15) who also observed inhibition of necking in rate sensitive materials. The stress at failure could not be determined since SHB strain gauge data is recorded only during the first tensile pulse.

c.   C1008 steel

Three necking experiments were conducted on the C1008 steel, and the results are summarized in Table 3. These experiments were also conducted at a high striker bar velocity, yet necking did not occur during the first pulse. The strain calculated from this photographic record agreed well with the strain computed from the SHB gauges, as shown in Figure 43.

At the end of the first pulse, the tensile specimens had reached a strain of 40% with no observable necking. During the second pulse, necking began at strains greater than 50% and proceeded rapidly to a failure strain of about 130 percent at the necking section.
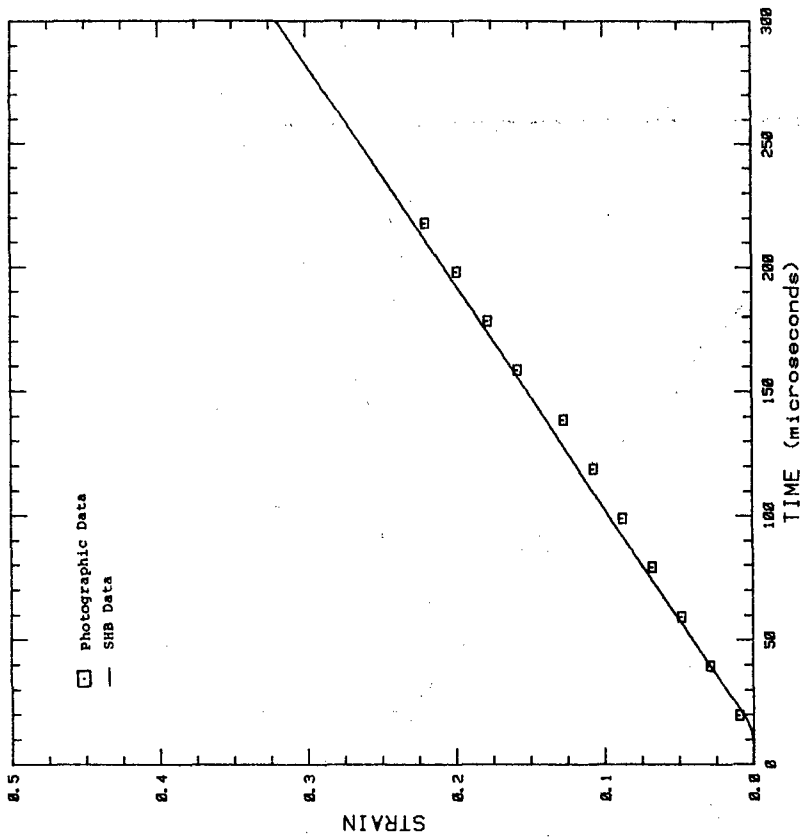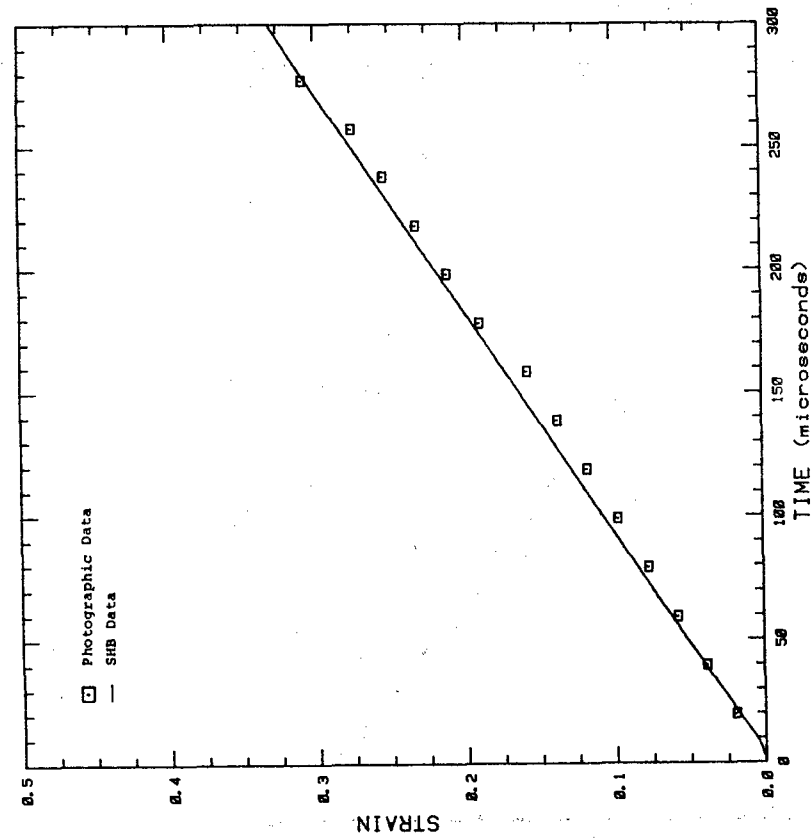
Figure 42.   Comparison of the Strain Calculated from the Hopkinson Bar
and from the Photograph for OFHC Copper.

67
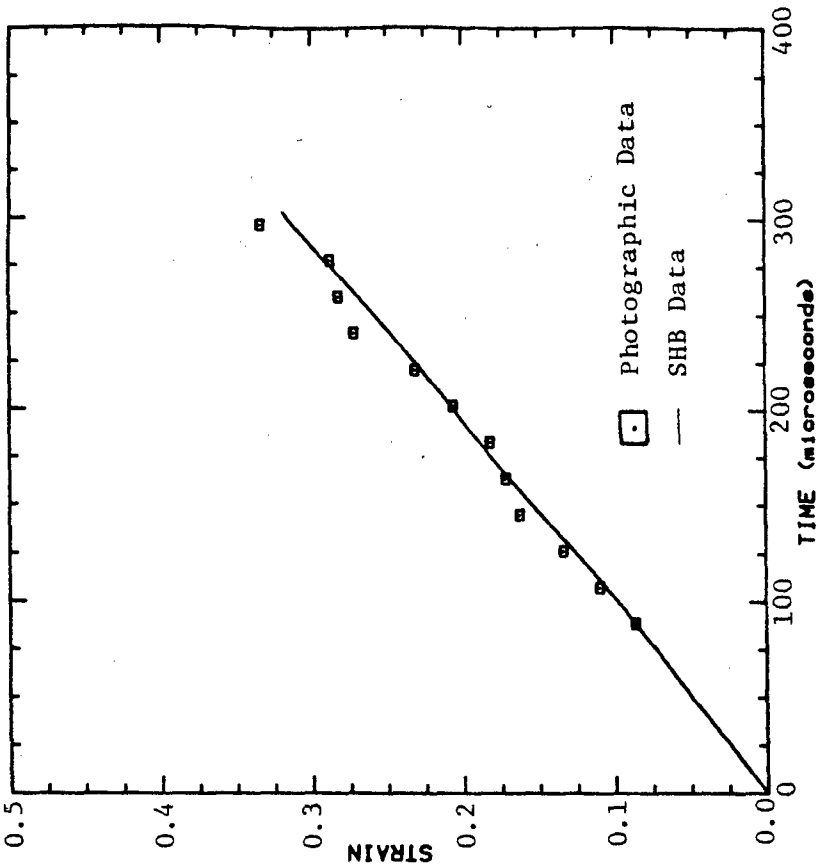
b. HB-244

a. HB-243
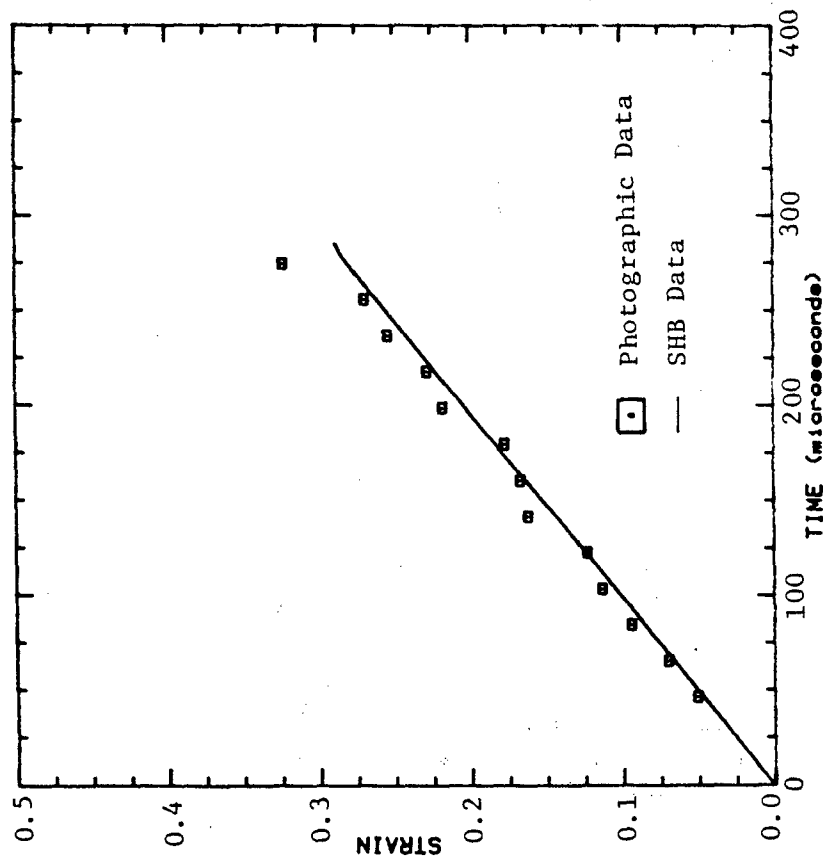
Figure 43. Comparison of the Strain Calculated from the Hopkinson Bar and from the Photographs for C1008 Steel.

d.   HY100 steel

Three necking experiments were conducted on the HY100 steel, and the results are summarized in Table 3. This local strain is compared with the average strain calculated from the Hopkinson bar data, as shown in Figure 44. The local strain agreed with the average strain until the onset of necking, which in this case occurred at about 25 percent strain. The maximum value of local strain observed is about 65 percent.

Figure 45 contains a plot of Bridgman's results and the results for the experiments on HY100 steel. The data from the HY100 steel fall within the scatter of Bridgman's data.

The effective stress vs. localized strain and the true stress vs. localized strain plots are shown in Figure 46 for each experiment. Since this material showed significant rate sensitivity, the flow stress increased considerably as the neck developed. The sharp rise in the flow stress is due to the increased strain-rates during necking. The maximum observed value of effective stress was 14 Kbar at 70 percent localized strain.

The specimens did not fail during the first pulse. However, they failed in the subsequent tensile pulse at local strains of around 100 percent, as summarized in Table 3. The relatively early onset of necking in HY100 steel, compared to C1008 steel, is consistent with the observation that HY100 steel is less rate dependent than C1008 steel.

e.   7039-T64 aluminum

Three necking experiments were conducted on 7039-T64 aluminum, and the results are summarized in Table 3. The comparison of local and average strain is shown in Figure 47. The strain from the two independent sources compares very well until necking begins.

The aluminum specimens did not begin to neck until the second pulse at a strain of 25 percent. Failure
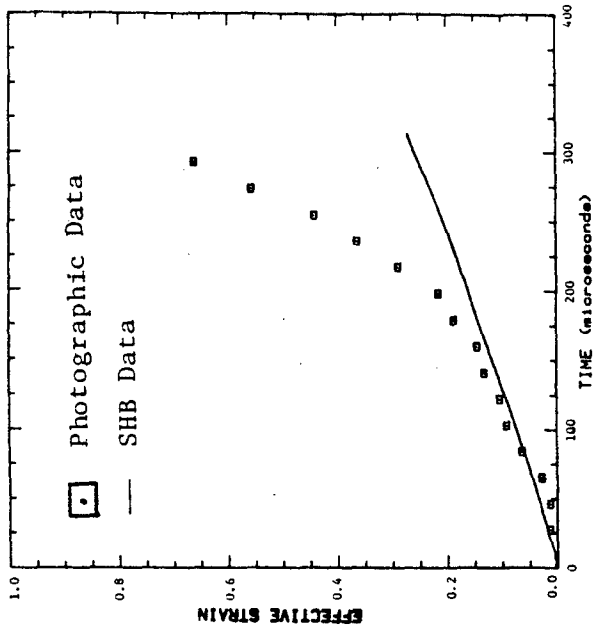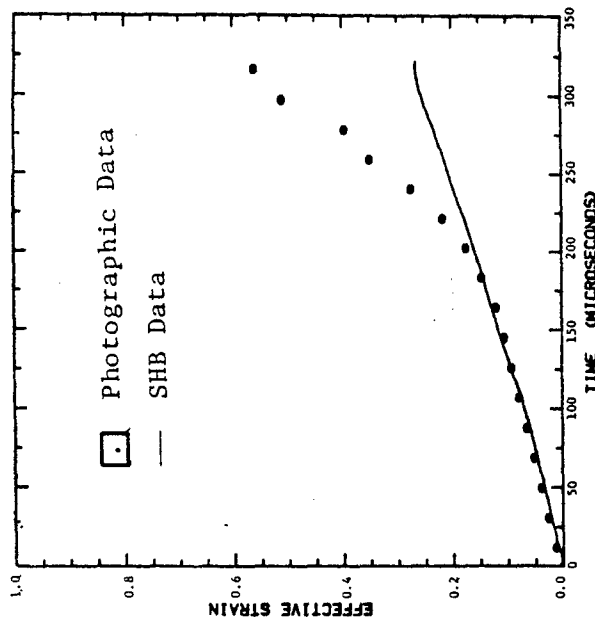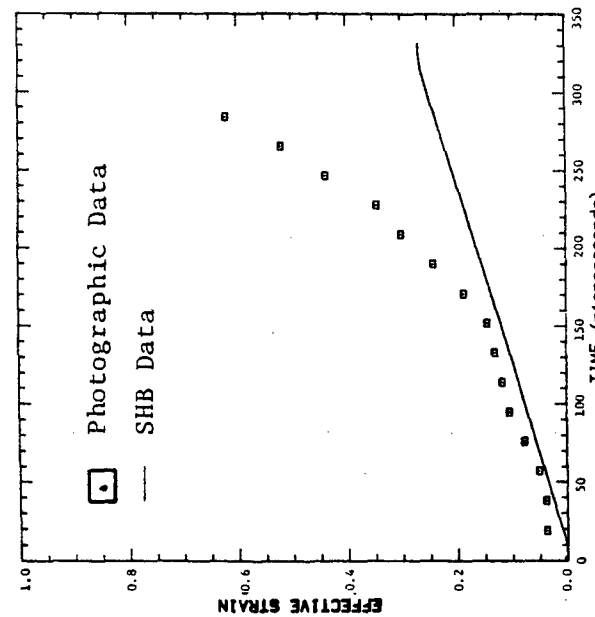
Figure 44.   Comparison of Strain Calculated from the Hopkinson Bar Data and
            from the Photographs for HY100 Steel.

70
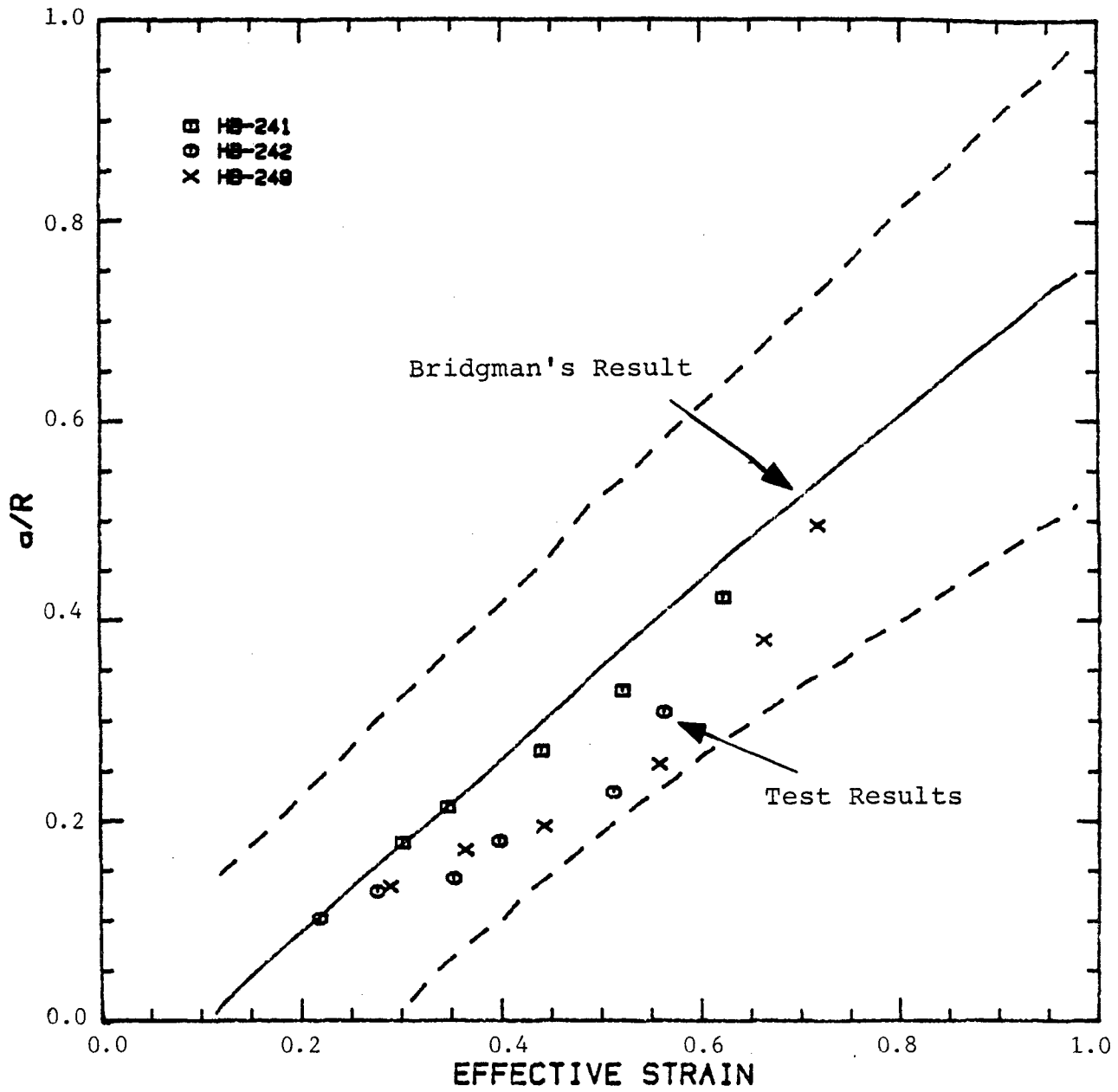
Figure 45.   Comparison of Bridgman's Observed Necking
              Behavior (with the Scatter Band) and the
              Necking Behavior of the HY100 Steel.
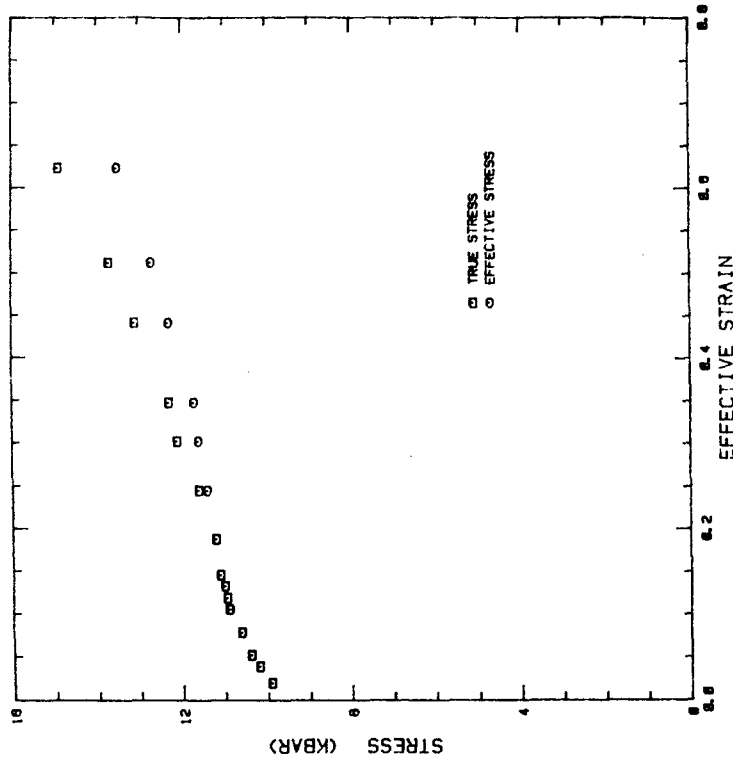
a. HB-241
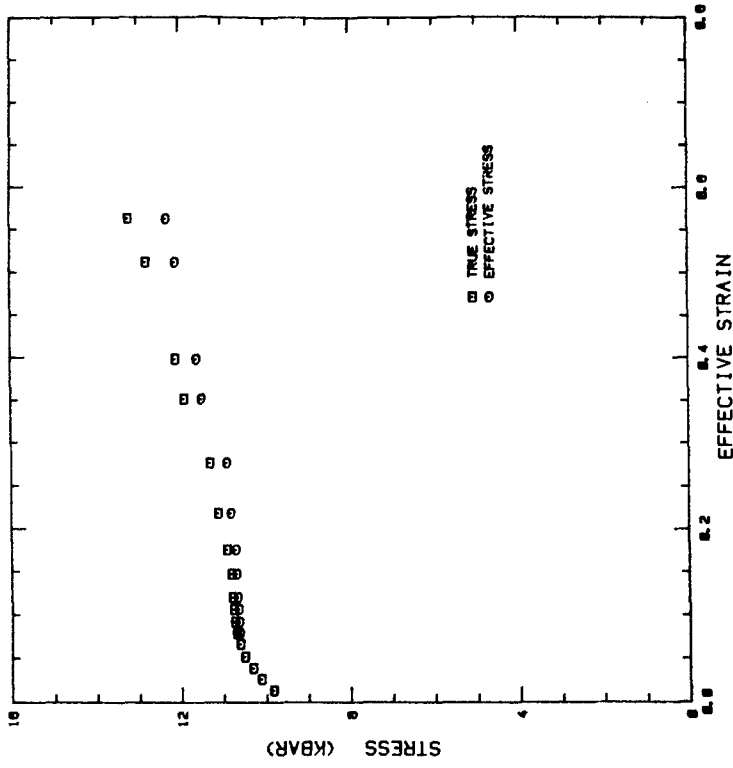
b. HB-242

Figure 46. The Effective Stress Calculated from the Necking HY100 Experiments.
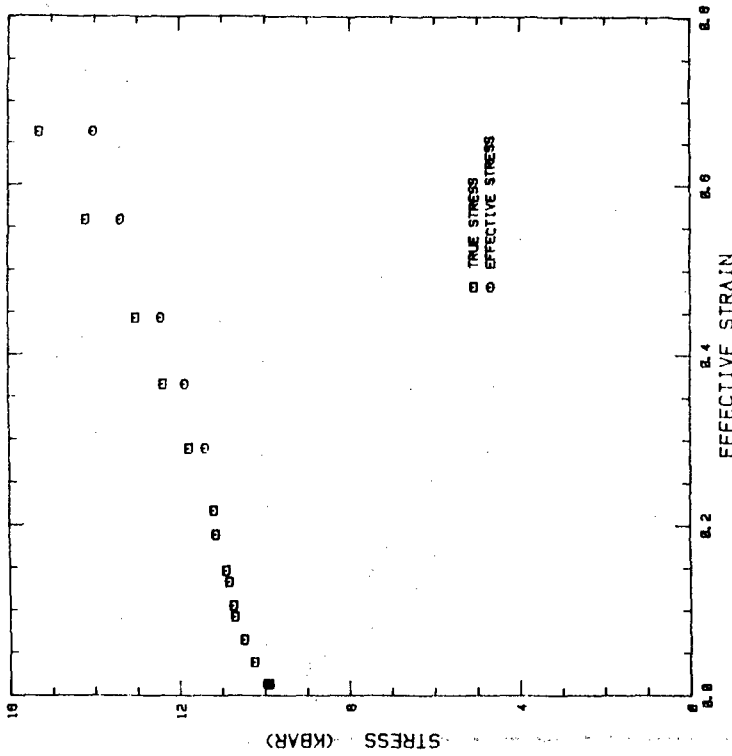
c. HB-249
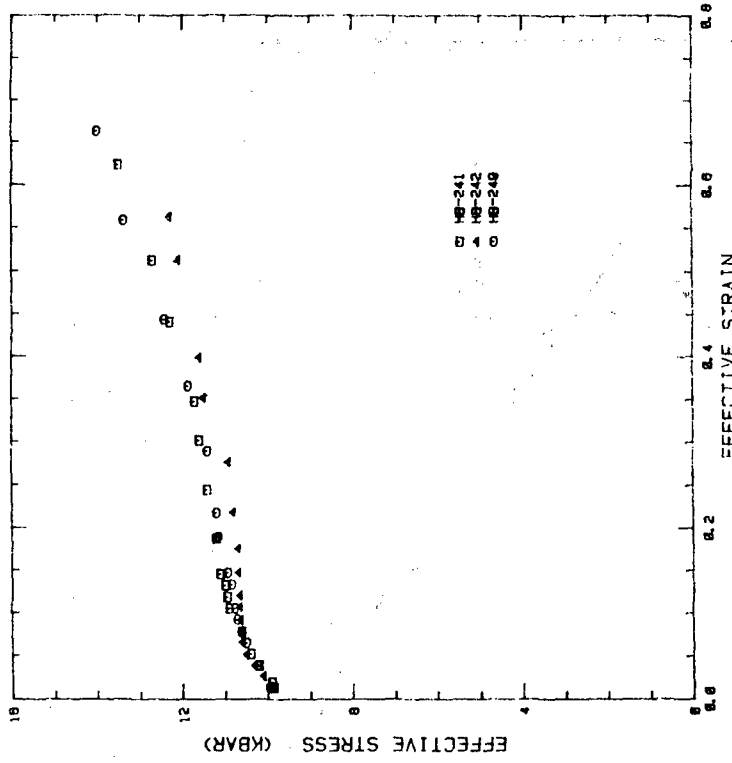
d. Combined Plot

Figure 46 (cont'd). The Effective Stress Calculated from the Necking HY100 Experiments.
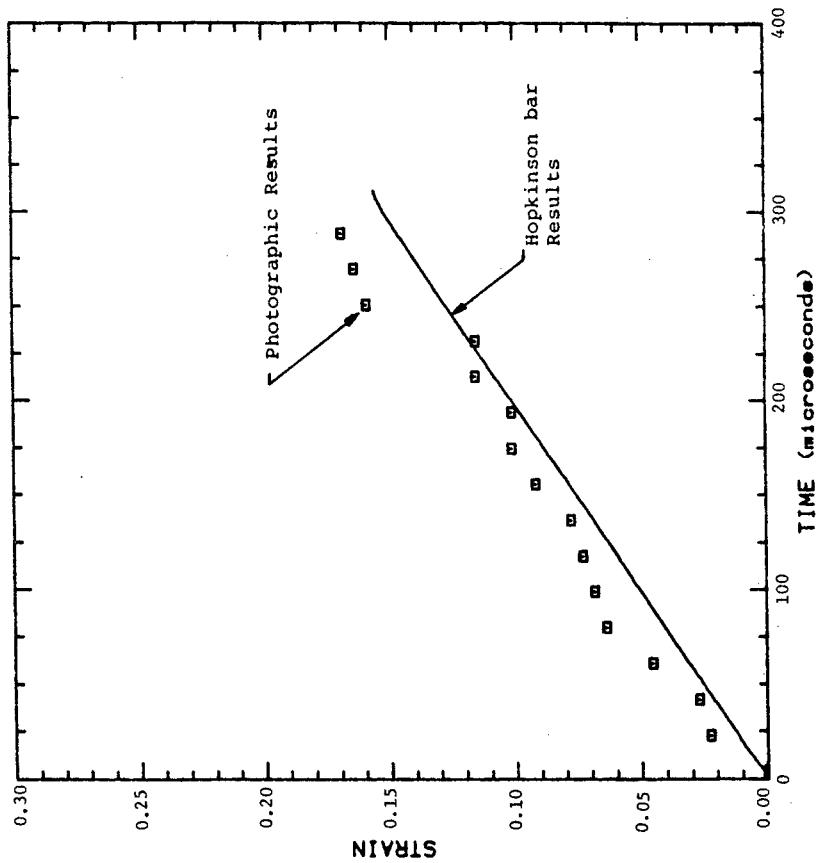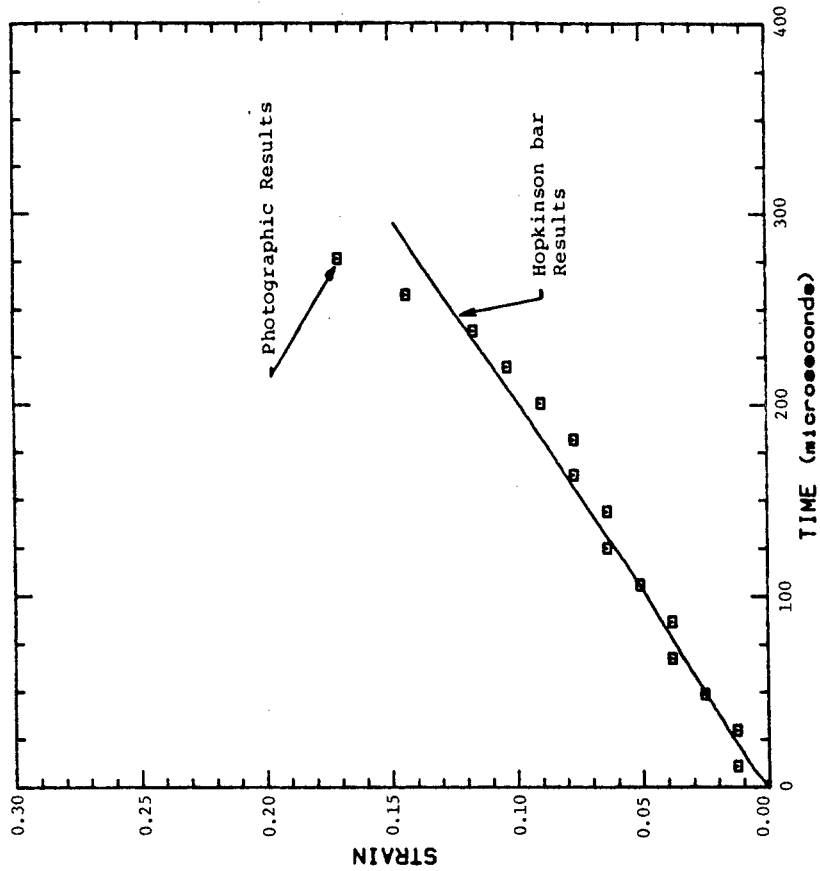
Figure 47. Comparison of the Strain Calculated from the Photographs with the Strain Calculated from the Hopkinson Bar for Two Tests of 7039-T64 Aluminum at a Strain rate 550 s^{-1}.

74

occurred at a local strain of 50 percent. Failure appeared to be brittle. Larger strains at failure were observed in 6061-T6 aluminum (Reference 15) than in this aluminum. This is true even though the yield stress of both materials is relatively insensitive to strain-rate. One explanation is that necking in 6061-T6 is triggered by void formation which does not occur in 7039-T64. Void initiated necking has been observed by Bluhm (Reference 16) in ductile metals at low rates. Ductile void growth is also known to occur in 6061-T6 aluminum (Reference 15).

2.3   PLATE IMPACT EXPERIMENTS

In the plate impact test, a flat flyer plate is made to impact against a target plate at a high velocity. The flyer and target may be of the same or different material. Compressive stresses are produced and transmitted immediately from the plane of impact to the adjacent stress free areas of the material in the form of a stress pulse. Many discussions of planar impact loading are available (References 17 and 18).

Plate impact test provide a loading path that is very different from conventional SHB compression or tension tests. The deformation is that of one-dimensional strain, and the mean stress is generally very high compared to that is SHB tests. Strain rates are 10^5 s^{-1} or higher. The material undergoes compression immediately followed by tension. Thus, plate impact experiments are essential for calibrating and validating high strain rate material models that aspire to general applicability. Specifically, plate impact data may be interpreted to infer compression and tensile yield strengths and failure parameters.

2.3.1   Techniques

The experimental techniques for plate impact experiments at the University of Dayton are described by Bless (Reference 19) and Bless et al., (Reference 6). Readers who are unfamiliar with this technique should look at Figure 48 which provides an (x,t) diagram. The origin represents the instant of impact on the target surface. Shock waves propagate into the

75
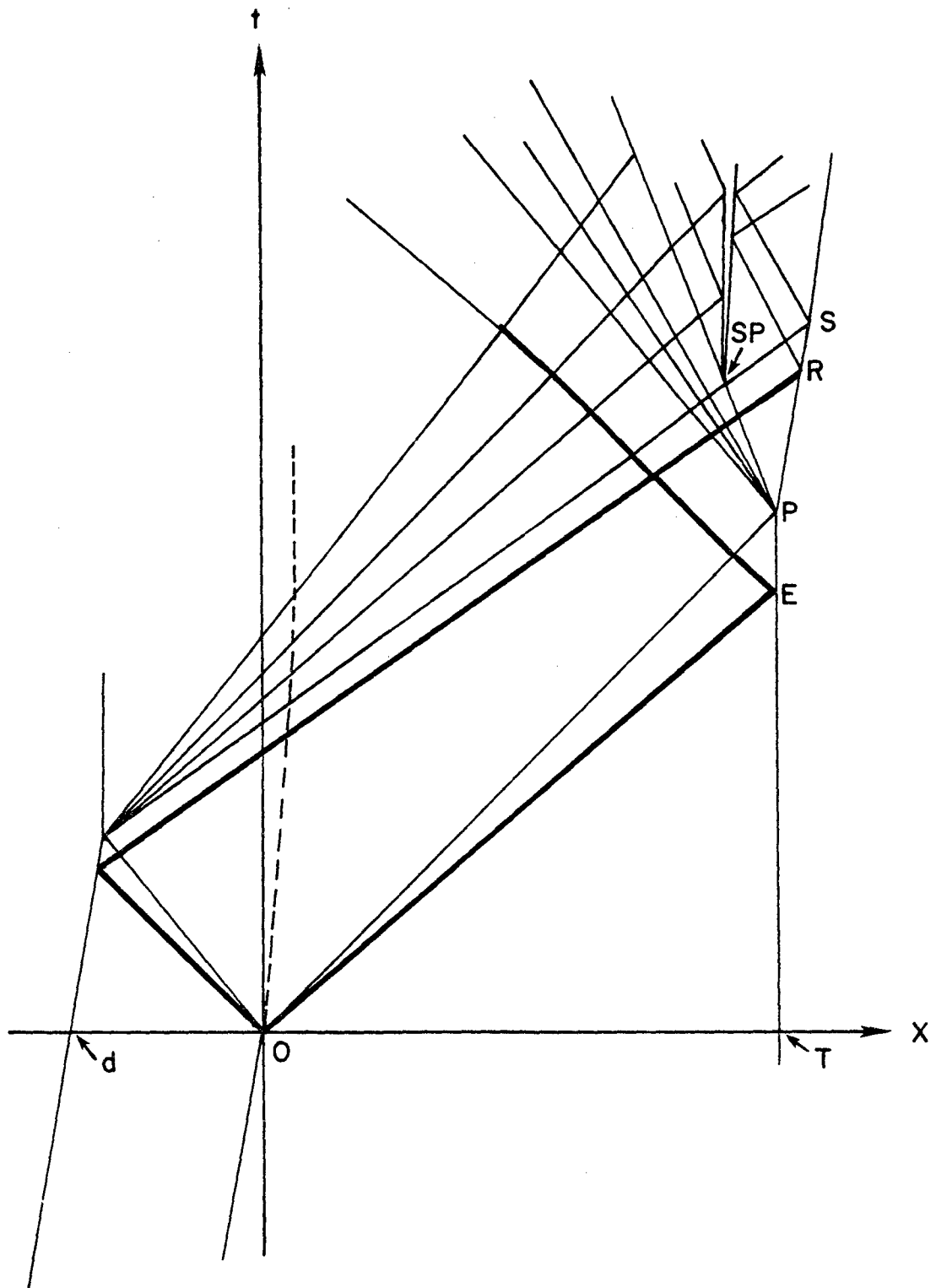
Figure 48. (x,t) Diagram for a One-Dimensional Impact.

target and into the flyer plate. Shock waves reflect from free surfaces as release (tensile) waves. In the example diagrammed, these lead to a spall at point SP. Shock waves emanate from the spall plane as the stress relaxes to zero. The velocity of the rear of the target is measured with a VISAR (Reference 20). In some experiments, a transparent window is placed behind the target in order to suppress release waves and prevent spall.

2.3.2   Yield Strength and Spall Threshold

The plate impact tests were conducted with three objectives: (1) determination of Hugoniot Elastic Limit, (2) determination of the unloading path from the free surface velocity history, and (3) determination of the threshold conditions associated with onset of spall fracture.

Impact induces an elastic shock and a plastic shock in the target. The amplitude of the elastic shock is σ_{HEL}. The Hugoniot elastic limit, σ_{HEL}, is the maximum stress for one-dimensional elastic wave propagation. This stress level is a material property, and above this level the material flows plastically. The stress σ_{HEL} can be determined from the experimentally obtained free surface velocity of the target that corresponds to the elastic shock, u_{HEL}.

$$\sigma_{HEL} = 1/2\ \rho C_L\ u_{HEL} \qquad (11)$$

where C_L is the elastic sound speed. The high strain rate yield strength Y_o can then be calculated from the relationship:

$$Y_o = \frac{\sigma_{HEL}}{(\frac{K}{2G} + \frac{2}{3})} \qquad (12)$$

where G is the shear modulus and K is the bulk modulus.

In conventional elastic plastic theory, the release process is initially elastic. Release waves travel at the elastic wavespeed. The elastic deviatoric stress possible in

77

release is 2Y. However, not all materials display this behavior. Brittle materials in particular are sometimes observed to undergo loss of shear strength behind the initial shock. In order to determine the release path from data, the material is modeled by a numerical method. The constitutive descriptions are varied until the observed free surface velocity decay associated with release wave arrivals is reproduced.

The "spall stress" σ_s, is defined as the highest tensile stress experienced by the target prior to spall. The spall stress is often computed from

$$\sigma_s = 1/2\rho \ C_L \ \Delta V_s \qquad\qquad (13)$$

(see Figure 49 for ΔV_s definition). However, wave propagation calculations show that this is incorrect if spall occurs abruptly because shock waves emanating from the spall plane will overtake release waves.

Equation (13) also is based on the assumption that all of the release characteristics which arrive at the rear surface before the spall signal propagate at speed C_L (Reference 19). In fact, only the lead characteristic has this speed. This assumption causes equation (13) to overestimate σ_s by possibly as much as ten percent.

2.3.3   Test Results

Plate impact experiments were conducted on C1008 and HY100 steels, and 7039-T64 aluminum, see Table 4. A few tests were conducted on 1020 steel to supplement previous data (References 6,19) and support the numerical analysis. Preliminary experiments were also conducted with a double flyer plate technique to observe void formation and recompaction.

Target-samples (77mm diameter and 6mm thickness) were fabricated for each of the metals to be tested. The target plates were mounted in the fixture which was attached to the
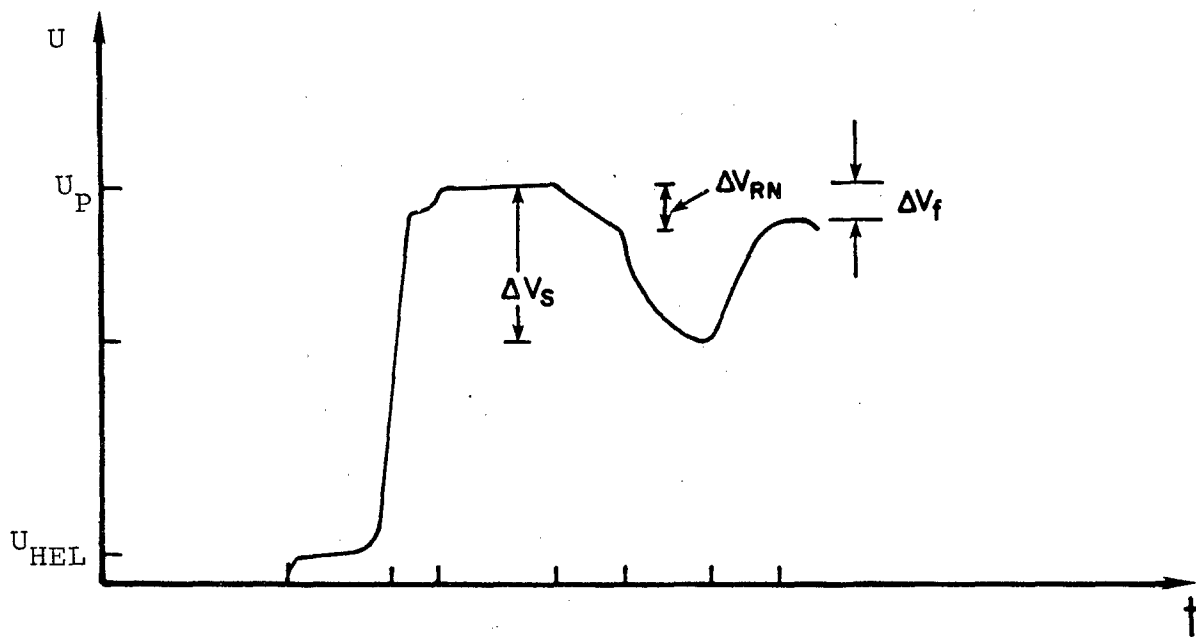
Figure 49.   Representative VISAR Trace, Showing Parameter
             Definitions.

TABLE 4

PLATE IMPACT TESTS ON C1008, HY100, and 7039-T64

Shot No.	Velocity (m/sec)	Target*	Projectile	Visible Spall
		C1008 Steel		
695	157	6 mm C1008	3 mm 1020	yes
696	373	6 mm C1008	3 mm 1020	yes
678	178	6 mm C1008	3 mm 1020	part.
685	134	6 mm C1008	3 mm 1020	no
687	134	6 mm C1008	3 mm 1020	no
679	192	6 mm C1008W	3 mm 1020 3 mm Lexan	n.a.
677	200	6 mm C1008W	3 mm 1020 1.6 mm WC	n.a.
		HY100 Steel		
694	203	6 mm HY100	3 mm 1020	part.
680	355	6 mm HY100	3 mm 1020	yes
681	180	6 mm HY100	3 mm 1020	no
686	200	6 mm HY100	3 mm 1020	part.
688	196	6 mm HY100W	3 mm 1020 3 mm Lexan	n.a.
689	187	6 mm HY100W	3 mm 1020 1.6 mm WC	n.a.
690	186	6 mm HY100W	3 mm 1020 3 mm Lexan	n.a.
		7039-T64 Aluminum		
693	180	6 mm 7039-T64	3 mm 1100	yes
682	375	6 mm 7039-T64	3 mm 1020 St	yes
683	187	6 mm 7039-T64	3 mm 1100 Al	part.
684	162	6 mm 7039-T64	3 mm 1100 Al	no
691	200	6 mm 7039-T64 W	3 mm 1100 3 mm Lexan	n.a.
692	200	6 mm 7039-T64 W	3 mm 1.66 mm WC	n.a.

* W denotes SiO_2 window behind the target

muzzle of the 50mm compressed air gun as explained earlier. Projectile flyer plates were mostly 3mm thick.

In a few tests, the flyer plates were mounted on tungsten carbide (WC) backing plates so that the initial shock loading would be followed by reshock instead of release. Using both release and recompression data permits a check for relaxation of shear stress behind the shock waves. Many targets were backed with fused silica windows 6mm thick and 25mm in diameter. The windows prevent release waves from originating at the target rear surface, and thus suppress spall. This set-up allows observation of the complete release process, which might otherwise be blocked by spall fracture. The windows remained transparent at least until the initial shock wave had passed all the way through them, which gave a recording time of about one microsecond. The windows were depolished, silvered, and bonded to the targets with thin film epoxy. A stop was placed on the VISAR operator to block the spectral reflections from the window rear surface. The VISAR data collected were used to assist in determining the elastic yield, spall threshold, and spall strength.

a.   1020 steel

Experiments on 1020 steel have been chiefly motivated by a need to fully describe spall fracture. There are two approaches for deriving spall criteria in plate impact tests, and both have been utilized. The first is to vary the flyer plate thickness and velocity and determine the threshold impact conditions for target damage. It is usually found that thinner flyer plates require higher impact velocities to produce damage. The threshold criteria can be interpreted as the combinations of stress level and duration just sufficient to cause fracture.

The second approach is to measure transmitted wave profiles after damage has occurred. Target sectioning and wave profile data determine the time and location where spall first occurred.

The two approaches to spall characterization are sampling two rather different types of behavior. Threshold studies generally employ relatively long duration tensile pulses. Transmitted wave techniques operate on a much shorter time scale, and spall separation may be limited by time dependent processes. Experiments were performed with 1020 steel of hardness 62 to 75 on the Rockwell B scale. In most experiments, a conventional flyer plate was used. However, in some tests, the flyer plate had a step along a diameter on its rear surface. With this technique each impact was equivalent to two experiments with conventional flyer plates. In other shots, tapered flyer plates were used. The motive here was not so much to obtain damage gradients, as in Seaman et al., (Reference 21), but rather to efficiently define the spall threshold in regions in which the most important parameter is flyer plate thickness. This is the case for thin flyer plates; for thick plates, the damage is principally velocity-dependent. Use of wedge flyers has enabled us to obtain data for shorter loading pulses than are normally reported in spall experiments. The wedge technique is described in more detail by Bless et al., (Reference 6).

The microstructure of the steel consisted of equiaxial grains whose typical diameter was 30 μm. The flyer plates were backed with PMMA or air, except the wedges, which were backed with mating teflon wedges. Free surface velocity was measured in the center of the target disc. Complete spall was defined as a void content of over 50 percent on the spall plane. Partial spall was defined as visible (at 400X) damage less than complete spall. Results reported below are mainly based on additional analyses of data in Reference 6.

The σ_{HEL} data for 1020 steel were inconclusive, in spite of a large number of shots. Figure 50 shows a typical velocity profile. The HEL is not well defined, even though the target was 9mm thick and the shock rise was resolved. SHB results indicate a yield strength of about 4.5 Kbar and work hardening to 7 Kbar; 7 Kbar corresponds to σ_{HEL} = 11 Kbar and u_{HEL} = 0.05 mm/μs. This arrival is not evident in Figure 50;

82
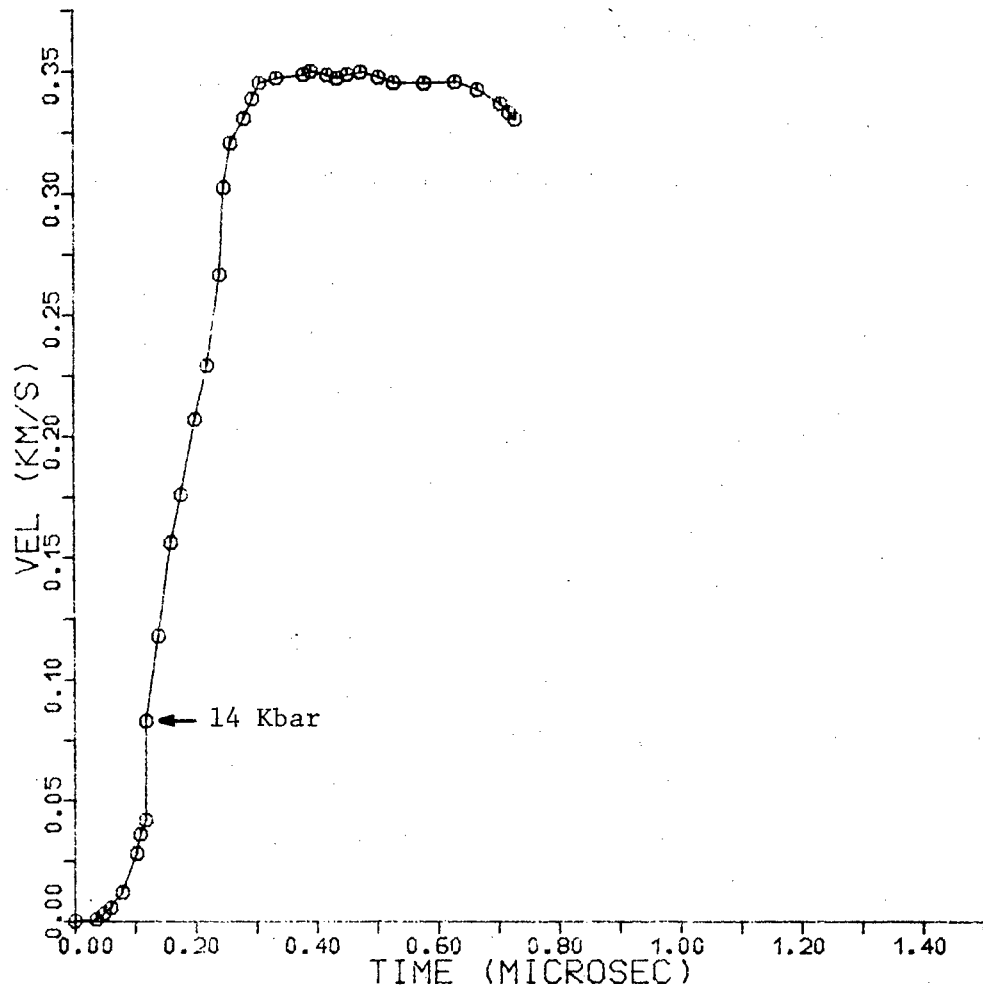
Figure 50.   VISAR Data for 1020 Steel, showing poorly
             Defined HEL. (Target was 9mm Thick, Flyer
             Plate was 4mm.)

nor is it apparent on other VISAR traces. However, reference 22
reports an HEL of 11 Kbar for 12.7mm thick targets of 1020 steel
very similar to our material.

The scatter in HEL data is probably due to the
"precursor decay phenomena" that has been observed in iron
(Reference 23). Data for Armco iron from several sources (e.g.,
References 23 and 24) indicate that in 5mm thick targets, the
amplitude of the elastic precursor is about 50 percent higher than
its equilibrium value.

It appears that the "spall signal" in 1020
steel is generated by void nucleation. The evidence is provided
by shot 529 which was at 400°C. The VISAR data is shown in Figure
51. A spall reverberation is clear. After sectioning and
polishing, this target appeared undamaged. An electron microscope
was necessary to reveal micron sized pores as shown in Figure 52.
These were widely distributed about the incipient spall plane.

The critical velocity for spall development
can be read from Figure 53. The flyer plates used in these
experiments were backed with PMMA. The threshold for partial
spall was about 200 m/s for 2mm flyer plates, and between 251 and
279m/s for 1mm thick flyer plates. Values of spall stress from
equation (13) were only available from three shots at impact
velocities about 500m/s. The range was 26 to 33 Kbar. The most
negative stress corresponding to incipient spall with 2mm thick
flyers is about 22 Kbar. Reference 22 found that for 3.2mm flyer
plates, incipient spall occurred at 15 to 17 Kbar. In Figure 53,
this corresponds to an impact velocity of about 150m/s.

b.   OFHC copper

No additional plate impact experiments were
performed with copper beyond those reported by Bless et al.,
(Reference 6). However, additional analysis of their data was
carried out. Figure 54 summarizes the observation of spall
failure in this material. The spall stress, σ_s, computed from

84
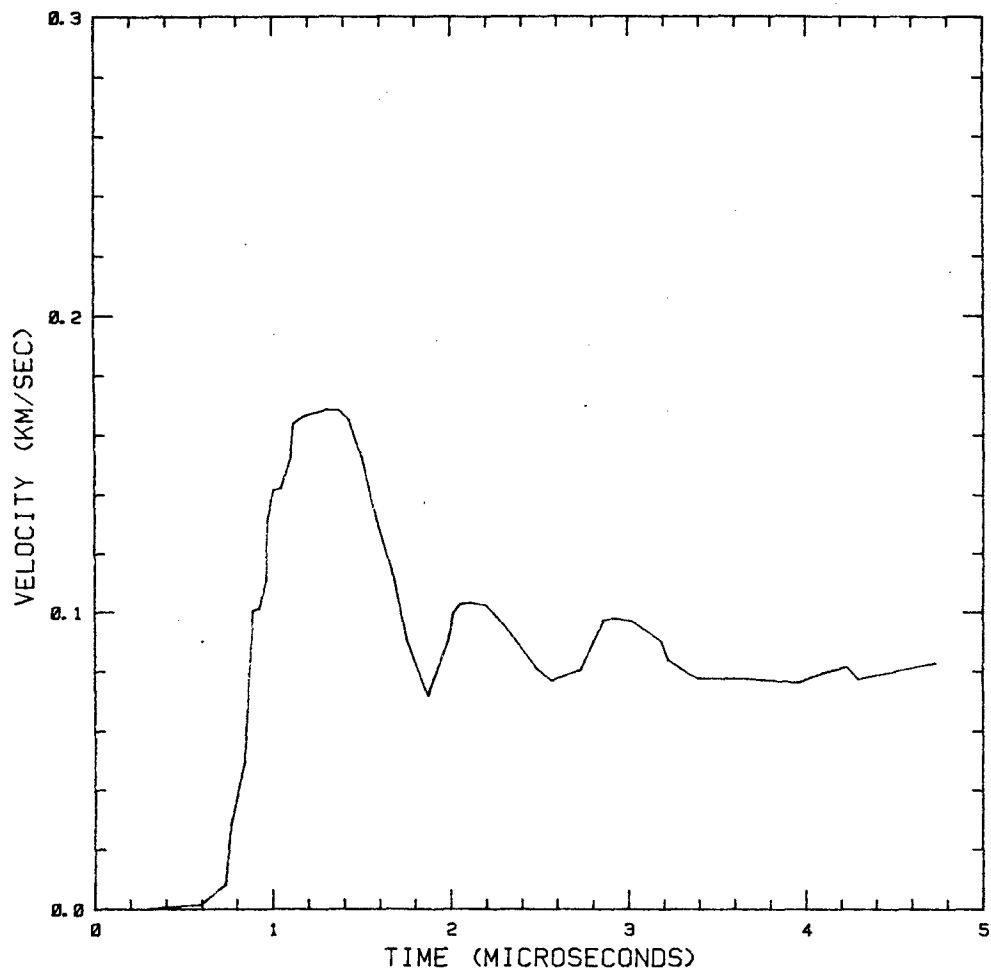
Figure 51. VISAR Data for Shot 529, 5mm 1020 Target, 2mm Flyer. (Target Temperature was 400°C.
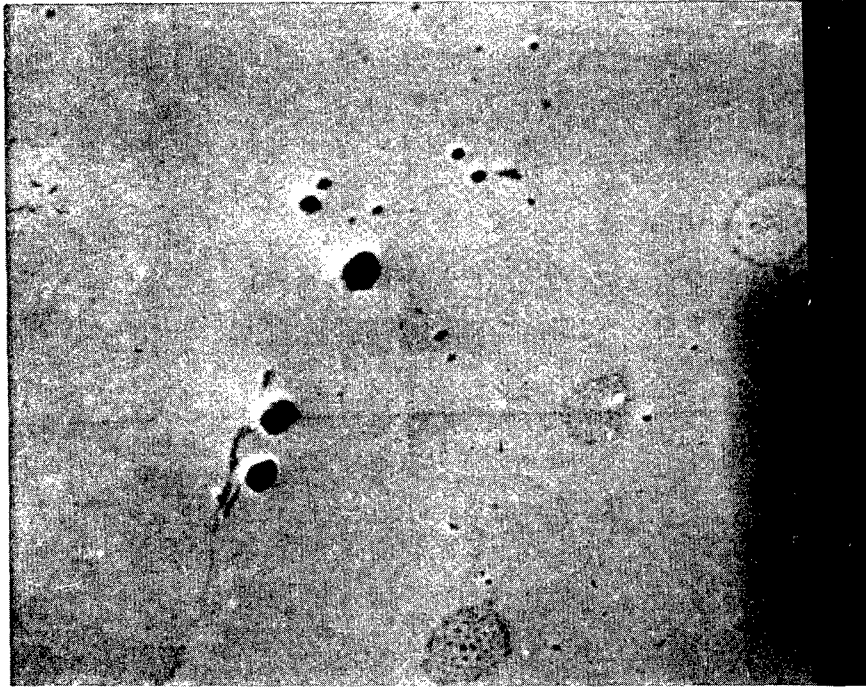
Figure 52.   Electron Microscope Photograph of
              Micron Sized Pores in 1020 Target,
              Shot 529, 1000x.
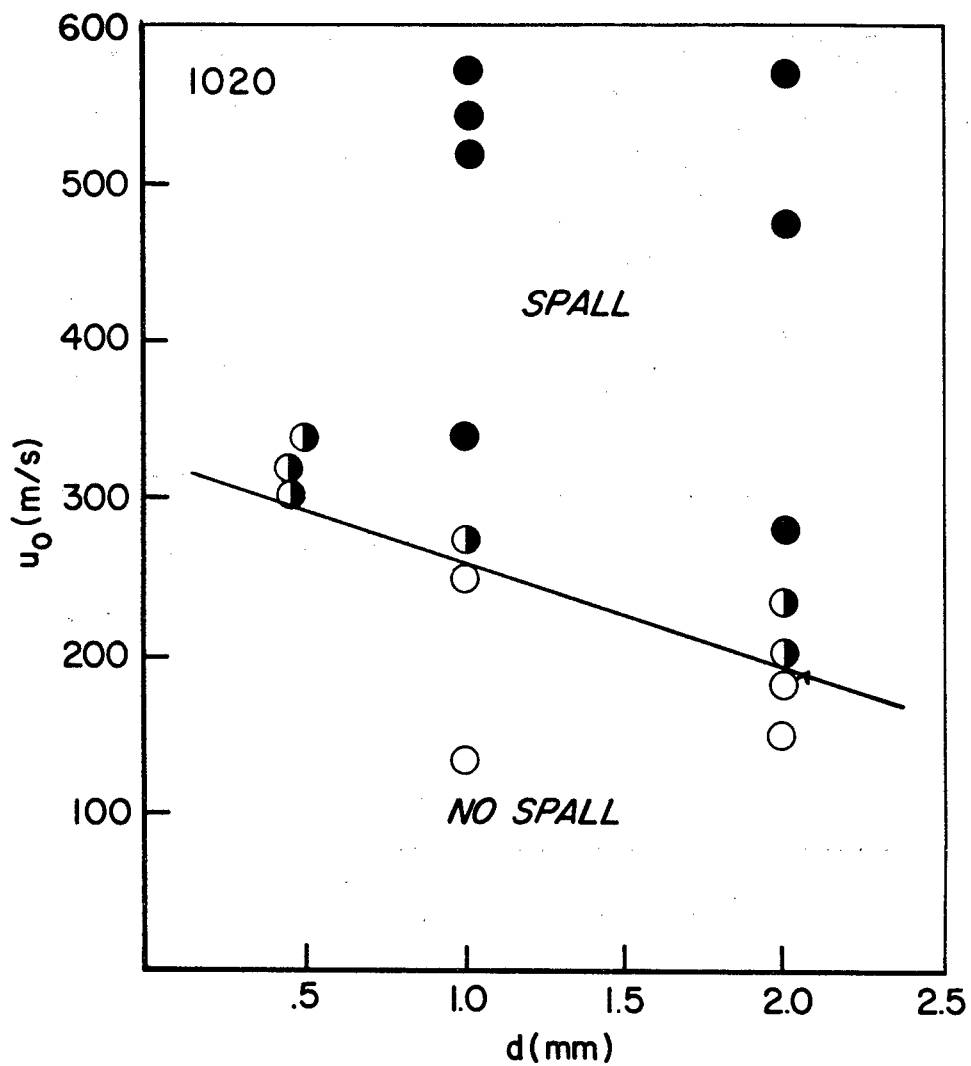
Figure 53. Critical Velocity for Spall Development of 1020 Steel. (Solid circles denote complete system; half-filled circles, partial spall; open circles, no spall. Flag shows widely separated micron-size voids.)
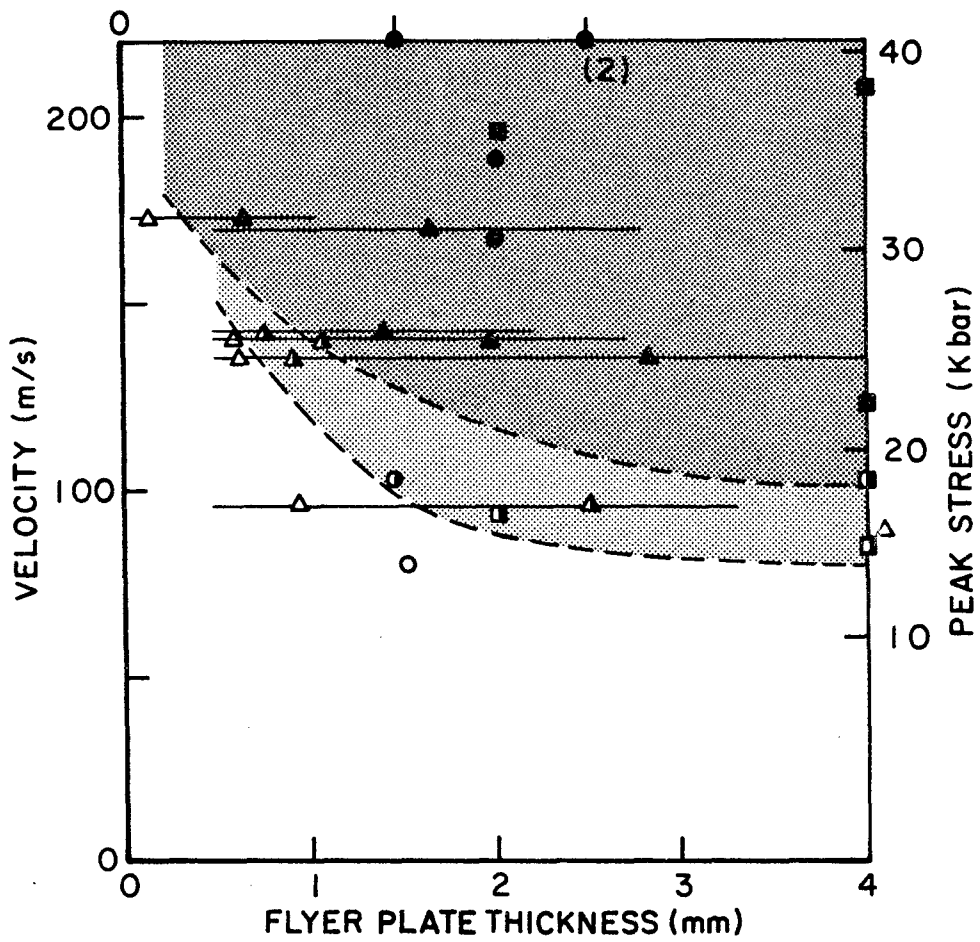
Figure 54.   Spall Threshold Data for OFHC Copper.

equation (13) was between 12 and 13 Kbar for all of the copper records.

c. C1008 steel

The evaluation of threshold conditions required several shots with different velocities. Five tests were conducted to determine the spall threshold velocity. For a better description of the shocked material's strength, two more tests were performed with the flyer plates mounted on WC/Lexan backing plates as explained in the preceding paragraph.

The VISAR was used on all shots except 695, the VISAR results are shown in Figure 55. A complete release wave profile was obtained in shot 679 because spall was suppressed by the silica window and Lexan backing plate behind the flyer plate. The release profile clearly shows the arrival of two elastic waves in agreement with conventional elastic-plastic theory.

Most of the VISAR traces show a ramp shock wave. Other impact tests on mild steel and iron have not shown this anomaly, although the data here are at slightly lower impact velocities than those reported elsewhere. This feature of the waves is so unusual that it should be checked in further experiments.

Four good observations of the elastic precursor were obtained. The value of the HEL varied from 11 to 12 Kbar. The average value was 11.3 Kbar. However, as pointed out in the section on 1020 steel, the true value of the HEL may be 50 percent less than this.

The spall threshold was bounded by shots at 157m/s and 178m/s. At the lower velocity, the voids were connected by a continuous crack. The threshold velocity for 3mm thick flyer plates is thus 168 ± 10m/s. The corresponding spall stress is 31 ± 2 Kbar. This stress should be used to predict spall when damage accumulation is not taken into account and the tensile pulse duration is about 1µs. The value of σ_s calculated from equation (13) was 18 Kbar for shots 678, 685 and 687.
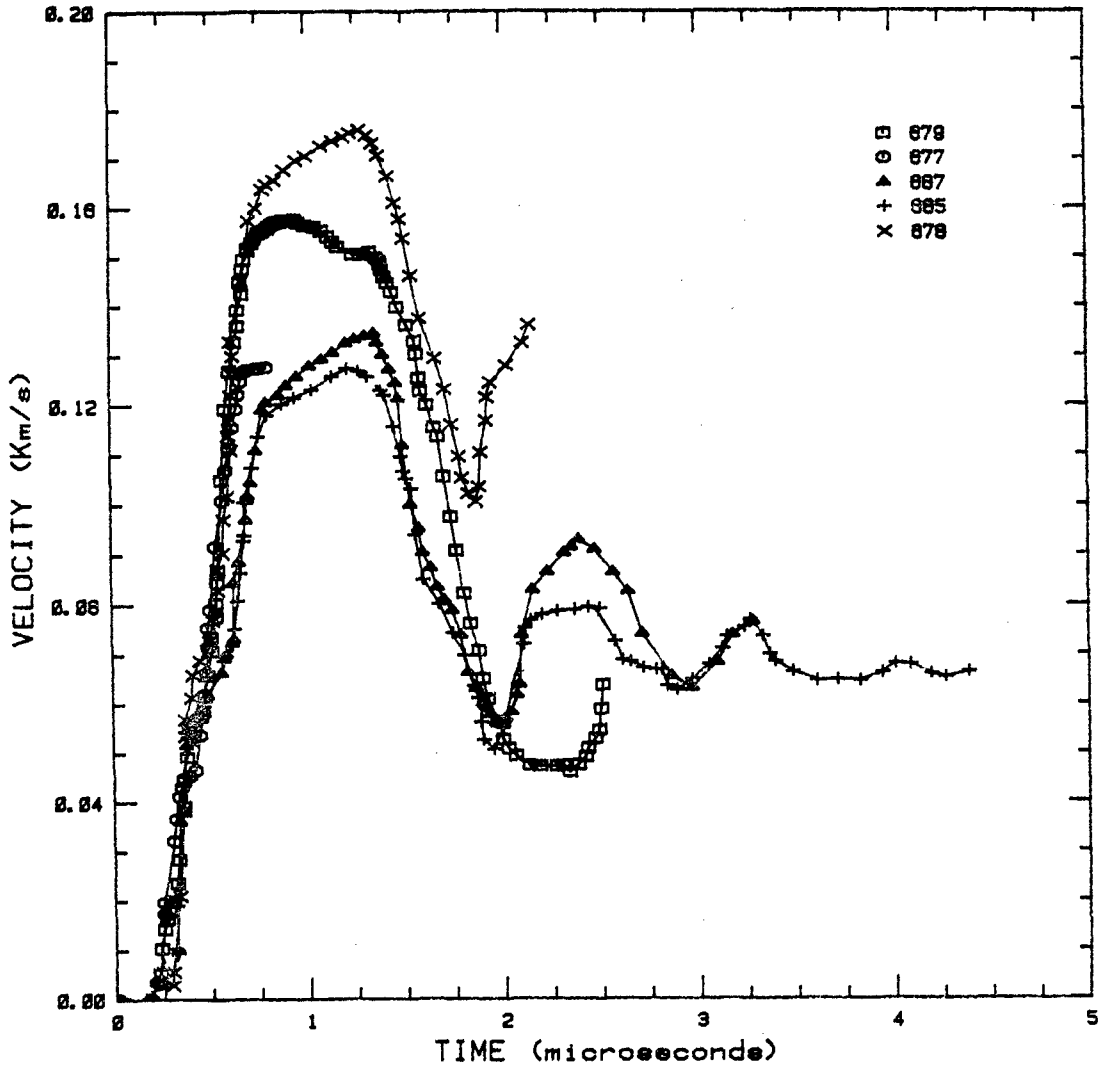
Figure 55.   VISAR Data from Impacts on C1008 Steel Plates.

The C1008 spall threshold is consistent with the 1020 spall data. This is shown in Figure 56. The curve in Figure 56 extended to 3mm thick flyer plates also shows the SHB data for 1020 steel. The point is plotted at the impact velocity that would have produced the same mean stress as occurred in the SHB specimen at failure

$$\sigma_m = 1/3 \left(1 + 3 \ln \left(1 + \frac{a}{2R}\right)\right) \sigma_{eff} \qquad (14)$$

The agreement between these data sets shows that the Tuler-Butcher criterion used with a mean stress formulation is capable of describing failure in both of these mild steels over stress states from one-dimensional stress to one-dimensional strain. The mean stress corresponding to σ_o in the Tuler-Butcher equation is

$$\sigma_m = \sigma_o - \frac{2}{3}Y \qquad (15)$$

d.   HY100 steel

Five tests were carried out on HY100 steel target plates. VISAR data were obtained in all the HY100 shots, as shown in Figure 57. In shot 690, the data were difficult to interpret, and since that shot was nearly the same as 688, the data from the latter were used for analysis.

The shock waves in the silica-backed targets do not appear steady. We believe that this is probably an artifact of the distortion introduced by the shock wave traversing the window. The release or reshock in these experiments appears sharp and unambiguous.

The HEL was well resolved in shots 680 and 681. In both, the value was 15.5 ± .3 Kbar. The release profiles in shots 680 and 681 clearly indicate elastic arrivals of amplitude similar to the initial HEL, in agreement with elastic plastic theory. However, the reshock in shot 689 is preceded by a release wave that travels at an elastic velocity, indicating that an air gap was present between the two flyer plates.

91
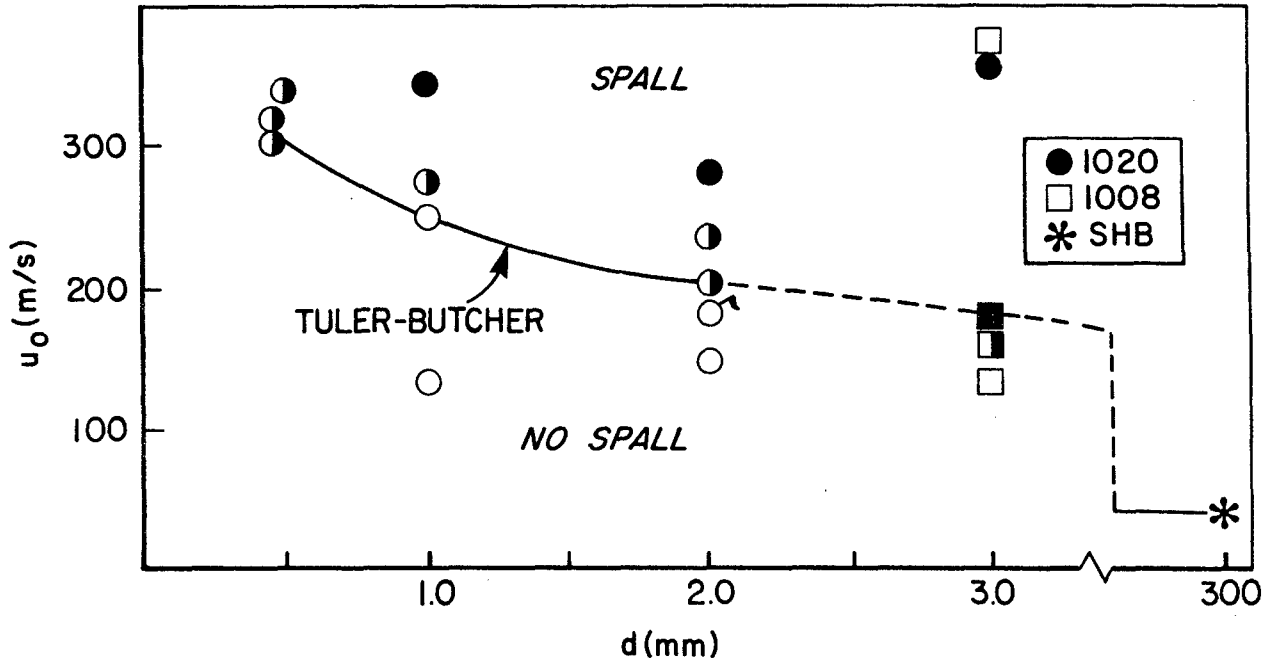
Figure 56.   Failure Observations in 1020 Steel and
             C1008 Steel. Line shows Tuler-Butcher
             Prediction; See Section 3.4.
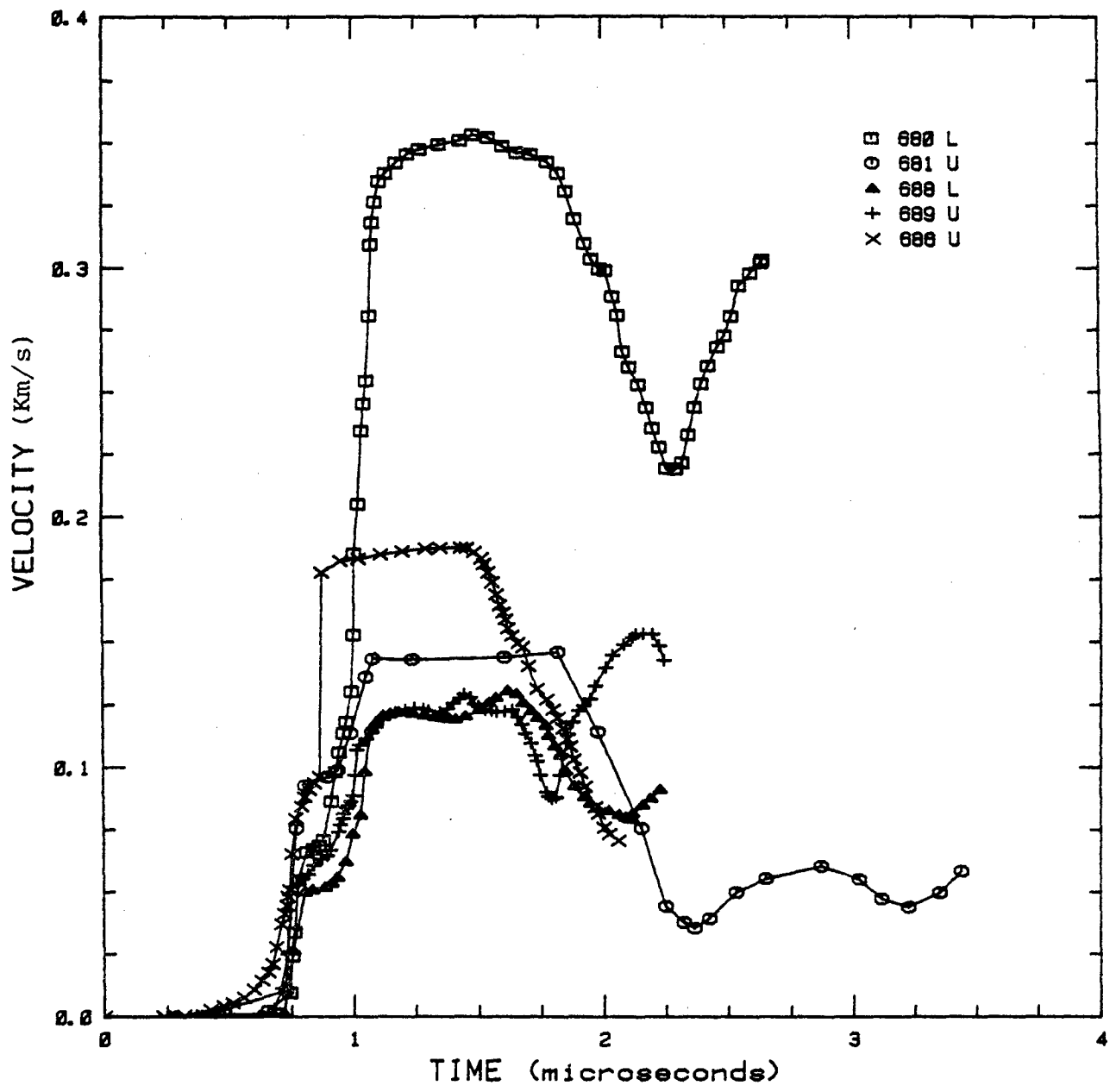
Figure 57.   VISAR Data from Impacts on HY100 Steel Plates.

Unfortunately, the presence of the air gap eliminates the possibility of measuring the speed of the reshock.

The spall threshold for HY100 is bracketed by shot 681, which resulted in isolated voids, and shot 686, which caused a spall crack. The threshold velocity is thus 190 ± 10 mm/μs, corresponding to a simple spall stress of 35 ± 2 Kbar. The value of σ_s from equation (18) seemed to vary with impact velocity: in shot 681, $\sigma_s = 27$ Kbar; in shot 686, $\sigma_s = 28$ Kbar, and in shot 680, $\sigma_s = 31$ Kbar.

e.   7039-T64 aluminum

Three shots were made with various velocities to determine the spall threshold of 7039-T64 aluminum. Two additional shots were done to obtain release and reshock wave profiles. VISAR data were obtained as shown in Figure 58.

Three values of the HEL were recorded: 8 Kbar in shot 683, 8.4 Kbar in shot 691, and 6.8 Kbar in shot 692. The weighted mean value is 7.7 Kbar. As was the case for steel, the data from shot 683 show separated elastic and plastic wave arrivals, and the first elastic wave has about the same amplitude as the HEL. Note that the release in shot 683 is essentially complete, since no spall occurred. Spall also did not occur in shot 684. Again, the release is nearly completed and a ringing period corresponding to a double wave transit through the target is present.

Comparing shots 691 and 692 (Lexan and WC backed flyer plates) is difficult because the first arrival in shot 692 is not clear. The most reliable time comparison is between the midpoint of the plastic shock and the midpoint of the arrival from the flyer/backing plate interface. This is 0.94 μs in shot 691 (release) and 0.87 μs in shot 692 (compression). Given the width of the wavefront, the time difference of 70 ns between these two transit times is probably not significant. The expected delay time between the arrival of the plastic wave and the arrival of the wave from the rear surface of the aluminum flyer plate is 0.94 μs, ignoring the relatively weak elastic wave

94
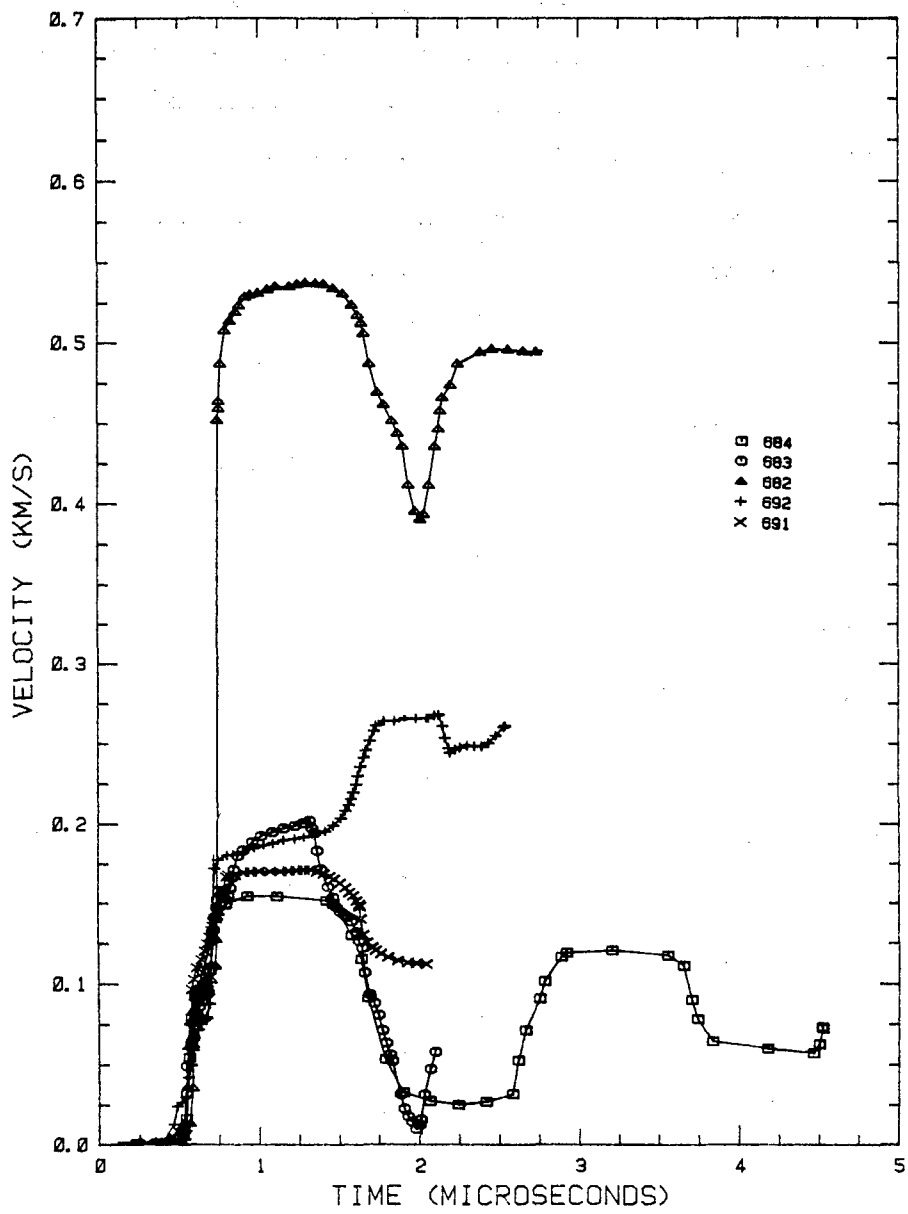
Figure 58.   VISAR Data from Five Impacts on 7039-T64 Aluminum Targets.

in the flyer plate. The expected difference if the release is wholly plastic in the target is 1.13 μs. Clearly both release and recompression waves are traveling with elastic wavespeeds in the target, indicating either substantial relaxation of shear stress or hardening of the material behind the shock.

The spall threshold of this material was not well determined. Shot 684 suffered no damage. However, shot 682, which was meant to provide an upper bound, was inadvertantly shot with a steel flyer plate, which produced a much higher stress than intended (and caused complete spall). Thus, only a lower bound for the simple spall stress is presently available: 13.5 Kbar. The value of σ_s (equation 13) was 13 Kbar in shot 682 (complete spall) and 17 Kbar in shot 683 (partial spall).

2.3.4 Experiments with BeO

The properties of porous polycrystalline BeO under shock compression below and just above the HEL were determined. The release and spall behavior were inferred from analysis of the VISAR data. Data for very high pressures and material identical to that used here are available in Marsh (Reference 25).

a. Material

The BeO was purchased from Ceradyne Inc. as Ceralloy 418. It was supplied as discs 40mm in diameter and thickness 4, 8, and 12mm. Eighteen specimens were obtained. They were ordered with a minimum density of 2.985 ± .005 g/cm^3. The crystal density of BeO is 3.008 g/cm^3.

Sample density, ρ was measured by the Archimedes method of liquid immersion. During immersion, the specimens were observed to gain weight, indicating water penetration. After the initial measurements, the specimens were boiled in deionized water for 5 minutes, cooled, and left immersed for 24 hours. Immersion weights were then remeasured.

96

If we denote the density calculated from the initial immersed weight as ρ_1, and the second as ρ_2 and the volumes of solid ceramic, open pores, and closed pores as V_s, V_o, and V_c, the apparent porosity is defined as

$$n = 1 - \frac{\rho_2}{\rho_1} = \frac{V_c}{(V_s + V_c)} \qquad (16)$$

The total porosity is

$$n_T = 1 - \frac{\rho_2}{\rho_1} = \frac{(V_c + V_o)}{(V_s + V_c + V_o)} \qquad (17)$$

Values for n are listed in Table 5.

For thick disc samples, n equaled n_T. For the 8mm samples, n_T was typically 20% greater than n. For 4mm samples, n_T was about three times n. The values of n_T were similar for all samples - about 2%. However, the data were not consistent with either of these two assumptions: (1) there is a constant porosity associated with the surfaces, or (2) all samples have the same values of n_T, and the liquid diffused similar distances into each specimen, resulting in differing values of n.

We have resolved this indeterminacy by assuming that in each specimen, the value of n represents the interior porosity. When n_T exceeds n, this is assumed to be caused by surface porosity. For shock wave analysis, therefore, n was considered to be the relevant porosity.

Sound speed was measured by a pulse-echo technique. The results are also listed in Table 5. It was found that sound speed correlated with n, as shown in Figure 59. The correlation substantiates the assumption that n is a measure of the interior porosity of the specimens. It is shown in Figure 59 that the extrapolated zero-porosity sound speed is 11.93 mm/μs. This is in good agreement with literature values: 11.99 (Marsh, Reference 25), 12.05 (Soga, Reference 26), and 11.54 (Gust and Royce, Reference 27). The dashed line in the figure is an

97

TABLE 5

POROSITY OF BeO SPECIMENS

Specimen number	Thickness (mm)	Porosity $n(\%)$	Sound Speed c_L (mm/μs)
4	12	2.7	11.94
5	12	1.9	11.72
6	8	1.4	11.85
7	8	1.6	11.43
8	8	1.4	11.85
9	8	1.4	11.47
10	8	1.4	11.64
11	8	1.2	11.85
12	8	1.5	11.85
13	8	1.1	11.64
14	4	0.6	11.74
15	4	0.6	11.74
16	4	0.6	11.74
17	4	0.6	11.74
18	4	0.6	11.74
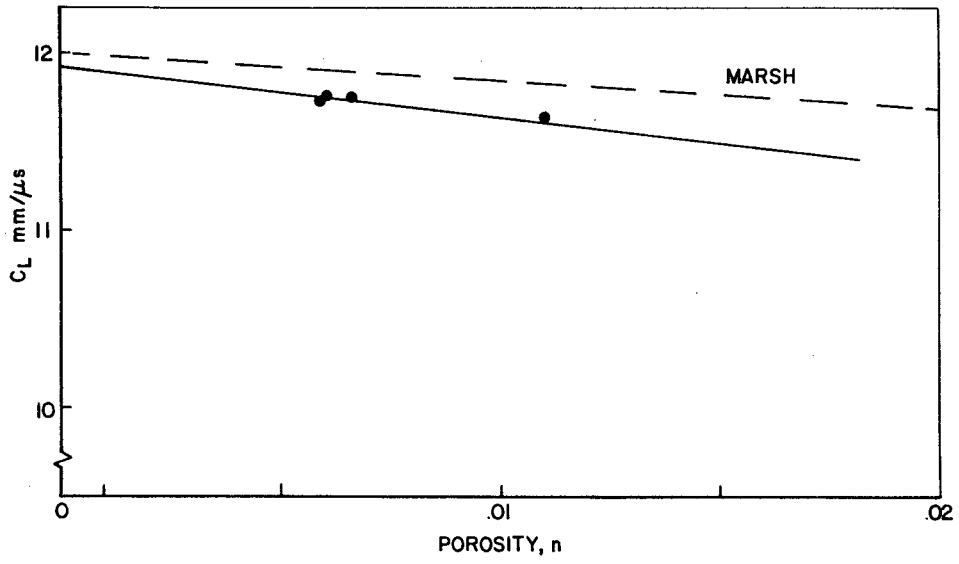
Figure 59.   Observed Variation of BeO Sound
Speed with Porosity.

extrapolation to data of Marsh, which were for much greater porosity.

b.   Shock Compression Experiments

Table 6 lists the experiments conducted with BeO targets. Flyer plates were annealed OFHC copper or annealed 1100 aluminum.

Preliminary tests with aluminum oxide ceramic targets (Reference 28) demonstrated that VISAR data could not be obtained from a ceramic free surface. The intensity and contrast appeared to drastically degrade when the plastic shock arrived at the rear target surface. It was not even possible to measure the magnitude of the peak particle velocity. Therefore, several targets were backed with PMMA windows for use with the VISAR. Thin film epoxy was used to bond the windows. The side adjacent to the target was depolished and vacuum-coated with aluminum. The rear surface was cut to a 7° angle to that the specular reflection which it generated did not enter the VISAR. Window corrections published by Barker (Reference 20) were used in the VISAR data reduction. Other targets were backed by a copper disc. VISAR measurements were made on the rear surface of the copper.

Figure 60 illustrates an x,t diagram and σ,u diagram for impacts with PMMA backing plates. The example shown is for shots 728 and 729, in which the flyer plate was aluminum. Point 1 denotes the impact. This point also denotes the material behind the shock waves emanating from the point referred to as state 1. The pressure in state 1 is below the HEL of the ceramic, so there is only a single elastic shock wave generated in the BeO. The HEL of the aluminum is so low that the elastic wave in that material is ignored; only the plastic wave is shown. Point 2 represents the arrival of the ceramic shock at the window; this is the arrival detected by the VISAR. The pressure at this point is reduced almost to zero, and the velocity is nearly twice the velocity in state 1. The shock in the aluminum reflects from the copper at point 3. It is at a higher stress

TABLE 6

BeO EXPERIMENTS

SN	Flyer Plate			u_o (m/s)	D (mm)	Target		
	Mat'l	d (mm)	Backup			No.	Backup	Thickness (mm)
728	Al	1	Cu	390	4	15	PMMA	15.7
729	Al	1	Cu	440	4	18	PMMA	15.7
730	Cu	1	Al	477	4	17	PMMA	15.7
732	Cu	1	Al	635	4	16	PMMA	15.7
734	Cu	3	PC	397	4	14	Cu	0.76
731	Cu	1	Al	512	8	7	PMMA	15.7
733	Cu	3	PC	649	8	6	Cu	0.76
735	Cu	3	PC	199	8	12	Cu	0.76
736	Cu	3	PC	200	8	13	Cu	0.76
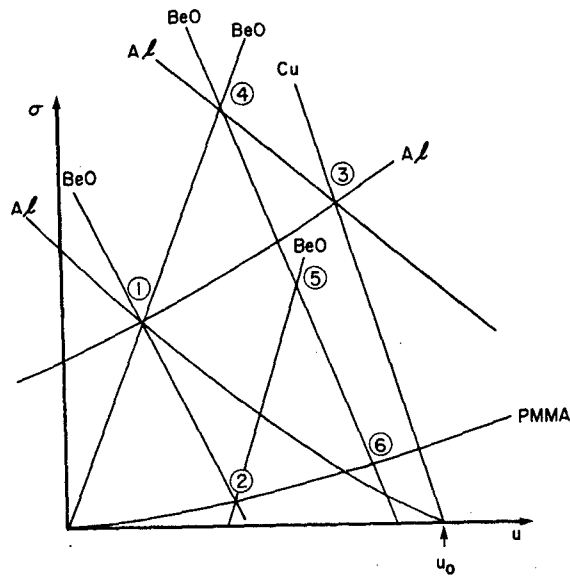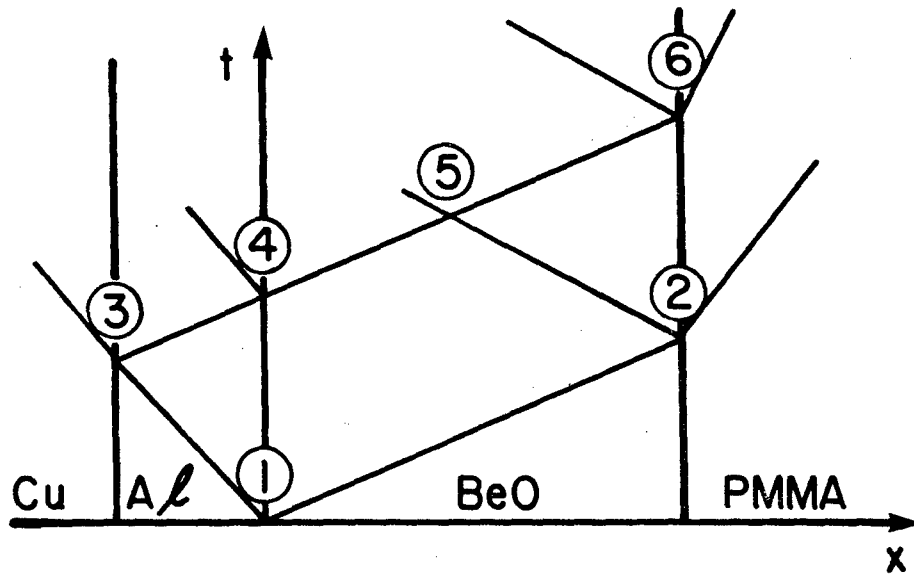
Figure 60. Solution Diagram for Shots with Aluminum
            Flyer Plate and PMMA Windows.

than state 1. The reflected shock enters the BeO at point 4. The stress is increased once again, as shown in the σ,u diagram. State 5 results from the intersection of the shock waves from points 2 and 4. Note that the state 5 stress is also greater than in state 1. Hence, this target does not spall. The time of the arrival at point 6 has no direct physical interpretation, since it depends on the speeds of the release wave from 4 to 5 and the shock wave from 2 to 5.

Figure 61 shows x,t and σ,u diagrams for shots 731 and 732 for copper flyer plates above the HEL of the BeO. The elastic wave in the BeO is shown as 1'. Again, the elastic wave in the flyer plate is so weak that it can be ignored. In this case, state 3 is at a lower stress than state 1. State 4 is a release from state 1. Finally, state 5 becomes tensile, and spall may be expected to occur at point 5. The VISAR observes points 2', 2, and the spall signal at point 6. The HEL (point 1') is calculated by assuming a symmetric BeO Hugoniot. The plastic stress, point 2, is calculated by using the observed arrival time of point 2 to calculate the shock velocity which corresponds to the slope of the segment from points 1' to 1 on the σ,u plot, and by assuming that the release path is elastic. The arrival time observed for state 2 indicated that the release path from state 1 to state 2 is elastic. This is consistent with Asay, Chhabildas, Dandekar (Reference 29) and Grady (Reference 30), who reported that even in elastic-isotropic materials, the initial release is elastic.

Figure 62 illustrates the solution diagrams for shots with a copper plate behind the target. These are relatively simple. Observation of the free surface arrival at points 3 and 5 can be used with the known Hugoniot of copper to calculate points 2 and 4 on the BeO Hugoniot. The slope of the measured Hugoniot gives the shock impedance of the BeO:

$$ Z = \frac{\sigma_2 - \sigma_4}{u_2 - u_4} \qquad (18) $$
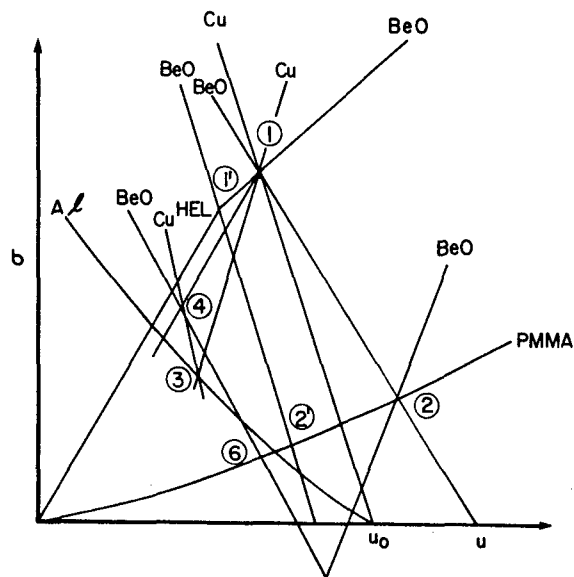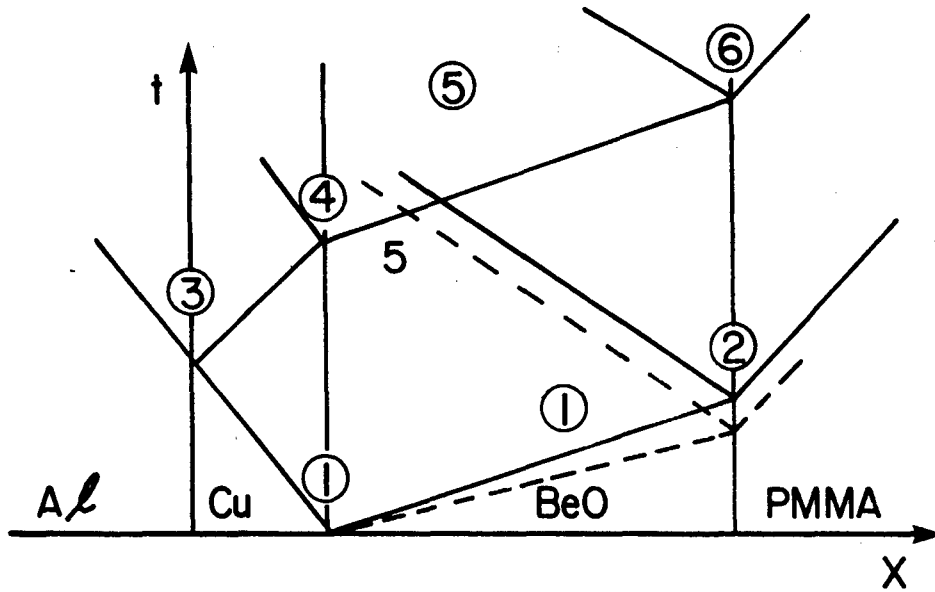
Figure 61.   Solution Diagram for Shots with Copper
Flyer Plate and PMMA Windows.

104
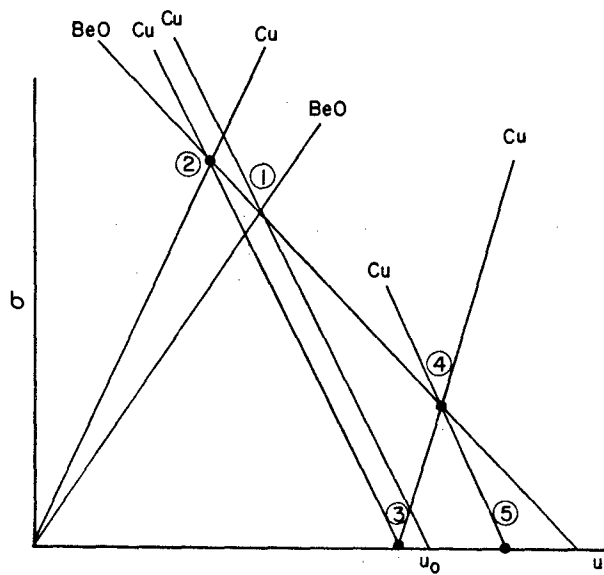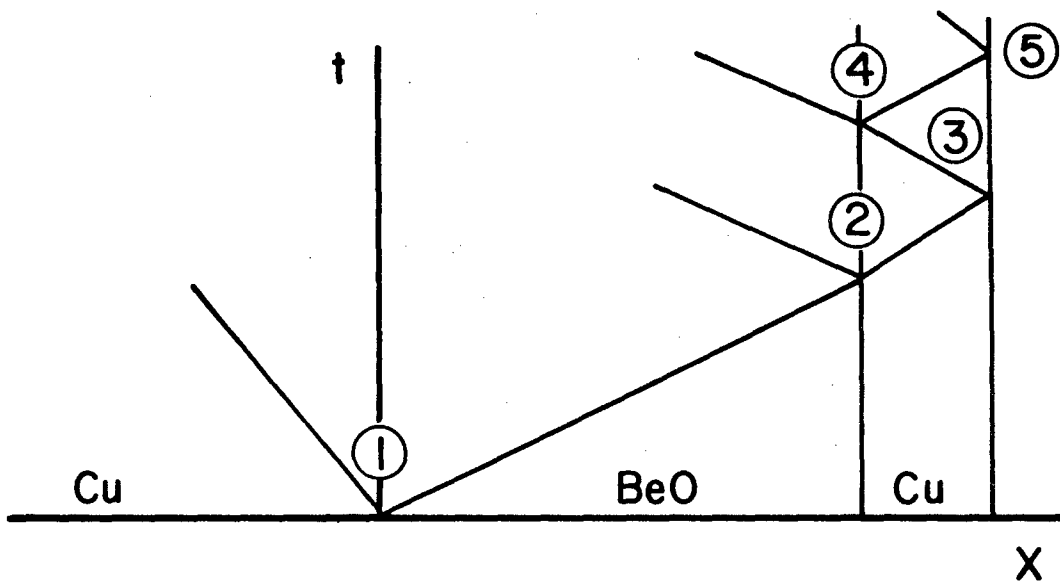
Figure 62.   The Solution Diagrams for Shots with Copper
             Flyer Plate on Target with Copper Back Plate.

Figure 63 illustrates sample VISAR data from a copper back plate. The two shock states are well defined.

Figure 64 presents the σ, ε Hugoniot calculated from the experiments. The impedance in the elastic region is 351 Kbar/mm/μs.

Yaziv (Reference 28 and 31) showed that the shock properties of fully dense BeO can be inferred from these data by using the Steinberg model (Reference 32) for the effect of porosity on the Hel. According to this model, when a porous material of initial specific volume V'_o is shocked to its HEL

$$V'_o - V'_{HEL} = V_{oo} - V_{HEL} = \frac{\sigma_{HEL} V_o^2}{c_L^2} \tag{19}$$

where V_{oo} refers to the fully dense solid. It follows that

$$V_{HEL} = V_{oo} - \frac{(u'_{HEL})^2}{\sigma'_{HEL}} \tag{20}$$

Steinberg based his model on aluminum oxide data from Gust and Royce (Reference 27). In order to assess its generality, we also applied the model to porous tungsten from data Linde (Reference 33), Dandekar (Reference 39), and McQueen (Reference 18). Using data from these three sources, $\Delta V = V_{oo} - V_{HEL}$ was computed as shown in the table below.

TABLE 7

EFFECT OF POROSITY ON HEL

	ρ_o	σ_{HEL} (Kbar)	c_L	ΔV (cm^3/g)
Linde	14.3	9.6	3.67	.00035
Dandekar	15.29	14.3	4.26	.00039
McQueen	19.2	37.5	5.22	.00037
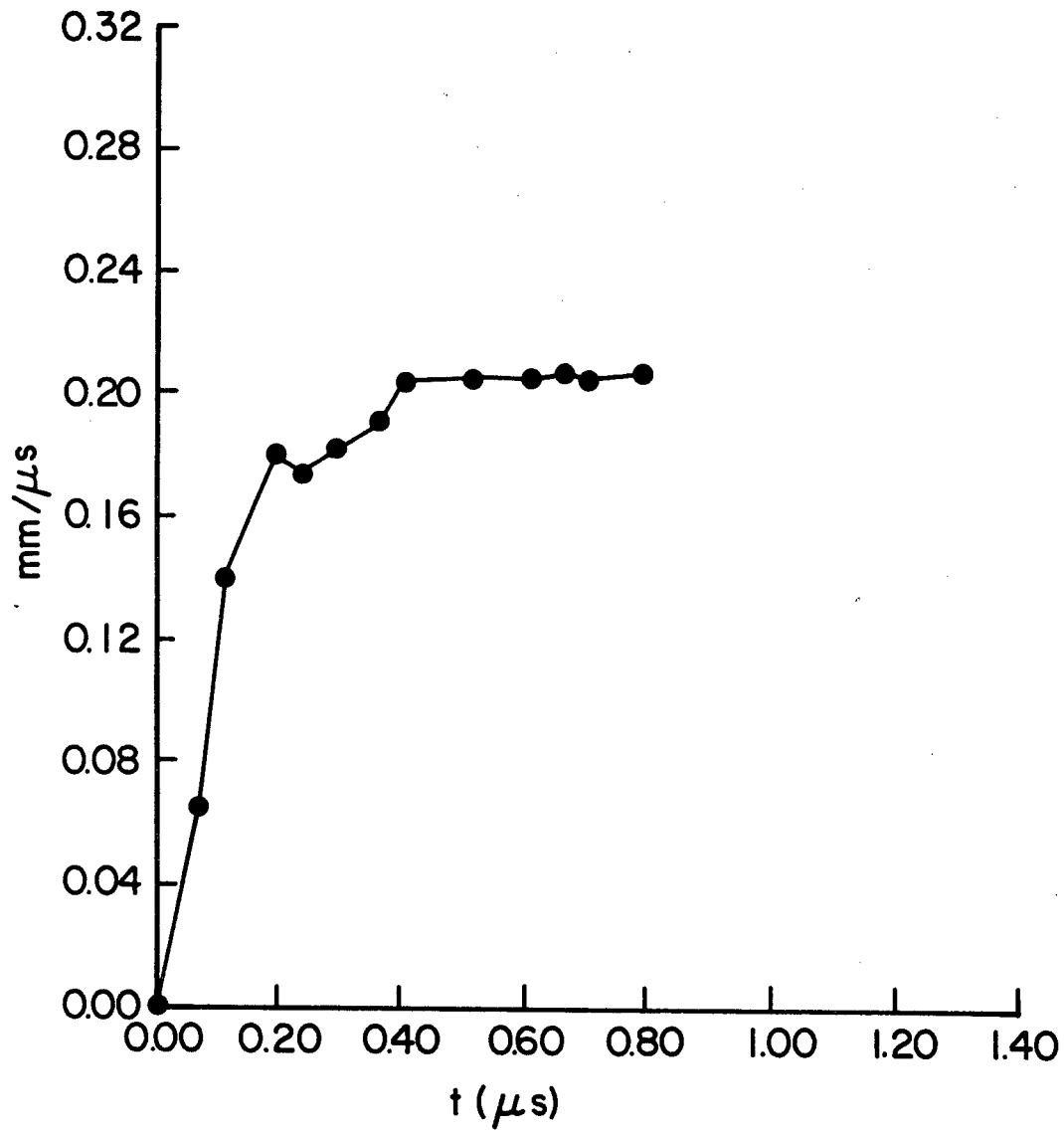
Figure 63.   Free Surface Velocity Measured in
              Shot 736.
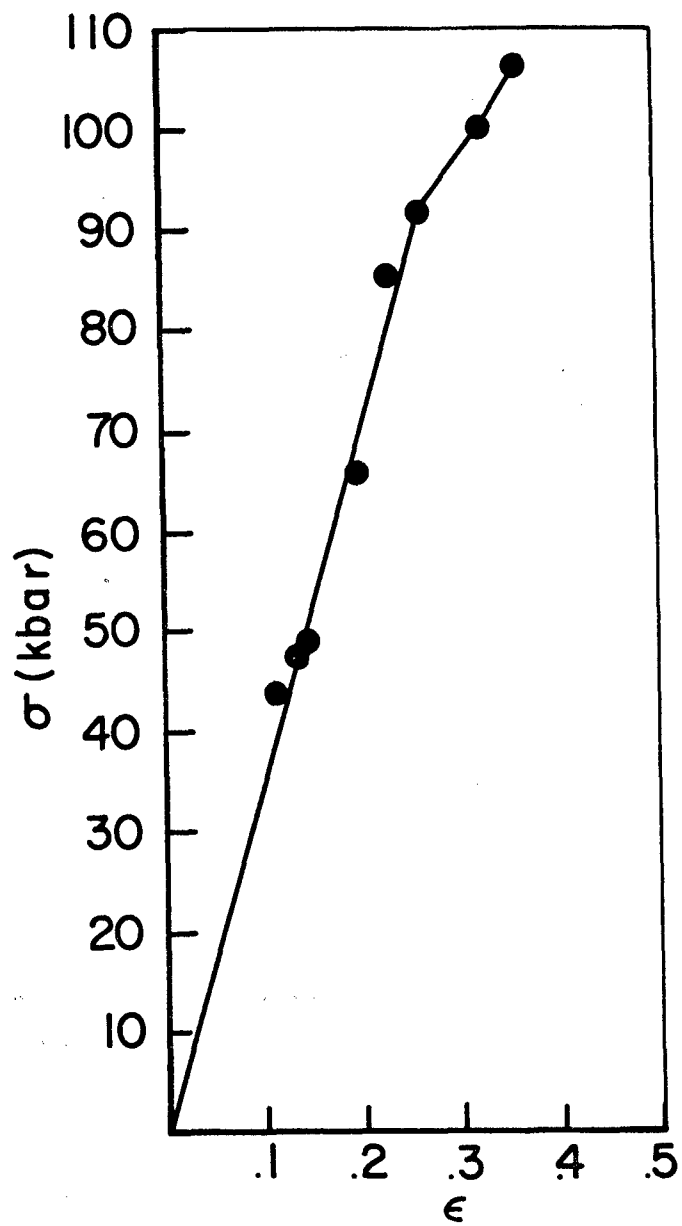
Figure 64.   Measured BeO Hugoniot.

The average value was .00035. The small deviation about the average demonstrates the accuracy of the Steinberg model. For BeO, $V_O - V_{HEL} = 0.0074$ cm^3/g.

Figure 65 compares the results of solid HELs computed by this technique with literature data. The solid HEL is calculated to be 96 Kbar.

The point labelled S is the value inferred by Steinberg from the data of Gust. Steinberg obtained this value by averaging data from Gust and Royce which was obtained for four different target thicknesses - 3, 6.4, 8.9, and 12.8mm. We believe that the variation of σ_{HEL} with target thickness is caused by precursor decay. If only the value from the 3mm thick target is used, the predicted solid σ_{HEL} is within the experimental uncertainty of our value.

c.   Spall Measurements in BeO

The relationship between the free surface velocity and the spall strength is affected by the presence of a window (Yaziv, Reference 28 and 31). Figure 66 illustrates the general forms of the window/target interface velocity. In the case of no spall, the trace will have form (a). In the case of spall, the form will be as in (b). The spall strength will be

$$\sigma_s = \frac{1}{2}(Z_{BeO} + Z_{PMMA}) \Delta u \qquad (21)$$

(where Z_{BeO} and Z_{PMMA} are, respectively, the shock impedances of the ceramic and the window) if shock waves generated at the spall surface do not overtake release waves originating from the flyer rear surface. When the shock compression remains elastic, this should be the case, and spall strength can be directly computed from the spall signal by the above equation.

Figure 67 shows an x,t diagram for spall in an elastically compressed solid. A release fan is generated in the metal flyer plate. However, in the ceramic, all of the release characteristics propagate at the same Lagrangian velocity. The release characteristic arrives at the observed interface at point R. The wave that reflects back into the
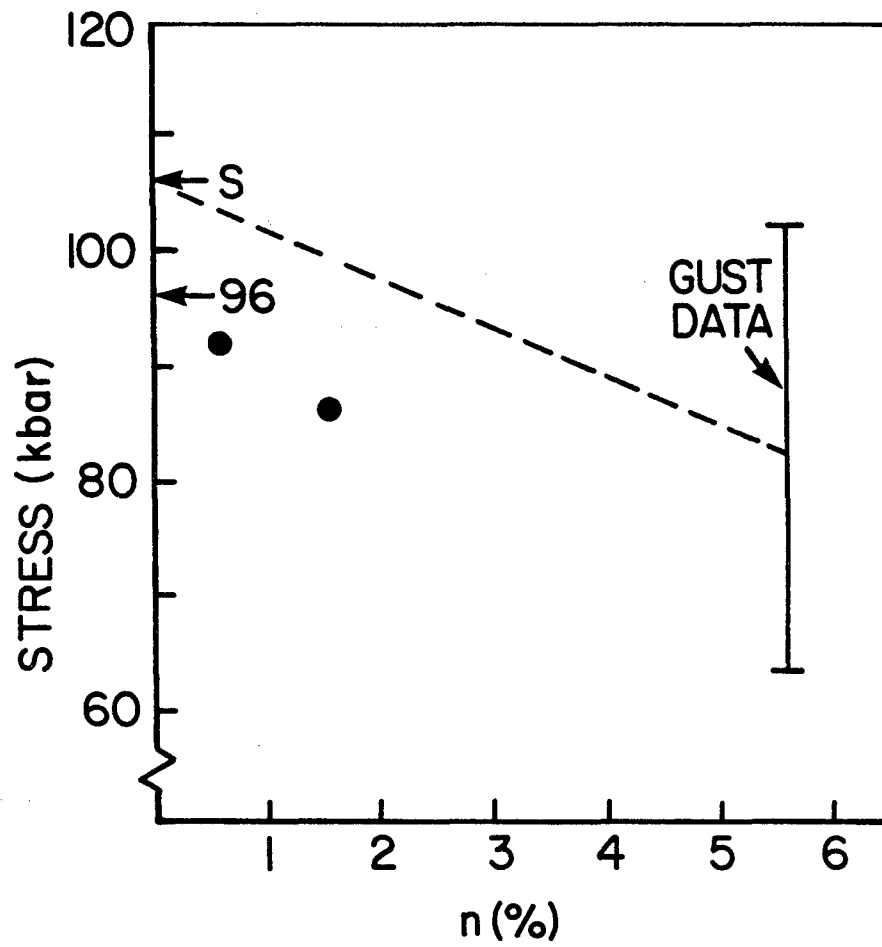
Figure 65.   Dependence of HEL of BeO on Porosity.
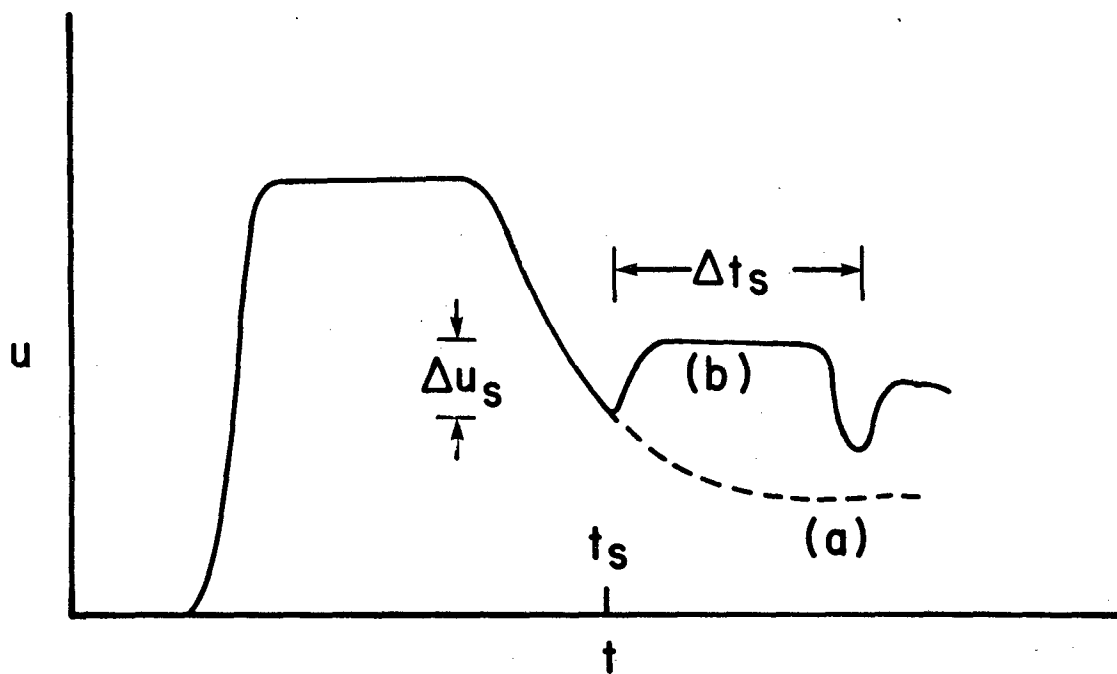
Figure 66. Generic Interface Velocity History.
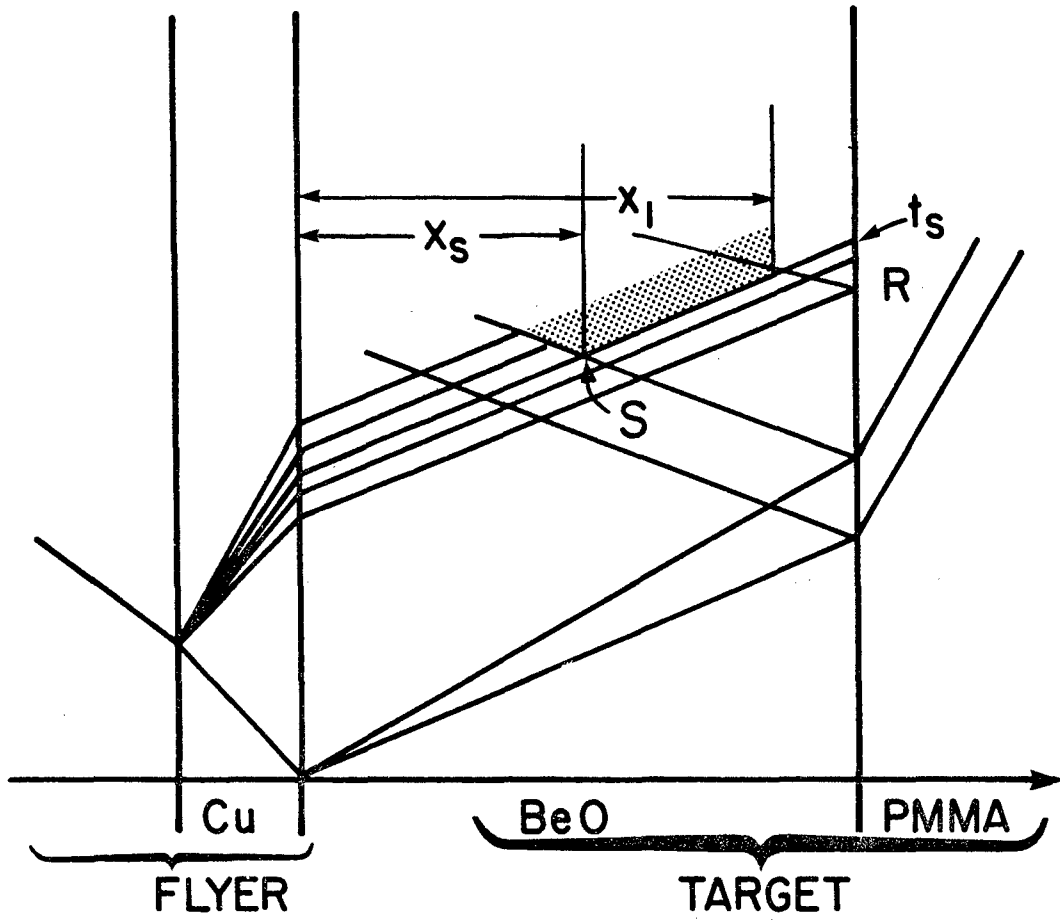
Figure 67. Lagrangian x,t Diagram for Spall in Ceramic Target.

target at point R is a shock. Spall first occurs at the point S.
A shock is generated that arrives at the window interface at time
t_s. The location of point S can be computed from t_s, since the
wave velocities are known to all be equal to C_L. The wave that
reflects from the window at time t_s is a release wave.

Spall was investigated in two experiments
that provided especially clear records: shots 731 and 732.
Figure 68 shows the interface velocity history from shot 731,
where there is a weak plastic wave also present. The spall
strength in 732 is 1.8 Kbar. The spall strength in shot 731,
which was compressed above the HEL, is negligible. These data
show that BeO loses its spall strength above the HEL.

Yaziv (Reference 28 and 31) showed that a
regional spall develops behind the spall signal that originates at
point S in Figure 67. The spall is quenched by the arrival of the
shock wave that originates at point R. The trapped stress waves
"ring", as shown in Figure 66. The distance x_1 can be computed
from the ringing period of the spall signal, Δt_s, while x_s can be
computed from t_s. In this way, the VISAR record can be used to
compute the distance $\Delta x = x_1 - x_s$ in Figure 67. In shot 731,
Δx = 2mm. In shot 732, Δx = 1.75mm. Both of these values are in
quantitative agreement with the spall region hypothesis.

Although the spall data are limited, they
point to a consistent picture of spall behavior. The spall
strength for elastically stressed material is about 1.8 Kbar.
This value diminishes above the HEL. Lack of spall strength
above the HEL has also been observed by Munson and Lawrence
(Reference 35) in alumina. In the elastic region, spall occurs
not in a plane, but over a region that can be predicted by simple
characteristics analysis.

2.4 NEW EXPERIMENTAL TECHNIQUES

In this section we present developments of improved
techniques for high strain rate characterization. However, these
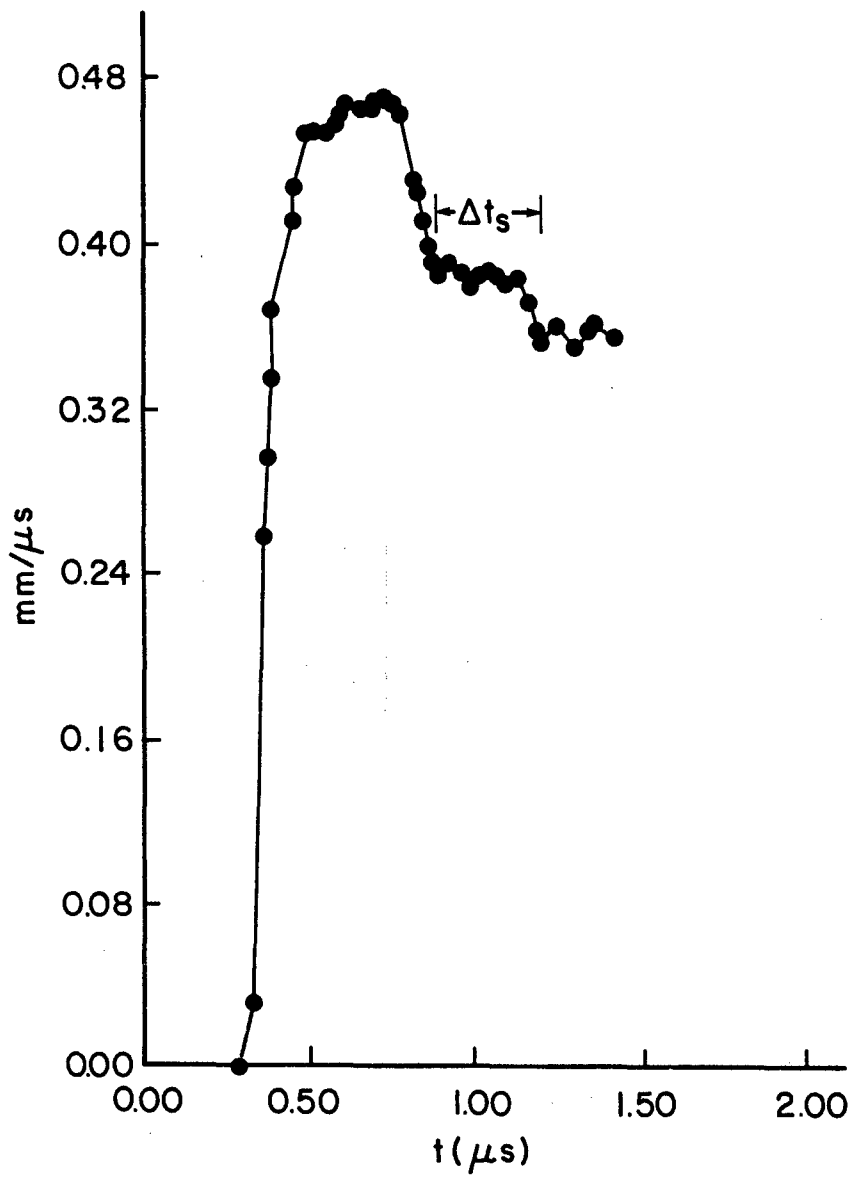
Figure 68.   Interface Velocity History from
              Shot 731.

techniques have not yet been used in the material modeling efforts.

2.4.1 Double Flyer Plate Technique

Preliminary experiments were conducted to show feasibility of a powerful new technique to study the properties of shock damaged materials. Progress on this task was also reported by Yaziv and Bless (Reference 36).

Two flyer plates are separated by a small gap (Figure 69). The first plate causes spall in the target, as in a conventional experiment. The second plate is of higher shock impedance. Impact of the second plate closes the fracture. The advantage of this technique is that it allows determination of the properties of the damaged material in the spall region.

Preliminary experiments have been conducted to demonstrate feasibility. A 2-inch (50mm) diameter compressed gas gun was used to launch 50mm diameter flyer plates. Target rear surface motion was measured with the VISAR. The wave interactions in the target and flyer plates were anlaysed with the SWAP method of characteristics code. The target was fully annealed OFHC copper. The first flyer plate was 2024-T3 aluminum, and the second was copper or 1020 steel.

Five shots were completed that demonstrated fracture/recompaction in copper. The velocity range was 250 to 400 m/s. Targets were 0.16, 4mm thick and flyer plates were 2mm thick. Shots 719 and 720 were typical; the velocities were 365 and 388 m/s, respectively. Figure 70 shows the x,t diagram generated by the SWAP code for shot 719. In this shot and in shot 720, only half of the aluminum first flyer was backed by a copper second flyer; the other half was air backed. Figure 71 shows the appearance of the targets after impact. The two halves of the target display different damage, as predicted by the SWAP simulation. The single flyer plate impact produced partial spall (a region containing porosity), while no damage is readily visible opposite the two-flyer plate impact.
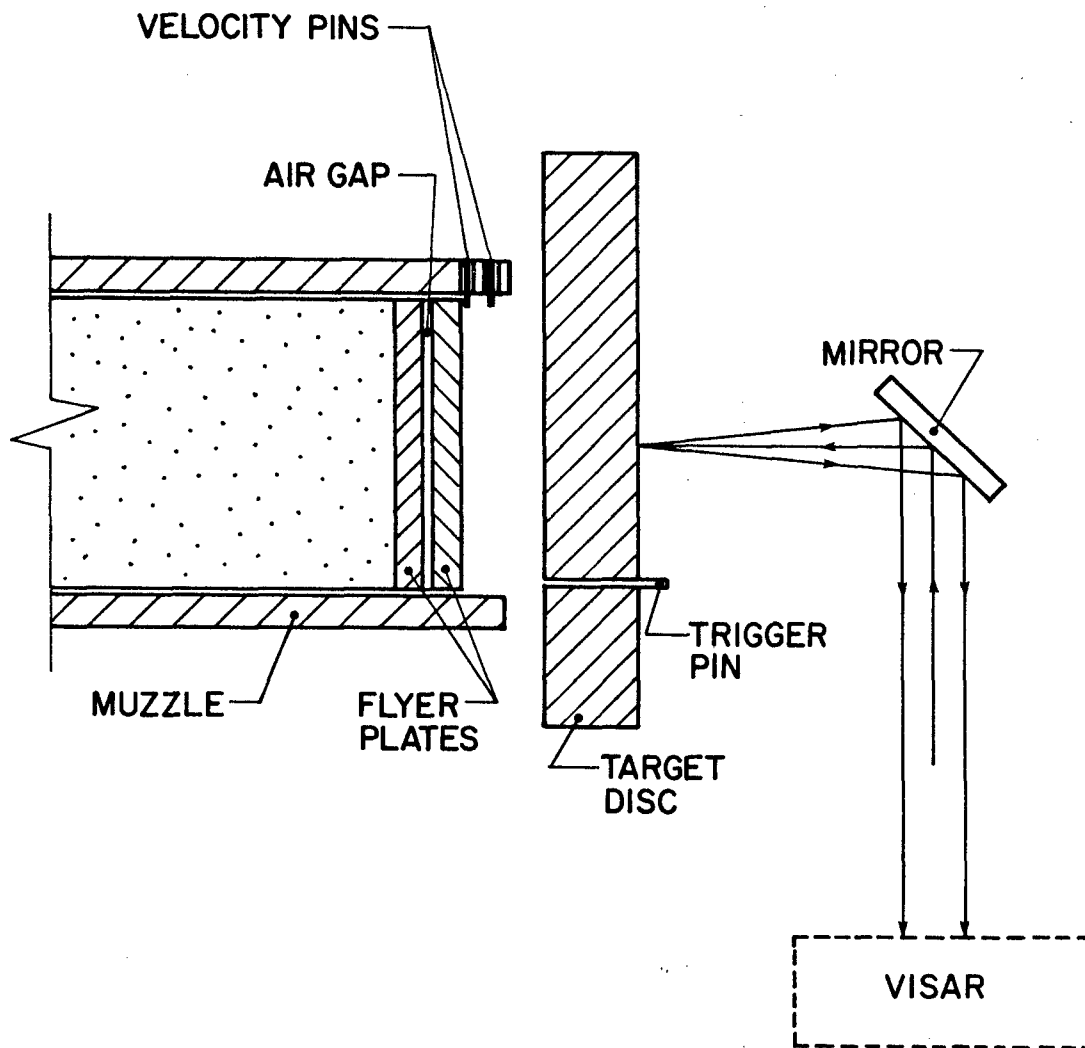
Figure 69.   Experiment Configuration for Double
              Flyer Impact Experiment.
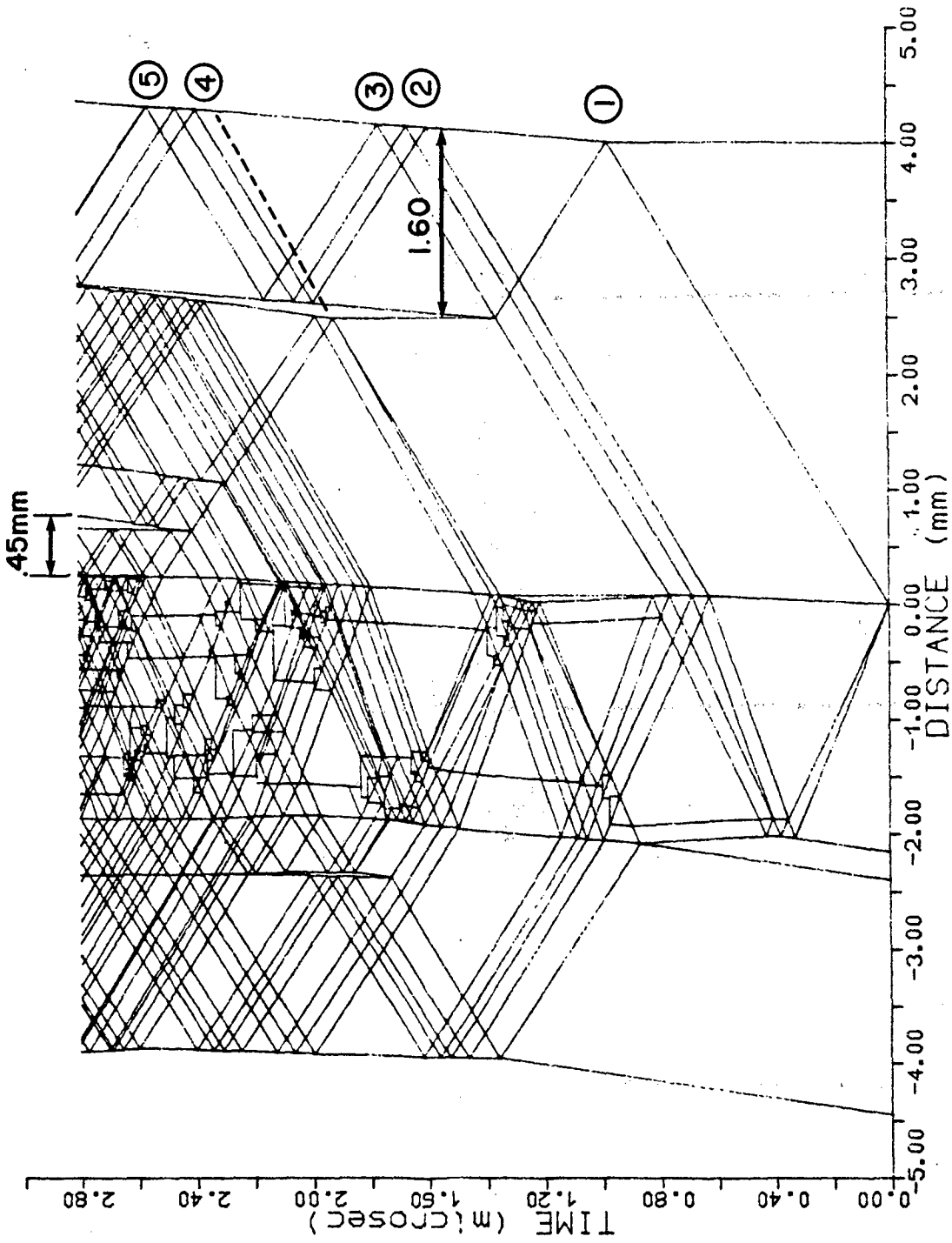
Figure 70. (x,t) Diagram Generated by the SWAP Code for Shot 719.

117

FLYERS · TARGET #720 · TARGET #719

Cu(2mm) · AIR · Aℓ(2mm) · Cu(4mm) · Cu(4mm)

1.5 mm · .6 · .65
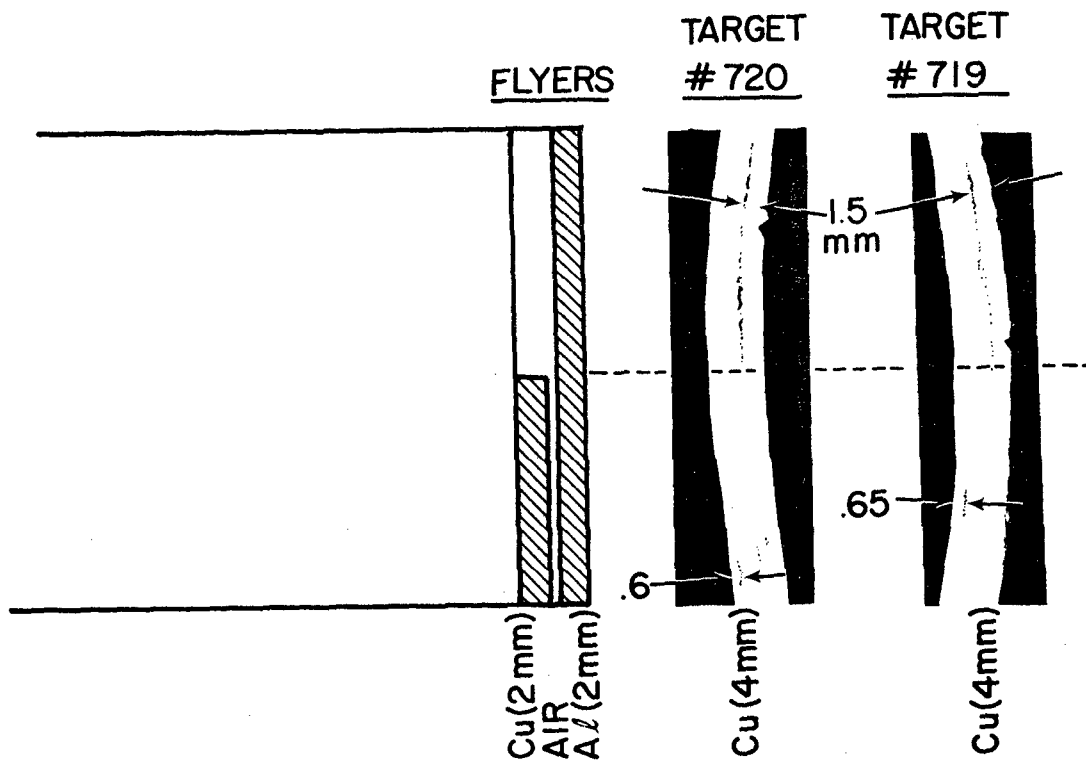
Figure 71.   Shot 719 and 720 After Impact.

The free surface velocity record from shot 719 is shown in Figure 72. In addition to the conventional "spall signal" (point 3) there is an arrival from the second flyer impact (point 4) that has "leaked" through the damaged region, and a shock arrival (point 6) caused by final closure of the spall plane.

2.4.2   Cranz-Schardin Camera

A Cranz-Schardin camera was developed in order to obtain high resolution sequential photographs of projectiles. The intended application was photography of Taylor-impact specimens.

The basic configuration of the Cranz-Schardin camera is illustrated in Figure 73. An array of short-duration light sources, generally closely spaced, produces light which fills a main lens. The main lens is designed to focus the source array onto a lens array. A small diameter camera lens is positioned at each of the source images so that as each source is pulsed, a single camera lens receives the light that it produces. The light produced by all the sources overlaps in the region close to the main lens. The subject is located close to the main lens, and the small camera (objective) lenses are designed to form images of the object on a photographic film. As each light source pulses, a distinct image of the object is recorded. By firing the light sources in sequence, the time evolution of an object may be studied via back-lit photography.

Conventional Cranz-Schardin cameras employ an array of spark gaps as sources. Instead of using spark sources, the University's camera incorporates commercially-available Light-Emitting Diodes (RED-1000). These sources are very small, require relatively little power, are semiconductor-compatible, and should require no maintenance for thousands of photographs.

a.   Light-Emitting Diodes (LED)

A variety of commercially-available LED's have been investigated as possible sources for the Cranz-Schardin
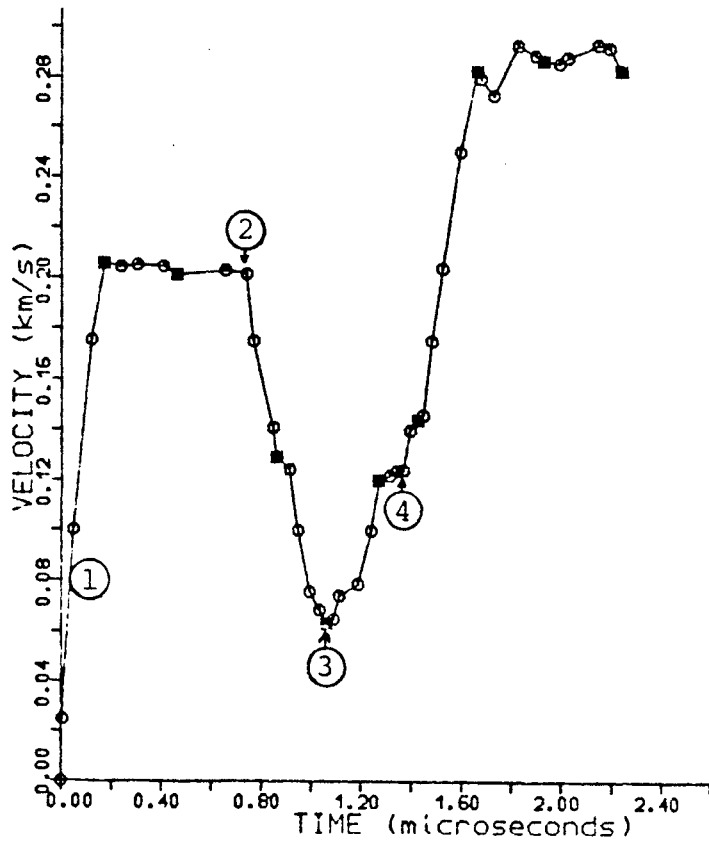
Figure 72. Free Surface Velocity for Shot 719.
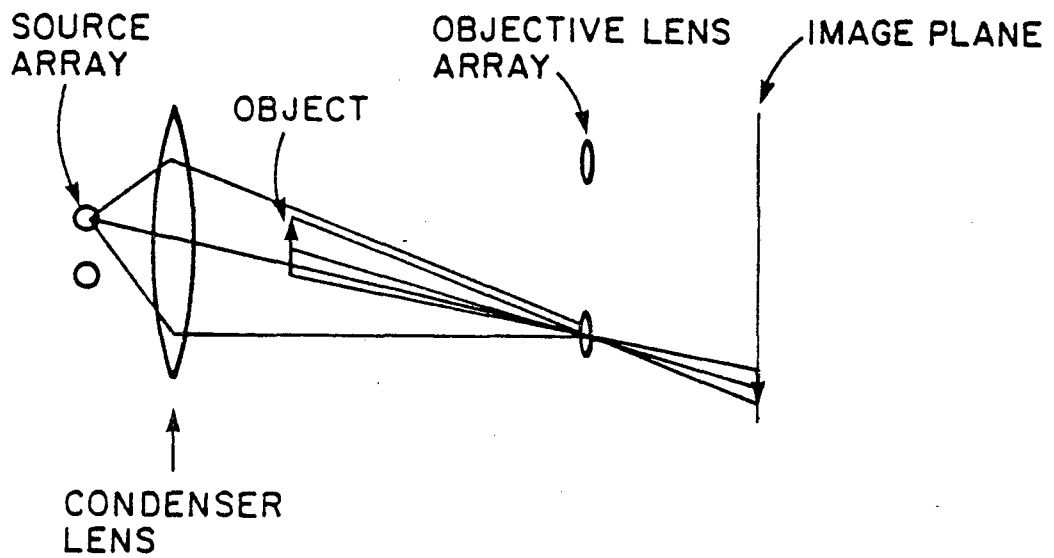
Figure 73. Cranz-Schardin Camera Operation. Two of array of
twenty sources and objective lenses are shown.

camera. It was found that the manufacturers' specifications for LED time-response were unreliable. Several manufacturers' data sheets list a variety of response times for LED's, and we found that invariably these were very conservative, i.e., the quoted time response was very much slower than that which was actually observed when the LED's were operated with a current-driving circuit which was capable of producing very short pulses. This is what one would expect of a solid state source which produces light by electron-hole recombination. Outside of a small resistance (a few ohms) and a small capacitance (a few hundred pF at most) there is no basic physical process which should practically limit the turn-on and turn-off times of solid state emitters. We chose to test only those commercially available LED's which had the highest brightness in the forward direction. Among those tested, no correlation was found between the specified time response and that of the measured response when an LED was used with the proper circuitry.

Some light emitting diodes exhibit a saturation in the light output intensity as a function of current, as can be seen in manufacturers' specification sheets. LED's exhibiting this behavior were avoided.

In pulsed operation, the magnitude of the current pulse is at least a factor of 100 higher than the DC current values at which the performance of an LED is usually specified. Therefore, pulsed performance tests of candidate LED's were necessary in order to identify those which emitted the highest energy light flash. It was found that the specified DC light output values were often very misleading; in the pulsed mode, "high intensity" LED's may perform much poorer than "lower intensity" ones.

Infrared laser diodes were also considered as sources. In general, the total amount of light which can be produced by an Infrared Laser diode is an order of magnitude greater than available from LED's. However, extended red sensitivity films have such superb speed and resolution (compared

122

to infrared films) that the practical advantages of laser diodes are greatly diminished. In the extreme case of a very rapidly moving subject, however, a nanosecond duration infrared laser diode would be the only usable source.

Two types of emitter-film combinations were tried in the camera: (1) a long-wavelength LED whose peak emission wavelength is about 660 nm and Kodak 2485 film, and (2) a shorter wavelength LED whose emission wavelength is about 630 nm and Polaroid film. The total light energy output from the latter LED was very much smaller than from the former but the much higher sensitivity of Polaroid film made up for the decrease in light emission. The use of Polaroid film is very convenient but a penalty is paid in terms of resolving power, since Polaroid film can resolve only about 25-30 lp/mm whereas the Kodak film can resolve about 50.

b. Camera Description

The final Cranz-Schardin camera design used an array of RED-1000 LED's arranged in a 4 x 5 pattern on 0.283 inch centers. The LED's are individually driven by a set of GA301 (4) silicon controlled rectifiers fired in sequence. The sequencer consists of a set of three type 74164 IC shift registers driven by an external pulse generator. Initially, a logical "one" is fed into the first bit of the first 74164 IC. All the other bits of the other chips are logical "zeroes". As pulses are fed into the first shift register, the "one" shifts over from bit to bit and as each transition is made, a trigger pulse is generated which is fed into one of the GA301 SCR's. The shift registers have been tested up to a shifting rate of 23 MHz. Usually, however, the use of such a high framing rate is unnecessary. In the experiments described below, no rate higher than 500 kHz has been used.

The discharge of each SCR dumps a 0.01-mFd capacitor charged to between 40 and 60 volts. The maximum holdoff of the GA301 SCR is 80 volts but it has been found that little increase in the total light output from an LED occurs

123

above a 60 volt capacitor charging voltage. The light output
pulse from each LED has a FWHM of 60 ns indicating an effective
resistance for the LED of approximately 3 ohms at a peak current
of nearly 10 amp. A smaller image size, say 1.25-cm diameter,
would have allowed the capacitor to be reduced in size by about a
factor of four and yielded a light pulse with a considerably
shorter pulse duration. However, in the Taylor impact test, the
subject velocity was generally less than 500 m/s. Maximum
subject spatial resolution was of primary importance, so temporal
resolution was sacrificed. For subject velocity of 500 m/s, the
motion blur due to the exposure time was insignificant.

The main lens of the camera is a simple
biconvex glass lens of 100mm diameter and 167mm focal length.
The separation between the main lens and the plane of the LED's
is 31.8 cm. The LED's are therefore imaged at a magnification of
about 3 onto a set of small camera lenses spaced on 20mm centers.
The camera lenses are 19mm diameter achromats of 190mm focal
length. The separation between the main lens and the plane of
the camera lenses is approximately 102 cm. The camera lenses
were adjusted to have a field of view approximately 7.0 cm in
diameter located about 19 cm from the main lens. The shadow
image of any test object is therefore recorded at a magnification
of about 0.36. The camera is relatively insensitive to alignment
and precision optical adjustments are not necessary. A calibra-
tion target was always located in the field of view so that each
individual image could be calibrated for absolute magnification
and parallax.

Kodak 2485 4 inch by 5 inch sheet film was
used as the recording medium and it was developed under the
standard conditions specified by the manufacturer; D-19
developer, 95°F for 2.5 minutes. The first was a prototype for
proof of principle testing. It was used for the Taylor impact
study described in the following section. It is pictured in
Figure 74a. The second camera was a self-contained unit that was
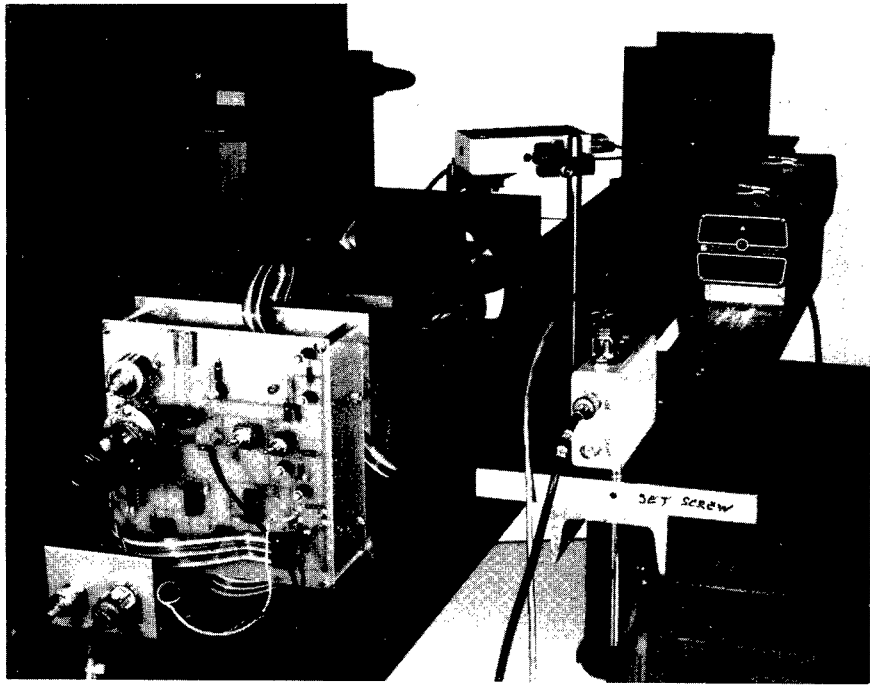
(a)   Phototype Cranz-Schardin Camera.
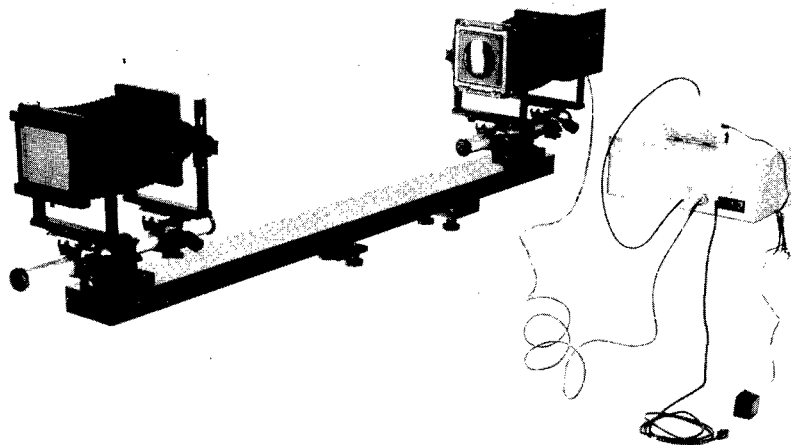
(b)   Cranz-Schardin Camera Delivered to AFWL/DLJW.

Figure 74.   Cranz-Schardin Cameras.

delivered to AFATL/DLJW. It was housed in a modified 4 x 5 camera body. Figure 74b shows this unit.

In the delivered camera, the spacing between the LED's was 0.250 inches to allow for a longer distance between the main lens and the subject volume. The main lenses diameter and focal length were unchanged. The camera lenses were changed to 16mm diameter achromats of 124mm focal length to allow the working distance of the camera to be increased.

c.   Photographic Results

The camera has been employed in two types of impact studies, both of which have involved small steel rod impactors. The first of these, described as a Taylor Impact Test, involves launching a small metal rod onto the surface of a hardened steel impact plate and studying the deformation of the rod as time proceeds. In our experiments, the rod was of annealed Armco iron (nearly impurity free iron) launched at velocities between 135 and 360 m/s from a 0.3-inch smooth bore barrel either by means of compressed helium gas or by gunpowder (above 180 m/s). The rods were 0.3 inch in diameter and one inch long. Independent of the projectile velocity, the framing rate employed was 500 kHz.

A triggering system located close to the projectile impact point was required in order to run the camera relatively fast. The triggering pulse to initiate the firing of the sequence of LED's was generated by the interruption of a beam from a Fairchild Type FPE104 IR LED. This LED produces a very high brightness, low-divergence beam which was detected by a Motorola type MDR500 photodiode. The FPE104 and the MDR500 were positioned so that the IR light beam was interrupted by the passage of the projectile approximately 5mm in front of the impact plate. Figure 75 illustrates a sequence of several images obtained at a projectile velocity of 344 m/s. (All of the frames recorded by the camera are not illustrated.)

A saw blade with 20 teeth per inch was positioned in the same vertical plane as the projectile. It
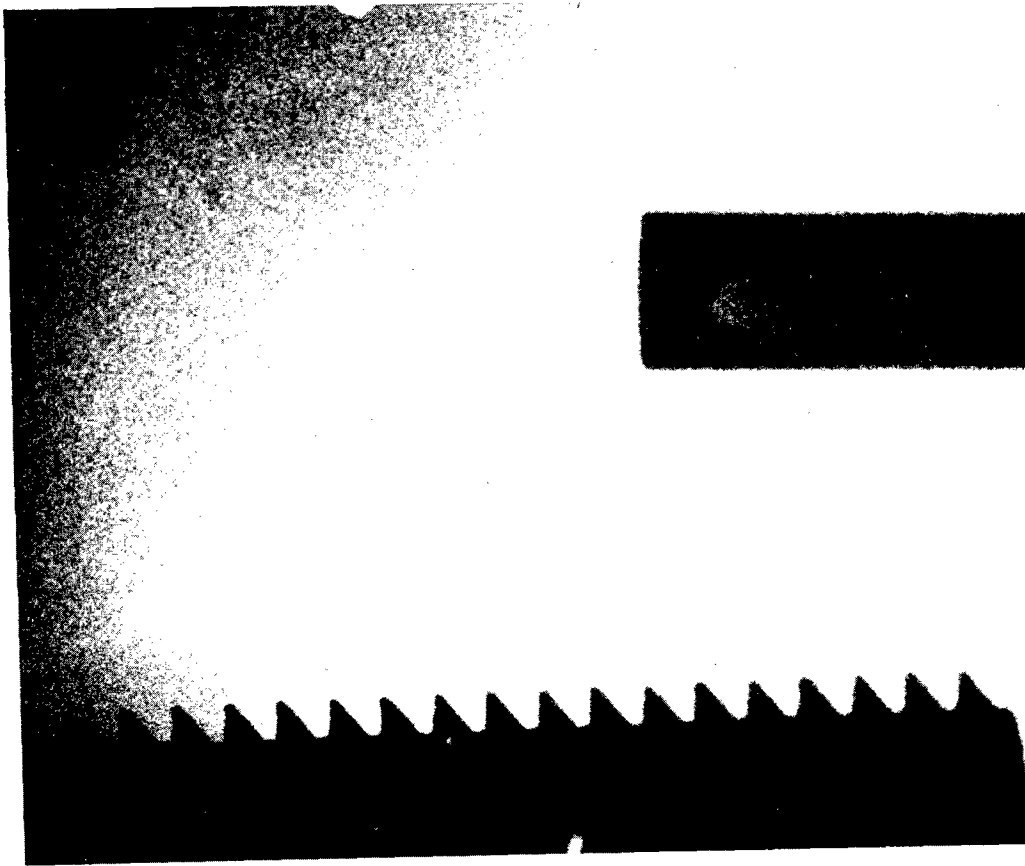
(a)

(b)

Figure 75.   Preimpact Photos from Shot 94, 344 m/s.

appears at the bottom of every image. The distance between the various teeth of the blade were measured with a microscope and compared to those measured from a final print of an enlargement of the 4 x 5 Cranz-Schardin negative. The lateral magnifications of the camera depends upon the cosines of the angles that the LED optic axes make with the optic axis of the main lens. The maximum value of the angle is only 0.0491 radians and the correction factor would be only 0.999. Measurements made on printed images verified that the frame-to-frame differences in magnification were too small to resolve. For most data analyses, the 2.5 cm diameter images were magnified by a factor of about 8 during the printing process. By measuring all the points of the saw blade and comparing the digitized values with the known values, an average value for the Cranz-Schardin magnification could be determined. A typical magnification was 0.3770. The standard deviation of the magnifications determined for the various saw tooth intervals was 0.0001.

The 2485 film employed to record these images is reported to be capable of resolving 50 lp/mm. Since the object image ratio of the camera was 3:1, the resolution in the object plane was about 16.7 lp/mm or 0.006 cm (0.0024 inch). At a projectile velocity of 450 m/s and an exposure time of 60 ns, the projectiles were capable of moving only 0.0027 cm during the recording. This amount of motion blur is completely negligible because it cannot be resolved on the film.

The second type of experiment conducted using this camera was for the purpose of studying crack formation and propagation in glass. Steel rods were fired into a reservoir containing fine aluminum oxide powder. The reservoir external dimensions were 2.5 x 2.5 x 1.25 cm. It was constructed of 1.6mm thick PMMA. The open top of the reservoir was capped by a piece of plate glass of the same size as the reservoir and the two were clamped together to ensure a firm contact between the powder and the glass. This assembly was positioned inside the Cranz-Schardin camera so that the view was of the 1 x 1 inch face of the glass. Steel rods 0.3 inch x 1.0 inch were fired into the

powder reservoir just below the interface between the glass and the powder. When a rod impacted the powder, the powder was driven ahead of the rod and the high pressures generated by this process eventually cracked the glass. The objective of the experiment was to determine exactly where and when the glass cracked (relative to the position off the rod tip). After each experiment, the glass was always fragmented into many small pieces. However, the photographs illustrate that not many cracks are actually formed during the impact itself.

Figure 76 illustrates four frames recorded during an experiment. The projectile velocity was 431 m/s and the camera framing rate was 225 kHz. Small cracks were always observed to form in the portion of the glass nearest the impact point. These small cracks are on the extreme right of the image of Figure 76. As the projectile velocity was increased, first one and then two cracks such as are illustrated in the figure were formed. The first crack always propagated upwards through the glass and terminated at the base of a screw which was used to hold the glass and reservoir together. The propagation velocity of the crack through the glass was approximately 1690 m/s as measured during these experiments. Figure 76 also illustrates the images of the leading edge of an air shock which was generated by the impact. This curved edge is on the far left in each of the images and can be seen to propagate further to the left as time proceeds. We have computed the velocity of propagation of a shock in air.

2.4.3   Taylor Impact Tests

Taylor impact tests provide a technique to measure compressive flow stress at high strain rates (References 37, 38). The objective of the University's test program was to show that the Cranz-Schardin camera could be used for obtaining profile data during the impact process. A secondary objective was to obtain deformation contours for analysis by personnel at AFATL/DLJW.
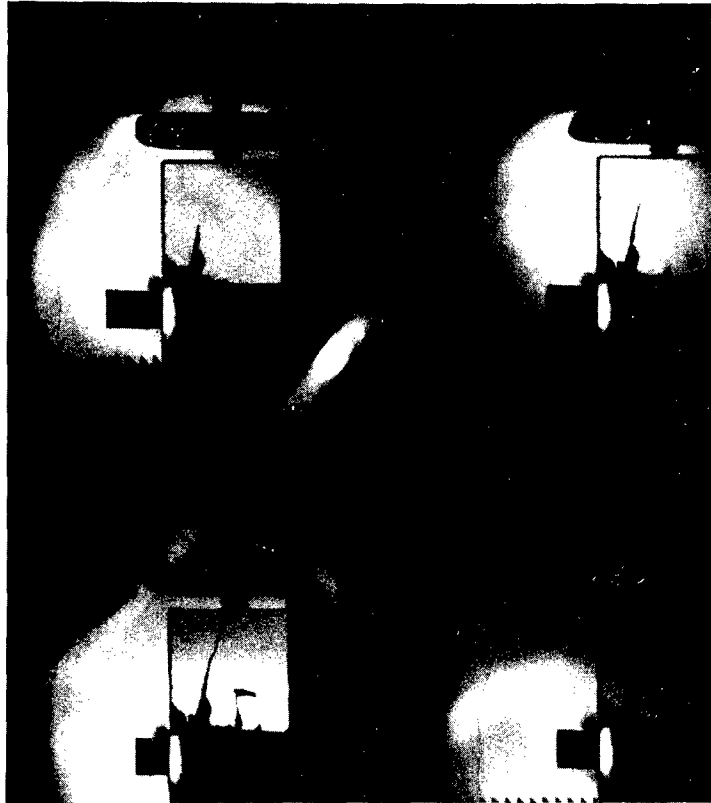
Figure 76.   Four Frames from Test Shot into
             Ceramic/Glass Target.

The tests were conducted on 7.62mm diameter 2.54mm steel projectiles launched from a 1.5mm long 7.62mm diameter smooth bore barrel. The propellant was either compressed helium gas or gunpowder. The gas was used for velocities below 180 m/s, the gunpowder at velocities above this. The projectile velocity was determined by measuring the time interval between the interruption of two He-Ne beams which illuminated MRD500 PIN photodiodes.

The projectiles were formed from three types of steel: (1) common mild steel (type unspecified), (2) Armco iron which was annealed in air, and (3) vacuum-annealed Armco iron.

The Armco iron specimens were annealed at 1700°F for one hour, and cooled at a rate of 250°F per hour. The first two projectile types were used to generate a loading curve for the gun and to conduct tests for the Cranz-Schardin camera.

The steel or Armco iron rods impacted normally upon a massive impact block which was machined from BD30 steel and hardened to Rockwell C53-57. Figure 77 shows a photograph of one of these blocks. At first, the blocks were made flat across the whole front surface. It was found that the images produced by the Cranz-Schardin camera were affected by the extreme edges of the block. Experience showed that aiming accuracy was extremely good, so that in later tests the block was bevelled away from the impact site.

The impact yaw could be detected in the Cranz-Schardin camera images and from the condition of the projectile recovered after the experiment was over. On occasion, particularly at low velocities, the projectile elastically rebounded from the impact plate, out of the camera, and onto the laboratory floor. More frequently, it was found to lie inside the Cranz-Schardin camera housing.

The deformation of the rod during impact was detected via the Cranz-Schardin camera images. Data analysis began with an examination to determine which of the 20 frames should be enlarged for further quantitative study. The selected

131
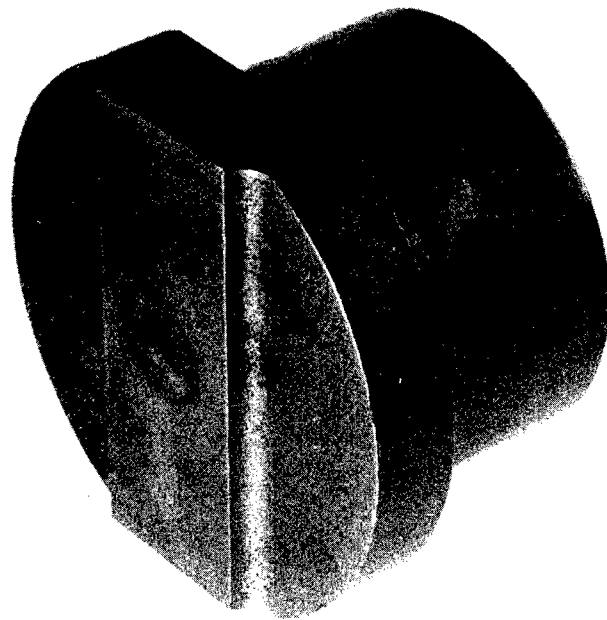
Figure 77.   Photograph of Taylor Impact Target.

images from each experiment were enlarged to 4 x 5 inch prints and anlayzed using a Talos digitizer. A computer program was developed specifically for this task. The methodology of the image analysis included several steps: (1) A small saw blade was located in the field of view of the camera and was recorded on each image. The positions of the teeth tips were digitized and compared to the known distances between the teeth as measured with a traveling microscope. This comparison allowed the calcution of the average and variance of the magnification of each image. (2) Two points defining the direction of the surface of the impact plate and two points defining the rear end of the rod were digitized. This allowed the calculation of the length of the rod in the particular image and defined the origin of the coordinate system of the image. The origin was defined as the intersection of the rod axis and the shadow of the impact plate. (3) A grid was laid down on the image and pairs of points diametrically opposite one another were digitized. The computation of the distance between these points allowed the calculation of the instantaneous rod diameter as a function of length along the rod.

A total of 38 projectile firings were performed. Fifteen were for the purpose of generating a loading curve for the gun for both helium and gunpowder propellants. An additional 11 shots were made while the operating procedures for the Cranz-Schardin camera were being developed. The final shots were with projectiles made of vacuum-annealed Armco iron furnished by AFATL.

The framing rate necessary for the Cranz-Schardin camera was estimated. A typical projectile velocity was taken as 240 m/s. The projectile was assumed to collapse to 75 percent of its original length during the impact and to decelerate uniformly. Thus it stops in 0.6 cm with a mean velocity during the slow down of 126 m/s. The time over which the projectile stops is 50.6 µs. Therefore, the camera can record all of the impact in 20 frames if the interframe time is 2.5 µs. This

corresponds to a framing rate of 400 kHz. The rate used in all data tests was 500 kHz to account for nonuniform deceleration.

Difficulty was initially encountered in synchronizing the Cranz-Schardin camera properly with the impact. The last photodiode trigger signal from the velocity station was used to trigger the camera. A signal delay generator was inserted in the line between the last photodiode and the trigger input to the camera. From the anticipated projectile velocity and the known distance between the last timing station and the impact plate, it was possible to calculate the time delay and to trigger the camera at an appropriate time. However, this turned out to be an unreliable technique. It was possible to set the time interval of the delay generator accurately enough to run the camera at a suitable framing rate. The chief problem was the inherent variations in the velocity of the gun.

Precise trigger delays are usually achieved by installing an up-down counter on the range. While this approach would have been acceptable for the experiments conducted at the university, where such a counter was available, this solution was not acceptable for AFATL, who may not have this specialized device available. Therefore, it was decided that another type of triggering system should be developed.

Larger and larger variations in the projectile velocity can be tolerated by the camera system as the triggering point is moved closer to the impact plate. Accordingly, a third He-Ne laser-Pin diode station was installed on the range. The beam of this He-Ne laser was aligned so that it crossed the trajectory of the projectile about 2.5 cm in front of the impact plate. In this configuration, very large projectile velocity variations were tolerable because the total time from when the laser beam was interrupted to when the projectile struck the impact plate was so short. However, this technique proved to be unacceptable because the scattering of the laser light from the dust in the air caused an intense streak to be recorded on the film, partially overwriting some of the Cranz-Schardin images.

134

Nevertheless, several test films were made showing that trig-
gering the camera so close to the impact point worked very well,
except for the streak on the film. The solution that provides an
adequate trigger was use of an infrared diode and detector, as
described in the previous section.

The most complete set of experiments were those
conducted with annealed Armco iron. The test matrix is given in
Table 8. There exists a critical velocity above which radial
cracks form along the perimeter of the impact face of the rod.
Taylor impact tests are normally conducted below this critical
velocity. The critical velocity was determined experimentally
from shots 0094 to 0102. In shot 94, the velocity was 344 m/s,
and severe radial cracking occurred. The launch velocity was
lowered step-by-step (shots 0095 to 0099). At 225 m/s, cracks
formed, but at 198 m/s (shots 0099 to 0100) no radial cracks were
formed. In order to determine the threshold velocity to greater
accuracy, the launch velocity was slowly raised until a region
where crack formation was problematical was found. This region
was demonstrated to lie around 216 m/s, since in shot 0101 there
was no crack formation at a velocity of 217 m/s but in shot 102 a
crack formed at 215 m/s. It was observed that a small chip of
iron was always released when a crack formed. If the front edge
of the sample was not chipped, there never was a crack formed.
End-on and side-on views of the impacted rods for the shots 0094
to 0105 are illustrated in Figure 78. Figure 79 show a dynamic
profile obtained with the Cranz-Schardin camera.

As illustrated in the figures, at high velocities a
debris cloud was produced. The debris cloud was unexpected and
tended to obscure the end of the rod near the plate. Three
additional firings were conducted at lower velocities to try to
obtain images in which there was no cloud. Success was obtained
for shots 0103 to 0105. Thus, the velocity at which the cloud
appeared was determined to lie between 137 and 168 m/s. Unfortu-
nately the rod was yawed in shots 103 and 104, and the negative
in shot 105 turned out to be unaccountably light so that no
pictures are available that show complete rod profiles for normal

135

TABLE 8

TAYLOR TEST SHOT MATRIX

Shot #	Velocity m/s	Comments
0094	344	Good impact, radial cracks, tip diameter = 0.710"
0095	293	Good impact, radial cracks, tip diameter = 0.620"
0096	225	Good impact, radial cracks, tip diameter = 0.687"
0097	169	Projectile yawed, no radial cracks, frame rate = 500,180 Hz
0098	197	Projectile yawed, one radial crack, frame rate = 500,100 Hz
0099	197	Good impact, no radial cracks, tip diameter = 0.450"
00100	198	Good impact, no radial cracks, tip diameter = 0.454" frame rate = 500,000 Hz
0101	217	Good impact, no radial cracks, tip diameter = 0.455", frame rate = 5000,000 Hz
0102	215	Good impact, one radial crack, tip diameter = 0.472"
0103	138	Good impact, no cracks, tip diameter = 0.380", pictures underexposed.
0104	158	Good impact, no cracks tip diameter = 0.405", projectile yawed.
0105	133	Projectile yawed.
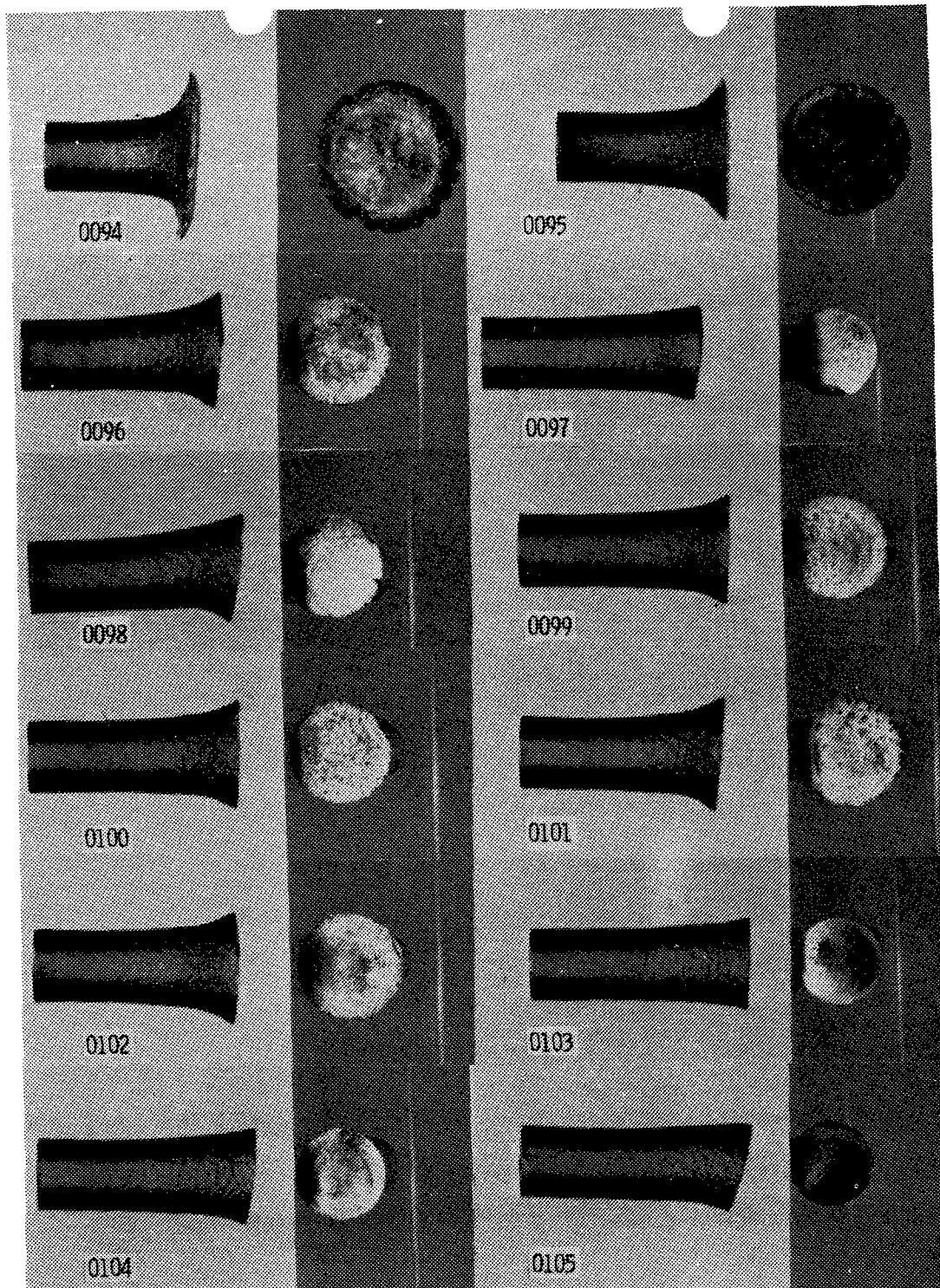
Figure 78. Post-impact Photographs of Armco Iron Rods.

137
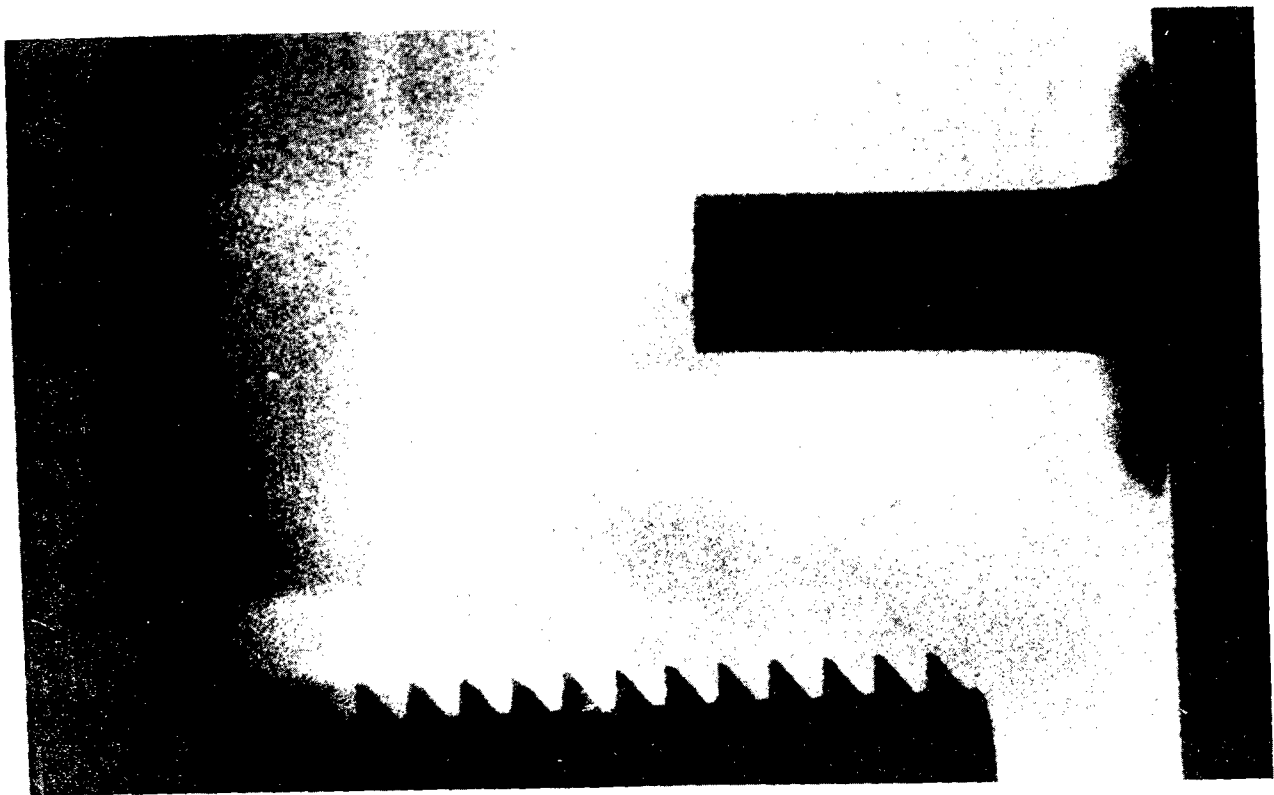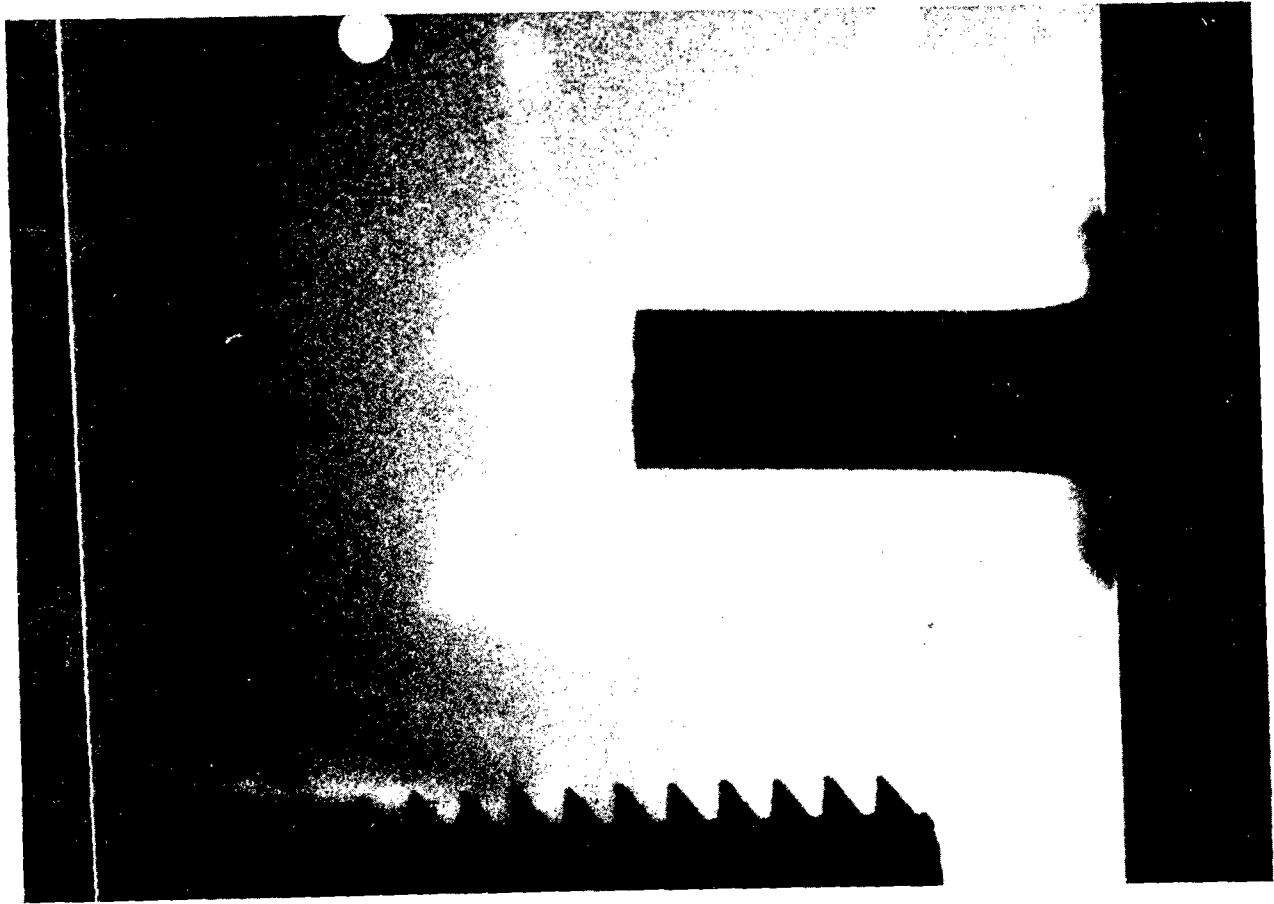
Figure 79. Impact Photos from Shot 94, 344 m/s.

138

impacts.   At this stage, the experiments were discontinued because no more Armco iron samples were available.

The images from a total of four shots: 0094, 0100, and 0101, were digitized and the diameters of the rods as a function of time computed.   As the rod was crushed during the impact, the number of diameter measurements naturally decreased. All length measurements are relative to the back end of the rod. The number of places where diameter measurements could be made also diminishes as the rod advances due to the rising debris cloud.   Figure 80 presents the data for these measurements.

TAYLOR IMPACT EXPERIMENT: 1-0094
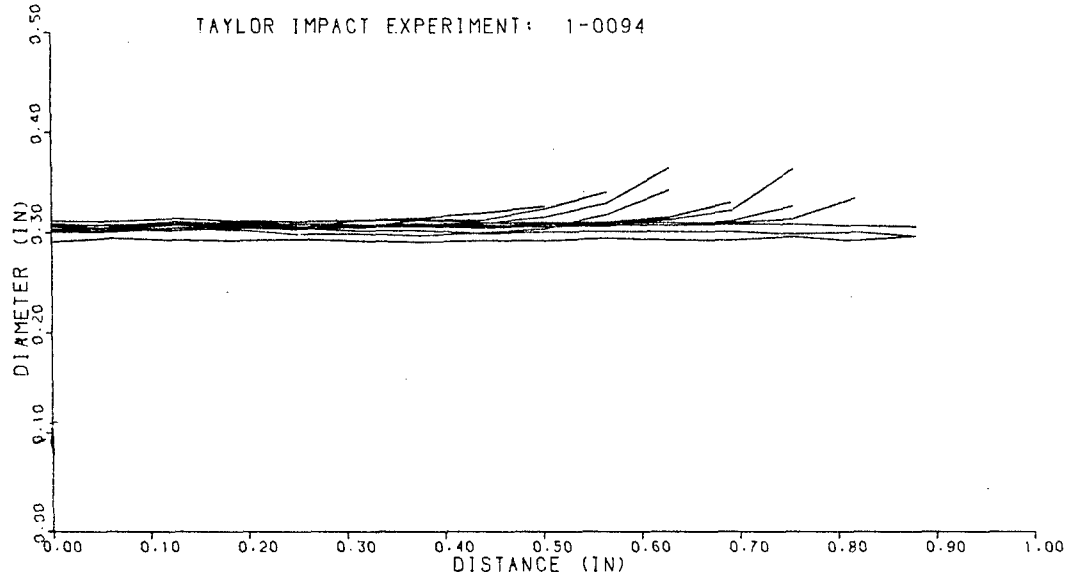
Figure 80.   Profiles Determined by Digitizing Successive
             Frames in Shot 94.

SECTION 3
CONSTITUTIVE MODELING

The mathematical description of the relationship between stresses, strains, and their time derivatives is referred to as the constitutive relationship of the material. Correct and complete constitutive models describe material behavior over the entire range of states that may be experienced in impact and explosive loading. However, this may be extremely difficult to achieve (even for uniaxial stress) and therefore most constitutive relationships are applicable only for a narrow range of stress and strain-rate conditions. The most elementary constitutive models are appropriate only for a rate-independent material under uniaxial monotonic loading conditions. Perzyna (Reference 39), Malvern (Reference 40), and several other investigators proposed various visco-plastic constitutive models for describing the material response at high strain-rate loading conditions [>1000 s^{-1}]. In those models, stress can be computed for a given strain-rate and strain, but load history dependency of the material response can not be explicitly handled.

Several constitutive theories based on state variables have been developed by Bodner and Partom (Reference 4), Krieg et al., (Reference 41), and Chaboche (Reference 42). One of the advantages of state variable theories is that changes in constitutive behavior with load history can be modeled by suitably modifying the evolution equation of the corresponding state variable. Depending on the complexities of the loading, more than one state variable may be introduced into the theory.

For the present work, the state variable based constitutive theory developed by Bodner and Partom was selected for three reasons: (1) ability to predict the response of material to a broad range of load histories; (2) adaptability to finite difference analyses of structural components; and (3) ease with which the parameters in the constitutive models can be determined from high strain-rate test data. The model has been incorporated

in the MAGNA finite element code and the STEALTH finite difference code.

3.1   BODNER-PARTOM MODEL

For assumed small strains, the total strain rate is taken to be decomposable into elastic (reversible) and inelastic (non-reversible) components

$$\dot{\varepsilon}_{ij} = \dot{\varepsilon}^e_{ij} + \dot{\varepsilon}^p_{ij} \tag{22}$$

which are both non-zero for all loading/unloading conditions. Inelastic stresses and strains corresponding to time dependent reversible deformations with energy losses (anelastic behavior) are not treated in this formulation because they are considered to be relatively unimportant.   They could be introduced at a later stage to account for certain transient effects associated with creep and stress relaxation.

The elastic strain rate, $\dot{\varepsilon}^e_{ij}$, is related to the stress rate by the time deviation of Hooke's Law (based on the assumption of small strains).   The inelastic strain rate $\dot{\varepsilon}^p_{ij}$ can be expressed in the general form

$$\dot{\varepsilon}^p_{ij} = \dot{\varepsilon}^p_{ij}(\sigma_{ij}, Z_k, T) \tag{23}$$

where Z_k are one or more internal (inelastic) state variables and T is the temperature.   In particular, $\dot{\varepsilon}^p_{ij}$ is taken to follow the Prandtl-Reuss flow law of classical plasticity, (assuming incompressibility):

$$\dot{\varepsilon}^p_{ij} = \dot{e}^p_{ij} = \lambda S_{ij} \tag{24}$$

where $\dot{e}^p_{ij}$ and S_{ij} are the deviatoric plastic strain rate and the stress.   Squaring equation (24) gives

$$1/2 \; \dot{\varepsilon}^p_{ij} \; \dot{\varepsilon}^p_{ij} = D^p_2 = 1/2\lambda^2 S_{ij} S_{ij} = \lambda^2 J_2$$

or

$$D_2^p = \lambda^2 J_2 \qquad (25)$$

where D_2^p is the second invariant of the plastic strain rate and J_2 is the second invariant of the stress deviator.

The basic assumption of the formulation is that all inelastic deformations are governed by a continuous relation between D_2^p and J_2. The particular form that was established to describe this relation was based on the concepts and equations of dislocation dynamics and is given by:

$$D_2^p = D_o^2 \left\{ \exp(-\frac{z^2}{3J_2})^n \frac{(n+1)}{n} \right\} \qquad (26)$$

where D_o is the limiting value of the plastic strain-rate in shear. n is a material constant that controls strain rate sensitivity and also influences the overall level of the stress-strain curves. It is a fundamental constant and it is not dependent on the loading history. Z is the inelastic state variable which represents the measure of the overall resistance to plastic flow caused by microstructural barriers that impede dislocation motion. Combining equations (24) through (26), the plastic strain-rate takes the form

$$\dot{\varepsilon}_{ij}^p = D_o \exp \left\{ -\left(\frac{z^2}{3J_2}\right)^n \frac{(n+1)}{2n} \right\} \frac{S_{ij}}{\sqrt{J_2}} \qquad (27)$$

The general form for the evolution equations, i.e., history dependence, of the inelastic state variable Z is,

$$\dot{Z} = F(J_2, Z, T) \qquad (28)$$

For conditions of uniaxial stress of constant sign, the strain hardened material is assumed to be represented by a single state variable Z which depends on plastic work. This corresponds to isotropic hardening and the evolution equations employed can be shown to be in the form of equation (28). The corresponding form is then based on the concept that plastic work, W_p, controls the hardening process, and that the plastic work and its time

143

derivative are functions of σ_{ij} and $\dot{\varepsilon}_{ij}$. The evolution equation for the state variable is assumed to have the form:

$$\dot{Z} = m(Z_1 - Z) \dot{W}_p \qquad (29)$$

where, $\dot{W}_p = \sigma_{ij} \dot{\varepsilon}_{ij}^p$. The above equation can be integrated with m and Z, as material constants. The relation between Z and W_p becomes,

$$Z = Z_1 - (Z_1 - Z_o) e^{-mW_p} \qquad (30)$$

Z_o is the initial value of Z corresponding to the reference state from which W_p is measured. It is noted that Z_o could take any value between 0 and Z_1. The initial yield stress of the uniaxial stress-strain relation is directly influenced by Z_o. Z_1 corresponds to the saturation state of Z at which the material reaches a fully-work hardened condition. m is a material constant that controls the rate of work hardening.

For materials, such as OFHC copper, which exhibit strong strain hardening, m was made a function of W_p by Bodner and Partom (Reference 4). The expression for m was:

$$m = m_o + m_1 e^{-\alpha W_p} \qquad (31)$$

which adds two more constants. When m is defined by equation (31), the relationship (30) is not valid. The expression for $\dot{Z}$ when integrated after replacing m by the definition (31), yields the following relationship between Z and W_p:

$$Z = Z_1 - (Z_1 - Z_o) e^{-m_o W_p} \cdot e^{-\frac{(m_o + m_1 - m)}{\alpha}} \qquad (32)$$

For evaluating the BP-model constants from the SHB and plate impact test results, we need to develop 1) a computer program to solve the BP-model equations under uniaxial stress condition (SHB test), and 2) special purpose subroutines for

144

STEALTH to describe the BP-model under one dimensional strain condition (plate-impact test).

A program called, BPSOLVE was developed to calculate the uniaxial stress for a given strain-rate history. This program was effectively used in the BP-model constants evaluation. The following section describes the efforts that were taken to program the BP-model in STEALTH.

3.2   BODNER-PARTOM MODEL IN STEALTH

Currently, the standard STEALTH code is not capable of describing a visco-plastic material. Since the state variable based Bodner-Partom constitutive equations were selected for high strain-rate material characterization, it was essential to incorporate the BP-model algorithm into the STEALTH code for the plate impact test simulations using the BP-model parameters. To incorporate the BP-model into STEALTH, various subroutines were developed.

A subincremental time stepping scheme was used to calculate the deviatoric stresses, S_{ij} for each finite difference time step. The global time step, Δt is further divided into small steps in a special purpose subroutine to describe the BP-model. At the end of each global time step, STEALTH provides the volumetric strain rate, $\dot{e}$, and the pressure, p; S_{ij}, σ_{ij}, $\dot{\varepsilon}^p_{ij}$ are unknown.

In the current numerical scheme, the plastic strain-rates were estimated for each subincremental time step using equation (25) with the value for J_2 calculated from the known S_{ij} values at the beginning of the step. The elastic strain-rates, $\dot{\varepsilon}^e_{ij}$, were estimated from the estimated $\dot{\varepsilon}^p_{ij}$ and the known total strain rate, $\dot{\varepsilon}_{ij}$. The new estimates for S_{ij} can be made from the following relationship:

$$\dot{S}_{ij} = \dot{\sigma}_{ij} + \dot{p} \tag{33}$$

where

$$\dot{\sigma}_{ij} = E_{ij}\dot{\varepsilon}^e_{ij} \tag{34}$$

145

and

E_{ij} are the elements of the elastic modulus matrix.

Using the new estimates for $\dot{S}_{ij}$, the improved values for the plastic strain-rates at the end of the subincremental time step can be computed. This procedure is continued until the values of $\dot{S}_{ij}$ computed for the two successive iterations converge to the same value within the tolerant limits. A series of flowcharts, given in Appendix A describe the steps involved in the numerical scheme.

Rajendran and Grove (Reference 43) discuss in detail the various newly developed subroutines for STEALTH and also the methods that were used for the validation of the special purpose routines.

3.3   EVALUATION OF BODNER-PARTOM MODEL PARAMETERS

The Bodner-Partom constitutive model contains seven empirically derived constants; D_o, n, m_o, m_1, α, Z_o and Z_1; these constants were defined in Section 3.1. D_o is a reference maximum strain-rate level which can be conveniently assigned a large value. In this investigation, D_o was arbitrarily chosen to be $10^8 s^{-1}$. The constants n, Z_o, Z_1, and $m(=m_o)$ were determined by first estimating the values based on the Hopkinson bar data, then modifying the values so that the stress-strain predictions from the model match both the Hopkinson bar and the plate impact test results as closely as possible. For most materials, m was assumed to be a constant and represented by 'm_o'. For strong strain-hardening materials like OFHC copper, m_1, and α had to be added to the other material constants.

The plastic strain rate, $\dot{\varepsilon}^p$ under uniaxial stress condition is given by

$$\dot{\varepsilon}^p = \frac{2}{\sqrt{3}} D_o \, e^{\left\{-\left(\frac{n+1}{2n}\right)\left(\frac{Z}{\sigma}\right)^{2n}\right\}} \tag{35}$$

146

The plastic strain rate (approximately equal to the total strain rate, since $\dot{\varepsilon}^e \ll \dot{\varepsilon}^p$) and the maximum stress (at which the stress-strain curve is approximately flat) can be obtained from each Hopkinson bar tensile test. At, $\sigma = \sigma_{max}$, the state variable Z saturates and reaches its maximum value ($Z = Z_1$). Then, equation (35) can be rewritten, after taking natural logarithms twice, as:

$$Y = M\ X + C \tag{36}$$

where

$$Y = \ln[-\ln(\frac{\sqrt{3}\ \dot{\varepsilon}^p}{2D_o})] \tag{37}$$

$$X = \ln(\sigma_{max}) \tag{38}$$

$$M = -2n \tag{39}$$

and
$$C = \ln[(\frac{n+1}{2n})\ Z_1^{2n}] \tag{40}$$

Since various values of X and Y are known from different strain-rate Hopkinson bar tensile tests, a straight line can be fitted to the data and the corresponding constants M and C can be obtained from the slope and intercept of the straight line. Knowing M and C, the Bodner-Partom model constants n and Z_1 can be calculated from equations (37) and (38).

The initial estimates of the constants Z_o and m were determined from the plot of plastic work (W_p) vs. Z, where W_p and Z are defined as:

$$W_p = \int_o^{\varepsilon^p} \sigma d\varepsilon^p \tag{41}$$

and

$$Z = [-\ln(\frac{\sqrt{3}\ \dot{\varepsilon}^p}{2\ D_o})\ (\frac{n}{n+1})\ \sigma^{2n}]^{1/2n} \tag{42}$$

147

To allow for direct integration of equation (39), the Hopkinson bar stress-strain data were described in terms of a polynomial curve fit.

$$\sigma = f(\varepsilon^p) \tag{43}$$

A linear fit was used to describe the plot of W_p vs. Z.

$$W_p = A\ Z + B \tag{44}$$

The initial estimates for m and Z_o are determined from the slope (A) and intercept (B) of the curve fit.

$$m = -A \tag{45}$$

$$Z_o = Z_1 - e^B \tag{46}$$

Since regression of all the Hopkinson bar test data is a time consuming and a tedious process, a series of interactive automated computer programs was developed to evaluate the material constants. A flow chart for the interactive program is shown in Figure 81.

Since n controls the flow stress level due to strain rate effects and Z_o controls the initiation of plastic flow, these two parameters greatly influence the HEL in the plate impact test simulations; whereas all the four parameters (m, Z_1, n and Z_o) influence the stress levels in the SHB test simulations at strains >0.02. Due to the noise in the SHB test data at small strains, the SHB flow stress values at such strains are not dependable. Therefore, it is essential to use the plate impact test data (HEL) in the evaluation of BP-model parameters at small strains.

Unfortunately, in the interactive program it is not possible to include the flow stress, Y_o, obtained from the HEL of the plate impact test directly because the strain-rate associated with the HEL is not a measurable quantity. To overcome this difficulty and also to make use of the experimentally obtained

148

Hopkinson Bar Results for
Three or More Strain Rate Levels

INPUT
$\sigma = f(\varepsilon^p)$, σ_{max}
and $\dot\varepsilon^p_{ave}$

CALCULATE
α

$$\alpha = \ln[-\ln(\frac{\sqrt{3}\ \dot\varepsilon^p_{ave}}{2\ D_0})]$$

FIT A LINE TO
THE α VS $\ln$
(σ_{max}) DATA

PLOT
RESULTS

FIT A NEW
LINE TO
THE DATA

NO

IS
THE LINE
ACCEPTABLE

YES

$n = \frac{1}{2}$ SLOPE

$$\text{INTERCEPT} = \ln\ [(\frac{1}{Z_1})^{2n}(\frac{n+1}{2n})]$$

SOLVE FOR
n AND Z_1

CALCULATE THE
PLASTIC WORK
(W^p) FOR SOME
σ

$$W_p = \int_\sigma^{\bar\varepsilon^p} d\varepsilon^p\ ;\ \sigma = f(\varepsilon^p)$$

CALCULATE Z
FOR THE SAME
VALUE OF σ

$$Z = [-\ln(\frac{\sqrt{3}\ \dot\varepsilon^p}{2\ D_0})(\frac{n}{n+1})\sigma^{2n}]^{1/2n}$$

A
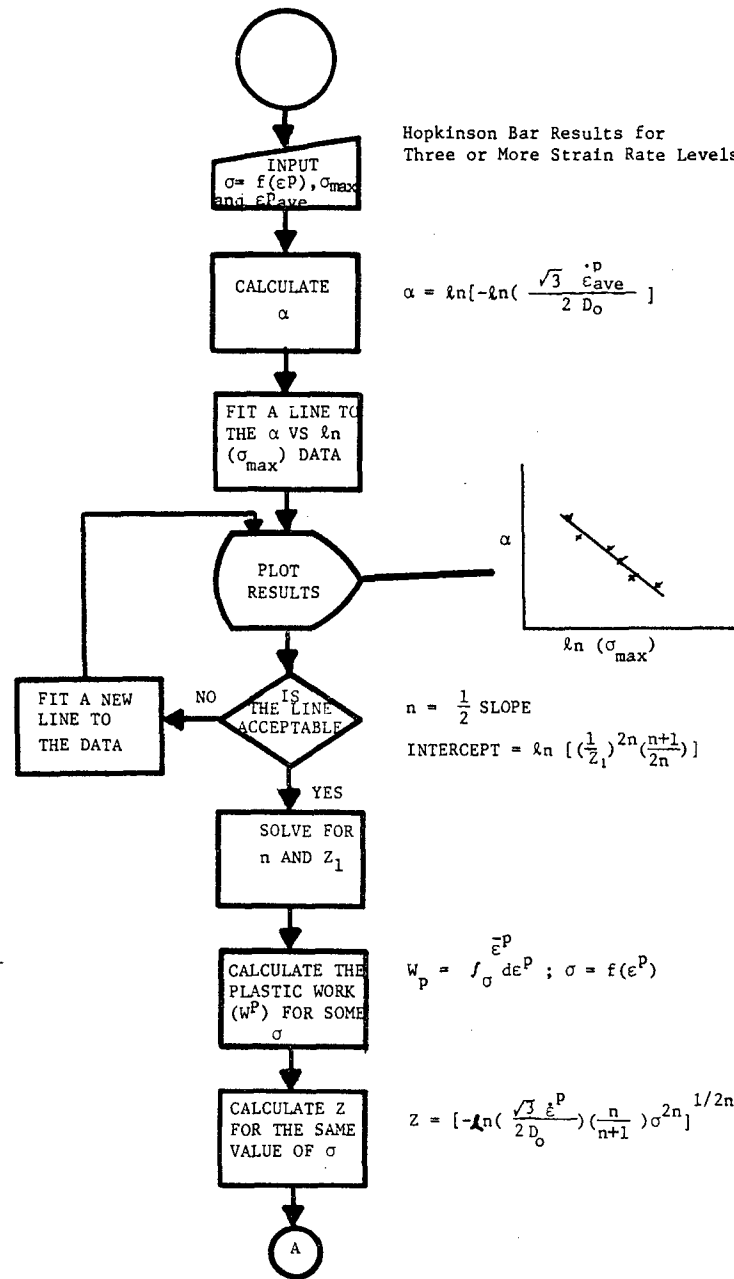
Figure 81.   Flow Chart for the Interactive Computer
Program Describing Bodner-Partom Model
Constants Evaluation.
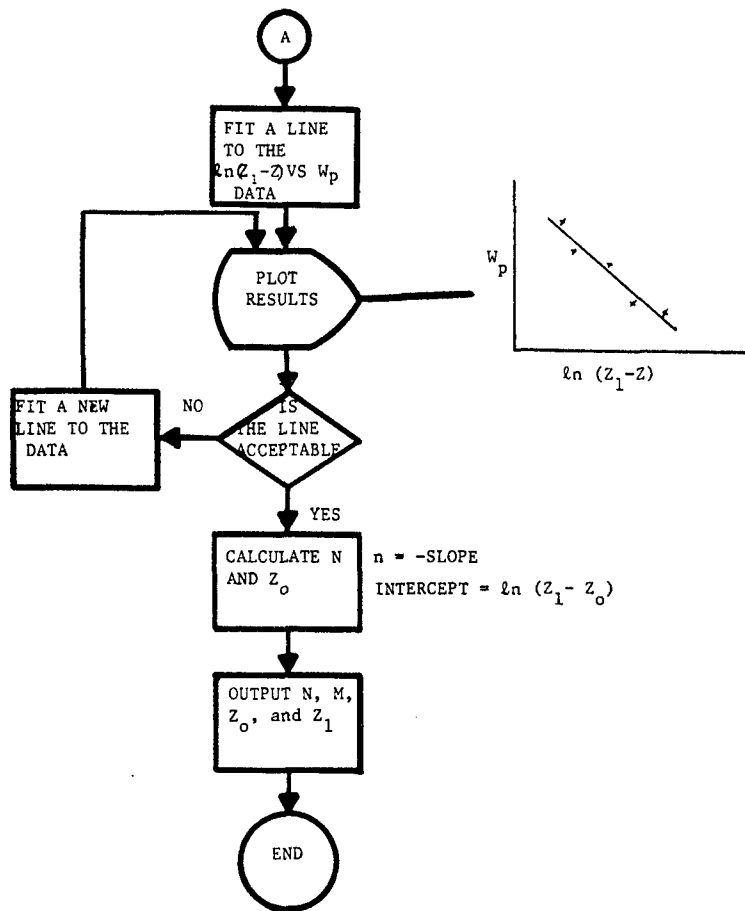
Figure 81 (cont'd). Flow Chart for the Interactive Computer Program Describing Bodner-Partom Model Constants Evaluation.

Y_O, an indirect data reduction scheme was developed and successfully used for all five metals. The steps involved in that scheme were:

1. Estimation of n, m_O, Z_O, Z_1, from the interactive program using only the SHB tension test results.

2. Simulate the plate impact test through STEALTH using the newly developed BP-model algorithm to check whether the HEL based on the estimated constants predicted the test data correctly. If the predicted HEL is above the test result, the value for n must be adjusted for less rate dependency and vice versa.

3. Reduce or increase the value of n according to Step 2. Simulate the SHB test results using BPSOLVE with the new estimate of n. Adjust other parameters interactively until SHB test data are matched.

4. Perform Steps 2 and 3 until both SHB and plate impact test data agreed with the model calibrations.

Using this data evaluation scheme, model constants for the five materials were successfully obtained. The values are listed in Table 9. Following sections describe the model predictions.

3.3.1   Model Evaluations

This section shows the results of the B-P simulations of tensile SHB and plate impact tests. We also demonstrate the ability of the model to predict the results of compression SHB tests, in which the strain rate varies continually. For most materials, it was only necessary to evaluate the constants n, m_O, Z_O, and Z_1 of the Bodner-Partom constitutive model. For OFHC copper the additional constants m_1 and α were needed to predict the SHB test data accurately. The constant D_O was assumed to be $10^8 \ s^{-1}$ for all the five materials. The continuously varying

TABLE 9

B-P MODEL AND ELASTIC CONSTANTS

	1020	OFHC	C1008	HY100	7039-T64
K (Kbar)	1540	1418	1540	1540	768
G (Kbar)	794	450	794	794	276
E (Kbar)	2033	1220	2033	2033	739
ν	0.28	0.36	0.28	0.28	0.34
Y_O (Kbar)	4.6	1.6	6.9	9.5	3.7
D_O (s^{-1})	10^8	10^8	10^8	10^8	10^8
n	4.0	0.4	0.4	1.2	4.0
m_O (Kbar^{-1})	3.0	1.1	1.5	1.0	2.8
m_1 (Kbar^{-1})	0	15.0	0	0	0
Z_O (Kbar)	6.4	8.0	55.	24.	5.6
Z_1 (Kbar)	9.3	65.5	70.	35.5	7.6
α (Kbar^{-1})	0	150	0	0	0

strain-rate data obtained from the tests were used as program input in the compression test simulations.

a. 1020 steel

The Bodner-Partom model constants for this material were obtained based on the selected SHB test results. It was observed that that Y_O (=4.6 Kbar) obtained from the plate impact tests was no higher than the yield values obtained in the SHB tests. This, along with observations summarized by Bless (Reference 19), supported the assumption that 1020 steel is a fairly rate-independent material. Matuska (Reference 44) carried out finite difference calculations to reproduce hemispherical impact data of Bless and Barber (Reference 45) for this material. He had to employ a work hardening model (with Y_O = 4.6 Kbar at initial yield, increasing linearly to 6.3 Kbar) designed to fit the observed velocity decay. In Figure 82 three different SHB tests and the model used by Matuska are shown. It clearly supports the conclusion that this steel is a fairly rate independent material in the high strain-rate regime.

The constants of the Bodner-Partom constitutive model for the true stress-true strain behavior of 1020 steel are summarized in Table 9. Figure 83 contains the actual test results and the Bodner-Partom predictions for each strain rate level tested.

The constants of the Bodner-Partom constitutive model, derived from the Hopkinson bar tensile experiment and the plate impact tests, were used to predict the dynamic compressive true stress-true strain behavior. The predictions and the original Hopkinson bar data are shown in Figure 84. The slight disagreement shows that there is some anisotropy present in the materials. However, the BP-model precision is adequate for engineering calculations.

Unfortunately, none of the VISAR plots for this material turned out to be useful. Among the various shots, shot #529 happened to be slightly better than the rest. Simulation of this test was attempted through STEALTH with the
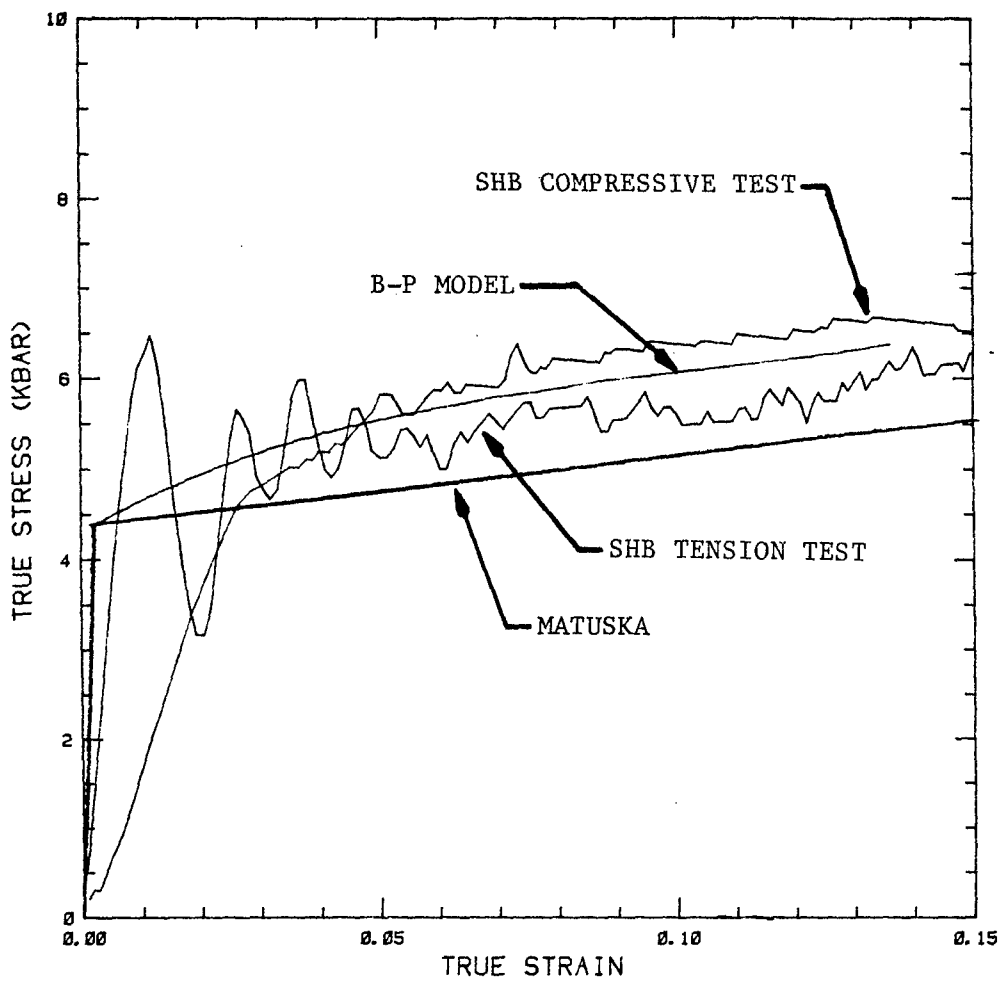
Figure 82. Three Different SHB Tests and the Model Used by Matuska (Reference 44).

154
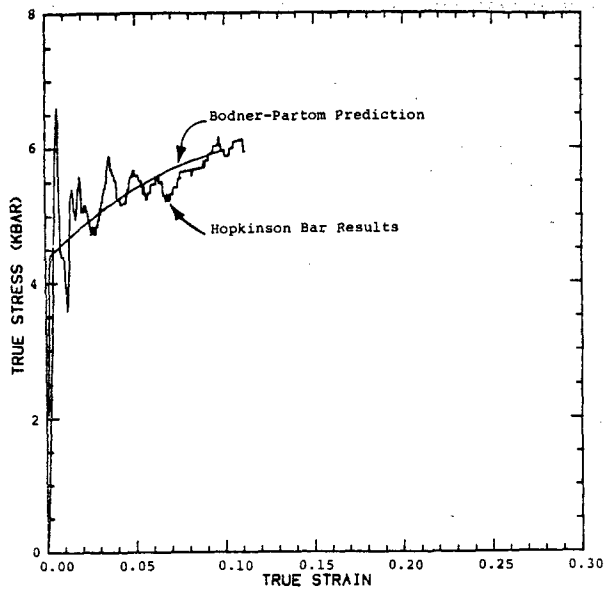
a. $\dot{\varepsilon} = 400 \text{ s}^{-1}$
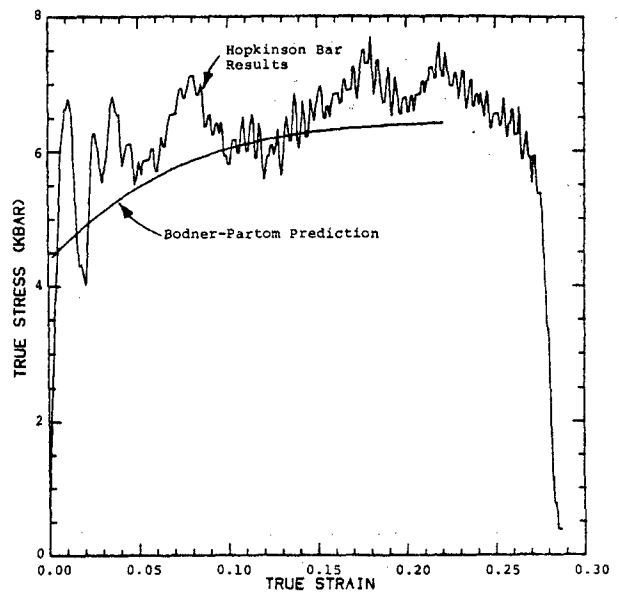
b. $\dot{\varepsilon} = 1100 \text{ s}^{-1}$
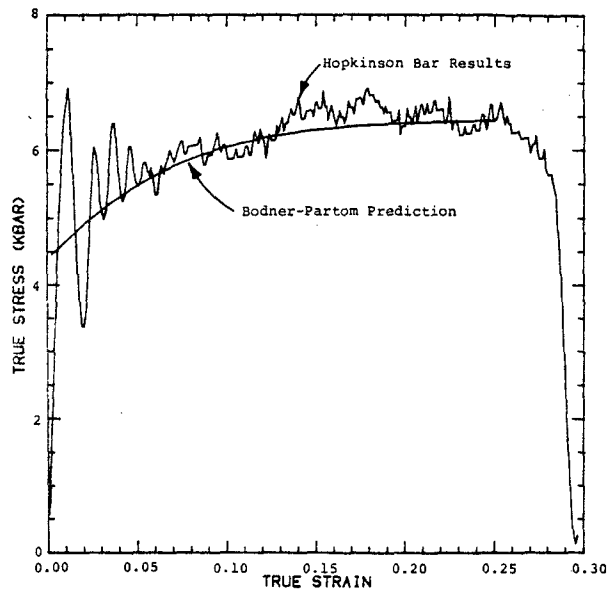
c. $\dot{\varepsilon} = 1200 \text{ s}^{-1}$
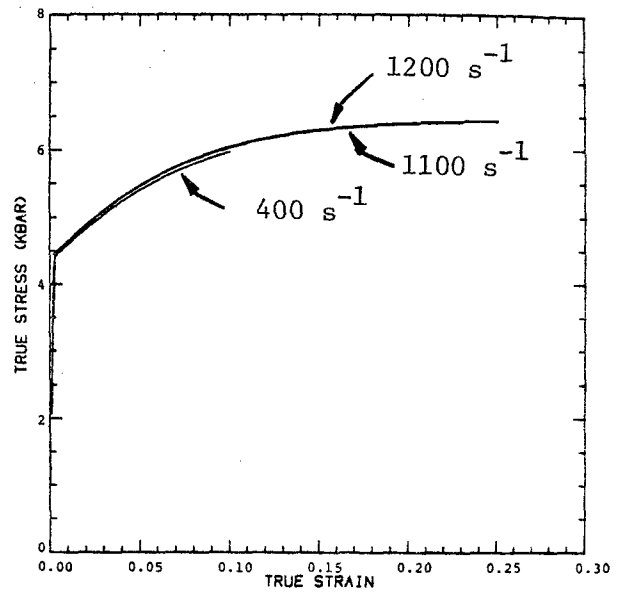
d. Combined Plot

Figure 83.   Bodner-Partom Predictions of the Dynamic Tensile
Behavior of 1020 Steel.

155
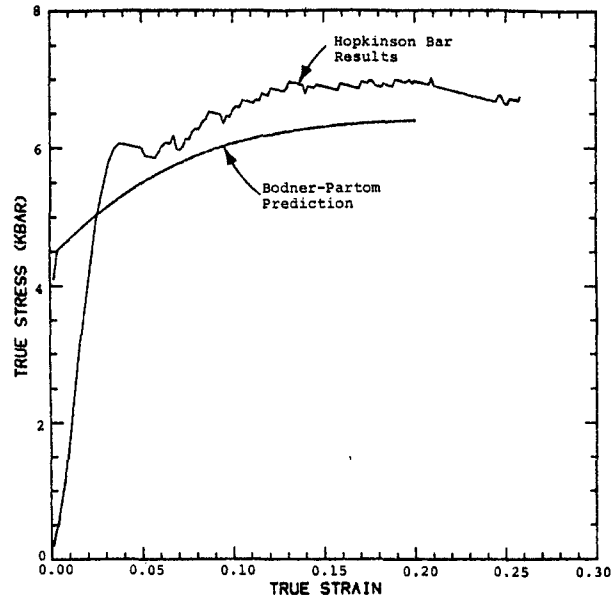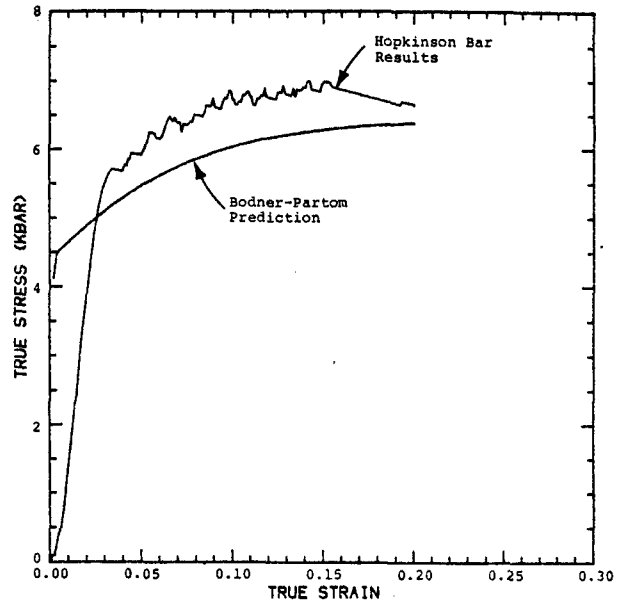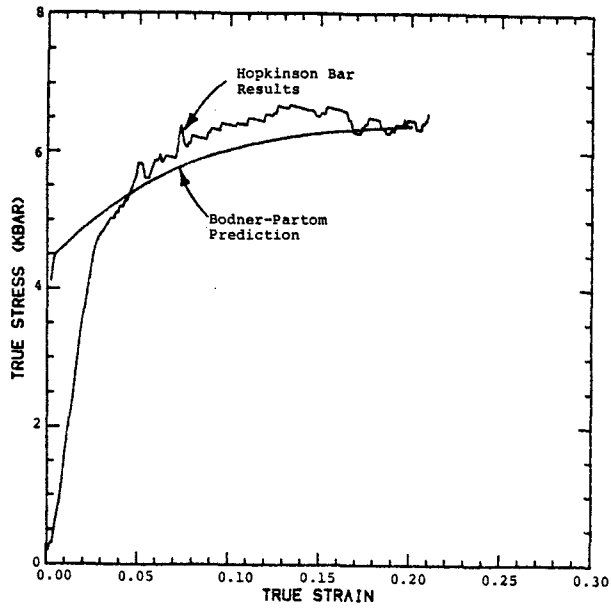
Figure 84. Bodner-Partom Prediction of the Dynamic Compressive Behavior of 1020 Steel.

Bodner-Partom model constants in Table 10 for 1020 steel. The VISAR trace of the free surface velocity history was compared with the simulation in Figure 85. Since the shape of the rising portion of the VISAR beyond the HEL was so poor, it is difficult to judge the accuracy of model predictions.

b.   OHHC copper

The constants of the Bodner-Partom constitutive model for the true stress-true strain behavior of OFHC copper are summarized in Table 9. Figure 86 contains the actual SHB test results and the Bodner-Partom simulation for several strain rate levels. Since this material exhibited substantial strain hardening, modeling with only four constants, n, m_o, Z_o, and Z_1 was not successful. As Bodner and Partom (Reference 4) reported earlier, additional constants m_1, and α were required in the modeling. The plate impact test results were not used in the model calibration because of the uncertainty in the σ_{HEL} value. Since, the HEL value was so low, it was not well resolved. However, a value of 1.6 Kbar reported earlier (Reference 19) seems to support the model predictions.

The constants of the Bodner-Partom constitutive model, derived from the Hopkinson bar tensile experiments, were used to predict the dynamic compressive true stress-true strain behavior. The predictions and the original Hopkinson bar data are shown in Figure 87. The disagreement indicates that the OFHC copper exhibits anisotropic behavior.

Excellent VISAR records for OFHC copper plate impact experiments are given in Bless (Reference 19) and Bless and Paisley (Reference 46). For model prediction, shot #560 (4mm flyer and 6mm target at 209 m/s) was simulated through STEALTH using the BP-model subroutines to describe the high strain-rate material behavior and the constants are given in Table 9. The model prediction of the free surface velocity of the target is compared directly with the VISAR plot in Figure 88. Since the HEL of copper is very low, it is difficult to compare the HEL; however, the plots beyond the HEL which includes the peak velocity and the
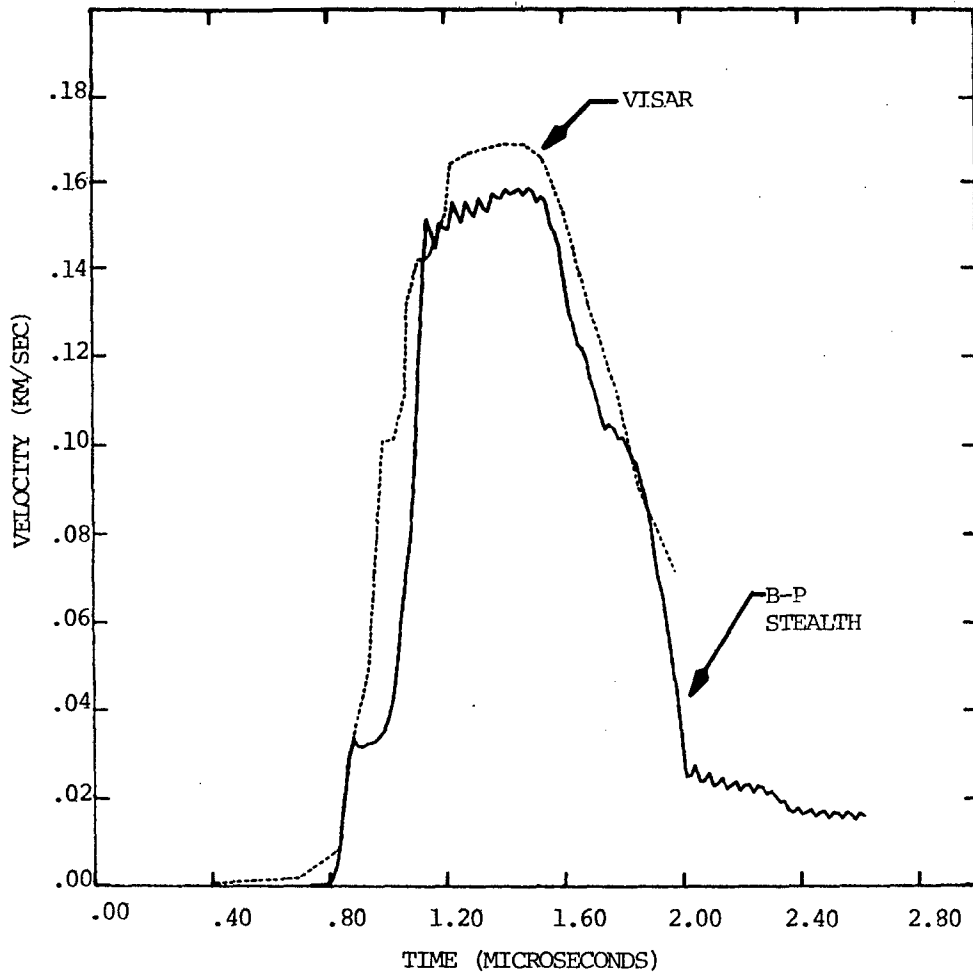
Figure 85. VISAR Trace and Bodner-Partom Prediction for 1020 Steel.
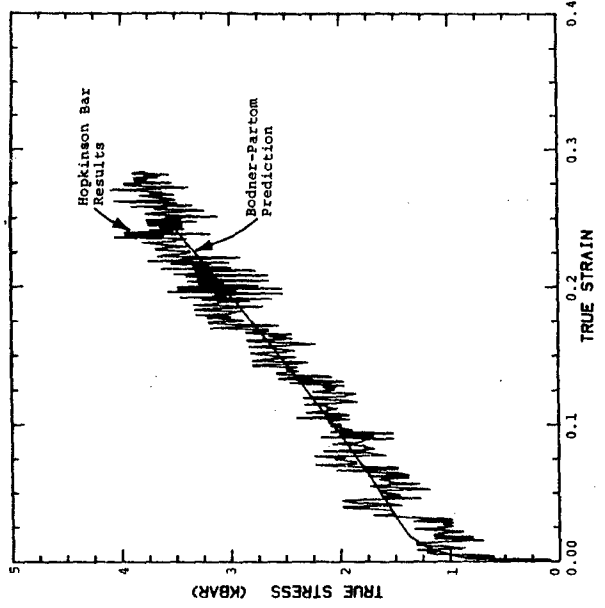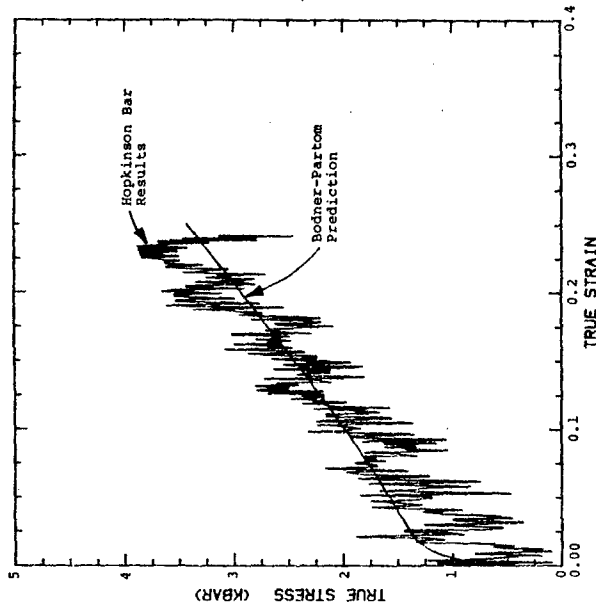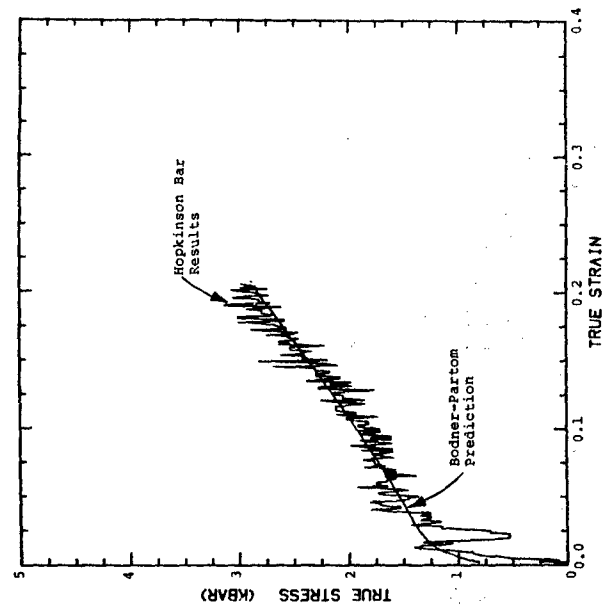
Figure 86. Bodner-Partom Prediction of the Dynamic Tensile Behavior of OFHC Copper.

159
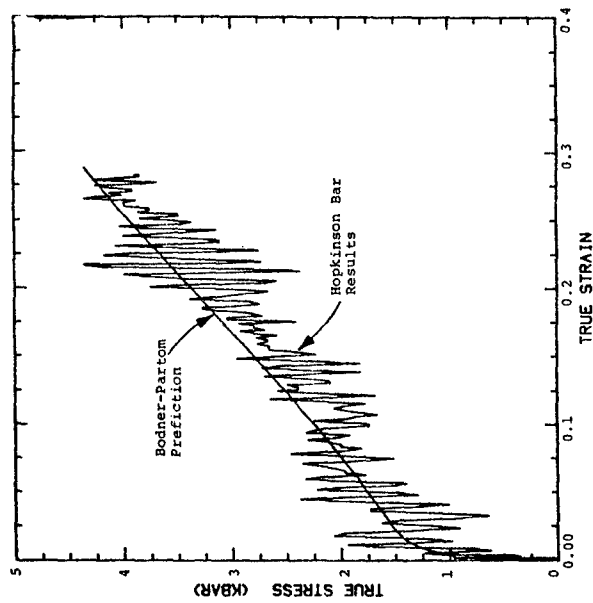
d. $\dot{\varepsilon} = 1800 \text{ s}^{-1}$
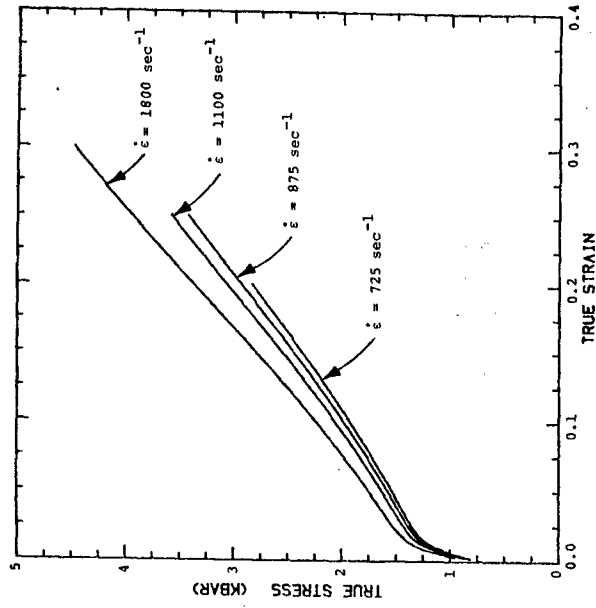
e. Combined Plot

Figure 86 (cont'd). Bodner-Partom Predictions of the Dynamic Tensile Behavior of OFHC Copper.

160
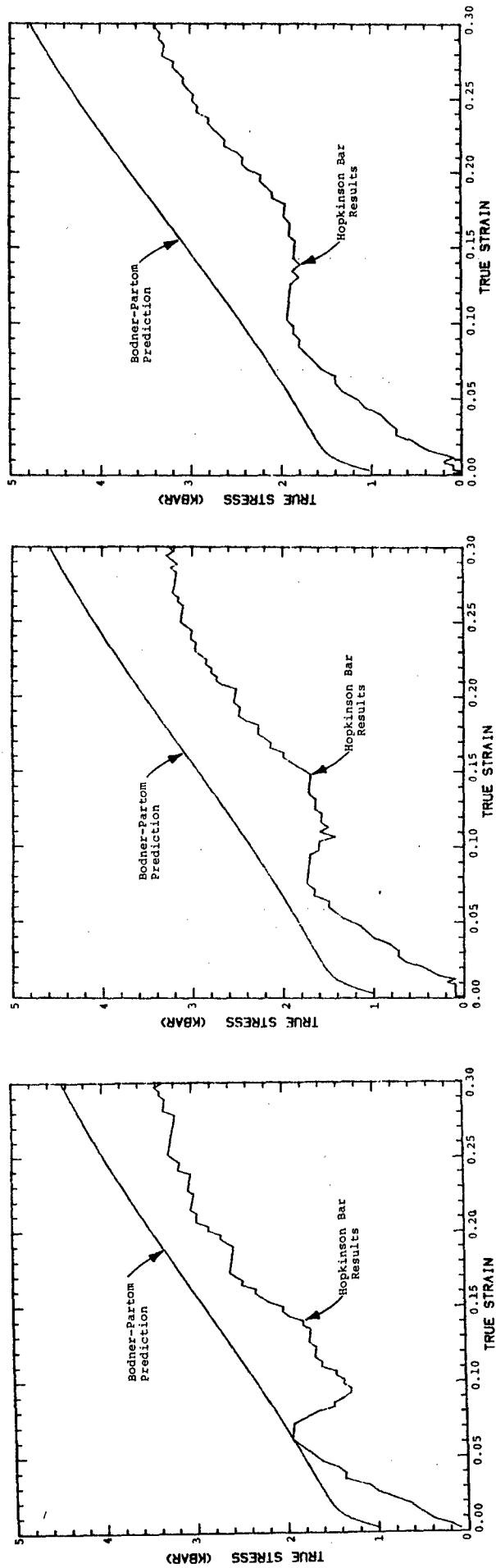
Figure 87.   Bodner-Partom Predictions of the Dynamic
             Compressive Behavior of OFHC Copper.

161
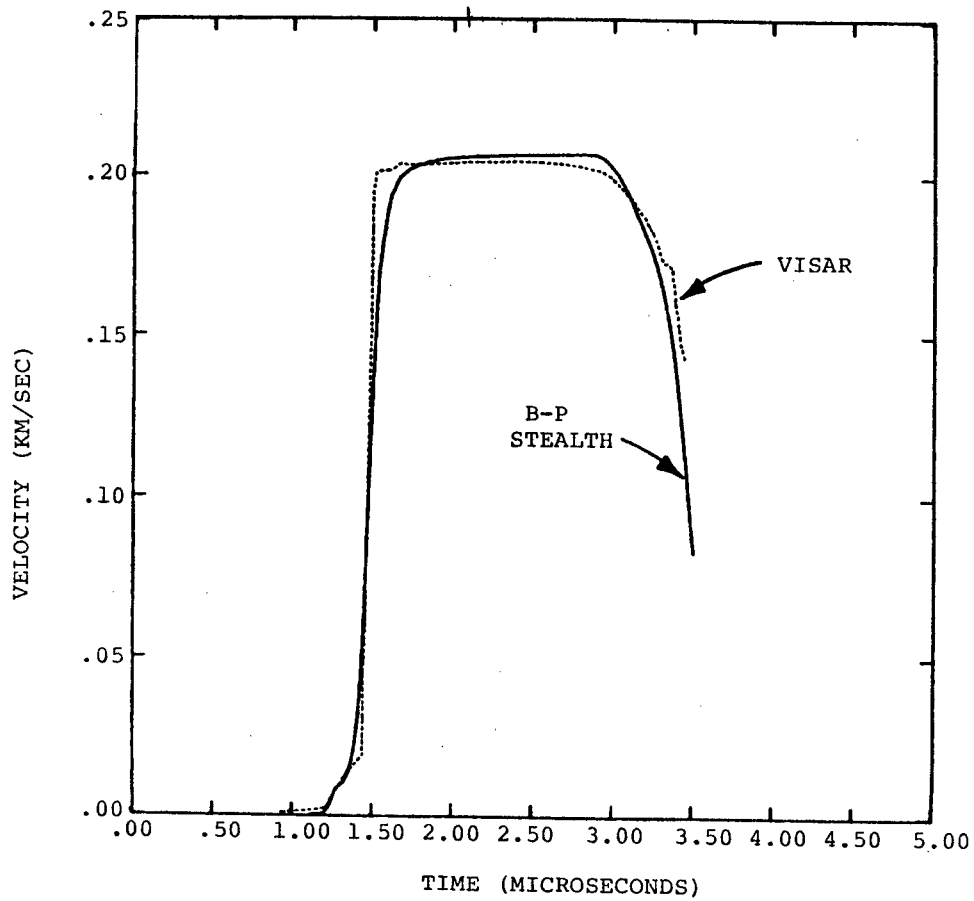
Figure 88. Comparison of Velocity History Between
STEALTH with Bodner-Partom Routines
and VISAR Data (OFHC Copper).

shape of the release portion compared extremely well. A typical STEALTH plot of the stress-strain history in the spall plane is shown in Figure 89. The complex dynamic stress history at the spall plane can be calculated with great detail by STEALTH due to the sophisticated constitutive model (BP-model) description.

The similar SWAP code was also used for an analysis of OFHC copper. The objective was to infer the uniaxial stress-strain curve that is consistent with the release data from shot 560. This code can include strain hardening, but not strain rate dependency. The approach was to incrementally vary the hardening model while continually comparing predicted and actual release wave profiles. It was found that the release wave profile in these relatively thick targets was very sensitive to the assumed hardening model.

Hardening is introduced into SWAP by making the yield strength a function of the plastic strain. The equation used was

$$Y = Y_O + a\varepsilon^b \tag{47}$$

where a and b are empirical constants.

The effect of changing the hardening behavior is shown in Figures 90 and 91. Both figures show the surface velocity profiles for shot 560. In Figure 90, the material is assumed to be elastic-perfectly plastic with a yield strength of 1.0 Kbar (a = 0). In Figure 91, the material is assumed to yield at the same initial stress with a = 3.4 Kbar and b = 0.28. The figures include a comparison with the observed velocity profile. The agreement is excellent, until spall occurs. (Spall was suppressed in the calculation.) Similar good results were obtained for other shots with this model.

Figure 92 presents the uniaxial stress-strain curve implied by these parameters. This curve represents the average stress strain relationship pertaining to a tensile test
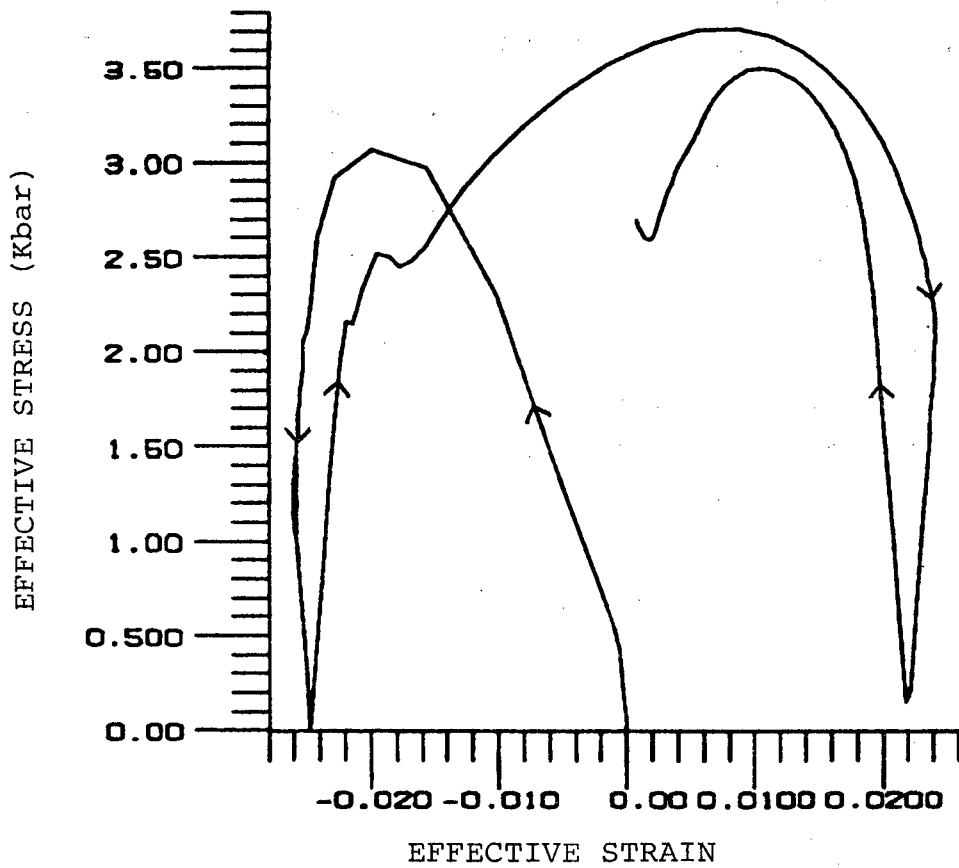
Figure 89.   The Effective Stress vs. Effective Strain
at the Spall Plane for OFHC Copper from
STEALTH with Bodner-Partom Routines.
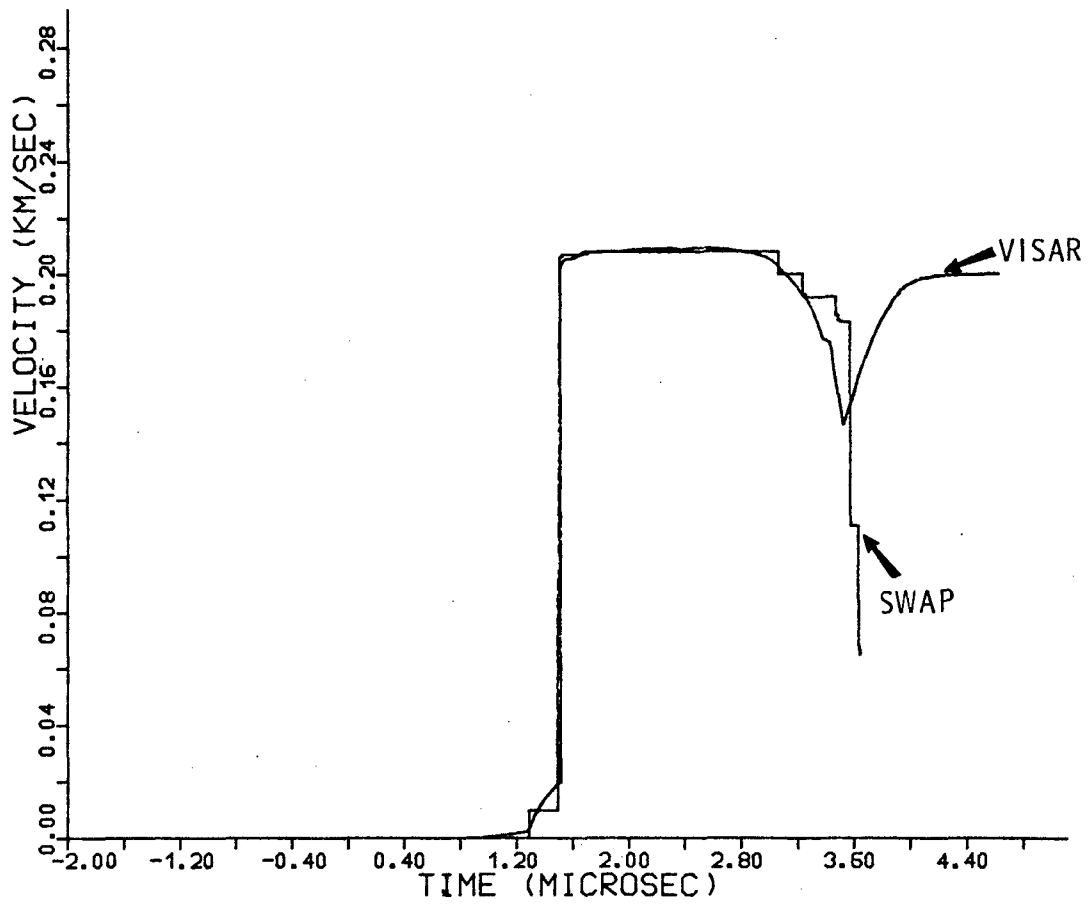
Figure 90.   Comparison of SWAP with VISAR Data for OFHC
             Copper, No Hardening.
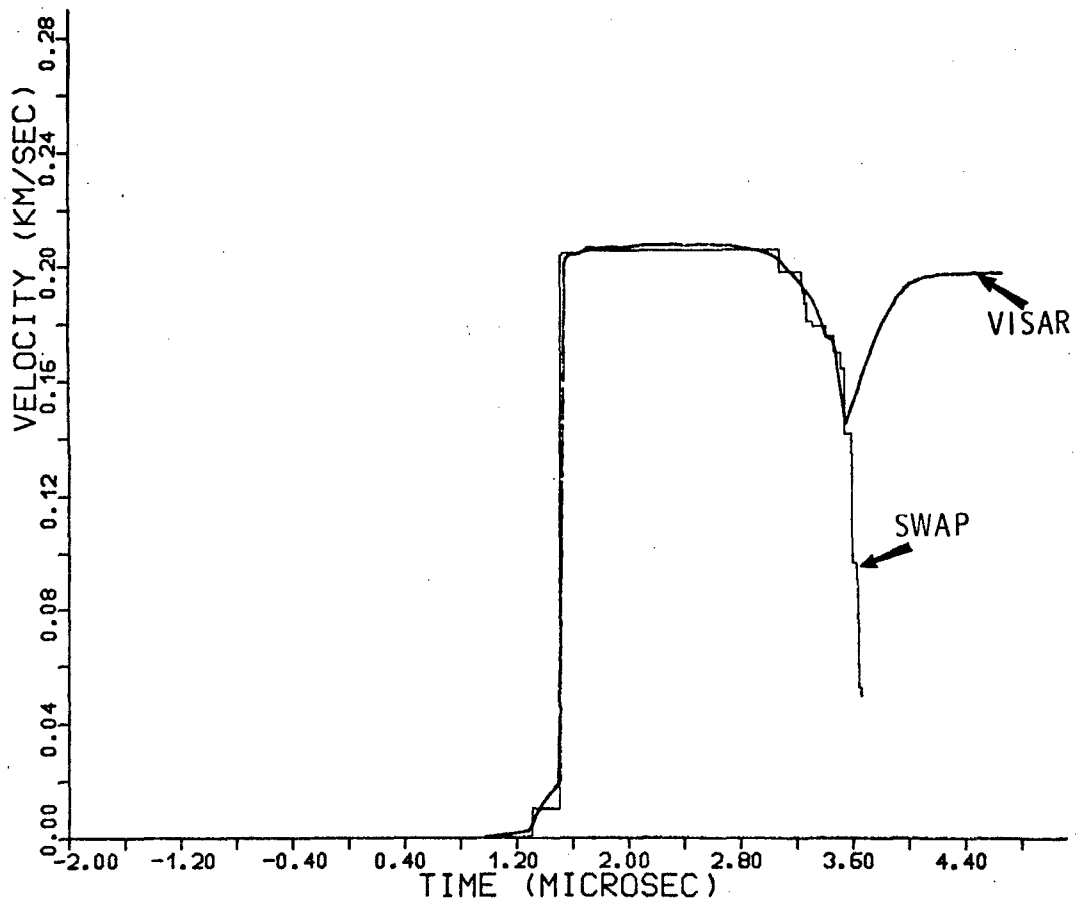
Figure 91. Comparison of SWAP with VISAR Data for OFHC
            Copper, Using Hardening Shown in Figure 92.
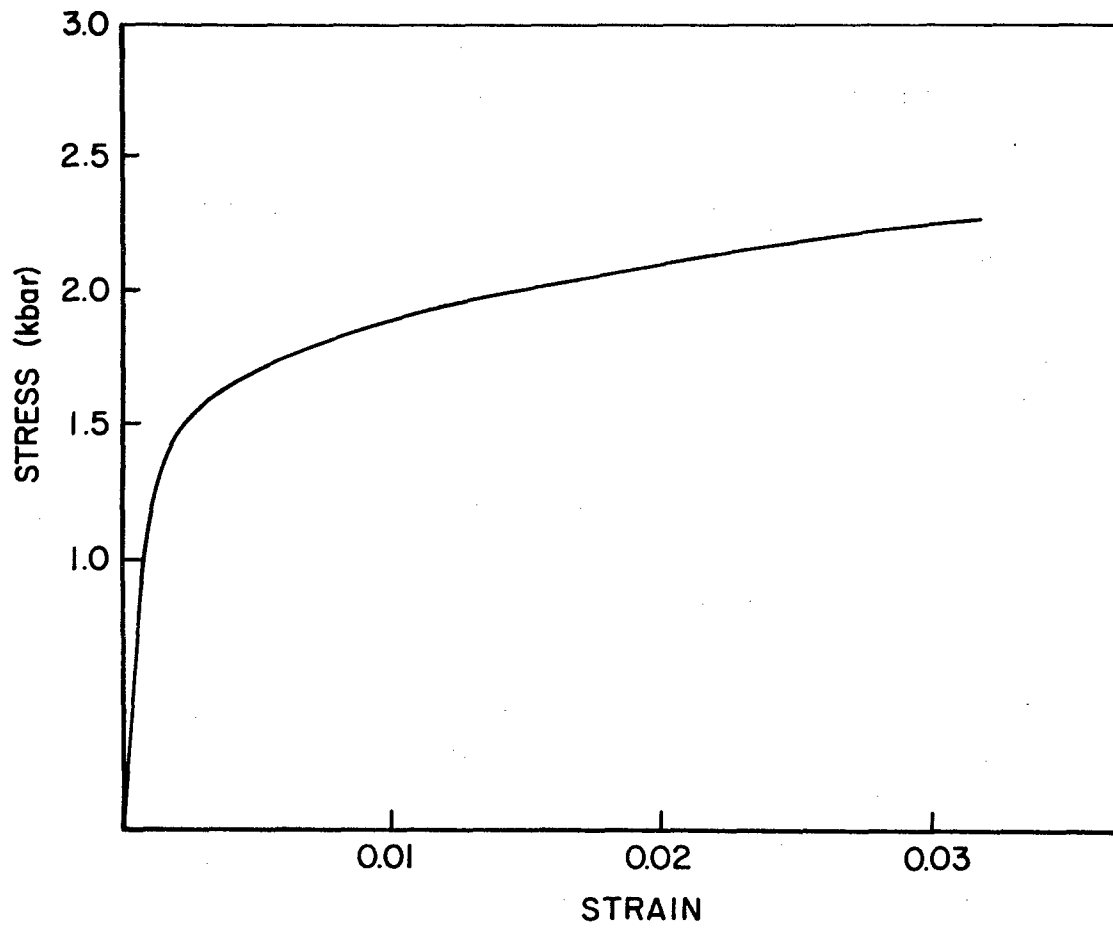
Figure 92.   Uniaxial Stress-Strain Curve for OFHC Copper
Derived from SWAP Simulation.

167

at ultra high strain rates. It lies considerably above even the highest strain rate SHB test data (see Figure 86e).

c.   C1008 steel

The constants of the Bodner-Partom constitutive model for the true stress-true strain behavior of C1008 steel are summarized in Table 9. Figure 93 contains the actual test and the Bodner-Partom model results for each strain rate level tested.

The constants of the Bodner-Partom constitutive model, derived from the Hopkinson bar tensile experiments, were used to predict the dynamic compressive true stress-true strain behavior. The predictions and the original Hopkinson bar data are shown in Figure 94. The slight disagreement shows that there is some anisotropy present in the materials. However, the BP-model precision is adequate for engineering calculations.

The plate impact test of shot #678 was simulated through STEALTH. A 3mm, 1020 steel flyer and 6mm, C1008 steel target were modeled. The impact velocity was 178 m/s. The simulated free surface velocity history is compared with the VISAR plot in Figure 95. The observed HEL is slightly higher than the calculated value. This is consistent with the precursor decay discussed in Section 2.3.3.

The STEALTH simulation reproduces the ramp on loading and the ramp behind the plastic wave arrival. This latter feature is apparently caused by rate dependency. However, the peak velocity is not compared well. To check this point, particle velocity (u_p) vs. stress (σ) diagram was constructed using the shock relationship:

$$\sigma - \sigma_{HEL} = \rho_{HEL} \ (U_s - u_{p_O}) \ (u_p - u_{p_O}) \qquad (48)$$

where σ_{HEL}, ρ_{HEL}, and u_{p_O} are the stress, density and the particle velocity at the elastic limit, respectively. The
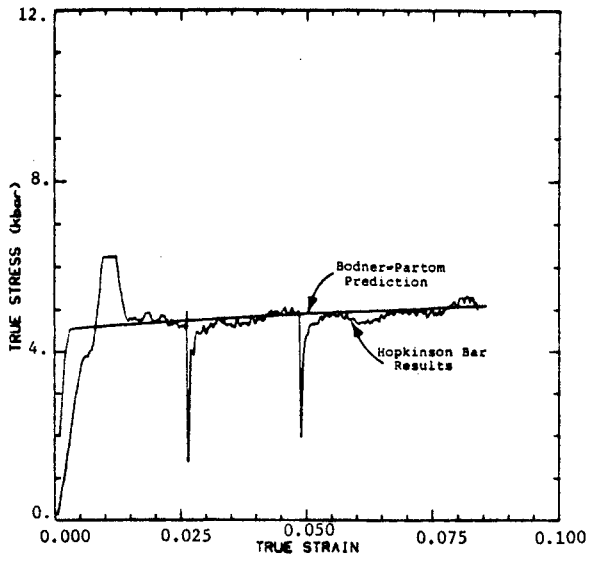
a. $\dot{\varepsilon}=300$ sec^{-1}
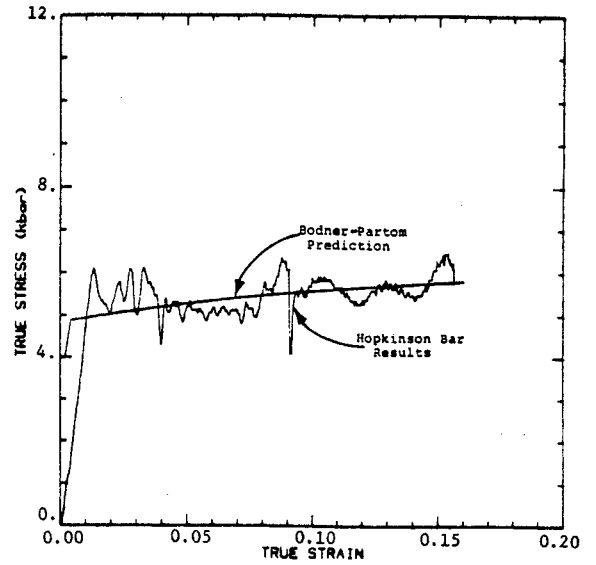
b. $\dot{\varepsilon}=600$ sec^{-1}
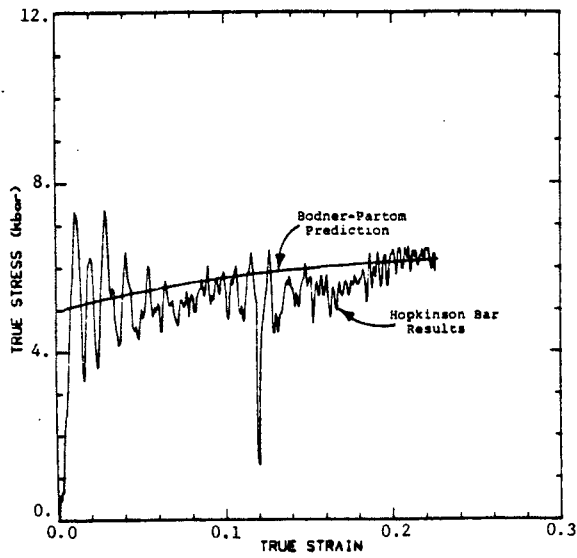
c. $\dot{\varepsilon}=800$ sec^{-1}
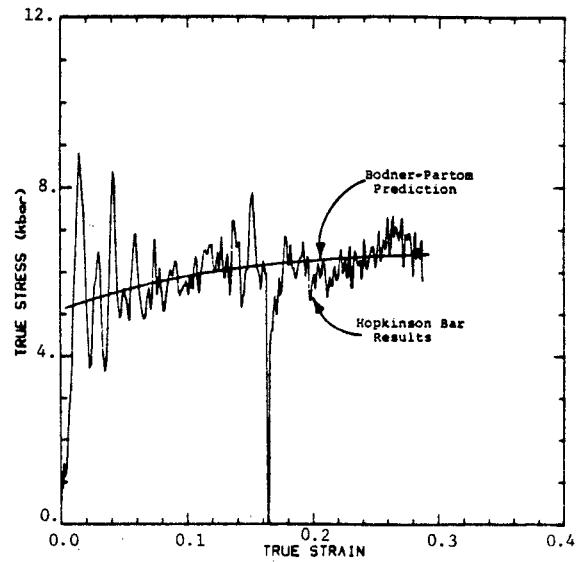
d. $\dot{\varepsilon}=1000$ sec^{-1}

Figure 93.   Bodner-Partom Predictions and the Original
Hopkinson Bar Results for Tensile SHB Tests
of C1008 Steel.

169
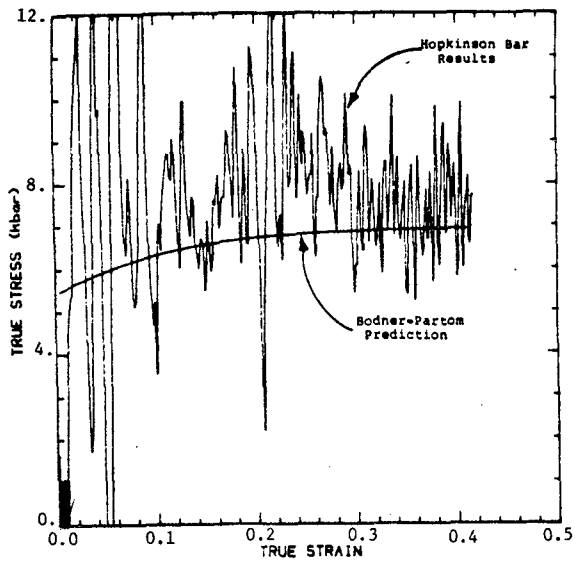
e. $\dot{\varepsilon}=1750$ sec^{-1}
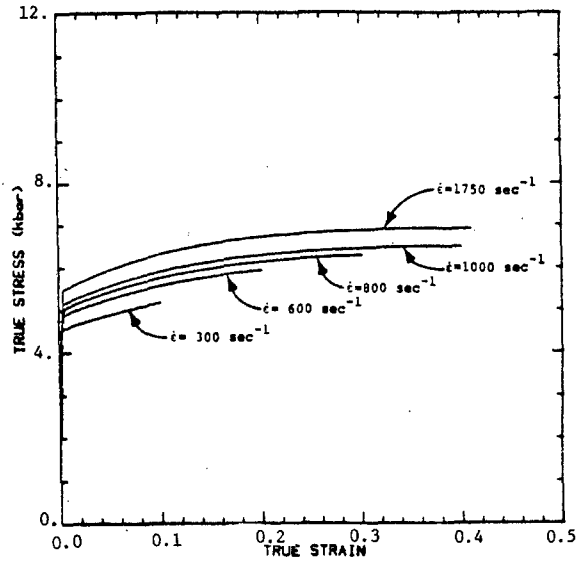
f. Bodner-Partom Results

Figure 93 (cont'd). Bodner-Partom Predictions and the Original Hopkinson Bar Results for Tensile SHB Tests of C1008 Steel.
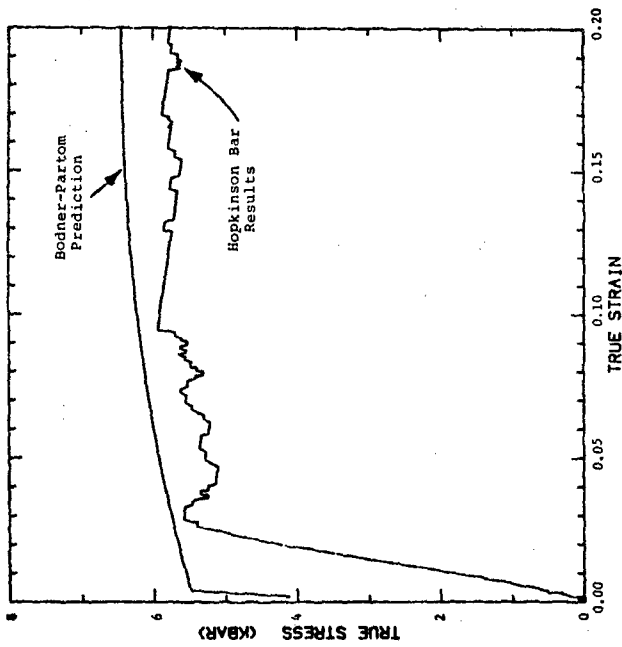
a. Low Strain Rate Range
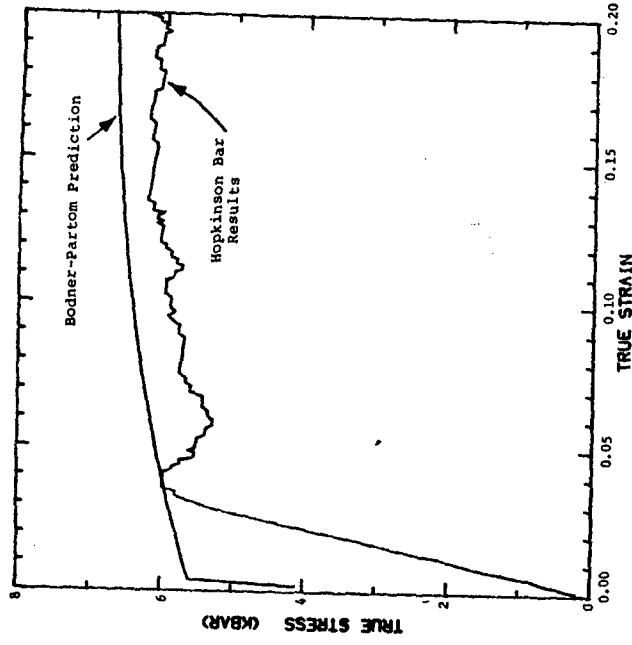
b. Mid Strain Rate Range

Figure 94. Bodner-Partom Predictions of the Dynamic Compressive Behavior of C1008 Steel.

171
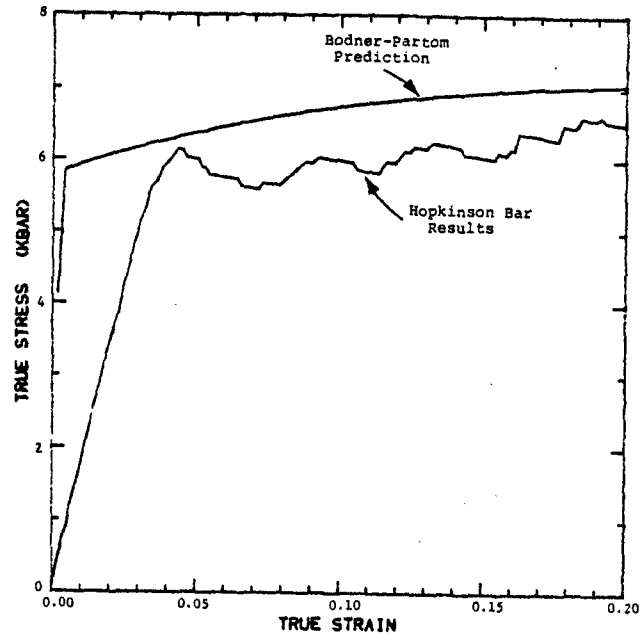
c. High Strain Rate Range

Figure 94 (cont'd). Bodner-Partom Predictions of the Dynamic
Compressive Behavior of C1008 Steel.
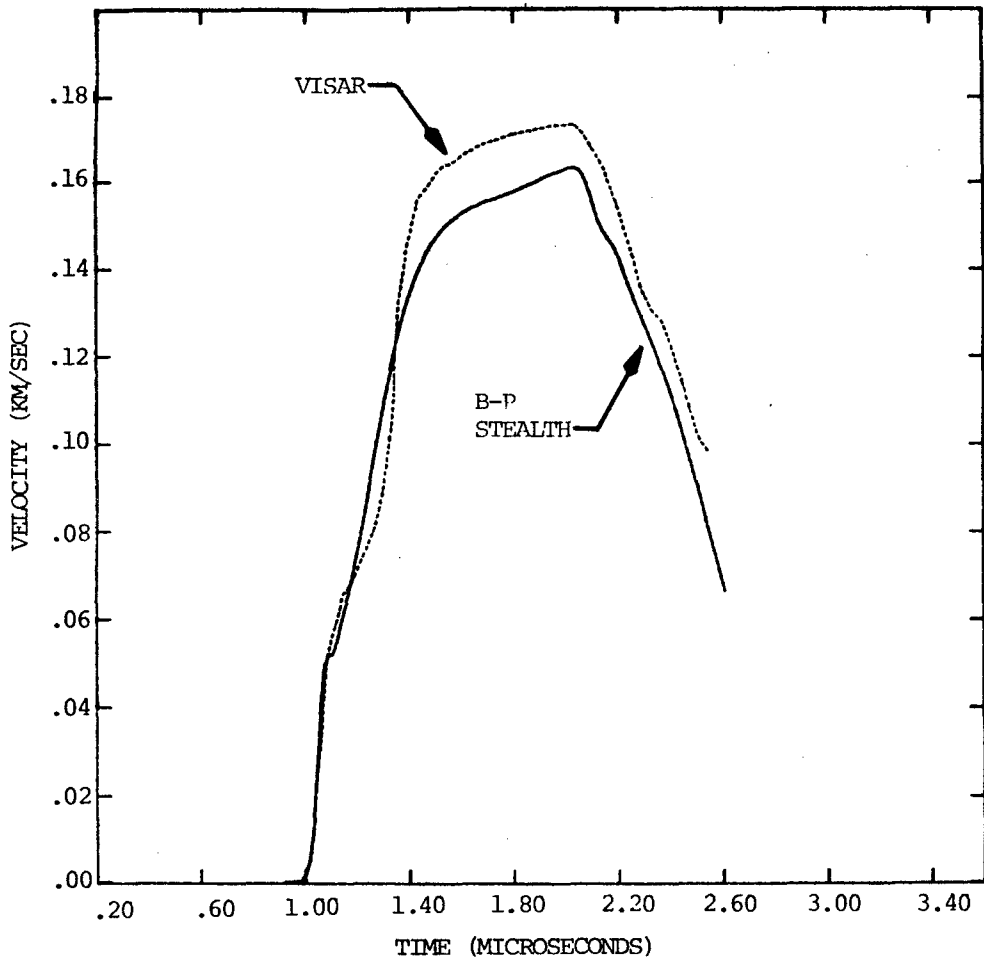
Figure 95.   Comparison of Velocity History Between
STEALTH with Bodner-Partom Routines and
VISAR Data (C1008 Steel).

173

diagram constructed for shot #678 is given in Figure 96. For the impact velocity of 178 m/s, the calculated peak velocity of the target's free surface was 0.163mm/μsec. It can be seen from Figure 95 that the velocity in the simulation ramps to the same peak velocity. The peak velocity of the VISAR plot was around 0.174mm/μsec. The difference between the theoretically obtained peak velocity and the VISAR can be attributed to uncertainty in the VISAR data reduction. Due to the discrepancy in the peak velocities, the release characteristics of the plots in Figure 95 did not match well; however, the slopes and the trends are very similar. It appears from these plots, that the VISAR data corrected to the theoretically predicted peak velocity, may compare well with the simulation.

To validate the BP-model constants further, shot # 685 (u_o = 134 m/s) was simulated and compared with the VISAR plot in Figure 97. The results were similar. The HEL was slightly underprecicted due to precursor decay. The ramped shock wave was reproduced. Additional experiments should be conducted with thin material to verify the shape of the ramped wave. This is a usual practice. Tests are needed to verify its reality and determine the impact conditions that give rise to its occurrence.

d.   HY100 steel

The constants of the Bodner-Partom constitutive model for the true stress-true strain behavior of HY100 steel are summarized in Table 9. Figure 98 contains the original Hopkinson bar results and the Bodner-Partom predictions for each strain rate level tested.

The constants of the Bodner-Partom constitutive model, derived from the Hopkinson bar tensile experiments, were used to predict the dynamic compressive true stress-true strain behavior. The predictions and the original Hopkinson bar data are shown in Figure 99. Rate dependency in the model is slight, and the agreement with predicted and measured flow stress is within 10 percent.
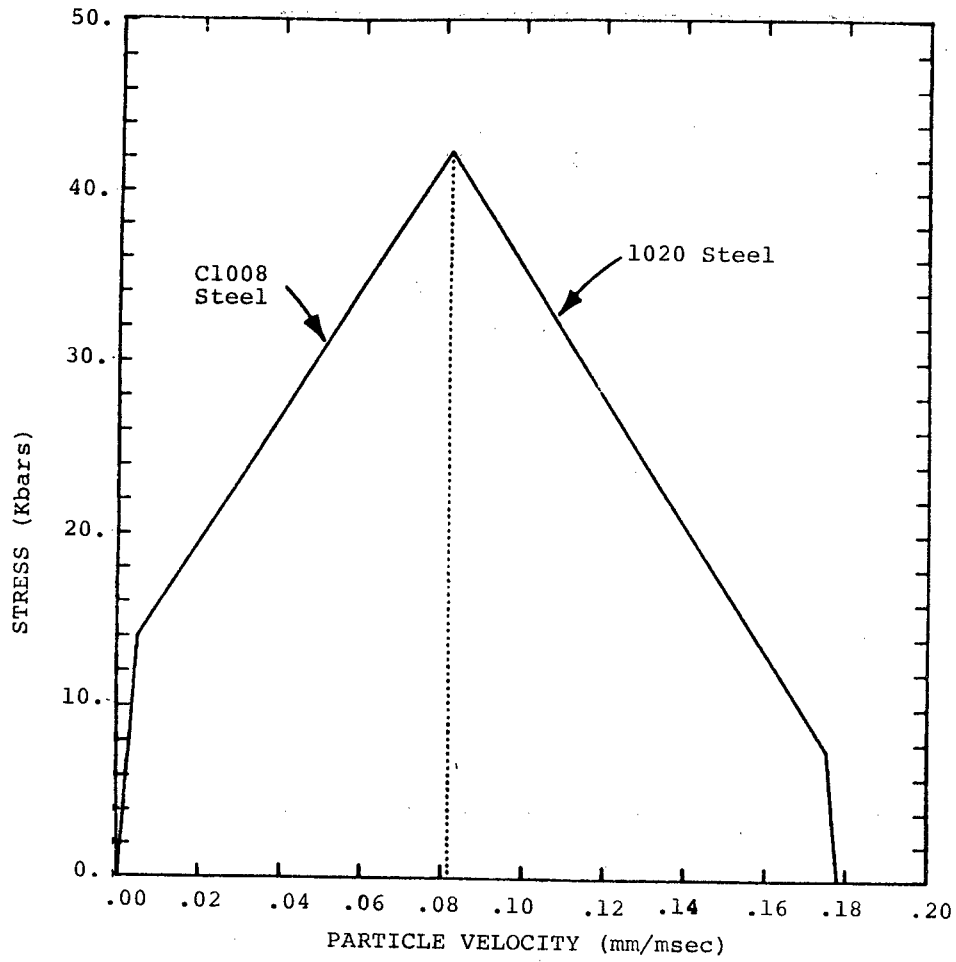
Figure 96.   Stress vs. Particle Velocity Diagram for
C1008 Target and 1020 Flyer Plate.
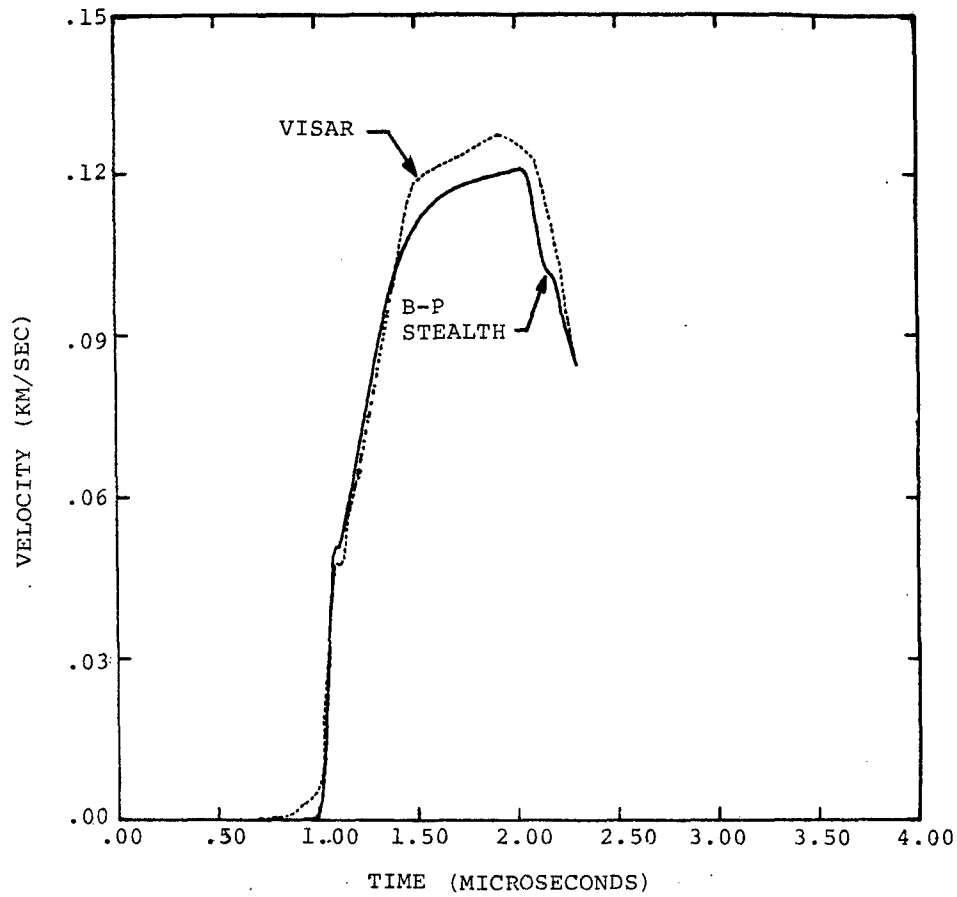
Figure 97. Comparison of Velocity History Between STEALTH with Bodner-Partom Routines and VISAR Data for C1008 Steel (Impact Velocity = 134 m/s).
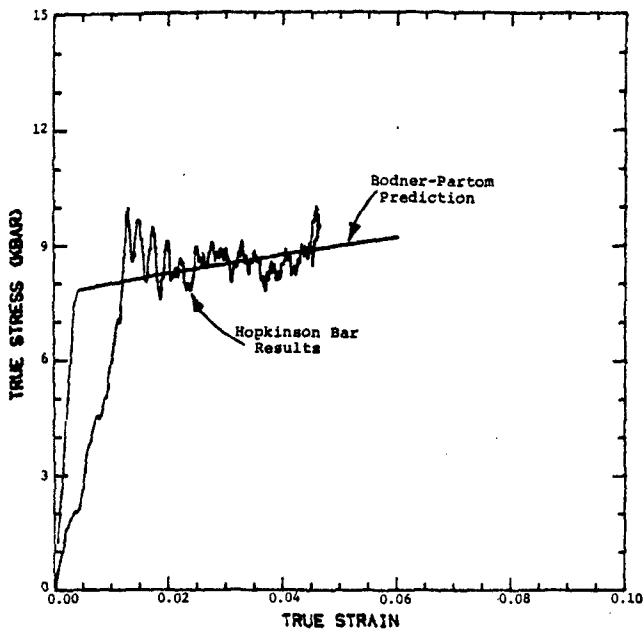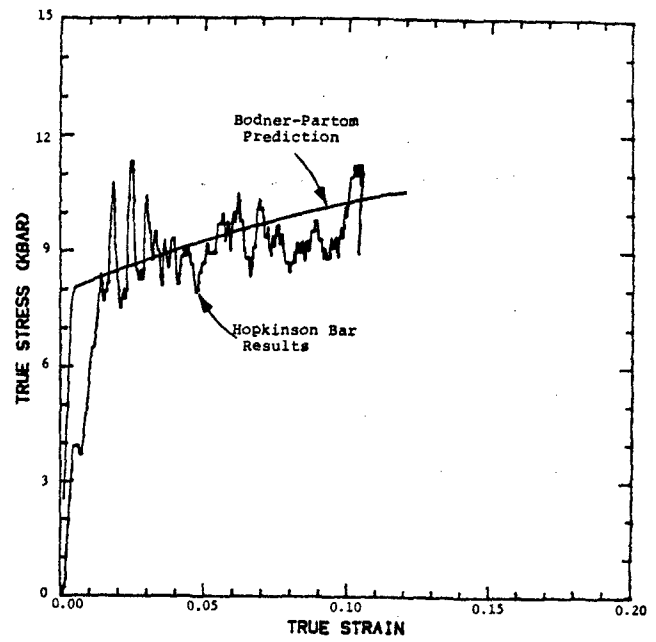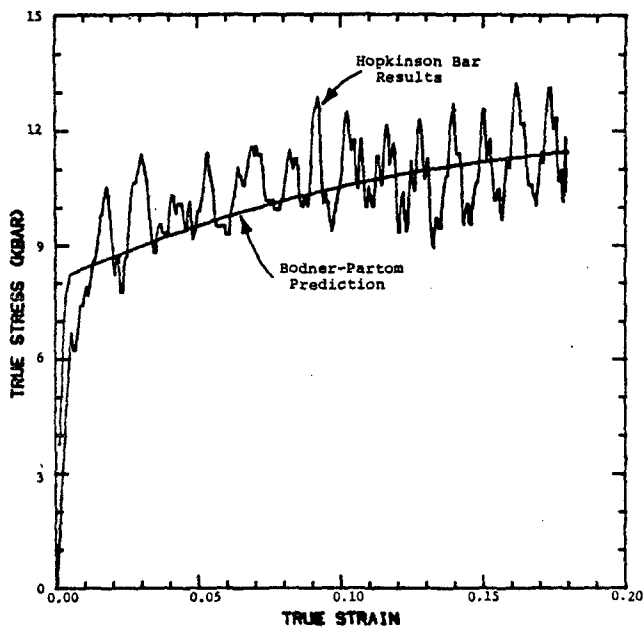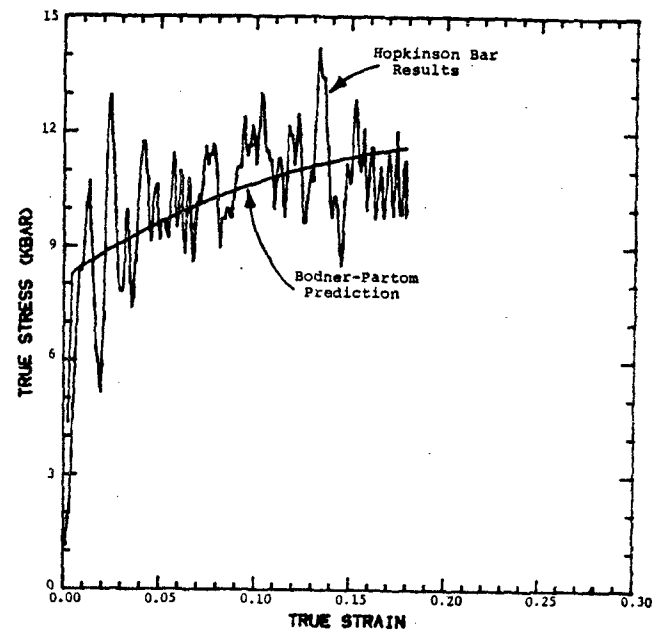
Figure 98.   Bodner-Partom Predictions and the Original
Hopkinson Bar Results for Tensile SHB Tests
of HY100 Steel.

177
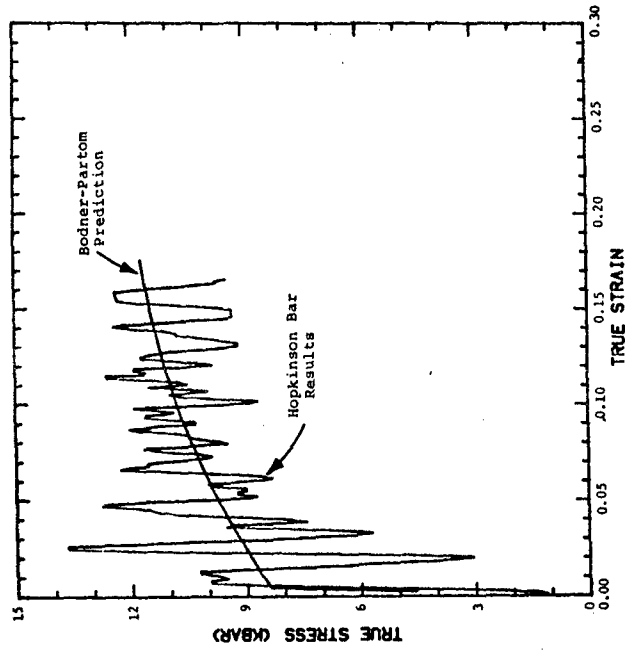
f. Bodner-Partom Results

e. $\dot{\varepsilon} = 1200\ \text{sec}^{-1}$
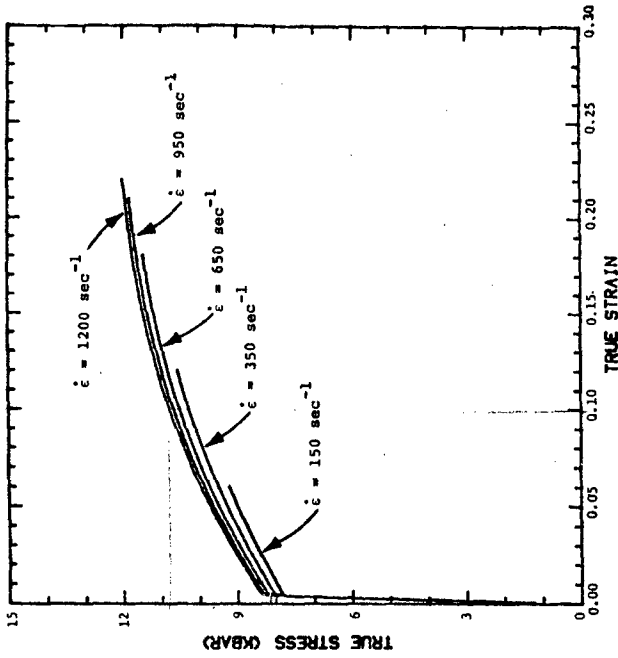
Figure 98 (cont'd).   Bodner-Partom Predictions and the Original
Hopkinson Bar Results for Tensile SHB Tests
of HY100 Steel.

178
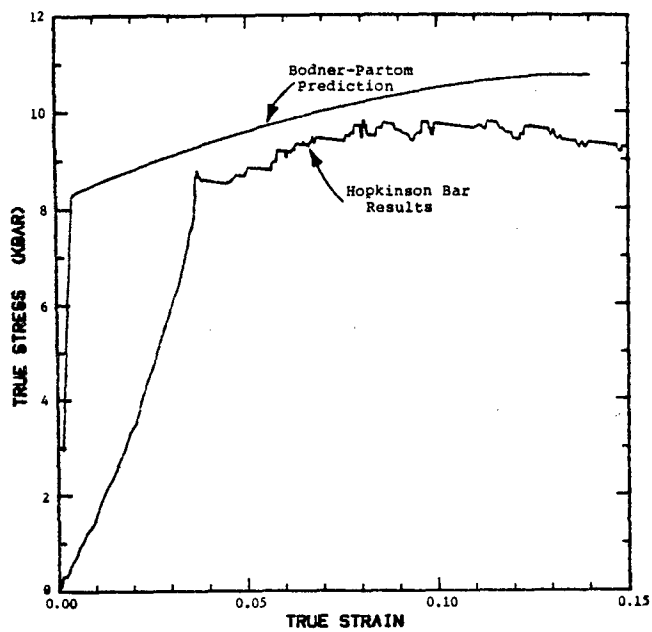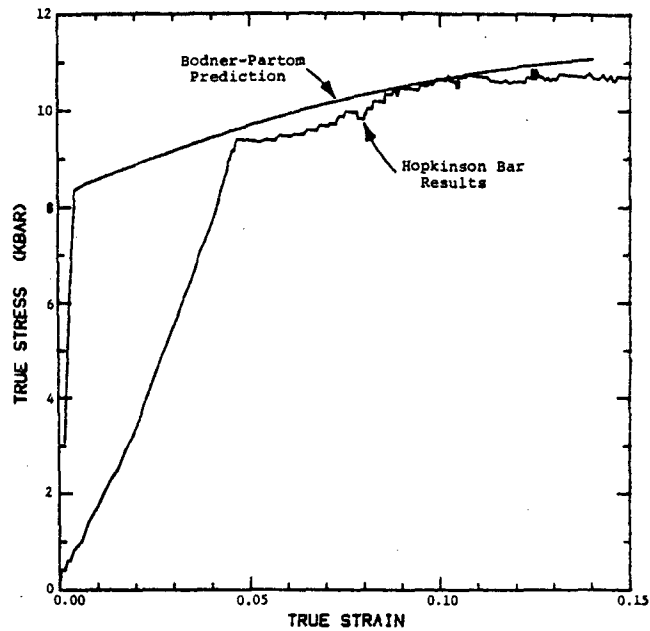
a. Mid Strain Rate Range   b. High Strain Rate Range

Figure 99.   Bodner-Partom Predictions of the Dynamic
Compressive Behavior of HY100 Steel.

179

The plate impact test of shot #680 was simulated with STEALTH with the same BP-model constants that were used in the SHB-test simulations. The impact velocity was 355 m/s. The simulated free surface velocity plot compared reasonably well with the VISAR plot as shown in Figure 100. The HEL and the release characteristics of these two plots match extremely well. The peak velocity in the simulation is within 10% of the observed value. Since theoretical estimation of the peak particle velocity using the equation (48) coincided with the velocity simulation, one believes that the difference may be caused by drift in the VISAR signal (e.g., slow change in fringe contrast).

e.   7039-T64 aluminum

The Bodner-Partom constants for 7039-T64 aluminum are summarized in Table 9. Figure 101 contains the original Hopkinson bar results and the Bodner-Partom simulations for each strain rate level tested. Since the material is relatively rate independent, n takes on a large value. Based on the tensile results, the Bodner-Partom model was used to predict results of compressive true stress-true strain measurements. The predictions and the original Hopkinson bar data are shown in Figure 102. The predictions are generally good and indicate little anisotropy in the material.

Shot #682 was simulated using the BP-model constants given in Table 9 for 7039-T64. The impact velocity was 375 m/s. The simulation is compared with the VISAR plot in Figure 103. The HEL, the rising portion beyond HEL, the peak velocity and also the release characteristics of the simulation compared extremely well with the VISAR. The accuracy with which both the SHB and plate impact test were simulated strengthens confidence in the values for the B-P constants and indicates the dependability of the modeling techniques.

3.4   SPALL FAILURE PARAMETERS

Spall damage is also a function of the amplitude of the tensile stress and the stress duration. Often experiments are
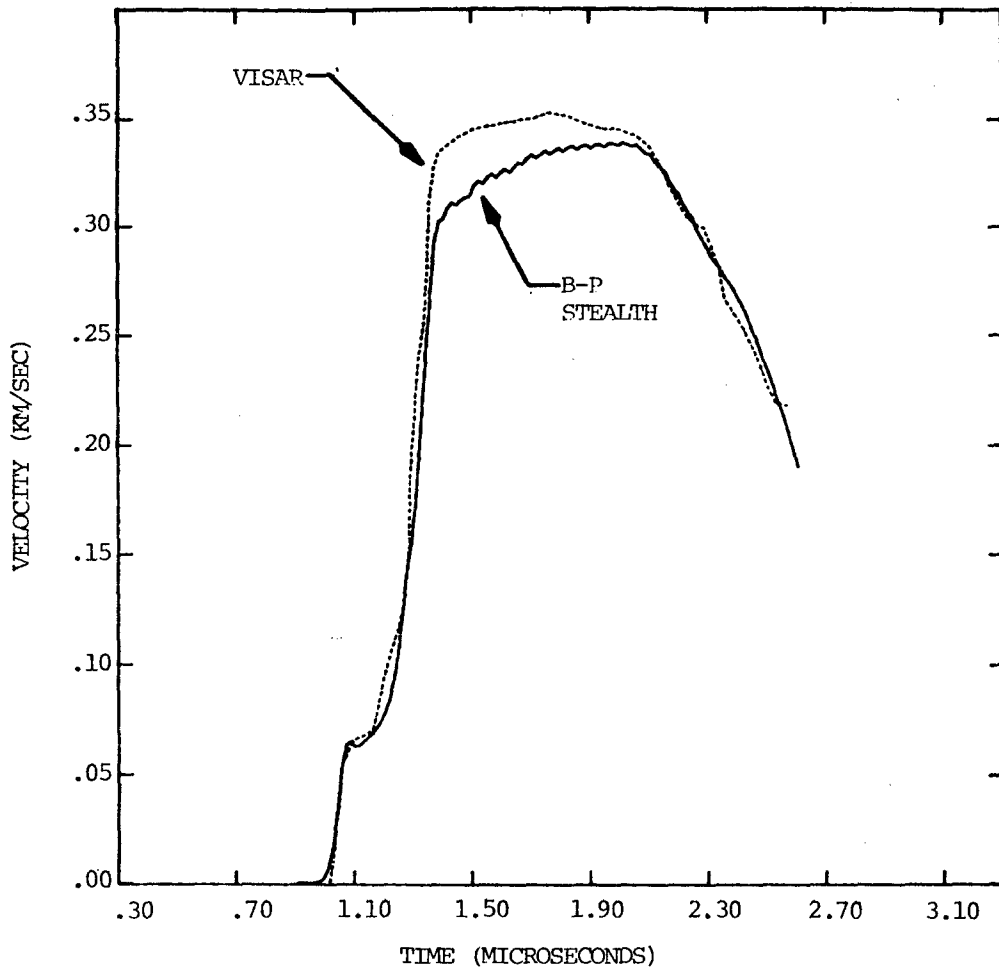
Figure 100.   Comparison of Velocity History Between
             STEALTH with Bodner-Partom Routines and
             VISAR Data for HY100 Steel.

181
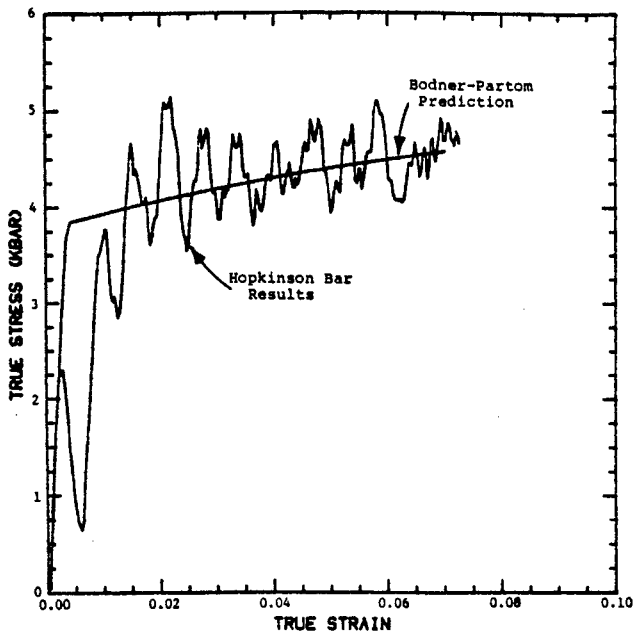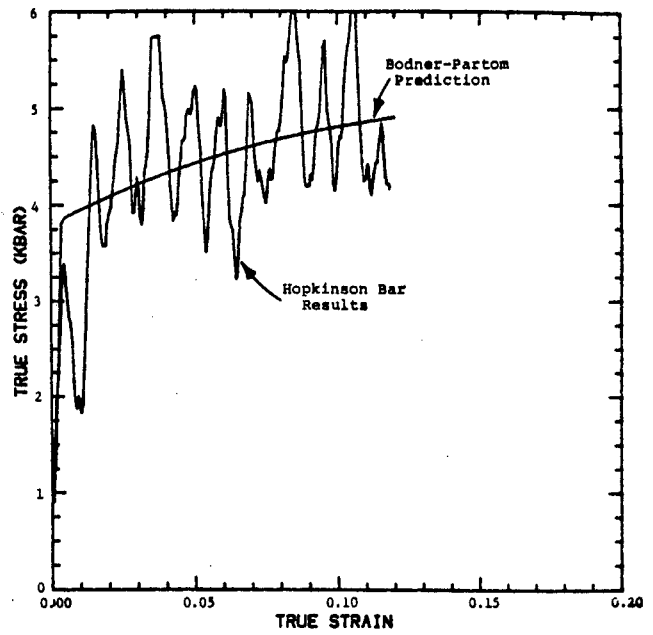
a. $\dot{\varepsilon}$=300 sec^{-1}

b. $\dot{\varepsilon}$=500 sec^{-1}
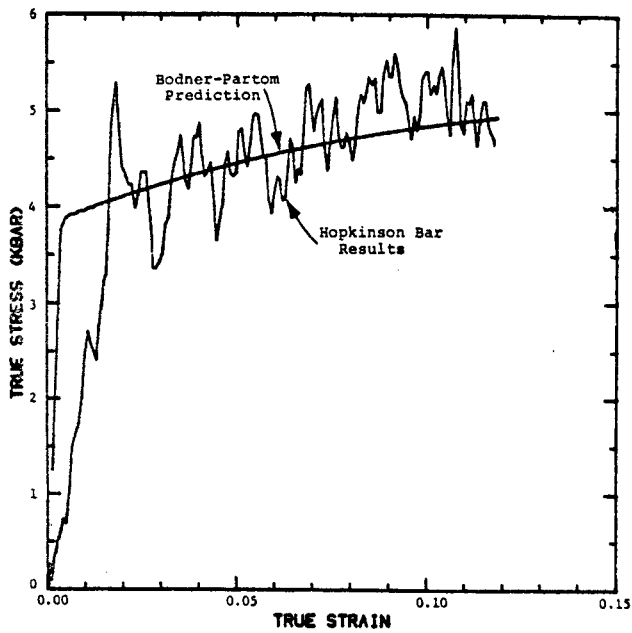
c. $\dot{\varepsilon}$=800 sec^{-1}
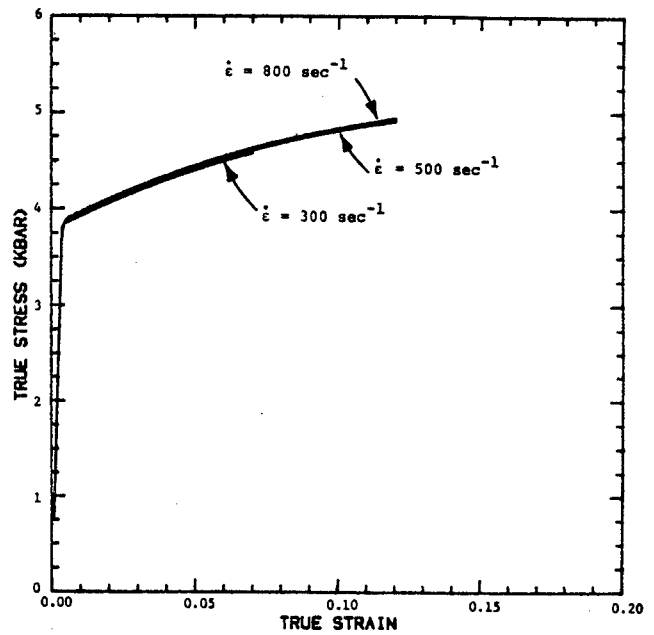
d. Bodner-Partom Results

Figure 101. Bodner-Partom Model Predictions and the Hopkinson Bar Results for Tensile SHB Tests of 7039-T64 Aluminum.

182
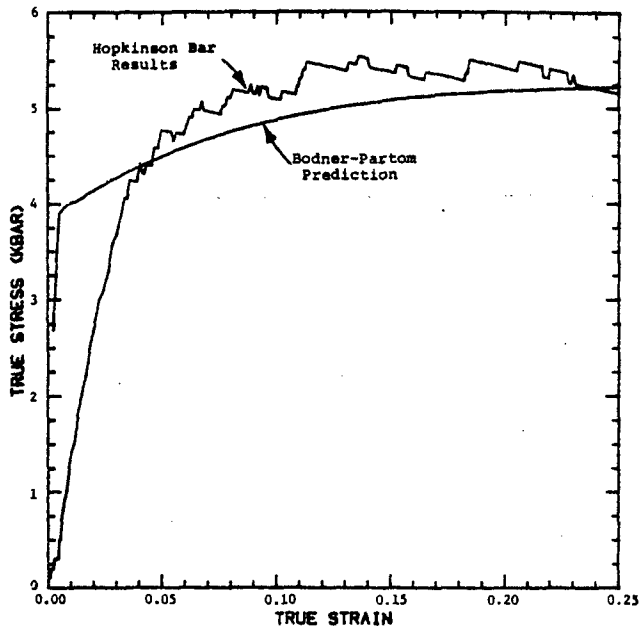
a. Low Strain Rate Range
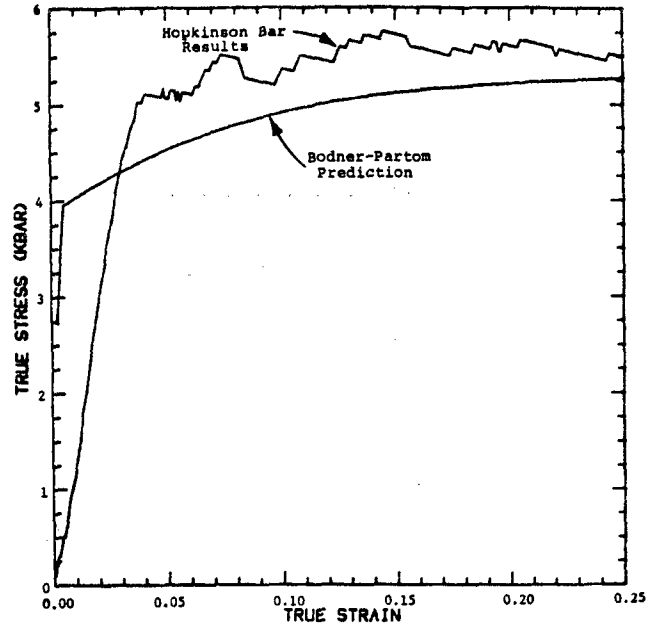
b. Mid Strain Rate Range
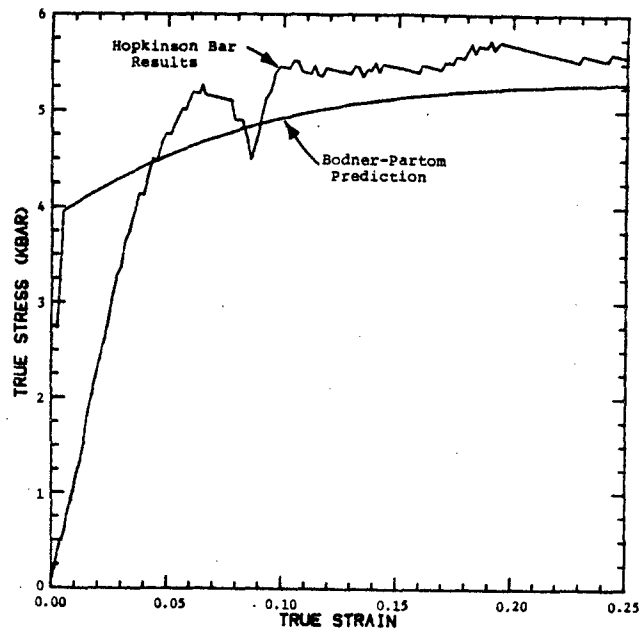
c. High Strain Rate Range

Figure 102.   Bodner-Partom Predictions of the Dynamic
Compressive Behavior of 7039-T64 Aluminum.
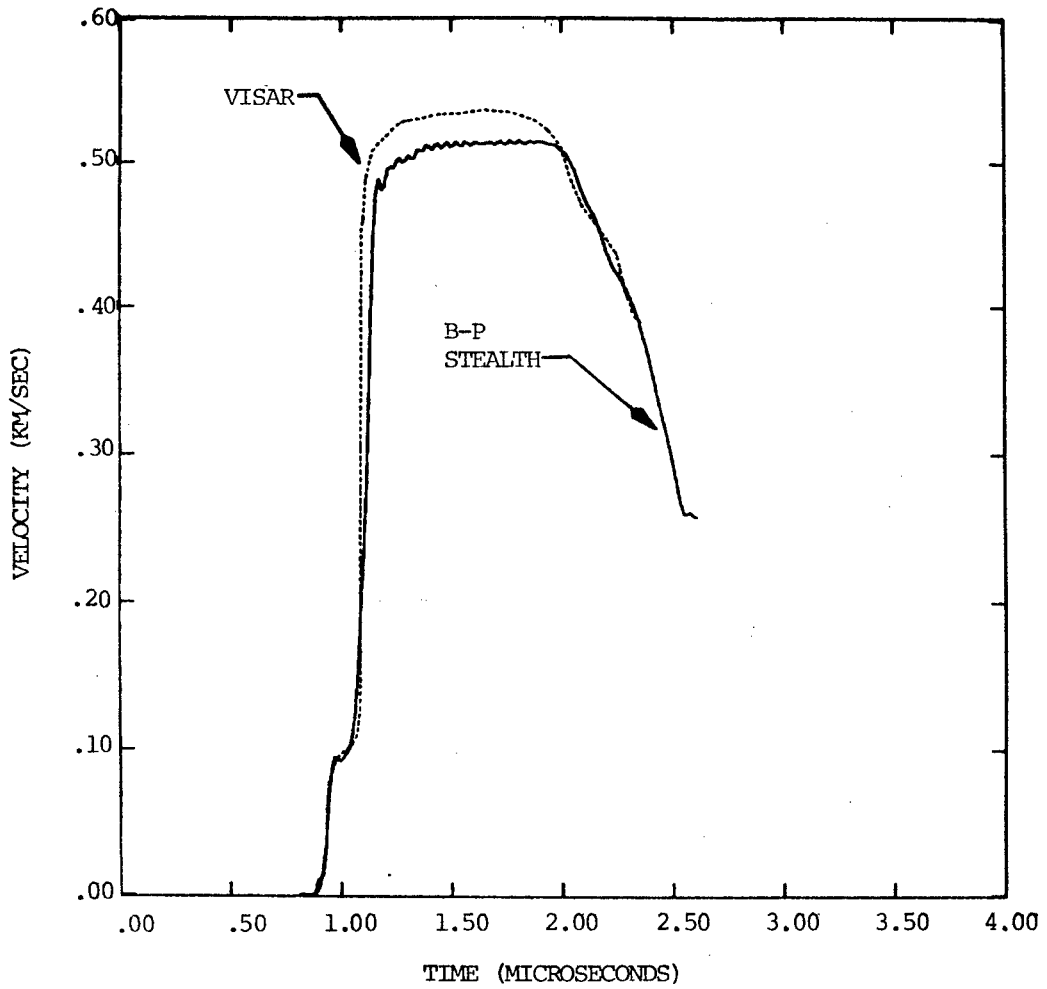
Figure 103.   Comparison of Velocity History Between
STEALTH with Bodner-Partom Routines and
VISAR Data for 7039-T64 Aluminum.

performed with various thickness flyer plates so that the amplitude/duration criterion for spall may be explicitly developed.

Thus, there are several different ways to specify spall criteria:

1. The spall stress, σ_s, given by equation (13). This stress probably represents the physical stress in the target associated with initial void formation. It is normally determined from experiments in which the spall is complete.

2. The peak tensile stress in a shot that causes incipient spall failure. This is a function of the tensile pulse duration. It is plausible that for thick enough flyer plates, this stress would be equal to σ_s, although that has not been experimentally verified. For steels, there is relatively little change in this stress for flyer plates 3mm thick or greater.

3. The spall parameter that predicts spall damage in elementary numerical models which treat spall fracture as instantaneous. When the spall threshold is greatly exceeded, the numerical models become more accurate, since spall is very rapid. However, for near threshold conditions, the model parameters do not correspond to physical stresses, since the actual mechanics of spall damage (i.e., gradual void growth and coalescence) is not described by the model. The spall models used in SWAP, STEALTH, and most practical finite difference codes are in this category.

Table 1 lists several spall criteria. The first four columns give parameters that correctly describe spall when used with simplified material models. Those values are recommended for numerical simulations. The last column is the estimate of the most tensile stress that the material can actually sustain. These

185

are the only values that represent material properties. They should be used in developing theories for void nucleation, growth, and coalescence.

Present efforts were not focussed on modeling the spall failure through application of the Bodner-Partom constitutive model. Instead, for engineering applications, two spall criteria were selected to simulate a plate impact test in which the target plate was partially spalled. A simple material model based on elastic-perfectly plastic material behavior was used with the experimentally obtained Y_O for describing the flyer and target plates. The first criterion was time independent and based on a critical spall stress. When the tensile stress reaches a critical level σ_c, the spall fracture occurs instantaneously. The second criterion was time dependent and based on a critical level of damage. The Tuler and Butcher (Reference 47) formulation was employed. The criterion was given by:

$$K_\lambda = \int (\sigma - \sigma_O)^\lambda \, dt \qquad (49)$$

$$K_\lambda \geq K_{\lambda c} \quad \text{For spall} \qquad (50)$$

where K_λ, σ_O and λ are fracture parameters. According to this model, there is a minimum normal stress, σ_O, at which spall can occur. At $\sigma = \sigma_O$, the tensile stress must be applied for an infinitely long time for a spall plane to form. When $\sigma > \sigma_O$ spall can occur even for a short pulse duration, depending on the impact velocity and the thickness of the flyer plate. For large values of $(\sigma - \sigma_O)$ spall takes place very rapidly and the time dependence is less manifest. Under such circumstances it often turns out that spall can be described by a single spall stress σ_c, thus, the first criterion may be sufficient, according to Zukas (Reference 1), Bertolf et al., (Reference 48), and Bless and Paisley (Reference 46). The Tuler-Butcher model was programmed into both STEALTH and SWAP as a user supplied failure criterion.

a. <u>1020 steel</u>

Bless (Reference 19) has presented a discussion on the spall fracture of this steel. In his work, spall parameters were evaluated through SWAP (Reference 49) and HULL-code simulations. The present work used the value for Y_o (=4.6 Kbar) as reported by Bless (Reference 19). The shot #529 was simulated through STEALTH. The critical spall stress and the Tuler-Butcher criteria were used in the evaluations of the spall parameters. The simulations and the VISAR data are compared in Figure 104. Figure 105 shows the rapid fall of stress preceding fracture on the spall plane. The value of 2 was assumed for the λ as reported by Bless. The threshold stress σ_o in the Tuler-Butcher model was assumed to be the σ_{HEL}. The K_λ was calculated so that the arrival time of the spall signal in the simulation matches the experiment. K_λ = 14 Kbar - μs was found to be the best value.

A more complete evaluation of the Tuler-Butcher parameters was conducted with the SWAP code. Many calculations were performed for flyer plate thicknesses between 0.25 and 2mm. Like STEALTH, SWAP does not provide for growth of damage. Therefore, it is inconsistent to use this code to calculate complete spall, since the material properties on the spall plane are affected by cracks that open before complete separation takes place. Instead, the code was used to calculate an incipient spall criterion. Fracture was suppressed, and values of K were computed for impacts that lie on the no spall/spall threshold. The best agreement between K-contours and the observed damage threshold was for $\lambda = 2$, $\sigma_o = -10$ Kbar, and $K_{crit} = 125$ Kbar^2 μs. The curve for these values is drawn in Figure 56. It was calculated with d = 2mm, D = 5mm; d = 1mm, D = 5mm; and d = 0.5mm, D = 2mm; thereby encompassing a slight dependence on target thickness. For example, at d = 1mm, the predicted threshold for D = 2.5mm is about 20 m/s lower than the curve as drawn.

The Tuler-Butcher parameters used in Figure 56 are relatively unique. Smaller values of σ_o result in curves that rise too steeply for thin flyer plates, while larger values are
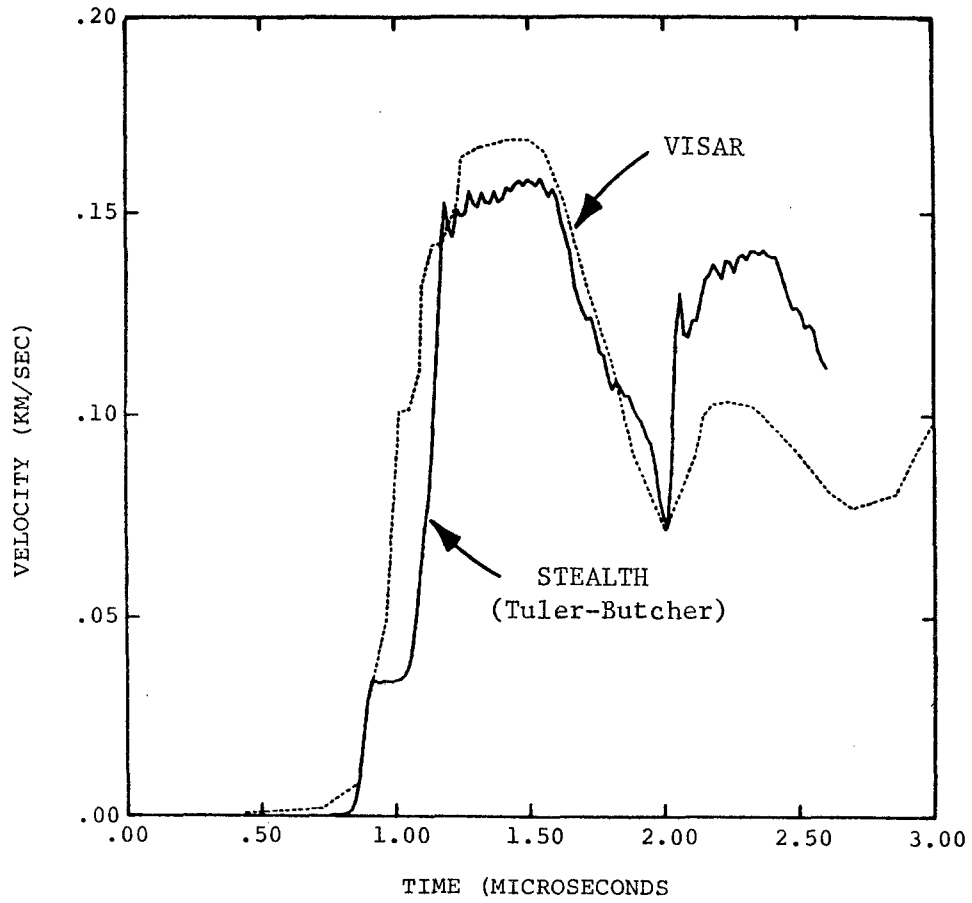
Figure 104.   Spall Simulation for 1020 Steel Target and
Flyer from STEALTH using Tuler-Butcher Spall
Model is Compared with VISAR Data.
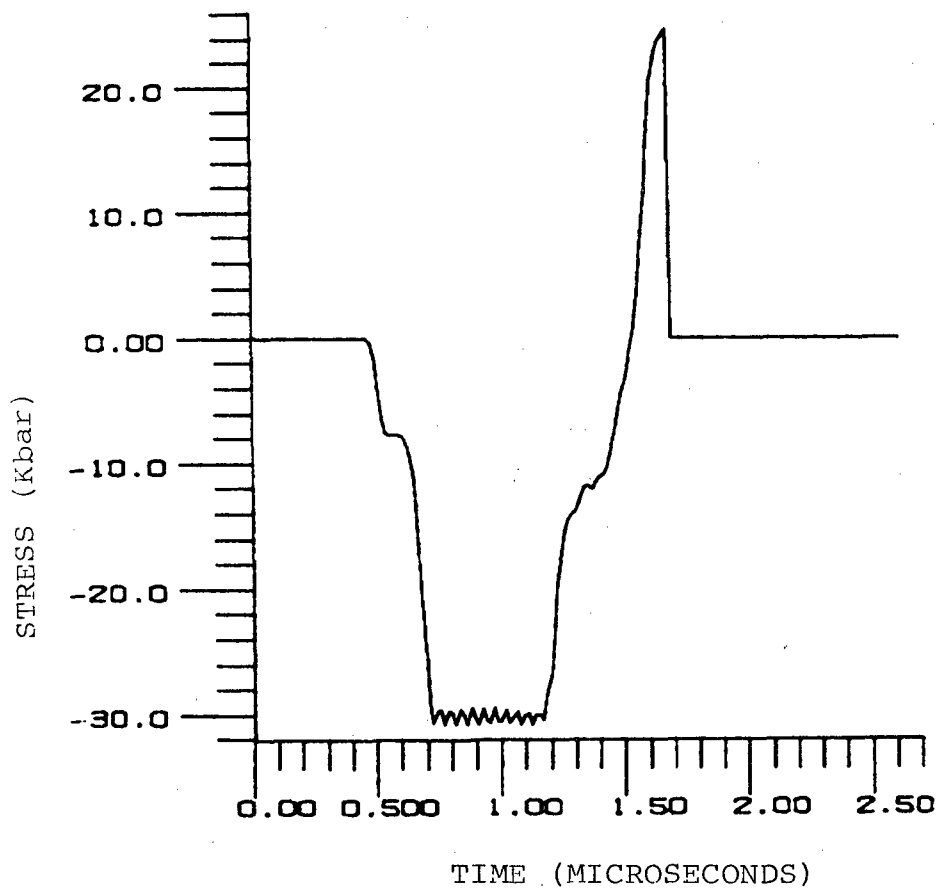
Figure 105.   Stress History at the Spall Plane from
              STEALTH Simulation of Shot No. 529
              (1020 Steel).

inconsistent with shot 553. Curves with $\lambda = 3$ also rise too steeply as d decreases.

SWAP was used to calculate K on the spall plane for overdriven spall for shots 13, 24, 63, and 223 (Reference 19). Values of K were computed up to the genesis of the spall signal. These values were consistently about one-half K_{crit} in agreement with the STEALTH calculation. However, the discrepancy in K values for threshold and overdriven spall is probably of little practical importance. The delay in the genesis of the spall signal, if spall is assumed to occur at $K = K_{crit}$ is only about 20 ns. This is comparable to the uncertainty in wave arrival times that is caused by the assumption of perfectly elastic/plastic behavior embedded in SWAP.

While the Tuler-Butcher model can be used to predict spall, it is probably not physically correct. The spall data indicate that void nucleation begins at $\sigma_s = 17$ Kbar, not 10 Kbar in the plate impact tests (see Section 2.3.3 a). The spall signals show the σ_s increases with impact velocity.

b.   OFHC copper

Bless et al., (Reference 6) summarized the available spall results on fully annealed copper. A STEALTH simulation of their test No. 560 was carried out (4mm flyer, 6mm target, impact velocity 209 m/s). The spall parameters for the two criteria were obtained from the simulation. The simulations and VISAR data are compared in Figure 106. The corresponding values are given in Table 10. The σ_o value was assumed to be equal to the Hugoniot stress 3.6 Kbar, and λ was arbitrarily assigned a value of 2. The value for K_λ in equation 49 was obtained by matching the arrival times of spall signals in the simulation and test.

It was found that the spall stress computed from equation 13 was always between 11 and 12 Kbar. A much higher value of spall strength, 31 Kbar, was required to obtain agreement between velocity profiles calculated with SWAP and observed with the VISAR for shots well above the spall threshold.

190
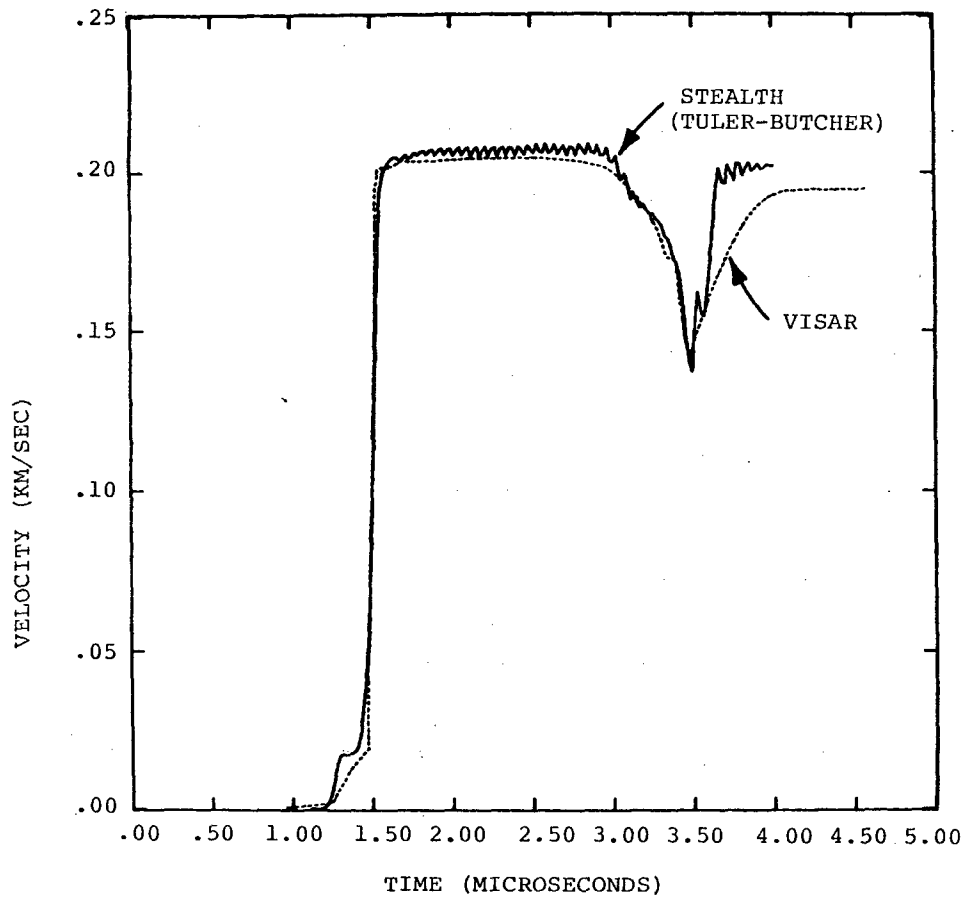
Figure 106.   Spall Simulation ·for OFHC Copper Target and
1020 Flyer from STEALTH Using Tuler-Butcher
Spall Model as Compared with VISAR Data.

191

TABLE 10

CRITICAL SPALL STRESS AND
TULER–BUTCHER MODEL PARAMETERS

Material	TULER–BUTCHER MODEL			SIMPLE SPALL MODEL	ACTUAL SPALL STRESS
	σ_o (Kbar)	λ	$K_{\lambda c}$	σ_c (Kbar)	σ_s (Kbar)
1020 STEEL	10	2	12.5	30	17
OFHC	3.6	2	10.0	24.7	13
C1008	14.0	2	0.38	20.0	18
HY100	15.7	2	61.0	56.8	27
7039–T64	8.6	2	3.0	18.2	13

A constant spall stress model in SWAP could not explain observations near the spall threshold (Reference 46).

Several SWAP calculations were conducted to match the observed variation of critical impact velocity with flyer plate thickness (Reference 6). The variation of the spall threshold with flyer plate thickness could be described with a Tuler-Butcher model with $\lambda = 2$ and $\sigma_o = 7.5$ Kbar.

As noted previously, the spall signal in 1020 steel appeared to be associated with void nucleation. If that is true for OFHC copper also, and if the spall develops gradually, then the interpretation that 11 Kbar is the stress at which damage initiates may be physically correct. However, when using a computer code in which complete rupture occurs instantaneously, accurate predictions of threshold are obtained with the derived Tuler-Butcher parameters, and predictions of spall signals for high impact velocities are obtained with a spall stress of 31 Kbar. These results are discussed more extensively by Bless and Paisley (Reference 46).

An error in the SWAP-based Tuler-Butcher predictions was revealed during experiments with double flyer plates (described in Section 2.4.1). In those experiments, aluminum flyer plates and copper targets were employed. SWAP simulations were used to predict spall in the copper. However, it was found that the Tuler-Butcher parameters given above substantially underestimated the impact velocity required to cause damage. The cause of this discrepancy has not yet been resolved. It may be related to the strain rate on the spall plane. The strain rate varies when a given peak stress value is obtained by changing flyer plate materials and velocities. Strain rate does not explicity appear in the Tuler-Butcher formulation. Therefore, the spall criterion for OFHC copper must be used with caution for situations that differ greatly from those in the copper/copper plate impact experiments.

c.   <u>1008 steel</u>

The 3mm thick flyer plates induced spall
(defined as 50 percent voids in the spall plane) at a critical
velocity of 168 m/s. This corresponds to a stress of 31 Kbar.
However, σ_s, was found to be 18 Kbar. A STEALTH simulation of
shot 678 reproduced the observed spall signal with a simple stress
model with σ_s = 20 Kbar. These observations suggest that in these
three shots, spall developed over a finite period of time. The
spall signal is associated with void nucleation, and this takes
place at about 20 Kbar.

A STEALTH simulation was also made with the
Tuler-Butcher model for test 678. The exponent λ was assumed to
be '2', as for 1020 steel. The stress σ_o was set equal to σ_{HEL},
14 Kbar. The parameter K_λ was adjusted in the simulations until
the experimental results were matched. The calculated free
surface velocity of the target is compared with the VISAR data in
Figure 107. The corresponding stress history at the spall plane
is also shown. When $K_\lambda = K_{\lambda c}$, spall occurred and the stress in
the spall plane was instantaneously set to zero in the
simulation. The free surface velocity history and spall plane
history from these two models are almost identical as can be seen
from Figure 107. Neither model precisely predicts the post spall
behavior, but they are probably accurate enough for most
engineering applications. Since the simple spall criterion is
easier to use than the Tuler-Butcher model, it is recommended.
However, it must be remembered that these models do not describe
damage development. Their utility is for prediction of the onset
of tensile failure. The value of $K_{\lambda c}$ was only 0.38 Kbar^2 μs.
Thus, the material spalled very near σ_o. Probably, the Tuler-
Butcher model would have worked equally well with $\sigma_o = \sigma_s = 18$
Kbar, since the stress on the spall plane falls extremely rapidly
when the release waves arrive.

The Tuler-Butcher fracture parameters
estimated from simulations of shot 678 were used to simulate test
#687 which was at a lower impact velocity (u_o = 134 m/s). The
VISAR traces for shot 687 indicated a "spall signal". The

678: STEALTH
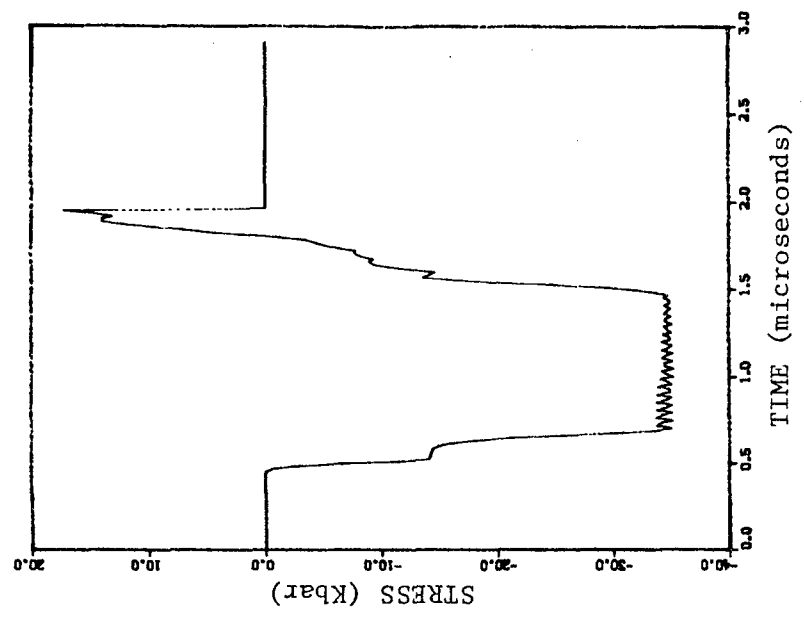
678: VISAR, STEALTH
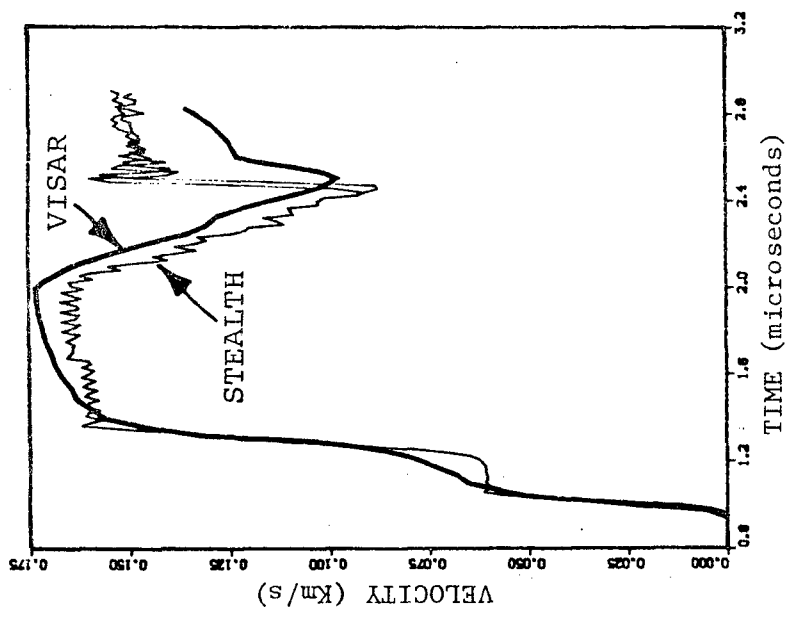
Figure 107. (a) Spall Predictions by the Two Failure Criteria Compared with VISAR.
(b) Stress History at the Spall Plane - Code Predictions - Cl008 Steel.

195

STEALTH simulation reasonably reproduced these features, as shown in Figure 108. Metallographic and SEM examination showed the damage in shots 685 and 687 (same velocity) consisted of isolated voids, rather than complete spall. In summary, based on these limited data (only one thickness flyer plate), spall initiation can be described by a simple spall stress , σ_s = 20 Kbar, or a Tuler-Butcher model with λ = 2, σ_o = 15 Kbar, and K_{crit} = 0.38 Kbar^2 μs. Complete rupture on the spall plane requires a stress of 31 Kbar if damage development is not simulated. However, the value of the stress actually associated with void formation is probably 18 Kbar.

d. HY100 steel

A STEALTH simulation of test #680 on HY100 was carried out with the two spall criteria. The overlapping results are shown in Figure 109. The critical spall stresses and the Tuler-Butcher fracture parameters that were assumed in these simulations are given in Table 10. The σ_o value was assumed to be equal to the Hugoniot stress, σ_{HEL} obtained from the plate-impact tests. (Preliminary values were used that differ slightly from those of Table 2.) The λ was arbitrarily taken to be 2. The values of the critical damage parameter, $K_{\lambda c}$ are adjusted to predict the experimental results.

e. 7039-T64 aluminum

The test #682 on 7039-T64 was simulated through STEALTH with a simple material model. The elastic-plastic models with Y_o = 4.6 for the flyer (1020 steel) and Y_o = 4.2 for the target (7039-T64), were used in the simulation. Since the release characteristics depend only on the Y_o, the VISAR and the simulation compare extremely well in Figure 110. Two spall criteria were used in the model calibration. The critical spall stress (σ_s) and the Tuler-Butcher fracture parameters that were assumed in the simulations are given in Table 10. The σ_o value was assumed to be equal to σ_{HEL}. For aluminum, λ was also arbitrarily taken to be 2. The value of the critical damage parameter, $K_{\lambda c}$ was adjusted to predict the experimental results.
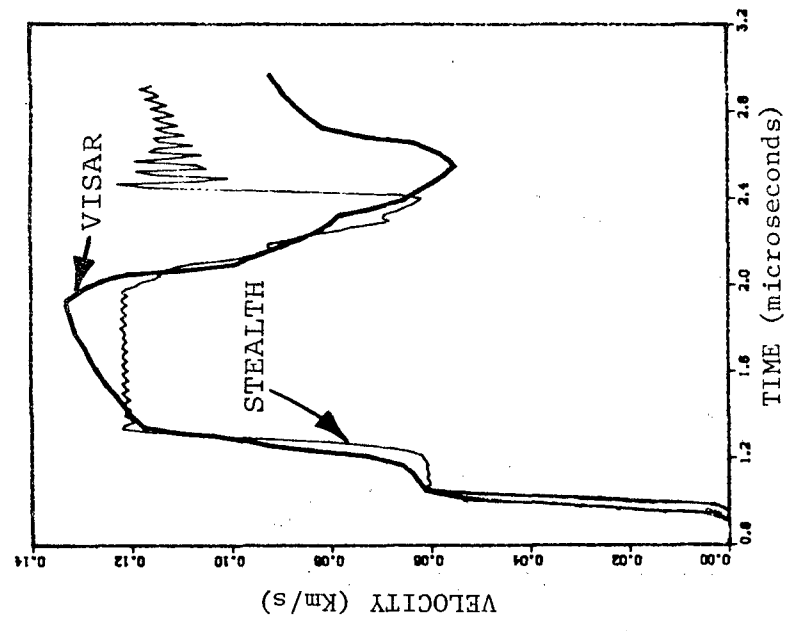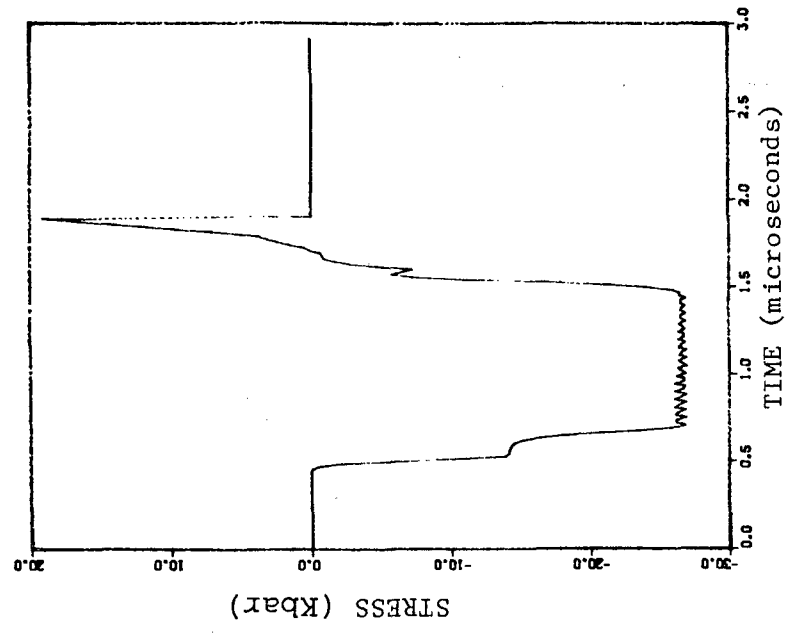
Figure 108. (a) Spall Prediction using the Tuler-Butcher Model compared with VISAR.

(b) Stress History at the Spall Plane - Code Prediction - C1008 Steel.
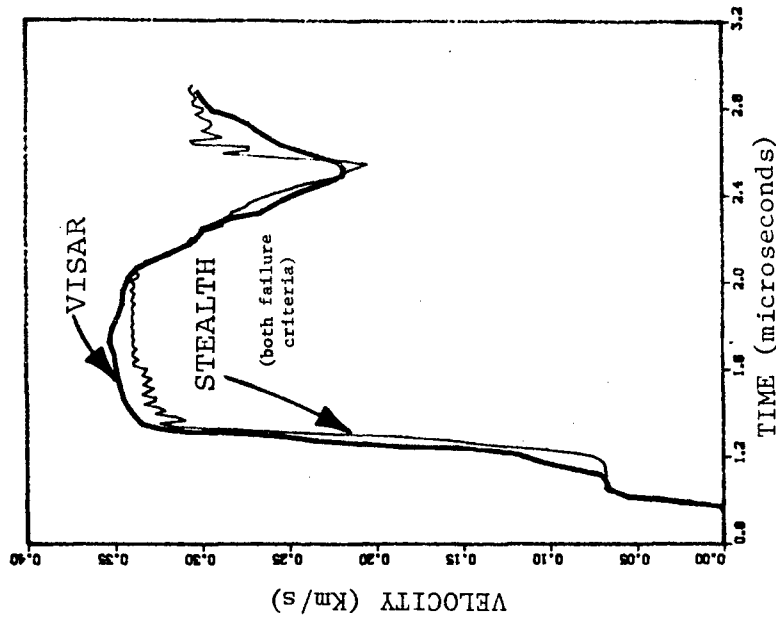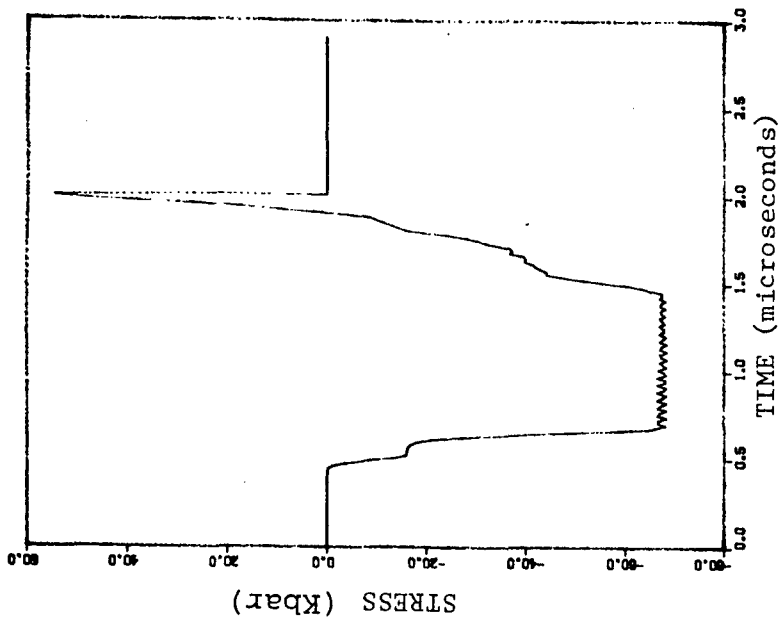
Figure 109. (a) Spall Predictions by the Two Failure Criteria Compared with VISAR.

(b) Stress History at the Spall Plane - Code Predictions - HY100 Steel.

682: STEALTH

682: VISAR, STEALTH
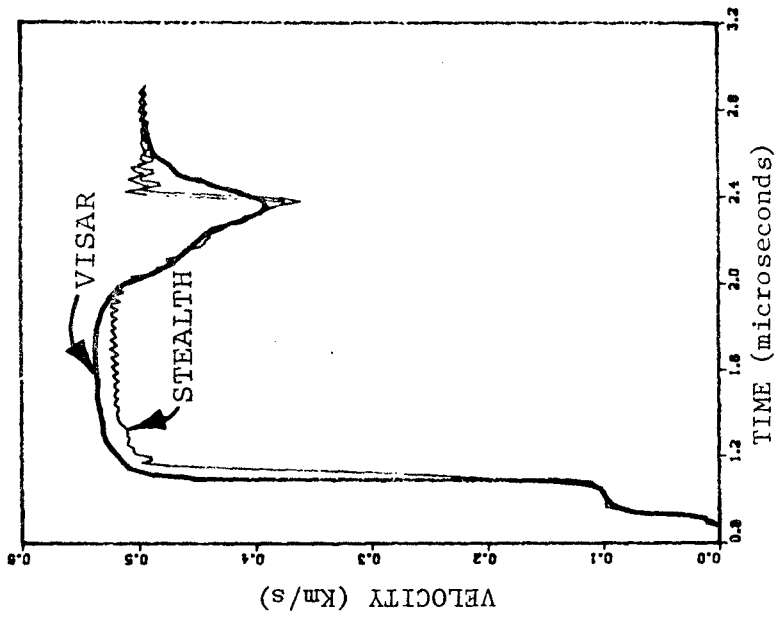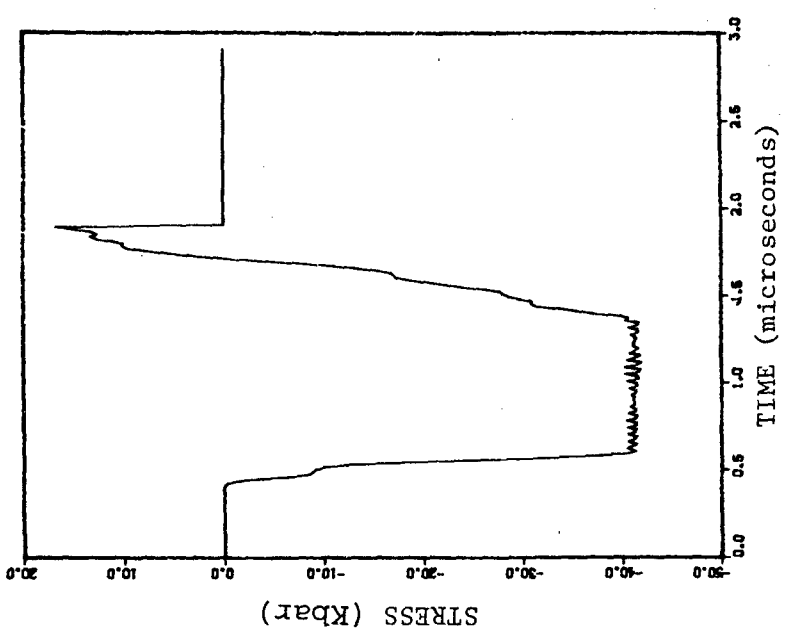
Figure 110. (a) Spall Predictions by the Two Failure Criteria Compared with VISAR.

(b) Stress History at the Spall Plane - Code Predictions - 7039-T64 Aluminum.

Though the VISAR data are well matched in these predictions, the estimated fracture model parameters are probably not unique and may lack generality. (Experiments would need to be conducted with other flyer plate thicknesses to check this point.) In these models, failure is assumed to occur almost instantaneously. Models which predict failure successfully under high impact velocity conditions often cannot predict failure under threshold conditions (Reference 19). Zukas (Reference 1) has documented well the varying nature of several other failure models and their inherent inadequacies in supporting numerical investigations of impact events.

SECTION 4

SUMMARY

High strain-rate material characterization was carried out for 1020, C1008, and HY100 steels, OFHC copper, 7039-T64 aluminum, and BeO ceramic. Tests were conducted under (1) uniaxial stress (compression and tension); (2) triaxial stress (necking specimen); and (3) one dimensional strain conditions. Split Hopkinson bar tensile and compression tests were used to achieve uniaxial stress states. High speed photography of necking SHB tensile test specimen provided data under triaxial stress states and large strain conditions. Plate impact tests were used to achieve one dimensional strain conditions. Table 11 summarizes the principal diagnostics, conditions and the experimental parameters involved in these three test configurations.

The wide range of experimental data obtained from the various tests were used for high strain-rate material modeling. The state-variable-based visco-plastic theory of Bodner and Partom was used to describe material behavior under a broad range of stress, strain, and strain-rate conditions. Computer programs and additional subroutines for the STEALTH finite difference code were developed to evaluate material model parameters. A unique iterative algorithm was formulated to use both SHB and plate impact test results. The parameters for the B-P model, D_o, n, m_o, m_1, α, Z_o, and Z_o were obtained for all five metals tested with D_o assumed constant. The three steels and aluminum were characterized using only D_o, n, m_o, Z_o, and Z_1. However OFHC copper, due to its strong strain-hardening behavior, was modeled with additional constants m_1 and α.

Dynamic tensile failure in the selected metals was characterized. Since the objective was to provide the capability to predict failure in engineering calculations, simple failure models were used. Spall failure was characterized with 1) a simple time independent critical spall stress criterion, and 2) the Tuler-Butcher time dependent damage model. The spall models

TABLE 11

HIGH STRAIN RATE MEASUREMENT TECHNIQUES
USED IN THIS PROGRAM

Apparatus	Deformation	Strain Rate (s^{-1})	Parameters Determined
SHB-Tension	1-D σ	Steady to 10^3	σ_t, ε_t
	$\sigma_{m/y}$ to about 1	10^4 in neck	σ_{eff}, ε_p
			σ_{ult}
SHB-Compression	1-D σ	Accelerated to 10^3	$Y(\varepsilon)$
Plate Impact	1-D strain	10^8 - 10^6	HEL
	First Compression then tension		Spall
Taylor Impact* (C-S camera)	Compression	Decellerate from 10^4	Y
Double plate Impact*	1-D strain	10^5 - 10^6 s^{-1}	Recompaction

* Technique that was developed, but has not yet been used for evaluating material parameters.

were used only with a rate-independent, elastic-perfectly plastic material description.

The following sections summarize the critical test data and the model parameters in the high strain-rate material characterization of 1020, C1008, HY100 steels, OFHC copper, 7039-T64 aluminum, and BeO ceramic.

4.1   SUMMARY OF CRITICAL TEST DATA

The critical test data from the various experiments are presented in terms of figures and tables for all six materials. Based on these results, certain observations on rate dependency, strain at failure, stress at failure, and spall characteristics were made and are summarized in the following paragraphs.

a.   <u>1020 steel</u>

This steel showed considerable rate dependency between the strain rates of 10^{-4}/s and 400/s as can be seen from Figure 111. Since the strain rates associated with the HEL were not experimentally obtained, the HEL is represented by a scatter band between the strain rates of 10^4 and 10^5 s^{-1} in Figure 111. Between 400 and 1200/s, there was less rate dependency. However, trends could not be quantified due to test to test variability. Compression data at 2000 s^{-1} agreed with tensile data at 1200 s^{-1} and HEL data, which implies rate independency and isotropy. Key data are displayed in Figure 5.

The effective stress vs. effective plastic strain data obtained from necking specimens are shown in Figure 41. The increase in stress due to an increase in strain-rate during the necking, is not significant for this material. The stress at large strains and at higher strain-rates agreed with the stress at 1000/s, indicating that this material is relatively rate-independent above a strain rate of approximately 400/s.

The maximum stress obtained at the end of the first pulse from the SHB test, along with the strains at onset of necking and failure are summarized in Table 3.

203
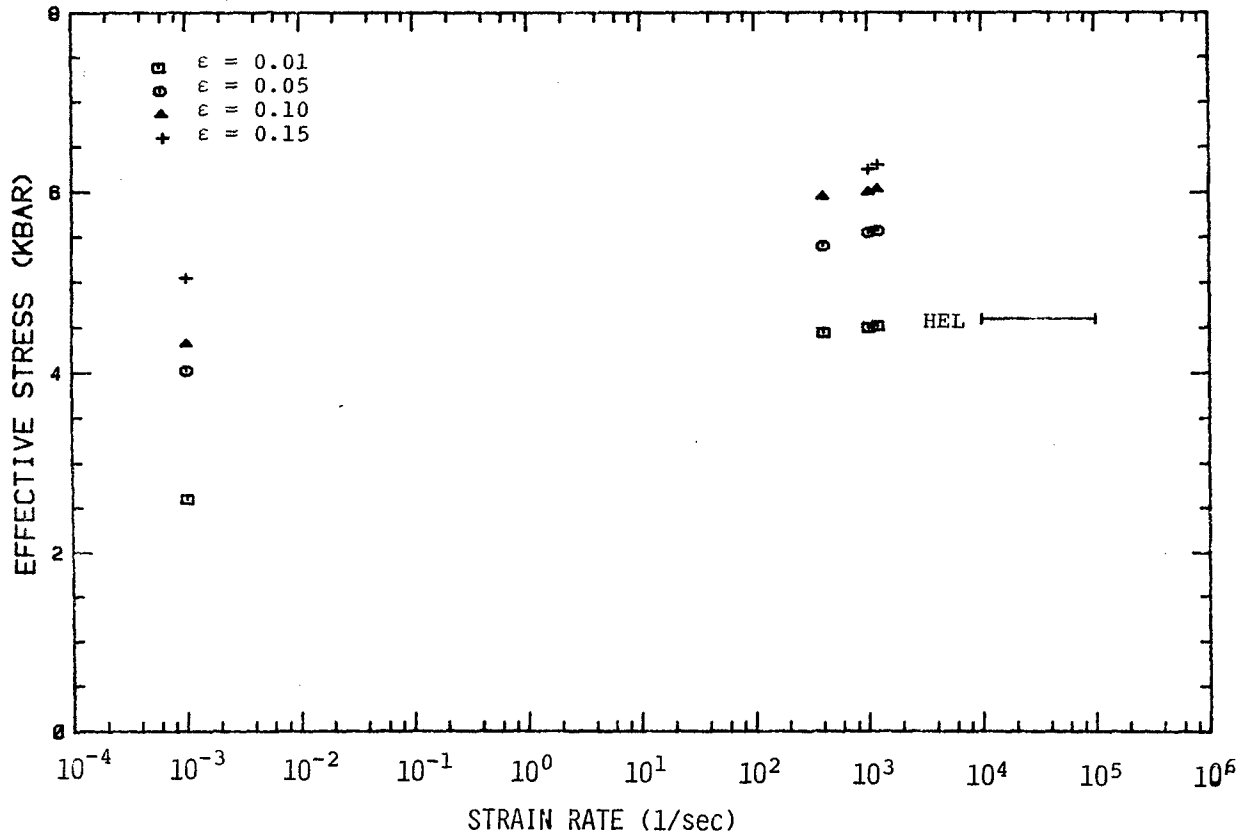
Figure 111.   Strain Rate vs. Stress Behavior for 1020 Steel.

b.   OFHC copper

It is well known that OFHC copper is a highly rate dependent material. SHB test data clearly showed this behavior. In Figure 112 stress vs. strain-rate at various strain levels is plotted. The quasi-static flow stresses are also included. This material exhibited a strong strain-hardening even at large strain values. The strain hardening, $\frac{\partial \sigma}{\partial \varepsilon}$, is an increasing function of strain rate over the range of strain and strain rate tested. Comparison of tension and compression data shows this copper is anisotropic.

The results of various SHB tensile tests are shown in Figure 11. Necking did not occur during the first tensile pulse, so the effective stress at large local strains could not be obtained. The failure parameters obtained from the photographs are summarized in Table 3. Various HEL and spall parameters from earlier work are summarized in Table 12.

c.   C1008 steel

Quasi-static and SHB tensile and compression tests were conducted. Stress vs. strain-rate plots at different strain rate levels are shown in Figure 15. Based on these data, it is concluded that C1008 steel is a rate dependent material. When the initial yield stresses at various intermediate strain-rate levels were compared with the σ_{HEL} (at very high strain-rate level), the rate dependency was quite evident. Figure 113 summarizes the various stress-strain data obtained from both the quasi-static and SHB tests.

Necking did not occur during the first load cycle. Hutchinson and Neal (Reference 50) proposed that rate dependency delays neck formation. This theory is consistent with our observation on OFHC copper and C1008 steel. Failure strains were calculated from post test measurements and are reported in Table 3.

Several plate impact tests were conducted and free surface data were obtained. Rounding and ramping were observed in most free surface velocity records. Code simulations showed

TABLE 12

OBSERVED HEL AND SPALL THRESHOLDS FOR CRACK FORMATION

Material	HEL** * (Kbar)	Spall Impact Velocity** (M/S)	Spall Stress, σ_s (Kbar)
C1008	11.3	168 $\pm$ 10	18
HY100	15.5	190 $\pm$ 10	27
7039-T64	7.7	>162	13

*
  1 Kbar = 14504 psi

        = 100 MPA

        = 10^9 dynes/cm^2

**
  3mm flyer plates
  6mm target plates
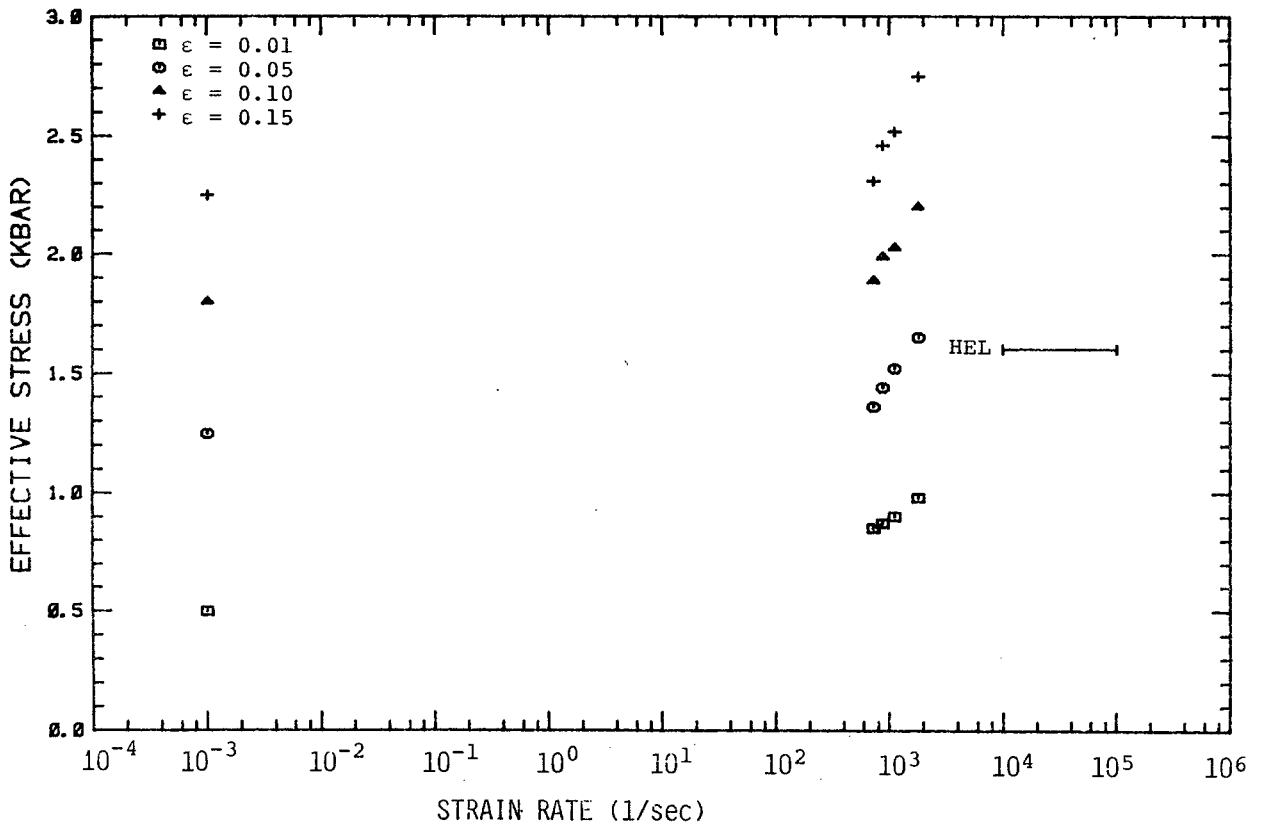
Figure 112. Strain Rate vs. Stress Behavior for OFHC Copper.
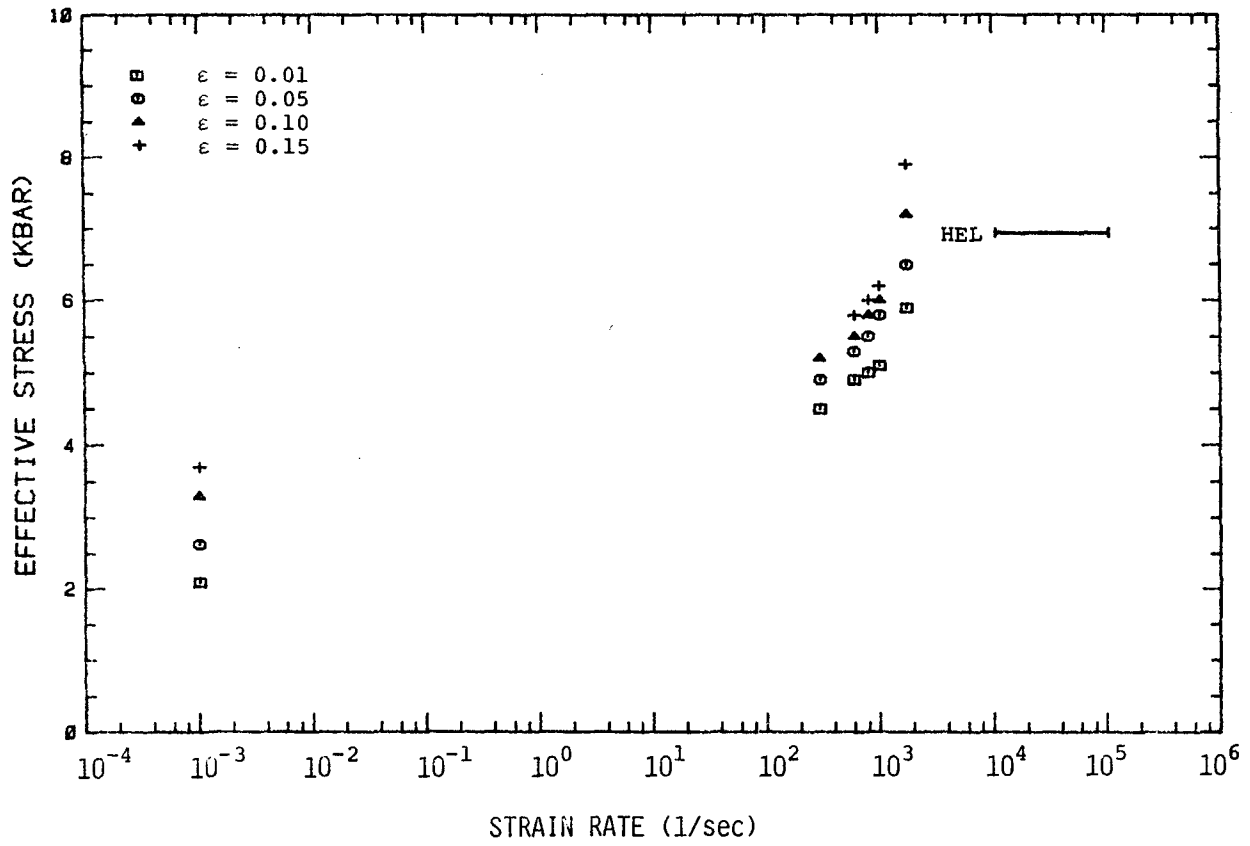
Figure 113.   Strain Rate vs. Stress Behavior of C1008 Steel.

that this behavior is caused by strong dependence of flow stress on strain rate. (This effect is masked in copper by large strain hardening.) In Table 12, results from the plate impact tests are summarized in terms of values for stresses and velocities at HEL and spall threshold.

d.   HY100 steel

The experiments on HY100 steel indicate that it is moderately strain-rate sensitive. Quasi-static and several SHB test results are summarized in stress vs. strain-rate plots at various strain levels in Figure 114. The Y_O obtained from the plate impact test results is also included in this figure. The increase in the initial flow stress due to strain-rate is moderate for this material. The stress-strain data (average curve fits of the test data) from the SHB tensile tests and the quasi-state test are summarized in Figure 19. The slight rate dependency of this material can be seen from this figure.

Three necking experiments were conducted on HY100 steel. The effective stress vs. effective plastic strain deduced from the photographs using Bridgman analysis is plotted in Figure 46. The value of effective stress at 60 percent strain was around 12 Kbar. Comprehensive failure parameters obtained from these necking tests are summarized in Table 3. Several plate impact tests were conducted. Excellent VISAR data were obtained and the results are summarized in Table 12.

e.   7039-T64 aluminum

The results in terms of stress vs. strain-rate from the SHB and quasi-static tests are plotted in Figure 115. Y_O derived from the plate impact tests is also included in the figure. The tests clearly indicate that 7039-T64 aluminum is a rate insensitive material. Sample stress-strain data are displayed in Figure 22.

Three necking experiments were conducted. The aluminum samples did not begin to neck during the first pulse. During the second pulse, the necking began at a strain of 25
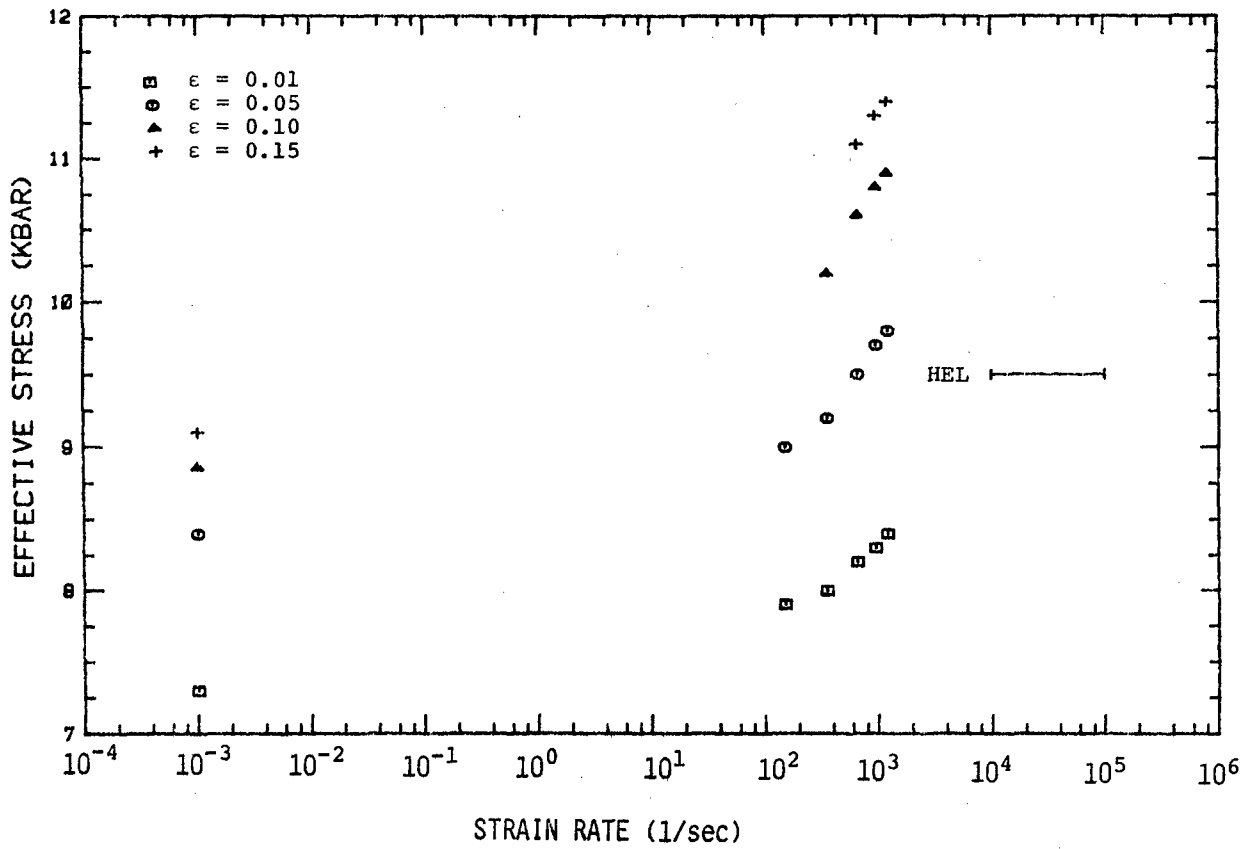
Figure 114.   Strain Rate vs. Stress Behvaior of HY100 Steel.
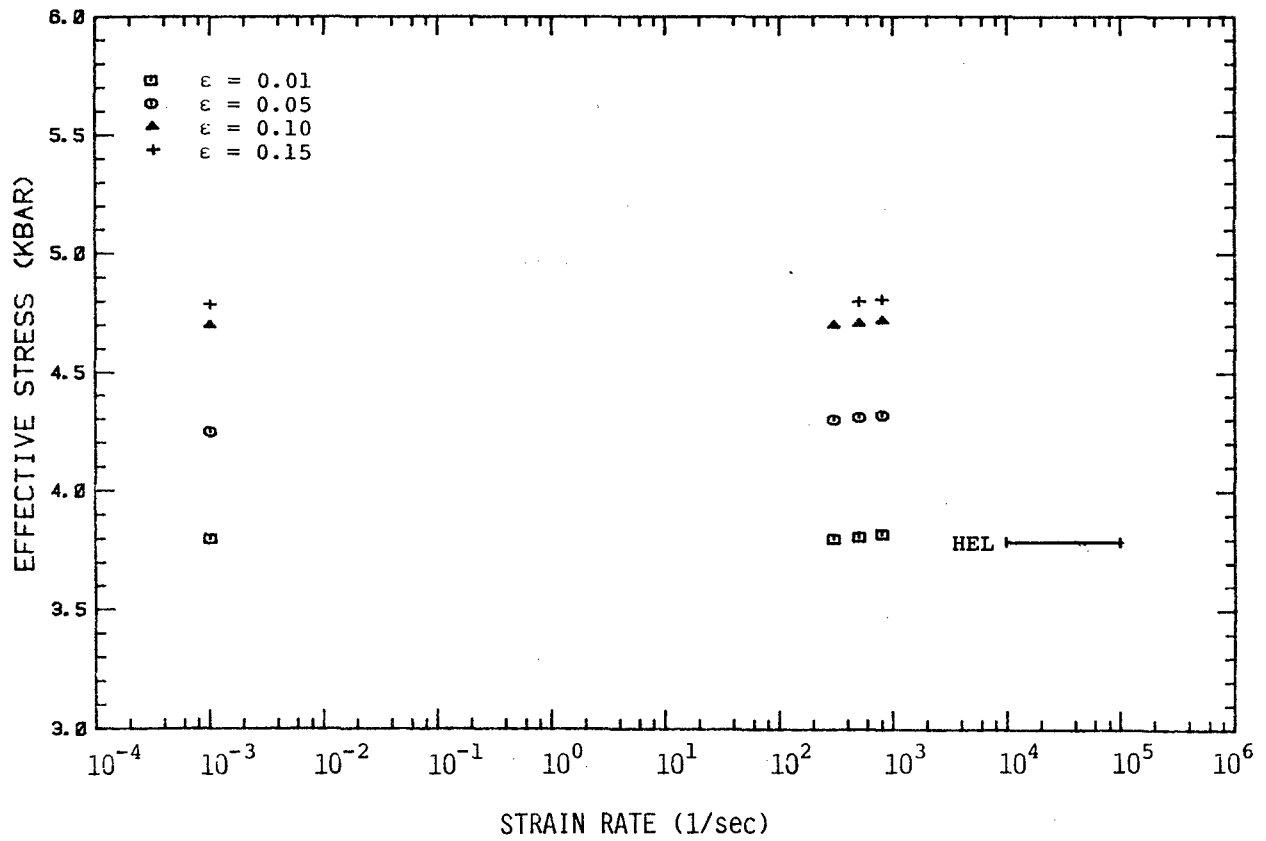
Figure 115.   Strain Rate vs. Stress Behavior of 7039-T64
Aluminum.

percent and the sample failed rapidly with little additional necking. The failure strain listed in Table 3 was obtained from post-test measurements. Reshocks in this material traveled at the elastic wavespeed. The plate impact test results are summarized in Table 12.

   f.   BeO ceramics

   The Hugoniot of polycrystalline BeO with 0.6 to 1.6 percent porosity was measured to 110 Kbar. The data are presented in Figure 64. The measured HEL values were extrapolated to 96 Kbar for zero-porosity ceramic. The spall stress for elastic shocked material was about 1.8 Kbar. The spall stress of material shocked above the HEL was negligible. In material experiencing only elastic shocks, spall seems to occur over a region, rather than on a well defined plane (Figure 67).

4.2   SUMMARY OF MODEL PARAMETERS

   In this section, the results from the Bodner-Partom material modeling are summarized for the five metals. The calibrated model parameters are described in Table 10. The parameter n indicates the level of strain-rate sensitivity. Its value is inversely proportional to the level of rate dependency. For example, a value of 0.3 indicates significant rate sensitivity and a value of 4 indicates negligible sensitivity. The parameter m (or m_0) indicates the level of strain hardening. A higher value for m indicates strong strain hardening. The difference in the values of Z_0 and Z_1 indicates the difference between initial yield stress and stress at large strain.

   For each material, the model simulations and the corresponding test results are summarized in various figures. Two spall criteria, (critical spall stress and Tuler-Butcher model) were used in the spall modeling. The model parameters were obtained from STEALTH simulations. The results are summarized in Table 10.

a.   1020 steel

        Based on the experimental results, this material is
characterized as rate independent (for the strain rates of
interest here). The interpretation is based on SHB and plate
impact data for 1020 steel targets and for C1008, HY100, and
7039-T64 aluminum targets struck by 1020 steel flyer plates. To
accurately simulate release characteristics with STEALTH, it was
necessary to describe 1020 steel with Y_o = 4.6 Kbar, the value
obtained in SHB tests. When Bless et al., (Reference 44) modeled
the behavior of 1020 steel with the HULL code, they had to assume
a stress-strain model which is consistent with the present SHB
test results, providing additional evidence that 1020 steel is
relatively rate independent. The Bodner-Partom material model
parameters are given in Table 9. This table also contains the
values of elastic constants obtained from the literature. The
program BPSOLVE was used to simulate the tensile and compression
SHB tests with the BP parameters (Table 9). The agreement with
the sets of SHB data was excellent. Representative comparisons
are shown in Figure 83. STEALTH was used with the same
parameters to simulate plate impact tests (Figure 85).

b.   OFHC copper

        This rate sensitive material could not be modeled
with only Z_o, Z_1, n, m_o, and D_o. Additional constants m_1 and α
were needed due to its strong strain hardening. Large differences
between the initial yield stress and the flow stresses at high
strains were observed. The values of Z_o(=9) and Z_1(=72) clearly
indicate this behavior. The model constants are given in Table 9.
The model predictions compared extremely well with the test results
as shown in Figures 86 and 88. The spall model parameters obtained
through SWAP simulations are summarized in Section 3.4.

c.   C1008 steel

        The ability of the BP model to describe the SHB and
plate impact data was fully satisfactory. The parameters are
summarized in Table 9. The relatively small value of n (0.4)
indicates significant rate sensitivity. Use of the simple spall

213

model was adequate to simulate the observed free surface velocity histories. However, data are available only for one flyer plate thickness, so the generality of the spall criteria could not be fully assessed. This is also true for HY100 and 7039-T64 aluminum.

      d.   HY100 steel

From the experimental results, HY100 steel was considered to be a moderately rate-sensitive material. This is reflected by the value of the BP-model parameter n (1.2) as given in Table 9. Using the model parameters in Table 9 for HY100 steel, simulations of SHB tests and the plate impact tests were successfully made and the results are summarized in Figures 100 and 102. The spall parameters for the two spall criteria are summarized in Table 10.

      e.   7039-T64 aluminum

The Bodner-Partom model constants were obtained from the SHB and plate impact test data. Since this material is a rate independent material, the model parameter n(=4) takes a large value. A convenient feature of Bodner-Partom visco-plastic model is its ability to describe even a rate independent solid through suitably selected material constants. The algorithm developed to describe BP-model in STEALTH is then valid for materials with and without rate-sensitivity. Similarly, both elastic-plastic strain hardening and elastic-perfectly plastic material can be described by the same algorithm. The BP-model parameters enabled successful simulations of both SHB tests and plate impact tests.

4.3   RECOMMENDATIONS

The following recommendations on experimental techniques and modeling are made based on the results presented in this report.

4.3.1   Experimental Technique

The expanding ring test technique should be refined and applied to ductile metals. Data from this test should be used to validate the Bodner-Partom parameters for very high tensile

strain rates, larger strains, and varying strain rates. This test has been developed in previous work by Warnes (Reference 51), Bless et al., (Reference 6) and Rajendran and Fyfe (Reference 52). It should not be difficult to develop procedures to routinely obtain reliable data with which constitutive models can be evaluated.

The double flyer plate technique should be applied systematically to metals and ceramics. It should be used to obtain data for the strength and modulus of damaged material in or near the spall plane. In order to be most useful, the double flyer technique should be combined with soft recovery techniques.

The pressure-shear impact technique developed by Kim and Clifton (Reference 53) should be used to obtain data for validating material modeling under combined normal and shear stress state conditions. Experiments in which conventional spall failure occurs will provide data for the strength of spalled material. Experiments in which failure occurs behind the shear wave will show how failure depends on shear stress. These experiments should be conducted for values of σ_{eff}/σ_m that are typical in impacts of engineering or military importance.

4.3.2   Material Modeling

The evaluation of constitutive model parameters must include the data obtained from the varieties of tests so that the calibrated model could predict the flow stresses under different extremes of stress, strain and strain-rate states.

More work is needed to develop a comprehensive failure criterion that is of sufficient generality. The spall criteria used in the present report, for example, will not in general describe failure in SHB tests and vice versa. Continuum mechanics based models that incorporate fundamental micro-mechanisms, should be exercised in finite difference codes for meaningful predictions.

The failure models that are currently available in literature, must be tested for their generality. Yield models of

215

damaged materials which explicitly include porosity, the second deviatoric stress invariant and the mean stress, must be validated through data obtained from the double flyer plate test. The spall data from the pressure-shear experiment will be useful to model the influence of shear stresses on damage nucleation, growth, and failure models.

Additional plate impact experiments with thicker flyer plates ($\sim$10mm) should be conducted on 1020, C1008, and HY100 materials. Data should be obtained for precursor decay. The anomalous ramping in C1008 steel should be verified and investigated.

Finally, the developed techniques must be used to characterize other materials of engineering importance, for example: high density penetrator alloys, structural metals, metals used in explosive forming, composite materials, and ceramics such as, BeO and TiB_2.

REFERENCES

1.   Zukas, J., "Numerical Simulation of Impact Phenomena,"
     Impact Dynamics, Chapter 10, John Wiley, New York,
     pp. 367-417, (1981).

2.   Nicholas, T., "Material Behavior at High Strain Rates,"
     Impact Dynamics, John Wiley, New York, New York, Chapter 8,
     pp. 277-331, (1981).

3.   Rajendran, A. M., Bless, S. J., Dawicke, D. S., Paisley, D. L.,
     and Grove, D. J., "High Strain Rate Characterization of
     C1008, HY100 Steel, and 7039-T64 Aluminum," AFWAL-TR-84-4103,
     June 1984.

4.   Bodner, S. R., and Partom, Y., "Constitutive Equations for
     Elastic-Viscoplastic Strain Hardening Materials," J. of
     Applied Mechanics, Vol. 42, pp. 385-389, (1975).

5.   Nicholas, T., "Dynamic Tensile Testing of Structural
     Materials Using a Split Hopkinson Bar," AFWAL-TR-80-4053,
     October 1980.

6.   Bless, S. J., Rajendran, A. M., Dawicke, D. S., and Paisley,
     D. L., "High Strain Rate Characterization of Materials,"
     AFWAL-TR-83-4038, August 1983.

7.   Considere, A., "L'Emplui Du Fer et De L'Acier Dans Les
     Constructions," Ann. Ponts Cahussee, Vol. 9, 574, 1885.

8.   Bridgman, P. W., Studies in Large Plastic Flow and Fracture,
     Chapter 1, McGraw Hill, 1952.

9.   Hancock, H. W. and Mackenzie, A. C., "On the Mechanisms of
     Ductile Failure in High Strength Steels Subject to Multiaxial
     States of Stress," J. Mech. Phys. Solids 1, 213, 107, (1976).

10. Norris, D. M., Moran, B., Scudder, J. K., and Quinones, D. F.,
     "A Computer Simulation of the Tension Test," J. Mech. Phys.
     Solids 26, pp. 1-19, (1978).

11. Brockman, R. A., "MAGNA: A Finite Element Program for the
     Materially and Geometrically Nonlinear Analysis of Three-
     Dimensional Structures Subjected to Static and Transient
     Loading," AFWAL-TR-80-3152, January 1981.

12. "STEALTH, Lagrange Explicit Finite-Difference Code for
     Solids, Structural, and Thermohydraulic Analysis," EPRI NP-
     2080, November 1981.

13. Cross, L. A., Bless, S. J., Rajendran, A. M., Strader, E. A.,
     and Dawicke, D. S., "New Technique to Investigate Necking in a
     Tensile Hopkinson Bar," Exp. Mech., pp. 184-186,
     September 1984.

14. Bauer. D. P., and Bless, S. J., "Strain Rate Effects on Ultimate Strain of Copper," AFML-TR-79-4021, November 1978.

15. Bless, S. J., Challita, T. C., and Rajendran, A. M., "Dynamic Tensile Test Results for Several Metals," AFWAL-TR-82-4026, April 1982.

16. Bluhm, J. I., and Morrissey, R. J., "Fracture in a Tensile Specimen," Proceeding of the First International Conference Fracture, 1739-1780, (1965).

17. Asay, J. R., and Lipkin, J., "A Self-Consistent Technique for Estimating the Dynamic Yield Strength of a Shock-Loaded Material," Journal of Applied Physics, Vol. 49, pg. 4242, (1978).

18. McQueen, R. G., Marsh, S. P., Taylor, J. W., Fritz, J. N., and Carter, W. J., "The Equation of State of Solids from Shock Wave Studies," in High Velocity Impact Phenomena, R. Kinslow, ed., (1970).

19. Bless, S. J., "Spall Criteria for Several Metals," AFWAL-TR-81-4040, June 1981.

20. Barker, L. M., and Hollenbach, R. E., "Lasar Interferometer for Measuring High Velocities of any Reflecting Surface," J. Appl. Phys., Vol. 43, No. 11, pp. 4669-4674, November 1972.

21. Seaman, L., Barbee, T. W., and D. R. Curran, "Dynamic Fracture Criteria of Homogeneous Materials," AFWAL-TR-71-156, December 1971.

22. Stevens, A. L. and Tuler, F. R., "Effect of Shock Pre-compression on the Dynamic Fracture Strength of 1020 Steel and 6061-T6 Aluminum," J. Appl. Phys., 42, pp. 5665-5670, (1971).

23. Taylor, J. W., "Dislocation Dynamics and Dynamic Yielding," J. Appl. Phys., 36, pp. 3146-3150, (1965).

24. Rosenberg, A. E. and Partom, Y., "Recording the Shock Wave Structure of Iron with Commercial Magnanin Gauges," J. Phys. E., 16, pp 198-200, (1983).

25. Marsh, S. P., ed., "LASL Shock Hugoniot Data," U. C. Press, 1980.

26. Soga, N., "Elastic Constants of Polycrystalline BeO as a Function of Pressure and Temperature," J. Am. Cer. Soc., 52, pp. 246-249, (1969).

27. Gust, W. H., and Royce, E. B., "Dynamic Yield Strength of Light Armor Materials," LRL-UCRL-50901.

28. Yaziv, D. and Bless, S. J., "Shock Properties of BeO Ceramic," Report UDR-TR-84-143, University of Dayton Research Institute, Dayton, Ohio, December 1984.

29. Asay, J. R., Chhabildas, L. C., and Dandekar, D. P., "Shear Strength of Shock-Loaded Polycrystalline Tungsten," J. Appl. Phys., 51, pp. 4774-4783, (1980).

30. Grady, D. E., "High Pressure Research," Edited by M. H. Manghmani, S. Akimoto, pp. 389-438, Acad. Press (1977).

31. Yaziv, D., PhD Thesis, University of Dayton, 1985.

32. Steinberg, D. J., "Equations of State for the Ceramics BeO and BeC," UClD-16946, November 1975.

33. Linde, R. K., Seaman, L., and Schmidt, D. N., "Shock Response of Porous Copper, Iron, Tungsten, and Polyurethane," J. Appl. Phys., 43, pp. 3367-3375, (1972).

34. Dandekar, D. P., "Loss of Shear Strength in Polycrystalline Tungsten Under Shock Compression," J. Appl. Phys., 47, p. 4703, (1976).

35. Munson, D. E., and Lawrence, R. J., "Dynamic Deformation of Polycrystalline Alumina," J. Appl. Phys., 50, p. 6272, (1979).

36. Yaziv, D., and Bless, S. J., "Shock Fracture and Recompaction of Copper," Proceedings of Army Symposium on Solid Mechanics, October 1984.

37. Taylor, G. I., "The Use of Flat-Ended Projectiles for Determining Dynamic Yield Stress," Proceedings Roy. Soc. London A 194, pp. 289-299, (1948).

38. Wilkins, M. L., and Guinan, M. W., "Impact of Cylinders on a Rigid Boundary," J. Appl. Phys., Vol. 44, No. 3, March 1973.

39. Perzyna, P., "Fundamental Problems in Viscoplasticity," Advances in Applied Mechanics, Vol. 9, Academic Press, New York, 1966.

40. Malvern, L. E., "The Propagation of Longitudinal Waves of Plastic Deformation in a Bar Exhibiting a Strain-Rate Effect," J. of Applied Mechanics, Trans. ASME, Vol. 18, p. 203, (1951).

41. Kreig, R. P., Swearenger, J. C., and Rohde, R. W., "A Physically-Based Internal Variable Model for Rate Dependent Plasticity," Proceedings ASME/CSME PVP Conference, pp. 15-27, (1978).

42. Chaboche, J. L., "Thermodynamic and Phenomenological Description of Cyclic Viscoplasticity with Damage," Translation of Publication No. 1978-3 of the Office National d'Etudes et du Researches Aeroatiales, France, Publication No. ESA-TT-548, May 1979.

43. Rajendran, A. M., and Grove, D. J., "Bodner-Partom Model in STEALTH," UDR-TM-84-47, University of Dayton, December 1984.

44. Bless, S. J., Barber, J. P., and Matuska, D., "Impact Induced Tensile Failures in Steel," High Pressure Science and Technology, ed. B. Vodar and Ph. Marteau, pp. 1029-1031, 1980.

45. Bless, S. J., and Barber, J., "Impact Induced Tensile Failures in Steel," AFML-TR-79-4020, February 1979.

46. Bless, S. J., and Paisley, P., "Dynamic Tensile Fracture of OFHC Copper," Proc. Third APS Topical Conference on Shock Waves in Condensed Matter, Santa Fe, July 1983.

47. Tuler, F. R., and Butcher, B. M., "A Criterion for the Time Dependence of Dynamic Fracture," Int. J. Fracture Mechs., 4, pp. 431-437, (1968).

48. Bertholf, L. D., Buxton, L. D., Thorne, B. J., Byers, R. K., Stevens, A. L., and Thompson, S. L., "Damage in Steel Plates from Hypervelocity Impact II. Numerical Results and Spall Measurement," J. Appl. Phys., Vol. 96, pp. 3776-3783, (1975).

49. Barker, L. M., and Young, E. G., "SWAP-9: An Improved Stress Wave Analyzing Program," SLA-74-0009, June 1974.

50. Hutchinson, J. W., and Neale, K. W., "Influence of Strain Rate Sensitivity on Necking Under Uniaxial Tension," Acta Metall., Vol. 25, p. 839, (1977).

51. Warnes, R. H., et al., "An Improved Technique for Determining Dynamic Material Properties Using the Expanding Ring," Shock Waves and High-Strain-Rate Phenomena in Metals, ed. M. A. Meyers and L. E. Murr, Plenum Press, 1981.

52. Rajendran, A. M. and Fyfe, I. M., "Inertia Effects on the Ductile Failure of Thin Rings," J. of Appl. Mech., Vol. 49, p. 31, March 1982.

53. Kim, K. S., and Clifton, R. J., "Pressure-Shear Impact of 6061-T6 Aluminum," J. Appl. Mech., Vol. 47, pp. 11-16, (1980).

APPENDIX A

A1. Flow Diagram for Bodner-Partom Model in STEALTH.

START

BODPAR requires K, G, $\dot{\varepsilon}$, Δt, s_{ij}^0, $\dot{s}_{ij}^0$, $(W^p)^0$, $(\varepsilon_{xx}^p)^0$, $\Delta\varepsilon_{max}$, (D_2^p) min. and the time step cut parameters

COMPUTE CONSTANTS FOR DEVIATORIC STRESS COMPUTATIONS

$C_1 = K + 4G/3$
$C_2 = K - 2G/3$
$C_3 = G$
$P = - K \dot{\varepsilon}$

COMPUTE NUMBER OF SMALL TIME STEPS

$N_s = \text{INT} \left[|\dot{\varepsilon}| \Delta t / \Delta\varepsilon_{max} + 0.99 \right]$

COMPUTE LENGTH OF SMALL TIME STEP

$\Delta t_s = \Delta t / N_s$

LOCALLY INITIALIZE OLD QUANTITIES

$s_{ij}^{old} = s_{ij}^0$, $\dot{s}_{ij}^{old} = \dot{s}_{ij}^{old}$,
$W^p = (W^p)^0$, $\varepsilon_{xx}^p = (\varepsilon_{xx}^p)^0$

LOOP OVER SMALL TIME STEPS

CALL SIJNEW

SIJNEW computes s_{ij}^{new}, $\dot{s}_{ij}^{new}$ for current time step

USE TIME STEP CUT FACTOR TO INCREASE N_s

ARE NEW STRESSES VALID ?

Did all the s_{ij}^{new} converge?

ARE MORE TIME STEP CUTS ALLOWED ?

STOP

CALL EPIJ

EPIJ computes the new plastic strain rates, $\dot{\varepsilon}_{ij}^p$

UPDATE PLASTIC WORK AND PLASTIC XX STRAIN

$W^p = W^p + \dot{W}^p t_s$
$\varepsilon_{xx}^p = \varepsilon_{xx}^p - \dot{\varepsilon}_{xx}^p \Delta t_s$

UPDATE LOCAL STRESSES FOR NEXT TIME STEP

$s_{ij}^{old} = s_{ij}^{new}$
$\dot{s}_{ij}^{old} = \dot{s}_{ij}^{new}$

END OF LOOP

STORE NEW PLASTIC FLOW AND DEVIATORIC STRESS QUANTITIES

$s_{ij}^N = s_{ij}^{new}$, $\dot{s}_{ij}^N = \dot{s}_{ij}^{new}$,
$(W^p)^N = W^p$, $(\dot{\varepsilon}_{xx}^p)^N = \dot{\varepsilon}_{xx}^p$
$(\varepsilon_{xx}^p)^N = \varepsilon_{xx}^p$

RETURN

BODPAR returns s_{ij}^N, $\dot{s}_{ij}^N$, (W^p), (ε_{xx}^p), and $(\varepsilon_{xx}^p)^N$ via common block /ZONVAR/

A2.   Flow Chart for the Subroutine BODPAR.

A-3

```
                    ┌─────────────┐
                    │    START    │─────────  SIJNEW requires $c_1$, $c_2$, $c_3$, $\dot{p}$,
                    └─────────────┘           $\Delta t_s$, $\dot{w}^p$, $s_{ij}^{old}$, $\dot{s}_{ij}^{old}$, and the
                           │                  input convergence parameters
                    ┌─────────────┐
                    │ CALL SIJEST │─────────  SIJEST computes the initial
                    └─────────────┘           deviatoric stress estimates, $s_{ij}^{est}$
                           │
                    ┌─────────────┐
                    │ LOOP OVER   │
                    │ MAXIMUM NUMBER │
                    │ OF ITERATIONS │
                    │ ALLOWED     │
                    └─────────────┘
                           │
                    ┌─────────────┐
                    │ CALL SDOTIJ │─────────  SDOTIJ computes the new
                    └─────────────┘           deviatoric stress gradients, $\dot{s}_{ij}^{new}$
                           │
                    ┌─────────────┐
                    │ COMPUTE NEW │
                    │ DEVIATORIC  │─────────  $s_{ij}^{new} = s_{ij}^{old} + \dot{s}_{ij}^{new}\Delta t_s$
                    │ STRESSES    │
                    └─────────────┘
                           │
                    ┌─────────────┐
                    │ CALL SIJDIF │─────────  SIJDIF computes the relative
                    └─────────────┘           difference between $s_{ij}^{est}$ and $s_{ij}^{new}$
                           │
                    ◇─────────────◇
                    │    HAVE     │
            YES     │ ALL THE DEVIATORIC │─────  Is the maximum relative
            ◄───────│ STRESSES CONVERGED │       difference (from SIJDIF)
                    │      ?      │             within the convergence
                    ◇─────────────◇             tolerance?
                           │ NO
  ┌──────────────┐  ┌─────────────┐
  │ INDICATE SUCCESSFUL │ USE RELAXATION │
  │ CONVERGENCE BY │  │ FACTOR TO DEFINE │
  │ SETTING CONVERGENCE │ DEVIATORIC STRESS │──  $s_{ij}^{est} = r s_{ij}^{new} + (1-r)s_{ij}^{est}$
  │ FLAG EQUAL TO 1 │  │ ESTIMATES FOR NEXT │
  └──────────────┘  │ ITERATION   │
                    └─────────────┘
                           │
                    ┌─────────────┐
                    │ END OF      │
                    │ ITERATION   │
                    │ LOOP        │
                    └─────────────┘
                           │
                    ┌─────────────┐
                    │ INDICATE CONVERGENCE │
                    │ FAILURE BY SETTING │
                    │ CONVERGENCE FLAG │
                    │ EQUAL TO 0  │
                    └─────────────┘
                           │
                    ┌─────────────┐
                    │   RETURN    │─────────  SIJNEW returns $\dot{s}_{ij}^{new}$,
                    └─────────────┘           $s_{ij}^{new}$, and a convergence
                                              flag via the argument list
```

A3.   Flow Chart for the Subroutine SIJNEW.

START

SIJEST requires C_1, C_2, C_3, $\dot{P}$, Δt_s, W^P, S_{ij}^{old}, and $\dot{S}_{ij}^{old}$

USE OLD STRESS GRADIENTS TO COMPUTE FIRST SET OF DEVIATORIC STRESS ESTIMATES

$(S_{ij}^{est})_1 = S_{ij}^{old} + \dot{S}_{ij}^{old} \Delta t_s$

CALL SDOTIJ

SDOTIJ uses the $(S_{ij}^{est})_1$ to compute new deviatoric stress gradient estimates, $\dot{S}_{ij}^{est}$

USE NEW STRESS GRADIENT ESTIMATES TO COMPUTE SECOND SET OF DEVIATORIC STRESS ESTIMATES

$(S_{ij}^{est})_2 = S_{ij}^{old} + \dot{S}_{ij}^{est} \Delta t_s$

AVERAGE THE TWO SETS OF ESTIMATES TO OBTAIN BETTER INITIAL ESTIMATES FOR THE DEVIATORIC STRESSES

$S_{ij}^{est} = \frac{1}{2}\left[(S_{ij}^{est})_1 + (S_{ij}^{est})_2\right]$

RETURN

SIJEST returns S_{ij}^{est} via the argument list

A4.   Flow Chart for the Subroutine SIJEST. Improved
      Sij Values are Estimated in this Routine.

START

$\left\{\begin{array}{l}\text{SDOTIJ requires } C_1, C_2, C_3, \dot{P},\\ W^P, S_{ij}, \text{ and } \dot{\epsilon}_{ij}\end{array}\right.$

CALL EPIJ

$\left\{\begin{array}{l}\text{EPIJ computes the plastic}\\ \text{strain rates, } \dot{\epsilon}_{ij}^P\end{array}\right.$

COMPUTE THE
ELASTIC
STRAIN RATES

$\left\{\ \dot{\epsilon}_{ij}^e = \dot{\epsilon}_{ij} - \dot{\epsilon}_{ij}^P\right.$

COMPUTE THE
DEVIATORIC
STRESS
GRADIENTS

$\left\{\begin{array}{l}\dot{S}_{xx} = C_1\dot{\epsilon}_{xx}^e + C_2\dot{\epsilon}_{yy}^e + C_2\dot{\epsilon}_{zz}^e + \dot{P}\\[4pt] \dot{S}_{yy} = C_2\dot{\epsilon}_{xx}^e + C_1\dot{\epsilon}_{yy}^e + C_2\dot{\epsilon}_{zz}^e + \dot{P}\\[4pt] \dot{S}_{zz} = C_2\dot{\epsilon}_{xx}^e + C_2\dot{\epsilon}_{yy}^e + C_1\dot{\epsilon}_{zz}^e + \dot{P}\\[4pt] \dot{S}_{xy} = 2C_3\,\dot{\epsilon}_{xy}^e\\[4pt] \dot{S}_{yz} = 2C_3\,\dot{\epsilon}_{yz}^e\\[4pt] \dot{S}_{xz} = 2C_3\,\dot{\epsilon}_{xz}^e\end{array}\right.$

RETURN

$\left\{\begin{array}{l}\text{SDOTIJ returns } \dot{S}_{ij}\\ \text{via the argument list}\end{array}\right.$

A5. Flow Chart for the Subroutine SDOTIJ. Sij are
     Computed in this Routine.

START

EPIJ requires S_{ij}, W^p, D_o, m, n, Z_o, Z_1, (σ_{eff})min, and (D_2^p)min

INITIALIZE PLASTIC FLOW PARAMETERS

$D_2^p = 0.0$
$\dot\varepsilon_{ij}^p = 0.0$

COMPUTE EFFECTIVE STRESS SQUARED

$\sigma_{eff}^2 = \frac{3}{2} \Sigma\, S_{ij}^2$

IS FLOW DEFINITELY ALL ELASTIC ?   YES

Is $\sigma_{eff} < (\sigma_{eff})$min?

NO

COMPUTE THE INTERNAL STATE VARIABLE THAT GOVERNS RESISTANCE TO PLASTIC FLOW

$Z = Z_1 - (Z_1 - Z_0)e^{-mW^p}$

COMPUTE SECOND INVARIANT OF THE DEVIATORIC PLASTIC STRAIN RATE

$D_2^p = D_o^2\, e^{-[(Z^2/\sigma_{eff}^2)^n\,(n+1)/n]}$

IS FLOW COMPLETELY ELASTIC ?   YES

Is $D_2^p < (D_2^p)$min?

NO

COMPUTE THE PLASTIC STRAIN RATES

$\lambda = \sqrt{3 D_2^p / \sigma_{eff}^2}$
$\dot\varepsilon_{ij}^p = \lambda S_{ij}$

RETURN

EPIJ returns D_2^p and $\dot\varepsilon_{ij}^p$ via the argument list

A6.   Flow Chart for the Subroutine EPIJ. $\dot\varepsilon_{ij}^p$ are Computed in this Routine.

START

SIJDIF requires S_{ij}^{est} and S_{ij}^{new}

INITIALIZE
MAXIMUM
RELATIVE
DIFFERENCE

$D_R^{max} = 0.0$

LOOP OVER ALL
DEVIATORIC
STRESSES

INITIALIZE RELATIVE
DIFFERENCE FOR
CURRENT DEVIATORIC
STRESS

$D_R = 0.0$

CAN
RELATIVE DIFFERENCE
BE COMPUTED
?

NO

Either $S_{ij}^{est} \neq 0.0$
or $S_{ij}^{new} \neq 0.0$?

YES

COMPUTE RELATIVE
DIFFERENCE BETWEEN
ESTIMATED AND
COMPUTED VALUES
FOR CURRENT
DEVIATORIC STRESS

$$D_R = \frac{|S_{ij}^{new} - S_{ij}^{est}|}{MAX(|S_{ij}^{new}|, |S_{ij}^{est}|)}$$

KEEP TRACK OF
MAXIMUM RELATIVE
DIFFERENCE

$D_R^{max} = MAX(D_R, D_R^{max})$

END OF LOOP

RETURN

SIJDIF returns D_R^{max}
via the argument list

A7.   Flow Chart for the Subroutine SIJDIF. Convergence
        Check of the Iterative Scheme.

A-8